Aus der

BioMed X Germany GmbH

Team Protective Tissue Factors in Autoimmune Diseases

Foundations for Pro-Resolution Target Discovery: Integrating Human Macrophage Phenotypic and Functional Diversity in Homeostasis and Immune-Mediated Inflammatory Diseases

Dissertation

zum Erwerb des Doktorgrades der Humanbiologie

an der Medizinischen Fakultät

der Ludwig-Maximilians-Universität München

vorgelegt von

Tamara Pfanner

aus

Heidelberg

Jahr

2025

Mit Genehmigung der Medizinischen Fakultät der
Ludwig-Maximilians-Universität München

Erstes Gutachten:	Prof. Dr. Christian Schulz
Zweites Gutachten:	Prof. Dr. Christoph Reichel
Drittes Gutachten:	Prof. Dr. Michael Vogeser

Dekan: Prof. Dr. med. Thomas Gudermann

Tag der mündlichen Prüfung: 20.11.2025

Table of Contents

Zusammenfassung:

Hintergrund

Die Remission bzw. das Abklingen von Entzündungen ist ein aktiver und regulierter Prozess, der nach einem akuten Entzündungsreiz die Gewebehomöostase wiederherstellt. Bei immunvermittelten entzündlichen Erkrankungen (IMIDs), wie der rheumatoiden Arthritis (RA), ist die Remission von Entzündungen entweder intrinsisch gestört oder wird durch eine übermäßige entzündliche und immunologische Reaktion auf körpereigene Strukturen aus dem Gleichgewicht gebracht, was die Chronizität und das Wiederaufflammen der Entzündung begünstigt. Infolgedessen bleibt eine langfristige Remission bei IMIDs größtenteils unerreichbar. Die therapeutische Förderung pro-resolutiver Antworten durch pro-resolutive Wirkstoffe könnte die Remissionserhaltung und den Gewebeschutz bei IMIDs unterstützen. Makrophagen (Mφ) gehören zu den zentralen Zelltypen, die die pro-resolutiven Gewebereaktionen während der Entzündung koordinieren. Einzelzell-RNA-Sequenzierungen haben unser Verständnis der transkriptionellen Vielfalt menschlicher Gewebemakrophagen in Homöostase und Krankheit erweitert. Dennoch bleiben funktionelle Spezialisierungen und pro-resolutive Zielstrukturen in menschlichen Mφ weitgehend spekulativ.

Forschungsziele

Diese Dissertation adressiert die Wissenslücke in Bezug auf die funktionelle Spezialisierung menschlicher Gewebemakrophagen durch die Entwicklung neuartiger multimodaler Einzelzellmethoden zur detaillierten Charakterisierung von Mφ-Phänotypen und -Funktionen in Gesundheit und Krankheit. Darüber hinaus werden in vitro Mφ-Modelle und funktionelle Analyseverfahren entwickelt, um Mφ-assoziierte Zielstrukturen für die Entwicklung pro-resolutiver Wirkstoffe zu identifizieren.

Hypothesen

Die Entwicklung integrierter Phänotyp-Funktion-Assays ermöglicht die Charakterisierung menschlicher Mφ-Funktionen in Gesundheit und Krankheit und hilft dabei, potenzielle Mφ-Zielstrukturen für pro-resolutive Wirkstoffentwicklungen bei IMIDs zu identifizieren.

Verschiedene *in vitro* Mφ-Modelle zeigen unterschiedliche Fähigkeiten zur Efferozytose und Eisenverwertung, was ihre Eignung für Gain- und Loss-of-Function-Studien zur Identifizierung pro-resolutiver Mφ-Zielstrukturen definiert.

Menschliche Gewebe-Mφ-Subtypen unterscheiden sich in ihrer Kapazität zur Efferozytose und Eisenverwertung, was ihre Rolle bei Entzündung und dessen Abklingen in IMIDs beeinflusst.

Methoden

Ich habe skalierbare *in vitro* Mφ-Plattformen etabliert und charakterisiert, darunter iPSC-abgeleitete und monozyten-abgeleitete Mφ-Modelle. Ich habe multimodale Phänotyp-Funktion-Mφ-Assays entwickelt, die spektrale Durchflusszytometrie mit mehr als 25 Oberflächenmarkern und drei funktionellen Ausleseverfahren kombinieren. Funktionelle Daten wurden zusätzlich mittels konfokaler Mikroskopie validiert. Primäre humane Mφ, isoliert aus Synovialgewebe und -flüssigkeit von Patienten mit aktiver bzw. remissionärer entzündlicher Arthritis, wurden mittels CITE-Sequenzierung und Phänotyp-Funktions-Analysen durch spektrale Durchflusszytometrie charakterisiert.

Ergebnisse

Der neu entwickelte *Discoverer Mφ Assay* ermöglichte eine robuste gleichzeitige Analyse von Mφ-Oberflächenmarkern und -Funktionen, einschließlich Efferozytose, Phagozytose und Eisenverwertung. Die Funktionsausleseparameter, z. B. Efferozytose, wurden über verschiedene ex-

perimentelle Bedingungen (z. B. unterschiedliche Inkubationszeiten, Zellverhältnisse, Inhibitorbehandlungen) und Mφ-Typen hinweg validiert und ermöglichten die Bestimmung optimaler Bedingungen für die Charakterisierung von Gewebe-Mφ sowie für funktionelle CRISPR-/Toolmolekül-Screenings.

Mit dem *Discoverer Mφ Assay* konnte ich funktionelle Unterschiede zwischen *in vitro* Mφ-Modellen nachweisen, was ihre differenzierte Eignung für Gain- und Loss-of-Function-Studien mit Toolmolekülen oder CRISPR-gestützten genetischen Manipulationen verdeutlicht. Beispielsweise zeigten iPSC-differenzierte Mφ eine erhöhte Efferozytose-Kapazität, was sie für Efferozytose Loss-of-Function Studien besonders geeignet macht, während iMicroglia ein geeigneteres Modell für Studien zum Zugewinn von Efferozytose darstellten. Einzelzell-CITE-Seq-Daten aus dem Synovialgewebe zeigten unterschiedliche FOLR2$^+$ gewebeständige und CCR2$^+$ inflammatorische Mφ-Subtypen. Mithilfe von *Discoverer Mφ* konnte ich eine variable Anreicherung dieser Mφ-Populationen in Synovialgewebe- und -flüssigkeitsproben von Patienten mit entzündlicher Arthritis nachweisen. Erste Daten zu Phagozytose und Eisenstoffwechsel wiesen auf mögliche subtypspezifische Funktionen synovialer Mφ hin. Die multimodale Integration von *Discoverer Mφ* mit Transkriptom- und Protein-Daten unterstützt ein verfeinertes Modell der Heterogenität synovialer Mφ und verknüpft spezifische Mφ-Subtypen mit Entzündung oder Gewebehomöostase.

Fazit

In dieser Dissertation habe ich eine neuartige funktionelle Analyseplattform sowie ein Multi-Omics-Analyse-Framework zur Untersuchung der Heterogenität menschlicher Mφ in Homöostase und Krankheit entwickelt. Die entwickelten Methoden stellen ein wertvolles Instrument für die Auswahl geeigneter Mφ-Modelle und funktioneller Ausleseparameter für Screenings mit Toolmolekülen oder genetischen Modifikationen dar. Meine Forschung liefert grundlegende Werkzeuge zur Identifikation und gezielten Ansprache pro-resolutiver Mφ-Subtypen und unterstützt die Entwicklung Mφ-orientierter Therapien bei IMIDs.

Stichworte:

Makrophagen, immunvermittelte entzündliche Erkrankungen, integrierte Funktion-Phänotyp-Makrophagenanalyse, Efferozytose, Eisenverwertung, Entzündung, spektrale Durchflusszytometrie, Einzelzell-Multiomics, CRISPR und Toolmolekül-Screening

Abstract (English):

Background

Resolving inflammation is an active and regulated process that restores tissue homeostasis following an acute inflammatory insult. In immune-mediated inflammatory diseases (IMIDs), such as rheumatoid arthritis (RA), the resolution of inflammation is either intrinsically impaired or outbalanced by an excessive inflammatory and immune response to self, fueling the chronicity and relapsing nature of inflammation. Consequently, long-term IMID remission remains largely elusive. Enhancing pro-resolution responses therapeutically with pro-resolution drugs could promote remission maintenance and tissue protection in IMIDs. Macrophages (Mφ) are one of the central cell types orchestrating the pro-resolving tissue responses during inflammation. Single-cell RNA-sequencing studies advanced our understanding of transcriptional diversity of human tissue Mφ in homeostasis and disease. Yet, functional specialization and pro-resolution targets in human Mφ remain largely speculative.

PhD Thesis Objectives:

This PhD thesis addresses the knowledge gap in functional specialization of human tissue Mφ by developing novel single-cell multimodal tools for in-depth characterization of Mφ phenotypes and functions in health and disease. Moreover, in vitro Mφ models and function readouts are developed, facilitating the discovery of Mφ-linked targets for pro-resolution drug development.

Hypothesis

Developing integrated phenotype-function assays facilitates the characterization of human Mφ functions in health and disease, helping us identify candidate Mφ targets for pro-resolution drug development in IMIDs.

Different *in vitro* Mφ models exhibit distinct efferocytosis and iron recycling abilities, defining their applicability in gain-and-loss of function studies to discovery pro-resolution Mφ targets.

Human tissue Mφ subsets differ in efferocytosis and iron recycling capacities, influencing their roles in inflammation and pro-resolution in IMIDs.

Methods

I established and characterized scalable *in vitro* Mφ platforms, including iPSC-derived and monocyte-derived Mφ models. I developed multimodal phenotype-function Mφ assays, employing spectral flow cytometry analyses with over 25 surface markers and three Mφ function readouts. Confocal microscopy was used to validate functional flow cytometry data. Primary human Mφ, isolated from synovial tissue and fluid of patients with active/remission inflammatory arthritis, were characterized using CITE-sequencing and function-phenotype spectral flow cytometry analyses.

Results

The newly developed *Discoverer Mφ* Assay enabled robust simultaneous profiling of Mφ surface markers and functions, including efferocytosis, phagocytosis, and iron recycling.

The function readouts, e.g., efferocytosis, were validated across multiple experimental conditions (e.g, variable incubation times, cell ratios, inhibitor treatments) and *Mφ* types, determining optimal conditions for tissue Mφ characterization and functional CRISPR/tool molecule screens. Using *Discoverer Mφ,* I demonstrated functional divergence of *in vitro* Mφ models, guiding their differential utility for gain-and-loss-of-function studies with tool molecules/CRISPR-based genetic perturbations. For example, iPSC-derived Mφ showed enhanced efferocytosis capacity, supporting

loss-of-efferocytosis studies with tool molecules, while iMicroglia appeared to be a more suitable model for gain-of-efferocytosis studies. Synovial single-cell CITE-seq data revealed distinct FOLR2$^+$ tissue-resident and CCR2$^+$ inflammatory Mφ subsets. Using *Discoverer Mφ*, I demonstrated a variable enrichment of these Mφ populations across synovial tissue and synovial fluid samples from patients with inflammatory arthritis. Pilot phagocytosis and iron metabolism data revealed potential subset-specific synovial Mφ functions. The multi-modal integration of *Discoverer Mφ* with transcriptomic and protein-level data supports a refined model of synovial Mφ heterogeneity, linking specific Mφ subsets to inflammation or tissue homeostasis.

Conclusion

In this PhD thesis, I established a novel functional profiling platform and multi-omics analysis framework for dissecting human Mφ heterogeneity in homeostasis and disease.

The developed methods represent an invaluable tool for guiding the selection of Mφ models and readouts for function screens using tool molecules or genetic perturbations. My research provides foundational tools for identifying and targeting pro-resolving Mφ subsets and supports the development of Mφ-directed therapies in IMIDs.

Keywords:
Macrophages, immune-mediated inflammatory diseases, integrated function-phenotype macrophage analysis, efferocytosis, iron recycling, inflammation resolution, spectral flow cytometry, single-cell multiomics, CRISPR and tool molecule screening

List of Figures

List of Tables

Glossary

Abbreviation	Meaning
ACK	Ammoniumchlorid-Kalium-Lysepuffer
ADT	antibody-derived tag
ATF3	Activating Transcription Factor 3
ATP	adenosine triphosphate
Axl	AXL Receptor Tyrosine Kinase
BAI1	brain-specific angiogenesis inhibitor 1
BSA	Bovine serum albumin
C1Q	Complement C1q
CD	Cluster of differentiation
CharON	Caspase and pH Activated Reporter, Fluorescence ON
CR	Complement receptors
CSP	Cell Surface Protein
DAMPs	Danger-associated molecular patterns
DC	dendritic cells
DC	dendritic cells
DMARD	Disease-Modifying Anti-Rheumatic Drugs
DMSO	dimethylsulfoxide
ECM	extracellular matrix
EDTA	Ethylenediaminetetraacetic acid
FACS	Fluorescence Activated Cell Sorting.
FAS	ferric ammonium citrate
FBS	fetal bovine serum
FcRs	Fc receptors
FLS	fibroblast like synoviocytes
FOLR2	Folate Receptor Beta
FPR2	Formyl Peptide Receptor 2
Gas6	Growth Arrest Specific 6
GEM	Gel Bead-in-Emulsions
GM-CSF	Granulocyte-macrophage colony-stimulating factor
HEPES	(4-(2-hydroxyethyl)-1-piperazineethanesulfonic acid)
IBD	inflammatory bowl disease
IgG	immunoglobulin G
IL-10	Interleukin310
IL-1β	Interleukin 1 beta
iMicroglia	iPSC derived microglia cells
IMID	Immune mediated inflammatory diseases
iMφ	iPSC derived macrophage
IPF	induced pulmonary fibrosis
IPS	idiopathic pulmonary fibrosis
iPSC	induced pluripotent stem cell
JT	Jurkat T cell
KLF2	Krüppel-like factor 2
KLF4,	Krüppel-like factor 2
KO	knock out
LPC	lysophosphatidylcholine
LPS	Lipopolysaccharide
LXA4	Lipoxin A4
LXB4	Lipoxin B4
M-CSF	macrophage colony-stimulating factor
MDM	monocyte derived macrophages
MerTK	MER Proto-Oncogene, Tyrosine Kinase
MMP	matrix metalloproteinases

MS	Multiple Sclerosis
Mφ	macrophage
NFκB	nuclear factor-κB
NR4A1/2	Nuclear Receptor Subfamily 4 Group A Member 1
OA	Osteo Arthritis
PAMPs	pattern associated molecular patterns
PBMCs	Peripheral blood mononuclear cells
PBS	Phosphate-buffered saline
PDAC	pancreatic ductal adenocarcinoma
PEG	acid-sensitive polyethylene glycol
PS	phosphatidylserine
RA	Rheumatoid Arthritis
Rac1	Rac Family Small GTPase 1
RBC	Red blood cell
Rho	Rhodopsin
ROS	reactive oxygen species
RT	room temperature
RvD,	Resolvin D
RvE	Resolvin E
S1P	sphingosine-1-phosphate
scRNA	single cell RNA
scRNAseq	single cell RNA sequencing
SLE	systemic lupus erythematosus
SPARC	secreted protein acidic and rich in cysteine
SPM	specialized pro-resolving mediator
SPMs	specialized pro-resolving mediators
SR-A	Scavenger Receptor Class B Member 1
synMφ	synovial tissue macrophages
TAM	TAM receptor tyrosine kinases
taMφ	tumour associated macrophages (usually referred to as TAM, however this also stands for receptor tyrosine kinases)
TET	Tet Methylcytosine Dioxygenase
TGF-β	Transforming growth factor β
TIMD-4	T-cell immunoglobulin and mucin domain-containing protein 4
tiMφ	tissue infiltrating macrophage
TLR	toll-like receptors
TME	tumor microenvironment
TNF-α	tumour necrosis factor alpha
TREM2	Triggering Receptor Expressed On Myeloid Cells 2
trMφ	tissue resident macrophage
Tyro3	TYRO3 Protein Tyrosine Kinase
UTP	uridine triphosphate
VEGF	Vascular Endothelial Growth Factor
WHO	world health organization
WT	wild type
αvβ3	Integrin Subunit Alpha 3
αvβ5	Integrin Subunit Alpha 5

1. Introduction

1.1 Resolution of Inflammation in Immune-Mediated Inflammatory Diseases

Resolving inflammation is an active and tightly controlled biological process aimed at restoring tissue balance following an immune response to infection or injury (Schett & Neurath, 2018). The inflammatory phase and resolution of inflammation ensure the elimination of harmful stimuli while preventing excessive tissue damage and restoring normal function (Figure 1-1) (Buckley et al., 2013).

When resolution mechanisms fail or are dysregulated, inflammation persists, contributing to chronic immune activation and tissue damage. This failure underpins the pathogenesis of immune-mediated inflammatory diseases (IMIDs), including rheumatoid arthritis (RA), systemic lupus erythematosus (SLE), and multiple sclerosis (MS) (McInnes & Gravallese, 2021). Prolonged inflammation in these disorders leads to irreversible tissue destruction, increased susceptibility to secondary infections, and heightened risk of comorbidities such as cardiovascular disease and cancer (Schett & Neurath, 2018).

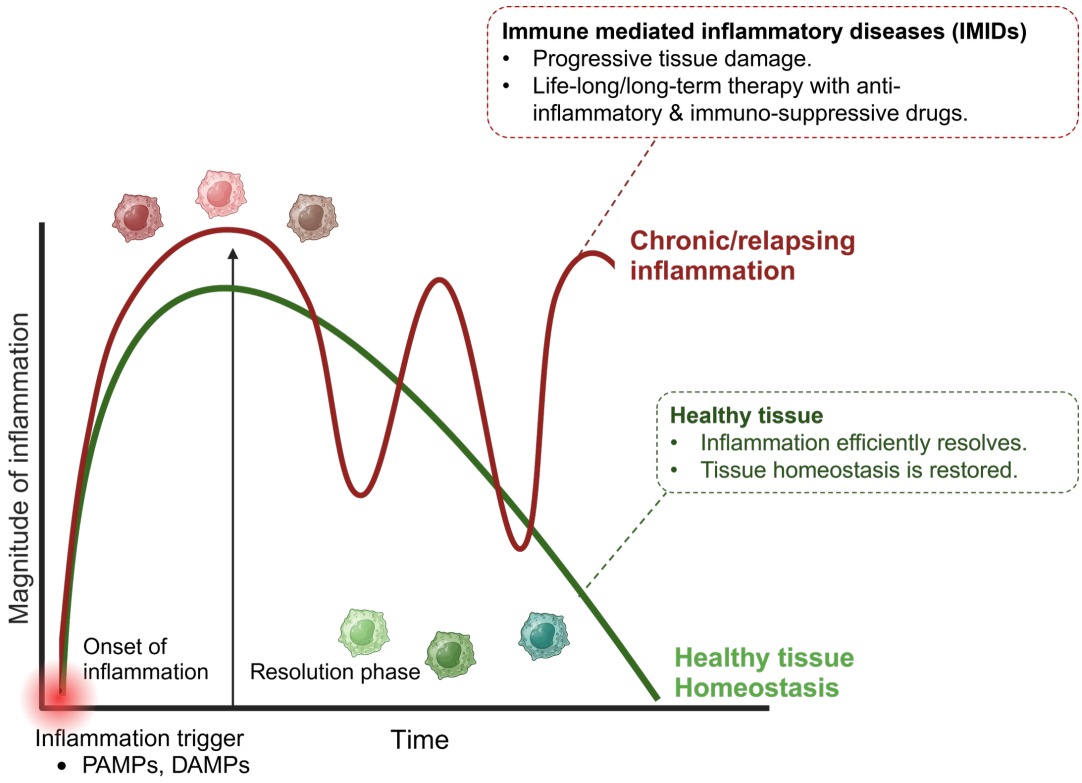

Figure 1-1 Inflammation and resolution of inflammation. The magnitude of inflammation rises upon infection or tissue injury, driven by generation of PAMPs (pattern associated molecular patterns) or DAMPs (danger-associated molecular

patterns), then declines during the resolution phase of inflammation, in which tissue homeostasis is reinstated. Resolution is impaired or imbalanced in immune-mediated inflammatory diseases. *Adapted from Schett & Neurath, 2018. Created with BioRender.*

The mechanisms underlying inflammation resolution involve multiple cellular and molecular pathways. One key aspect is the cessation of neutrophil recruitment and their removal through apoptosis and subsequent efferocytotic clearance of apoptotic neutrophils by macrophages (Mφ). The phenotypic shift of pro-inflammatory Mφ toward an anti-inflammatory and pro-resolving state, induced upon apoptotic cell engulfment, represents one of the mechanisms contributing to the termination of inflammation (Serhan & Levy, 2018). Additionally, specialized lipid mediators such as resolvins, as well as cytokines such as IL-10 and TGF-β, contribute to this process by modulating immune cell function and promoting tissue repair (Komai et al., 2018). Importantly, while many resolution mechanisms are conserved across tissues, additional organ-specific regulatory pathways modulate immune responses locally. Understanding both universal and tissue-specific resolution mechanisms is critical to identifying novel therapeutic targets that promote pro-resolving tissue mechanisms and help maintain remission in IMIDs.

Complementary to broadly suppressing immune responses by anti-inflammatory or immunosuppressive drugs, targeted approaches aiming to restore homeostatic balance by promoting pro-resolution mechanisms could offer effective treatments for IMIDs with potentially fewer long-term adverse effects and improved life quality (Serhan & Levy, 2018). Different cell types drive the resolution of inflammation, with resident Mφ playing one of the central roles. The capacity to clear dying cells, regulate inflammation, and promote tissue repair positions tissue resident macrophages (trMφ) as promising therapeutic targets (Morioka et al., 2019). This research focuses on RA as a prototypic non-resolving IMID model, in which Mφ drive diverse pathogenic as well as pro-resolving functions. IMIDs have unique but also shared pathogenic mechanisms. Studying Mφ functions in RA may provide valuable insight into RA-specific as well as IMID-shared pro-resolution mechanisms and therapeutic targets.

1.2 Rheumatoid Arthritis: An IMID Model for Studying Non-Resolving Inflammation and Remission

Rheumatoid arthritis (RA) is a systemic autoimmune disorder primarily affecting synovial joints, causing persistent synovial inflammation, progressive joint destruction, and significant disability. It affects around 1% of the global population and often begins during middle adulthood, with a higher prevalence in women (70%). Local RA symptoms and signs include joint pain, stiffness, tenderness, swelling, and redness (WHO, 2023). Beyond joint involvement, RA is associated with systemic manifestations and increased risk of comorbidities, including cardiovascular disease, which is the leading cause of death in RA patients (Smolen et al., 2018) diabetes and osteoporosis (Crowson et al., 2013; Moshayedi et al., 2022).

The primary site of the disease in RA is synovial tissue. The synovial tissue, or synovial membrane, is a connective tissue that lines the inner surface of the joint capsule of synovial joints. Healthy synovial lining consists of two layers: 1. the lining layer, which contains tissue resident lining Mφ and lining fibroblast-like synoviocytes (FLS), and 2. the sublining layer, composed of connective tissue, sublining FLS, trMφ, blood/lymphatic vessels, and scarce immune cells (Figure

1-2). The synovial tissue produces synovial fluid, a viscous liquid rich in hyaluronic acid and lubricin, which lubricates the joint, nourishes cartilage, and absorbs mechanical forces during joint movements (Smith, 2011).

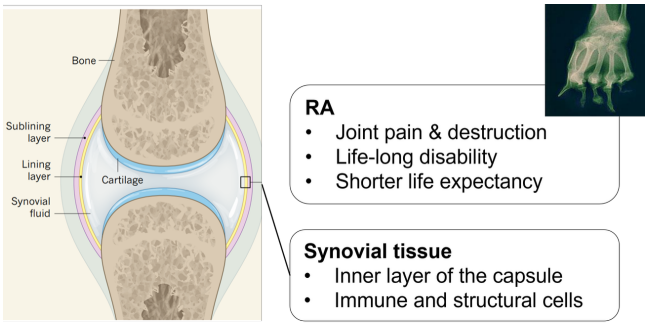

Figure 1-2 Synovium in Rheumatoid Arthritis. *Created with BioRender.*

RA is characterized by chronic immune system activation that is linked to the loss of immune tolerance for self. This process involves both the activation of innate and adaptive immune responses. Autoantibodies, including rheumatoid factors and anti-citrullinated protein antibodies, are present in a larger proportion of patients with RA, defined as seropositive RA, which commonly takes a more destructive disease course compared to seronegative RA (Weyand & Goronzy, 2021).

In RA, the synovial membrane is commonly infiltrated with various immune cells, which establish a self-sustaining inflammatory synovial niche (McInnes & Schett, 2011). Within the inflamed synovium, Mφ play a central role in driving inflammatory pathology. In a healthy joint, trMφ help maintain local immune balance through debris clearance, immune modulation, and tissue surveillance (Culemann et al., 2019). However, in RA, this balance is disturbed (Figure 1-3). Large numbers of monocyte-derived, pro-inflammatory Mφ infiltrate the synovium and adopt a phenotype that supports inflammation rather than resolution. These tissue-infiltrating Mφ (tiMφ) produce high levels of inflammatory cytokines such as TNF-α and IL-1β, which further amplify immune cell recruitment and activate resident structural cells such as FLS, contributing to tissue damage (Alivernini et al., 2020)

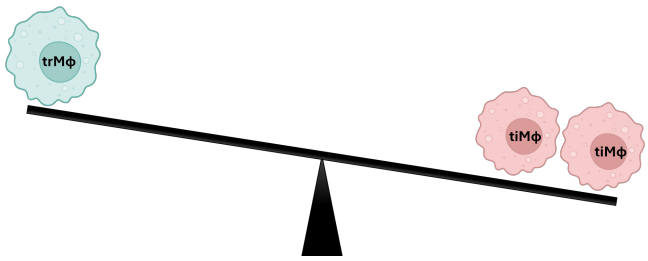

Figure 1-3 Tissue infiltrating Mφ (trMφ) outnumber tissue resident Mφ (tiMφ). *Created with BioRender.*

Importantly, the accumulation of tiMφ and the relative depletion or dysfunction of trMφ have been correlated with disease severity (Kai et al., 2024). The extent of Mφ infiltration into the synovial lining is strongly associated with clinical, imaging-based, and inflammatory indicators of arthritis activity, such as joint swelling, synovial vascularization, and circulating C-reactive protein levels, respectively (Baeten et al., 2005). Alivernini et al. (2020) further demonstrated that synovial tissue

Mφ are not only heterogeneous but also functionally distinct in different disease states. Specifically, patients in sustained remission exhibited a higher proportion of MerTK^{+}CD206^{+} Mφ that are associated with anti-inflammatory and tissue-resolving functions, while those who later experienced disease flare after anti-TNF withdrawal had increased frequencies of MerTK^{-}CD206^{-} subsets with pro-inflammatory profiles. The ratio of these subsets was found to be a strong predictor of clinical outcome following therapy cessation. These findings emphasize that Mφs are not only key effectors in RA pathogenesis but also dynamic indicators of disease trajectory and promising biomarkers for treatment stratification (Alivernini et al., 2020)

Due to its well-characterized immune landscape, RA is often used as a prototype for investigating chronic immune-mediated inflammation and failed resolution in IMIDs. Understanding how Mφ functions are altered in RA can provide a valuable framework for identifying disease-specific and universal resolution mechanisms that could inform new treatment approaches in a range of inflammatory conditions.

1.3 Macrophages

1.3.1 Macrophages in Homeostasis and Diseases

Mφ are crucial components of the immune system. They are highly adaptable cells within the hematopoietic system, present across all tissues, and exhibiting remarkable functional versatility. Mφ play essential roles in development, maintaining homeostasis, facilitating tissue repair, and supporting immune responses against pathogens. Even though Mφ in different tissues have distinct locations, unique gene expression patterns, and specialized functions, they all contribute to sustaining homeostasis (Mosser et al., 2021).

However, when exposed to persistent damage or stress, such as chronic infections, repeated tissue injury, metabolic or oxidative stress, or age-related degeneration, their beneficial functions can become dysregulated. Under these conditions, Mφ may remain in a prolonged pro-inflammatory state, overproduce cytokines, or drive excessive tissue remodeling. This maladaptive response links Mφ to the development of various diseases, making them key players in pathological conditions including autoimmune diseases, cancer, and fibrosis (Figure 1-4) (Ginhoux & Guilliams, 2016).

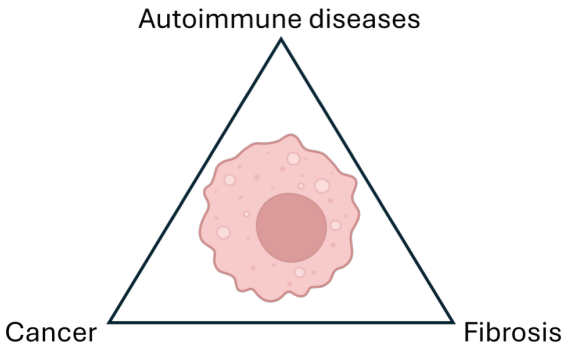

Figure 1-4 Disease triangle. *Created with BioRender.*

1.3.2 Macrophages in Homeostasis

Under steady-state physiological conditions, Mφ maintain homeostasis by performing immune surveillance, clearing apoptotic cells (efferocytosis), and modulating tissue metabolism, thereby ensuring tissue integrity and functionality. trMφ, such as Kupffer cells in the liver, resident synovial Mφ in the synovial tissue, and microglia in the brain, exhibit specialized functions tailored to their local environments. For instance, trMφ in the synovium display joint-specific immune-regulatory properties by coordinating responses to pathogens and inflammation (Knab et al., 2022). In most organs, trMφ originate from embryonic precursors, such as yolk sac and fetal liver progenitors, rather than from adult bone marrow-derived monocytes. These embryonically derived Mφ are capable of self-renewal within tissues, maintaining their populations independently of circulating monocytes (Gomez Perdiguero et al., 2015; Hoeffel & Ginhoux, 2015) and participate in metabolic regulation, debris clearance, and immune modulation to ensure tissue integrity. However, this is not true for all tissues. In the intestinal lamina propria, for instance, trMφ are not maintained by self-renewing embryonic precursors but are instead continuously replenished by circulating *Ly6C*$^+$ monocytes. These monocytes infiltrate the gut, undergo local differentiation, and acquire a tissue-specific anti-inflammatory phenotype in response to cues from the intestinal microenvironment, ensuring ongoing Mφ turnover and adaptation to microbial and dietary stimuli (De Schepper et al., 2018).

During infections or tissue injury, circulating monocytes rapidly infiltrate affected tissues and differentiate into inflammatory Mφ. What happens to these tiMφ after inflammation is resolved remains complex and context dependent. In the synovial tissue of RA patients, Alivernini et al. (2020) identified that a subset of synovial tissue macrophages (synMφ) characterized by *MerTK*$^+$*CD206*$^+$ and *CD163*$^+$ expression persists during remission and is enriched in transcriptional regulators of inflammation resolution, such as *KLF2*, *KLF4*, *NR4A1/2*, and *ATF3*. These synMφ produce inflammation-resolving lipid mediators and promote repair functions in synovial fibroblasts. Conversely, pro-inflammatory subsets (e.g., *MerTK*$^-$*CD48*$^+$*S100A12*$^+$ synMφ) are markedly diminished but not completely absent during remission, suggesting a partial but not absolute clearance of inflammatory cells. Moreover, the proportion of *MerTK*$^+$*CD206*$^+$ synMφ in remission predicts whether patients maintain remission or experience flare after treatment withdrawal, implying that some tiMφ may transition into a more regulatory phenotype. However, the persistence of certain *MerTK*$^-$ pro-inflammatory subsets even in remission, and the observation that repeated inflammatory episodes may alter Mφ ontogeny, support the hypothesis that over time, the trMφ pool becomes a mixture of embryonic and monocyte-derived cells. This finding highlights the plasticity of Mφ and the possibility that inflammatory imprinting may not be fully reversible, especially after chronic or repeated insult.

Indeed, much of what is known about Mφ functional states derives from in vitro models, where monocytes are polarized into so-called M1 or M2 phenotypes. M1-polarized Mφ, which rely heavily on glycolysis, are typically pro-inflammatory, while M2-like cells favor oxidative phosphorylation and support tissue repair (Chen et al., 2023). However, these in vitro-derived designations do not fully capture the complexity of in vivo Mφ biology. In tissues, Mφ states exist along a spectrum, with overlapping functions that include pro-resolving, pro-fibrotic, and even tumor-promoting activities. While M2-polarized cells may mimic aspects of resolution, they also share features with Mφ involved in pathological tissue remodeling (He et al., 2021). It is therefore critical to recognize the limitations of these simplified models and acknowledge that in vivo Mφ phenotypes are dynamic and highly context dependent.

1.3.3 Macrophages in Diseases

1.3.3.1 Autoimmune Diseases and IMIDs:

Mφ contribute to the pathogenesis of various autoimmune and IMIDs, including RA, SLE, MS, and inflammatory bowel disease (IBD), where they act as both initiators and sustainers of chronic inflammation. Roles of Mφ in autoimmune diseases and IMIDs are being increasingly recognized (Yang et al., 2023).

SLE has been associated with defective macrophage-mediated clearance of apoptotic cells (efferocytosis). In individuals with SLE, apoptotic cells often accumulate in the germinal centers of lymph nodes, and macrophages isolated from these patients frequently exhibit a diminished ability to engulf and digest these dying cells (Baumann et al., 2002). This impaired clearance of dead cells is considered a contributing factor to the development of SLE. In the accumulating cellular debris, nuclear antigens become exposed, fueling anti-nuclear autoantibody production and systemic inflammation (Mehrotra & Ravichandran, 2022). In MS, Mφ chronic microglial inflammatory activity is accompanied by the release of pro-inflammatory mediators, directly contributing to demyelination and neurodegeneration, both in patients and animal models (Distéfano-Gagné et al., 2023). In IBD, Mφ play an important, yet paradoxical role as they act on the one hand as maintainers of intestinal homeostasis and on the other hand, they are key drivers of inflammation. Under normal conditions, intestinal Mφ are highly specialized to remain hyporesponsive to microbial stimuli, supporting tissue repair and immune tolerance through mechanisms such as IL-10 production and efferocytosis. However, in IBD, this balance is disrupted, and a distinct population of monocyte-derived Mφ accumulates in the inflamed mucosa. These cells exhibit heightened pro-inflammatory activity, secreting cytokines such as TNF, IL-1β, IL-6, and IL-23, and are associated with pathogenic T cell response (Hegarty et al., 2023).

Despite differences in the affected organs, a common feature across IMIDs is the dysregulation of Mφ plasticity, the ability of Mφ to shift between inflammatory and regulatory phenotypes (Kourtzelis et al., 2021). The ratio between pro-inflammatory and anti-inflammatory Mφ is outbalanced and favors an inflammation-sustaining state, impairing resolution and promoting tissue pathology (Zheng et al., 2024).Targeting Mφ activation and promoting their reprogramming toward a pro-resolving, anti-inflammatory phenotype has emerged as a promising therapeutic avenue in autoimmune diseases. Rather than broadly suppressing immune responses, such approaches aim to restore immune balance by enhancing the natural resolution of inflammation.

1.3.3.2 Cancer

In cancer, Mφ within the tumor microenvironment (TME), defined as tumor-associated Mφ (taMφ) can make up to 50% of tumour infiltrating immune cells (Li et al., 2022). taMφ typically support tumor progression by suppressing immune responses (Pan et al., 2020). They secrete immunosuppressive cytokines such as IL-10 and TGF-β, which impair cytotoxic T-cell recruitment and activity, thereby promoting an immunosuppressive milieu. Furthermore, taMφ enhance tumor vascularization by releasing vascular endothelial growth factor (VEGF), which facilitates tumor growth and metastasis (Cendrowicz et al., 2021).

Beyond tumor progression, dysregulated Mφ can also contribute to cancer initiation and development. Chronic inflammation increases the risk of malignant transformation (Multhoff et al., 2012). Chronically activated Mφ release proinflammatory cytokines, including IL1a, IL1b and TNFα

(Coussens & Werb, 2002). While TNFα can initiate immune responses, it also has pro-tumorigenic roles. Upon binding to its receptors (TNFR1/2), TNFα activates the nuclear factor-κB (NF-κB) signaling pathway, promoting cancer cell proliferation and survival by regulating genes such as VEGF and IL-6 and Matrix Metallo Proteases (MMPs), and supporting neoangiogenesis (Chanmee et al., 2014). High taMφ infiltration often correlates with poor prognosis as they promote metastasis, making them a compelling target for therapeutic intervention (Zhao et al., 2021).

1.3.3.3 Fibrosis

Fibrosis arises from dysregulated tissue repair mechanisms and is marked by persistent fibroblast activation and progressive loss of normal tissue function. It plays a central role in the development of organ failure across a range of chronic illnesses and age-associated disorders (Benn et al., 2023). Although fibrosis is a natural component of the healing process following tissue injury, prolonged inflammation or severe damage can disrupt this balance, resulting in abnormal extracellular matrix (ECM) buildup and structural disorganization that compromises organ integrity (Coulis et al., 2023). In fibrosis, Mφ play a dual role by influencing fibroblast activation and ECM deposition (Duffield et al., 2005; Wynn & Ramalingam, 2012). In liver fibrosis, hepatic Mφ regulate disease progression by secreting pro-fibrotic cytokines such as TGF-β and platelet-derived growth factor, which promote myofibroblast proliferation, survival, and migration, thereby activating hepatic stellate cells to produce collagen (Wynn & Barron, 2010). In idiopathic pulmonary fibrosis (IPF), Mφ exacerbate fibrotic remodeling by enhancing fibroblast proliferation and survival (Misharin et al., 2017; Perrot et al., 2023).

Conversely, certain Mφ subsets contribute to the resolution of fibrosis by degrading ECM components through the secretion of matrix metalloproteinases (MMPs), including MMP-9 (targets denatured collagens), MMP-12 (degrades elastin), and MMP-1, MMP-2, and MMP-3 (involved in collagen breakdown) (Wynn & Ramalingam, 2012).

Emerging therapies aim to reprogram Mφ toward anti-fibrotic phenotypes. For example, pirfenidone and nintedanib, approved for IPF, have been shown to reduce Mφ activation and cytokine production (Richeldi et al., 2014). Moreover, a recent study showed that nanoparticles can effectively deliver small-interfering RNA targeting TGF-β1 to newly formed pro-fibrotic monocyte-derived alveolar Mφ, leading to a significant reduction in lung fibrosis in a mouse model (Singh et al., 2022). The therapeutic potential of Mφ reprogramming has also been highlighted in other research. For example, Zhang et al. (2020) developed a folate-conjugated TLR7 agonist (FA-TLR7-54) that preferentially localized to pro-fibrotic Mφ and inhibited the production of fibrosis-associated cytokines. Their findings revealed that FA-TLR7-54 converted M2-like, fibrosis-promoting Mφ into a phenotype with anti-fibrotic properties, which was associated with a marked decrease in both pro-fibrotic cytokine expression and pathological features of pulmonary fibrosis in mice (Zhang et al., 2020).

Cancer, autoimmunity, and fibrosis are interconnected through dysregulated Mφ activity. Here, we focus on a subset of Mφ functions, namely, clearance (e.g., efferocytosis) (Mehrotra & Ravichandran, 2022) and iron metabolism (Winn et al., 2020), as these are central to both maintaining tissue homeostasis and contributing to disease pathology. Understanding the shared and distinct Mφ-driven mechanisms underlying these diseases can inform novel therapeutic strategies. For instance, enhancing efferocytosis in autoimmune and IMIDs could reduce chronic inflammation and prevent fibrotic progression (Sangaletti et al., 2021), while targeting iron handling by tumor-associated Mφ may suppress tumor growth and metastasis(Y. Y. Zhang et al., 2024). However,

this therapeutic balancing act is challenging. Driving anti-inflammatory responses may inadvertently promote tumor tolerance and may be different across subtypes, while stimulating inflammation to boost anti-tumor immunity could exacerbate autoimmunity (Hou et al., 2021). Thus, precise modulation of Mφ functions, particularly those involved in clearance and iron regulation, offers a promising but delicate avenue for drug discovery.

1.4 Macrophage Functions Explained

To understand the role of Mφ in health and disease, the functions of distinct Mφ types and states must be elucidated. Currently, subset-specific Mφ functions are mainly inferred from single-cell transcriptomic studies of diseased and healthy human tissues.

1.4.1 Phagocytosis

Phagocytosis is a fundamental nutritional process in unicellular organisms and is also present in nearly all cell types of multicellular organisms (Uribe-Querol & Rosales, 2020). Nonetheless, a distinct class of cells termed professional phagocytes performs phagocytosis with exceptional efficiency, primarily Mφ, neutrophils, and dendritic cells (DCs), identify, engulf, and degrade extracellular particles larger than 0.5 µm in size, such as pathogens and cellular debris(G. C. Brown, 2024). The phagocytosis begins with the recognition of target corpuscles via specific receptors on phagocytic cells. There are several main types of phagocytosis receptors. Fc receptors (FcRs) bind to the Fc region of antibodies that have coated a pathogen, marking it for destruction. An example is the Fcγ receptor, which recognizes immunoglobulin G (IgG) antibodies. Complement receptors detect complement proteins like C3b that are deposited on target surfaces; common examples include CR1, CR3, and CR4 (S. Greenberg, 1999; Uribe-Querol & Rosales, 2020). Scavenger receptors bind to a wide range of ligands, including PAMPS such as oxidized lipids and components of dead or dying cells. Examples of these include Dectin-1(Herre et al., 2004), Mincle, MCL, and DC-SIGN. Although not classical phagocytic receptors, toll-like receptors (TLRs) also contribute by activating phagocytic cells and enhancing the expression or function of other receptors (Uribe-Querol & Rosales, 2020).

Upon binding, Mφ plasma membrane extends around the particle and changes its membrane composition to form a phagosome, which fuses intracellularly with lysosomes to become a phagolysosome (Jaumouillé & Grinstein, 2016). Within the phagolysosome, acidic pH and hydrolytic enzymes facilitate the degradation of the ingested material. Phagocytosis not only contributes to pathogen clearance but also activates signaling pathways that modulate inflammation and coordinate downstream immune responses (Kinchen & Ravichandran, 2008). Impaired or excessive phagocytic activity has been linked to infectious diseases, chronic inflammation, and immune dysregulation (G. C. Brown, 2024; Gordon, 2016).

1.4.2 Efferocytosis

Efferocytosis is a specialized form of phagocytosis, during which phagocytic cells (Mφ and DCs) clear apoptotic cells from the tissue to maintain homeostasis and prevent inflammation (Doran et al., 2020). Efferocytosis counteracts the accumulation of secondary necrotic cells with autoantigen exposure and promotes specialized pro-resolving mediator synthesis (SPM), thereby preventing autoimmune reactions, facilitating immune tolerance and accelerating resolution of inflammation (Gheibi Hayat et al., 2019)

Mechanistically, efferocytosis is divided into three sequential phases: the 'find me' phase, the 'eat me' phase, and the 'digest me' phase (Figure 1-5).

“Find Me” - Phase

In the initial ‘find me’ phase, apoptotic cells release soluble signals that attract phagocytes. Those cells release various 'find me' signals to attract phagocytes, including nucleotides like adenosine triphosphate (ATP) and uridine triphosphate (UTP), as well as molecules such as lysophosphatidylcholine (Lauber et al., 2003), sphingosine-1-phosphate (S1P) (Gude et al., 2008), and the chemokine CX3CL1, also known as fractaline (Truman et al., 2008). Phagocytes express corresponding receptors, such as P2Y2 for nucleotides, G2A for LPC, S1P receptors for S1P, and CX3CR1 for CX3CL1, thereby sensing find me signals and migrating toward apoptotic cells alongside chemotactic gradients of ‘find me’ signals (Moon et al., 2023).

'Eat Me' Phase – Apoptotic cell binding and internalization

Binding

During apoptosis, apoptotic cells relocate phosphatidylserine (PS) from the inner to the outer leaflet of their plasma membrane. Annexin 1 binds to PS, further enhancing its recognition by phagocytes. Alongside PS, C1Q is expressed on the surface, which binds to CD91 through calreticulin (Gardai et al., 2005; Ravichandran & Lorenz, 2007).Together, these molecules serve as ‘eat-me’ signals, facilitating the efficient binding and subsequent clearance of apoptotic cells (Moon et al., 2023).

Phagocytes recognize and bind to apoptotic cells through diverse surface receptors, which directly or indirectly engage with ‘eat-me’ ligands. One of the primary receptors involved in this process is TIMD-4 (T-cell immunoglobulin and mucin domain-containing protein 4) (Flannagan et al., 2014), which specifically binds to PS on the surface of apoptotic cells, facilitating their recognition. Similarly, brain-specific angiogenesis inhibitor 1 (BAI1) also recognizes PS and triggers intracellular signaling cascades that promote apoptotic cell engulfment (Das et al., 2011). In addition to these direct interactions between phagocytes and apoptotic cells, phagocytes utilize scavenger receptors such as SR-A and CD36 to bind oxidized lipids on apoptotic cells, aiding in their uptake (Greenberg et al., 2006). Another critical group of efferocytosis-linked receptors includes integrins, such as αvβ3 and αvβ5, which mediate recognition through bridging molecules for example, opsonins. Opsonins, such as milk fat globule-EGF factor 8 (MFG-E8), bind to PS on apoptotic cells and facilitate their engagement with integrins on phagocytes, enhancing apoptotic cell clearance efficiency (Arandjelovic & Ravichandran, 2015). The tyrosine receptor kinases (TAM) receptor family, comprising Tyro3, Axl, and MerTK play a crucial role in apoptotic cell recognition (B. Park et al., 2015; Seitz et al., 2007),. These receptors can interact with TIMD-4 to enhance corpse uptake (Moon et al., 2020) or bind to bridging ligands, such as Gas6 and Protein S, which interact with PS on apoptotic cells.

Together, the above-described recognition mechanisms ensure that apoptotic cells are efficiently identified, bound, and prepared for engulfment. By employing a combination of direct receptor-ligand interactions and opsonin-mediated bridging, phagocytes maintain specificity in recognizing dying cells, thereby preventing unintended engulfment of viable cells and ensuring the resolution of cellular debris in a non-inflammatory manner (Arandjelovic & Ravichandran, 2015; Ravichandran & Lorenz, 2007).

Internalization

Rac1, a Rho family GTPase, plays a crucial role in efferocytosis by driving actin-cytoskeletal rearrangement, which is essential for phagosome formation, enabling apoptotic cell internalization. In mammals, apoptotic cell recognition triggers Rac1 activation through engulfment receptors such as BAI1 (Nakaya et al., 2006,Ravichandran & Lorenz, 2007).

BAI1 directly recognizes PS on apoptotic cells and interacts with Elmo1-Dock180, functioning as a bipartite guanine-nucleotide-exchange factor to activate Rac1, leading to actin remodeling. This cytoskeletal reorganization drives membrane protrusions, such as lamellipodia or phagocytic cups, which enwrap and internalize the apoptotic cell, resulting in its engulfment (Elliott et al., 2010; D. Park et al., 2007). Similarly, Stabilin-2 promotes efferocytosis by interacting with Gulp, which also activates Rac1 (S. Y. Park et al., 2008). Integrins such as αvβ3 and αvβ5 mediate efferocytosis through a two-step process: first, they recognize bridging molecules like MFG-E8 or Gas6 bound to phosphatidylserine on apoptotic cells; second, they initiate intracellular signaling via focal adhesion kinase (FAK) and Src family kinases to activate Rac1 and promote cytoskeletal rearrangement (Ravichandran & Lorenz, 2007)

In contrast, TIMD4 primarily acts as a tethering receptor, securing apoptotic cell attachment on phagocytes, but does not directly activate Rac1. However, TIMD4 can interact with MERTK, a receptor tyrosine kinase that initiates intracellular signaling cascades leading to cytoskeletal rearrangement and apoptotic cell internalization. This interaction suggests that, beyond simply tethering apoptotic cells, TIMD4 may also contribute indirectly to signaling required for engulfment. (Moon et al., 2020).

'Digest Me' Phase

After engulfment, apoptotic cells are enclosed within a phagosome, which undergoes maturation through fusion with lysosomes, forming the phagolysosome (Mehrotra & Ravichandran, 2022). Inside the phagolysosome, apoptotic debris are degraded by lysosomal enzymes such as cathepsins and acid hydrolases. Beyond apoptotic cell clearance, efferocytosis triggers a pro-resolving response, promoting tissue repair and immune tolerance. A key component of this pro-resolving response is the production of SPMs, which include: resolvins D and E (RvD, RvE) (Dalli & Serhan, 2017), Mφ-derived SPMs called maresins (Serhan et al., 2009), protectins and lipoxins (LXA4, LXB4). Specialized lipid mediators, synthesized from omega-3 fatty acids such as eicosapentaenoic acid (EPA) and docosahexaenoic acid (Norris et al., 2018) play an active role in resolving inflammation(Serhan & Levy, 2018). SPMs enhance efferocytosis by increasing phagocyte motility and improving the clearance of apoptotic cells, while simultaneously inhibiting pro-inflammatory cytokines activity and production through decreased NFκB activity upon ALX/FPR2 interaction, such as TNF-α and IL-6 (Dalli & Serhan, 2017). Furthermore, efferocytosis leads to the secretion of anti-inflammatory cytokines, such as IL-10 and TGF-β, which suppress inflammation and stimulate tissue regeneration (Freire-de-Lima et al., 2006). Thus, the 'digest me' phase is not merely a degradation step but an integral part of the pro-resolution tissue program that restores immune homeostasis.

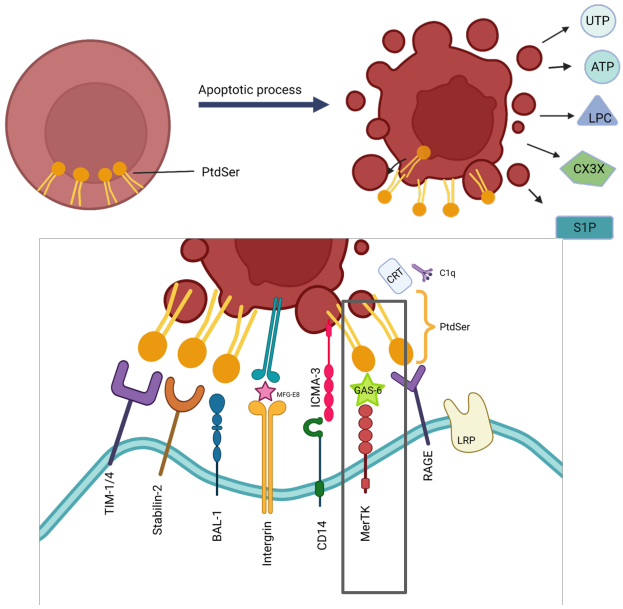

Figure 1-5 Efferocytosis process. Find me signals released from apoptotic cells into microenvironment to attract Mφ. Detection of PS on apoptotic cells by Mφ receptors leads to subsequent apoptotic cell binding and engulfment. PS phosphatidylserine, UTP: Uridintriphosphat, ATP: Adenosintriphosphat, S1P: sphingosine-1-phosphate SPM: specialized pro resolving mediator; MERTK: Proto-oncogene tyrosine-protein kinase MER. *Adapted from Gheibi Hayat et al., 2019. Created with BioRender.*

'Don´t eat me' signals

The efficiency of efferocytosis is tightly regulated by a balance between 'eat me' and 'don't eat me' signals. To evade efferocytosis, healthy cells express so-called don´t eat me signals such as CD24, CD31 (S. Brown et al., 2002) and CD47(Kojima et al., 2016). This mechanism is harnessed by cancer cells, which have been shown to be expressed across several cancer types. CD47, a transmembrane protein, interacts with ligands such as SIRPα, thrombospondin 1, and integrins, playing a crucial role in immune evasion by transmitting a "don't eat me" signal to phagocytic cells (Chao et al., 2012; Qiu et al., 2023a).

Harnessing efferocytosis in diseases; Clinical Trials and Therapeutic Promise

Targeting efferocytosis therapeutically can improve outcomes across various diseases, including autoimmune disorders, fibrosis and cancer.

In IMIDs such as SLE and RA, impaired efferocytosis contributes to persistent inflammation and autoantigen exposure. A similar defect in atherosclerosis leads to plaque progression and necrosis due to uncleared apoptotic foam cells(Adkar & Leeper, 2024). In these diseases, therapeutic strategies aim to boost efferocytosis to restore immune tolerance and resolve inflammation. For example, agents like Magrolimab (Gilead Sciences, NCT04313881) and ALX148 (ALX Oncology, NCT05002127) block the anti-phagocytic CD47–SIRPα axis to promote apoptotic cell uptake. However, Magrolimab has been stopped due to severe side effects (FDA, 2023). Likewise, Bemcentinib (BerGenBio, NCT03824080) (Kubasch et al., 2023) and MRX-2843 (Meryx Inc., NCT04872478) (Summers et al., 2021), which modulate TAM receptors (Axl, MerTK), enhance efferocytosis and anti-inflammatory Mφ phenotypes. Though these trials focus on oncology, their mechanisms are directly applicable to chronic inflammation and are candidates for repurposing in IMIDs and cardiovascular disease (Mehrotra & Ravichandran, 2022).

In contrast, in cancer, efferocytosis by TAMs fosters an immunosuppressive environment that enables tumor immune evasion. Blocking efferocytosis in this setting, by maintaining CD47 signaling or inhibiting TAM receptors, can restore anti-tumor immunity. In this context, the dual MERTK/AXL blocker ONO-7475 is tested to block efferocytosis in myeloid cell leukemia 1 (Post SM et al., 2022). Cabozantinib, a multi-target receptor tyrosine kinase inhibitor known to inhibit Axl signaling, is currently being evaluated in phase II clinical trials (NCT01639508) (Drilon et al., 2016).

Kim et al. (2018) demonstrated that efferocytosis of alveolar epithelial cells (AECs) by Mφ can actively drive lung fibrosis. In a transgenic mouse model, targeted apoptosis of type II AECs led to fibrosis, not simply through cell loss, but through Mφ activation following efferocytosis. Engulfing apoptotic AECs induced a pro-fibrotic gene program in Mφ. Crucially, mice lacking the efferocytosis receptor CD36 showed reduced fibrosis, identifying CD36-mediated efferocytosis as a pathogenic mechanism. These findings suggest that modulating efferocytosis, particularly via CD36 or Mφ reprogramming, represents a promising therapeutic strategy in fibrotic lung disease (Kim et al., 2018).

Thus, the therapeutic modulation of efferocytosis requires careful contextualization. In IMIDs and atherosclerosis, enhancing efferocytosis is a promising strategy to resolve chronic inflammation. In cancer and some fibrotic diseases, suppressing efferocytosis may prevent immune evasion or pathological tissue remodeling. Current clinical trials, especially those targeting CD47 (Magrolimab, ALX148) and TAM receptors (Bemcentinib, MRX-2843), illustrate how modulation of this fundamental clearance pathway is being tailored to diverse disease landscapes (Mehrotra & Ravichandran, 2022)

1.4.3 Iron Metabolism

Iron is an essential micronutrient involved in numerous physiological functions, such as transporting oxygen, synthesizing DNA, supporting mitochondrial respiration, and regulating cell death (Galy et al., 2024). Mφ are the main cells regulating the systemic and local tissue iron homeostasis by recycling iron from senescent erythrocytes, regulating iron storage, and influencing systemic iron homeostasis (Figure 1-6). Mφ tightly regulate the balance of iron uptake, storage, and release through various transporters, surface molecules, and systemic signaling molecules (Winn et al., 2020).

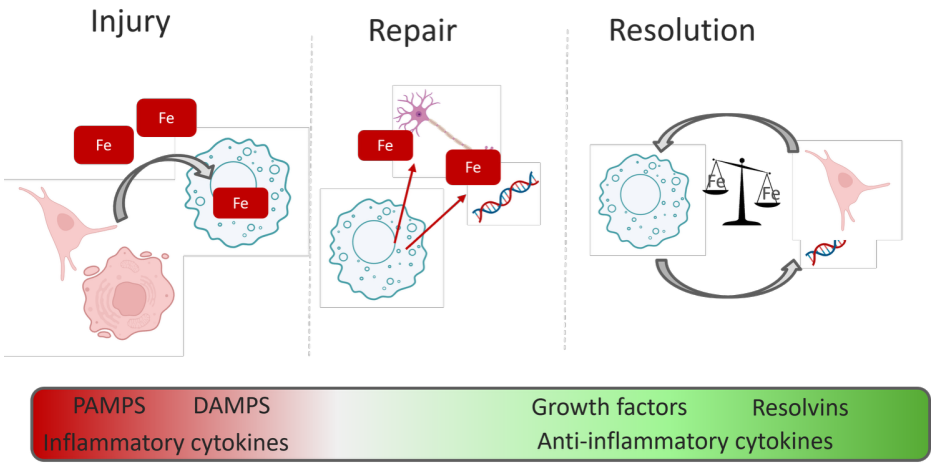

Figure 1-6 Iron-handling macrophages regulate iron recycling during tissue injury, repair/resolution and homeostasis, a proposed model. *Adapted from Winn et al. 2020, created with BioRender*.

Disruptions in Mφ iron metabolism are implicated in several pathological conditions, such as anemia of chronic disease (Theurl et al., 2009), infections (Moro et al., 2023) and iron overload disorders. Disruptions in Mφ iron metabolism are implicated in several pathological conditions, such as anemia of chronic disease (Theurl et al., 2009), infections (Moro et al., 2023) and iron overload disorders (Camaschella et al., 2020,Tański et al., 2021; Zhao et al., 2023a) Multiple studies highlighted the dynamic role of Mφ iron metabolism in inflammatory conditions, particularly in the context of autoimmune diseases, such as RA (Tański et al., 2021; Zhao et al., 2023a). For instance, Mφ in the inflamed synovial tissue of RA patients exhibit impaired iron-handling functions, contributing to disease progression and systemic iron dysregulation. In a study of 63 RA patients, Soares and Hamza (2016) found that 64% of the patients had iron deficiency and observed reduced levels of transferrin, ferritin, and hepcidin, along with elevated expression of soluble transferrin receptor (Soares & Hamza, 2016).

Macrophage Iron Import and Storage

Mφ acquire iron from multiple sources, primarily through the uptake of heme-bound iron and internalization of non-heme iron. Transferrin Receptor 1 (TfR1/CD71) is responsible for cellular uptake of iron (Fe^{3+}) that is bound to transferrin. Once transferrin attaches to TfR1 on the Mφ surface, the entire complex undergoes endocytosis and is transported into acidic endosomes (Cao et al., 2016). Within endosomes, the enzyme six-transmembrane epithelial antigen of the prostate (STEAP3) catalyzes the reduction of Fe^{3+} to its ferrous form (Fe^{2+}). The divalent metal transporter 1 (DMT1), also known as SLC11A2, then facilitates the transfer of Fe^{2+} into the cytosolic labile iron pool (LIP), where it becomes available for cellular metabolic processes (Galy et al., 2024). Together with ZIP14 (ZRT/IRT-like protein 14), DMT1 plays a key role in extracellular non-transferrin-bound iron uptake and erythrophagocytosis-derived iron transport and incorporation into cytosolic LIP (Philpott & Jadhav, 2019; Winn et al., 2020). Mφ also acquire iron through the clearance of hemoglobin (Hb) and heme, both of which originate from erythrophagocytosis or intravascular hemolysis. The CD163 scavenger receptor binds to hemoglobin-haptoglobin complex (Hb-Hp complexes), facilitating their internalization (Schaer et al., 2006). Once inside the cell, hemoglobin is degraded, and heme is released for further processing by heme oxidase (HO-1), which degrades heme into Fe2+, carbon monoxide, and biliverdin. Fe2+ can then be stored in the LIP or directly exported if needed. Free heme, which accumulates during tissue damage, is scavenged by the glycoprotein hemopexin (Hx) and taken up by Mφ via the low-density lipoprotein receptor-related protein 1 (LRP1/CD91). This prevents local heme-mediated oxidative tissue damage and inhibits heme from entering the circulation (Mehta & Reddy, 2015).

Intracellular iron is stored in ferritin, a cytosolic protein complex that sequesters excess iron in a bioavailable and non-toxic form by reducing Fe2+ to Fe3+ (Arosio et al., 2009). When extracellular iron levels are high or LIP is low, ferritin acts as a reservoir, preventing free iron from catalyzing the formation of harmful reactive oxygen species (ROS). In contrast, under conditions of iron deficiency, iron can be mobilized from ferritin via NCOA4-mediated ferritinophagy, a lysosome-mediated process where the protein NCOA4 helps degrade ferritin (an iron-storage complex), thereby releasing free iron within cells (Tang et al., 2018)

Iron Export and Regulation: Role of Ferroportin (SLC40A1)

Iron efflux from Mφ is mediated by ferroportin (SLC40A1), the only known mammalian iron exporter. Ferroportin regulates systemic iron availability by transporting intracellular iron (Fe2+) into the extracellular space, where it is oxidized to Fe3+ by ceruloplasmin or hephaestin and subsequently loaded onto transferrin (Tf-Fe3+) (Drakesmith et al., 2015; Winn et al., 2020).

The activity of ferroportin is precisely regulated by hepcidin, a peptide hormone produced by the liver, which binds to ferroportin and initiates its internalization and subsequent degradation (Muckenthaler et al., 2017). An overview of iron importers and exporters is presented in Figure 1-7. Elevated hepcidin levels, commonly observed during inflammation (induced by IL-6 and TNF-α), inhibit iron export from Mφ, leading to iron sequestration and hypoferremia (low serum iron levels) (Chung et al., 2009; Muckenthaler et al., 2017).

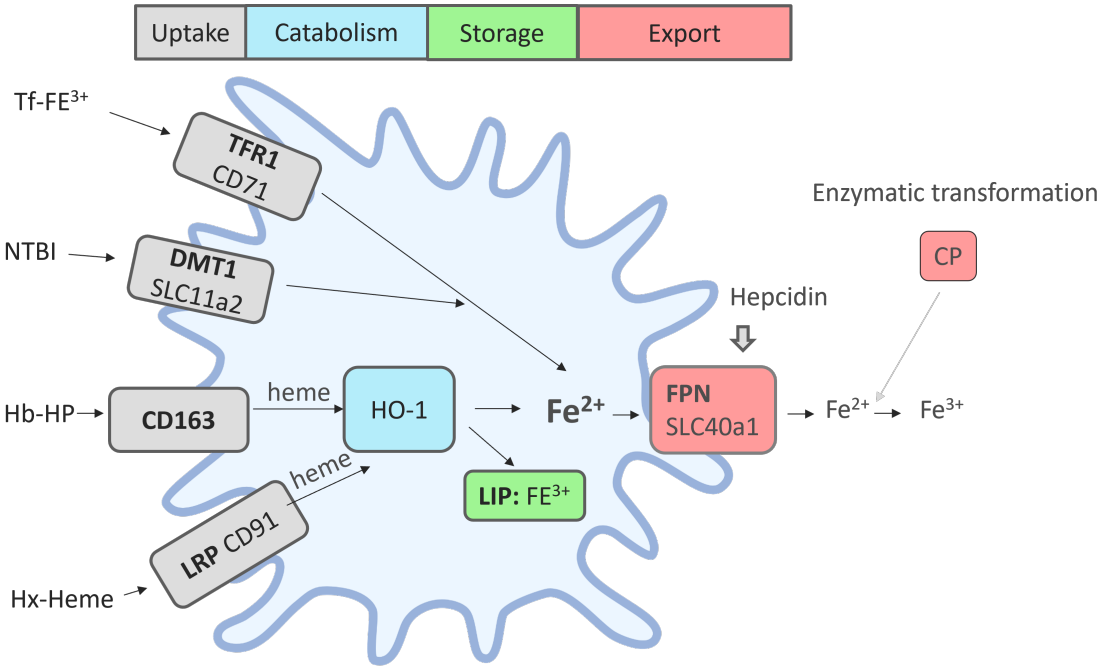

Figure 1-7 Iron recycling mechanistically. Uptake, catabolism, storage and export. TFR1 Transferrin receptor 1; DMT1 Divalent Metal Transporter 1, SLC11A2 Solute Carrier Family 11 Member 2, LRP1 LDL-related receptor 1 (LRP1; also known as CD91), Hb-HP hemoglobin-haptoglobin, Hx-heme heme-hemopexin, LIP labile iron pool, FPN ferroportin, (SLC40A1); HO-1 heme oxidase, NTBI non-Tf-bound Fe2+ iron. *Adapted from Winn et al. 2020, created with BioRender.*

Recent research has also highlighted the role of ferroptosis of FLS (which are resistant to most other forms of cell death), a form of iron-dependent cell death, in RA pathogenesis, which has been shown in mice and human arthritis (Liu, Liang, et al., 2024; Wu et al., 2022). Ferroptosis is characterized by iron overload, lipid peroxidation, and oxidative stress, which contributes to synovial inflammation and joint destruction (Zhao et al., 2023b). Iron accumulation in Mφ can sensitize FLS to ferroptotic death, amplifying inflammatory responses and exacerbating tissue damage (Liu, Luo, et al., 2024). Understanding the mechanisms linking iron metabolism, ferroptosis, and inflammation may offer novel therapeutic strategies for RA treatment by targeting key regulators of iron homeostasis and oxidative stress.

Furthermore, deregulated Mφ iron metabolism has been increasingly recognized as a critical factor in cancer progression. Mφ within the TME, particularly taMφ, exhibit altered iron handling that can promote tumor growth and immune evasion. Specifically, taMφ tend to adopt an iron-release phenotype, supplying iron to tumor cells, which supports their proliferation and survival. This iron-rich environment fosters tumor growth and contributes to immune suppression, aiding in the tumor's evasion of the immune system (Karimova et al., 2025). High iron levels in taMφ contribute to oxidative stress, DNA damage to cancer and surrounding stromal cells, and enhanced proliferation of cancer cells, while also supporting immune suppression by modulating T-cell activity

and cytokine release (Badran et al., 2024). Additionally, ferroptosis has been identified as a potential therapeutic target in cancer, as iron-induced lipid peroxidation can selectively eliminate tumor cells (Candelaria et al., 2021). Targeting Mφ iron metabolism, through strategies like inducing ferroptosis in cancer cells or reprogramming taMφ toward a pro-inflammatory state, may represent promising therapeutic avenues to limit iron supply and hinder tumor growth.

1.5 Macrophage Functionality: Protective in IMIDs, Pathogenic in Cancer

1.5.1 Harnessing Efferocytosis in the Resolution of Inflammation

While effective efferocytosis is associated with the resolution of inflammation, deficient efferocytosis can contribute to IMID worsening. Sangaletti and colleagues (2021) demonstrated that mice lacking the secreted protein acidic and rich in cysteine (SPARC) exhibited an earlier disease onset and more severe lupus-like symptoms, such as kidney disease, lung inflammation, and arthritis, compared to their wild-type counterparts. Their findings indicated that the downregulation of SPARC critically influenced the pathogenesis of SLE and arthritis. On a mechanistic level, decreased SPARC expression in neutrophils hindered their clearance by Mφ, resulting in the buildup of dying neutrophils in mouse tissues. Dying neutrophils represented a source of autoantigens for dendritic cells and directly activated T cells by presenting these autoantigens. Besides being processed by DCs, the dying neutrophils (especially those undergoing NETosis) also stimulate certain T cells directly, particularly γδ T cells. These T cells, especially in the joints, produce inflammatory cytokines such as IL-17, fueling autoimmune inflammation. The authors observed enhanced joint swelling in SPARC-deficient efferocytosis-impaired mice as compared to wild-type (WT) mice.

Kraynak and co-authors (2022) demonstrated that efferocytosis mechanisms can be harnessed to promote resolution of arthritis in a mouse model of lipopolysaccharide-induced inflammation. In this study, apoptotic body-inspired nanoparticles were used, designed to selectively target Mφ at sites of inflammation and promote an anti-inflammatory response. These nanoparticles are coated with a plasma membrane layer enriched with PS. PS serves as an "eat-me" signal that naturally attracts Mφ and encourages them to engulf apoptotic cells. Mimicking this mechanism, the nanoparticles are readily taken up by Mφ. To ensure site-specific targeting, the particles are also functionalized with an acid-sensitive polyethylene glycol (PEG) layer that detaches in the mildly acidic environment typical of inflamed tissues. This PEG shedding exposes the PS layer beneath, increasing Mφ recognition and uptake specifically at inflamed sites. Additionally, once internalized, these nanoparticles induce a shift in Mφ phenotype from pro-inflammatory (M1) to anti-inflammatory (M2), aiding in the resolution of inflammation without the need for traditional drugs or small molecule inhibitors (Urbano et al., 2015).

Taken together, these studies show that efferocytosis mechanisms can be harnessed for promoting the resolution of inflammation, thereby holding a promising potential for pro-resolution target discovery and drug development.

1.5.2 Efferocytosis and Its Role in Cancer Immune Escape and Therapy Resistance

In IMIDs, Mφ-mediated efferocytosis typically drives the resolution of inflammation. In contrast, within the TME, efferocytosis, primarily mediated by taMφs, but also involving DCs to a lesser extent, contributes to an immunosuppressive milieu that facilitates immune evasion and cancer progression (Tajbakhsh et al., 2021). Specifically, taMφ-mediated efferocytosis directly promotes an immunosuppressive phenotype in Mφ and indirectly suppresses anti-tumor immunity by inhibiting DC maturation and antigen presentation, as well as impairing T cell proliferation and cytotoxic function (Qiu et al., 2023b).

Building on this, Astuti et al. (2024) demonstrated that efferocytosis drives liver metastasis in pancreatic ductal adenocarcinoma (PDAC). In this pathology, monocyte-derived Mφ (MDMs) that engulf apoptotic liver parenchymal cells undergo reprogramming toward an immunosuppressive phenotype via a progranulin-dependent pathway. Progranulin modulates lysosomal acidification through the cystic fibrosis transmembrane conductance regulator, enabling efficient apoptotic cell degradation and activation of the nuclear receptor complex LXRα/RXRα, which in turn induces Arg1 expression. This conversion of MDMs into an immunosuppressive phenotype suppresses CD8+ T cell activity and promotes metastatic growth. Pharmacological blockade of efferocytosis via MerTK inhibition, or genetic deletion of progranulin in Mφ, impaired this immunosuppressive reprogramming and significantly reduced metastatic tumor burden (Y. Zhou et al., 2021). Furthermore, MDMs efferocytosis of apoptotic liver parenchymal cells was shown to be active in early metastatic niches, highlighting its role in both the initiation and progression of metastasis.

Efferocytosis plays a significant role in cancer progression and resistance to multiple therapies, including chemotherapy, radiotherapy, targeted agents, and immune checkpoint inhibitors (Lahey et al., 2022). In the TME, taMφ show an increased expression of the TAM receptors (Tyro3, Axl, MerTK) engage in efferocytosis of apoptotic cancer cells in various cancer types such as lung, breast, gastrointestinal cancer and leukemia. This process not only prevents the release of immunogenic content but also activates anti-inflammatory signaling pathways in Mφ, leading to an immunosuppressive microenvironment.

Activation of TAM family receptors, particularly Axl and MerTK, on both Mφ and tumor cells (Lahey et al., 2022) initiates key signaling pathways such as AKT and MAPK. These downstream signals promote cell survival, contribute to the establishment of an immunosuppressive tumor microenvironment, and are associated with increased resistance of cancer cells to chemotherapy, radiotherapy, and targeted agents like epidermal growth factor receptor-tyrosine kinase inhibitors (Myers et al., 2019). TAM receptors (especially AXL and MERTK) are expressed on both macrophages and cancer cells, and their presence has been linked to reduced efficacy of immune checkpoint inhibitors in multiple cancers, such as non-small cell lung cancer and melanoma (Zhou et al., 2021). This association highlights their potential as targets for combination treatment strategies.

Complementing these findings, Galluzzi et al. (2021) showed that apoptosis of cancer cells can paradoxically promote tumor growth when followed by rapid clearance through taMφ efferocytosis. Dying cancer cells release signals, such as growth factors and extracellular vesicles, that stimulate nearby tumor cells and modulate the microenvironment to support tumor growth. When apoptotic cells are swiftly removed, the resulting anti-inflammatory and tissue-repair responses suppress immune surveillance, facilitating tumor progression and metastasis (Morana et al.,

2022). This underscores the dual role of efferocytosis in the TME: while apoptosis is essential for eliminating damaged or malignant cells, its coupling with efferocytosis-driven immune suppression can reprogram Mφ toward a tumor-supportive phenotype. This paradox reveals a complex dynamic where efferocytosis, meant to maintain tissue homeostasis, promotes cancer resilience and therapy resistance (Y. Zhou et al., 2021).

1.5.3 Iron Metabolism and Its Role in Cancer Immune Escape and Therapy Resistance

Iron is essential for maintaining normal cellular activities, but it also plays a significant role in cancer development. Due to its redox properties, iron can catalyze the Fenton reaction, in which hydrogen peroxide is converted into highly reactive hydroxyl radicals (Meyerstein, 2021). These radicals can cause extensive oxidative damage to cellular components, contributing to both normal metabolic processes and pathological conditions such as tumor progression (Pfeifhofer-Obermair et al., 2018). DNA damage of this kind may lead to single or double-strand breaks, alterations in tumor suppressor genes like *TP53*, and the activation of oncogenes, all of which contribute to genomic instability, which is a key characteristic of cancer (Ying et al., 2021).

Cancer cells exploit iron's biological functions to support their aggressive proliferation. They commonly upregulate iron import mechanisms, particularly the TfR1, which has been reported in breast, ovarian, and hepatocellular carcinoma as well as hematologic malignancies (Brown et al., 2020). Conversely, the iron export protein ferroportin is downregulated in cancer cells, thereby increasing intracellular iron levels. This iron dependency fuels DNA synthesis and metabolic activity, giving cancer cells a growth advantage.

Furthermore, iron serves as a cofactor for key epigenetic regulators, including TET enzymes and Jumonji-domain histone demethylases. TET enzymes (Ten-eleven translocation methylcytosine dioxygenases) catalyze the oxidation of 5-methylcytosine, promoting DNA demethylation and influencing gene expression. In cancer, dysregulated TET activity can lead to aberrant activation or silencing of genes involved in proliferation, differentiation, and survival, thereby contributing to oncogenic transformation and progression (R. Brown et al., 2020)

The heightened reliance on iron also represents a potential therapeutic vulnerability. Targeting iron metabolism has emerged as a promising approach in cancer therapy. Iron chelators can limit tumor growth by depriving cancer cells of iron, while ferroptosis inducers trigger iron-dependent cell death selectively in iron-overloaded cells (Lei et al., 2024). Ferroptosis is particularly effective in tumors with high iron load or resistance to apoptosis, such as triple-negative breast cancer and glioblastoma (Rishi et al., 2021). Moreover, novel nanotechnology-based strategies, including iron oxide nanoparticles coupled with chemotherapeutics, are being explored to exploit this iron addiction with enhanced specificity and minimal off-target effects (Q. Zhou et al., 2024).

Beyond intrinsic tumor cell changes, iron also influences the tumor microenvironment. taMφ release iron into the surrounding tissue, creating an iron-rich microenvironment that promotes tumor growth. Moreover, iron can stimulate angiogenesis by enhancing vascular endothelial growth factor (VEGF) expression by which cells, thereby facilitating metastasis and sustained tumor expansion (Liang & Ferrara, 2021).

In summary, dysregulated iron metabolism promotes cancer through multiple mechanisms: ROS-mediated DNA damage, enhanced proliferation, epigenetic reprogramming, and modulation of the TME. These insights not only deepen our understanding of cancer biology but also highlight iron metabolism as a promising target for novel therapeutic strategies.

1.6 State-of-the-Art Knowledge About Human Tissue Mφ Diversity

Culemann et al. (2019) provided evidence that synovial trMφ perform critical protective roles in maintaining joint homeostasis. Their study identified a distinct population of synovial trMφ that formed a physical barrier at the synovial lining in mouse joints, thereby preventing the infiltration of inflammatory immune cells into the joint space. Using scRNAseq and high-resolution intravital imaging, they characterized this Mφ population as having epithelial-like features, including the expression of tight junction proteins such as Claudin-5 and ZO-1. These cells were shown to self-renew locally, independent of bone marrow-derived monocyte recruitment, indicating an ontogenically distinct and stable tissue-resident Mφ progenitor lineage. Lineage-tracing experiments confirmed that these Mφ populated mouse joints during embryogenesis and persisted in the adult joint through local proliferation. Functionally, the barrier-forming Mφ were demonstrated to play an anti-inflammatory role. Additionally, lining Mφ expressed efferocytosis-associated molecules, including Trem2, Axl and Mfge8. In preclinical serum transfer-arthritis and collagen-induced arthritis mouse models, selective depletion of Mφ subset led to a breakdown of the synovial lining barrier, followed by increased immune cell infiltration, synovial inflammation, and joint damage. Conversely, restoration of the Cx3cr1$^+$ lining Mφ population by differentiation from proliferating Cx3cr1-interstitial Mφ was associated with re-establishment of the synovial lining Mφ barrier and resolution of inflammation. These findings highlighted the dynamic homeostatic capacity of the synovial trMφ compartment. This study has significant implications for the understanding of the mechanisms of inflammatory arthritis. Further research is needed to understand whether a similar barrier demonstrated in mice also exists in human joints and preserving or enhancing this barrier may represent a novel joint-protective therapeutic approach.

Using scRNA-seq, Alivernini and colleagues (2020) analyzed over 32,000 synovial tissue Mφ (synMφ) isolated from synovial tissue biopsies of RA patients including patients with treatment-naïve RA, treatment-resistant RA as well as patients in sustained remission. This study revealed a remarkable heterogeneity in synMφ subsets, underscoring their divergent roles in arthritis pathogenesis and inflammation resolution. Nine transcriptionally distinct Mφ clusters were identified, grouped into four main synMφ subpopulations, specifically *TREM2*$^+$, *FOLR2*^{high}, *HLA*$^+$, and C*D48*$^+$ synMφ.

In healthy and remission synovia, MerTK$^+$ Mφ population, especially its TREM2high and *LYVE1*$^+$ *FOLR2*^{high} subsets, were enriched in healthy and remission synovial tissues and exhibited gene signatures linked to anti-inflammatory pathways, tissue remodeling, and immune regulation. Notably, these subsets were significantly enriched in genes linked to efferocytosis, such as *MerTK, TIMD4, GAS6* and *AXL*, inferring that these cells might exhibit efferocytosis capacity. Further, these *MERTK*+ Mφ showed high expression of regulatory genes such as *VSIG4, NR4A2, KLF4*, and *ATF3, DUSP1, NR4A1*, genes encoding the enzymes involved in resolvin D1 biosynthesis. MERTK$^+$ synMφ subsets, sorted from synovial tissues and cultured in vitro, produced and promoted fibroblast repair responses as defined by *COL1A1, TGFBI*, and *TGFB3* expression, suggesting their potential role in maintaining tissue homeostasis and drug-free remission. These effects were absent with *MERTK*$^-$*CD206*$^-$ synMφ, which instead promoted inflammatory phenotypes in FLS.

In contrast, synovial tissues from patients with active RA were dominated by *MerTK*$^-$*CD206*$^-$*CCR2*$^+$ inflammatory Mφ, many of which belonged to the *CD48*+*SPP1*$^+$ and

CD48⁺S100A12⁺ clusters. These *MERTK⁻* cells displayed a strong proinflammatory profile, including elevated expression of *TNF, IL1B*, and alarmin *S100A8/A9/A12*, and exhibited glycolytic and migratory transcriptomic signatures. Vice versa, genes associated with efferocytosis (*MERTK, AXL, GAS6*) were expressed low. Importantly, *CCR2⁺* Mφ appeared to contribute significantly to this inflammatory compartment, consistent with *CCR2's* known role in monocyte recruitment from the blood into inflamed tissues.

The proportion of *MERTK⁺CD206⁺* Mφ was significantly reduced in active RA but increased in remission, and their abundance inversely correlated with disease activity (DAS28-CRP). Moreover, a low ratio of *MERTK⁺CD206⁺* to *MerTK⁻CD206⁻* Mφ at the time of treatment-induced remission predicted future arthritis flare in patients stopping anti-TNF treatment, highlighting the potential of *CCR2⁺* inflammatory Mφ and *MerTK⁺* regulatory synMφ as biomarkers and therapeutic targets in RA.

1.7 Mφ Platforms and Assays for Functional Analysis

1.7.1 Comparison of Mφ Models for Functional *In Vitro* Studies

In vitro Mφ models include MDMs and induced pluripotent stem cell (iPSC)-derived Mφ (iMφ), whereas primary tissue Mφ are rarely accessible for broad in vitro experimentation given limited tissue accessibility and small quantities. Mφ models offer unique advantages and limitations depending on the research context. MDMs are derived from adult blood monocytes and are widely used due to broad monocyte accessibility and scalability of in vitro MDM production. MDMs are well-suited for modeling tiMφ because they share a common origin, both deriving from circulating monocytes that enter tissues during inflammation. MDMs exhibit functional plasticity, allowing them to polarize into inflammatory (M1) or healing (M2) phenotypes in response to environmental cues, similar to what occurs in vivo (Hickman et al., 2023). Unlike trMφ, which often originate from embryonic progenitors and possess self-renewal capacity, MDMs specifically reflect the dynamic and responsive nature of Mφ involved in active immune responses. Their ease of generation from human peripheral blood and their relevance in many disease contexts make them a practical and accurate in vitro model for studying the behavior of tiMφ during inflammation, infection, and tissue repair (Italiani & Boraschi, 2014). However, MDMs generally lack tissue-specific identity and embryonic/fetal ontogeny of most trMφ as they arise from definitive hematopoiesis (Lee et al., 2018). Most primary trMφ, in contrast, populate the tissues during embryogenesis from yolk sac or fetal liver erythro-myeloid progenitors and persist via local self-renewal (Ginhoux & Guilliams, 2016). These cells are imprinted by local niche signals, such as CSF1, IL-34, and GM-CSF, and perform specialized tissue functions (Guilliams et al., 2020). While highly physiologically relevant, they are difficult to isolate, exhibit inter donor variability and often lose their identity *ex vivo*. iMφ provide a scalable and genetically tractable alternative. They mimic embryonic Mφ development and replicate many characteristics of fetal-derived trMφ in transcriptional and functional profiles (Lee et al., 2018; Ginhoux & Guilliams, 2016). Notably, iMφ can adopt tissue-specific features when cultured with appropriate niche signals, making them a valuable platform for disease modeling and personalized medicine (Guilliams et al., 2020). Takata et al. (2017) developed a method to generate primitive macrophages (iMφ) from mouse and human iPSC, mimicking yolk sac-derived Mφ. These iMφ can further differentiate into tissue-specific Mφs like microglia or alveolar Mφ when exposed to appropriate environmental cues. In co-culture with neurons, iMφ adopt microglia-like features and functions, including phagocytosis and injury response. When introduced into the

brain or lungs of mice, iMφ integrate and restore tissue-specific Mφ function. Additionally, iMacs derived from a patient with familial Mediterranean fever showed disease-specific inflammatory behavior, supporting their use in disease modeling. This platform offers a powerful tool for studying tissue Mφ development and pathology (Takata et al., 2017).

1.7.2 Mφ Platforms and Their Suitability for Functional Analysis

The inherent capacity of different Mφ types for the study of functions in question (phagocytosis, efferocytosis and iron handling) defines the suitability of different Mφ platforms for gain-and-loss of function experiments, for example, with small molecule inhibitors or CRISPR genetic perturbations. MDMs express core phagocytic markers and machinery and respond robustly to inflammatory stimuli. Thus, MDMs are suitable for general studies of immune activation, cytokine secretion, and uptake of particles or pathogens (Geissmann, 2010). However, their phagocytic and efferocytic activity does not fully recapitulate the capacities of trMφ found in vivo (Lee et al., 2018). Receptors involved in efferocytosis, such as MERTK and AXL, are expressed at lower levels in MDMs compared to to primary trMφ and iMφ, possibly limiting the utility of MDMs in studies focused on apoptotic cell clearance (Wanke et al., 2021) or its inhibition. In contrast, primary trMφ These cells exhibit specialized phagocytic and efferocytic behaviors shaped by their local tissue environment. These cells express high levels of phagocytic and efferocytic receptors, making them the most physiologically relevant model for efferocytosis inhibition studies. trMφs are essential for iron recycling in the liver and synaptic pruning in the brain. They express high levels of phagocytic and efferocytic receptors, making them the most physiologically relevant model. However, they are difficult to isolate, subject to donor variability, and rapidly lose their tissue-specific phenotype in vitro (Guilliams et al., 2020).Likewise, primary trMφ, iMφ express high levels of MERTK and AXL receptors, particularly under homeostatic conditions, and exhibit robust phagocytosis and efferocytosis capacity. Wanke et al. (2021) demonstrated that iMφ effectively engulf apoptotic cells and that this process is enhanced by GAS6, a TAM receptor ligand. Notably, efferocytosis by iMφ was shown to depend on MERTK kinase activity, aligning with in vivo findings in mice, which showed impaired efferocytosis after MERTK KO in peritoneal Mφ. These data highlight iMφ as a potential model for dissecting and inhibiting the molecular mechanisms underlying apoptotic cell clearance.

1.7.3 Existing Platforms for Phagocytosis and Efferocytosis Functional Analysis

Several groups, including Clark et al. (2019) and Bravo et al. (2023), have developed pHrodo-based efferocytosis assays, building on the foundational research by Miksa and colleagues, (2009). Bravo and collegues (2023) have developed pHrodo-based efferocytosis assays, building on the foundational research by Miksa et al., (2009). These assays involve bacterial particles (for phagocytosis) or apoptotic cells (for efferocytosis) that are labeled with pHrodo™ Red SE, a pH-sensitive dye that fluoresces brightly upon internalization into acidic phagolysosomes (Lindner et al., 2020). This fluorescence shift serves as a specific indicator of successful particle/cell engulfment.

Clark et al. (2019) implemented this approach to a high-content imaging platform using primary human $CD14^+$ MDMs in a 384-well format, enabling fixed or live-cell readouts with multiparametric analysis (flow cytometry and confocal microscopy) (Clark et al., 2019). Similarly, Bravo et al.

(2023) developed a real-time assay using the Incucyte™ system, enabling live tracking of efferocytosis by TAMs (Bravo et al., 2023).

Expanding on this, Stöhr et al. (2018) introduced a novel molecular probe, the Annexin A5-pHrodo, which binds PS on apoptotic cells and fluoresces upon acidification. This method, validated in both murine and human Mφ lines, provides a more physiological alternative to bead-based assays and enables robust ex vivo and in vitro assessment of efferocytosis using either microscopy or flow cytometry readouts (Stöhr et al., 2018). Wang et al. (2024) explored efferocytosis in a murine model of ischemia/reperfusion cardiac injury. Their study identified *Sectm1a*, a Mφ-enriched gene, as a novel regulator of efferocytosis, employing both in vitro assays (with CellTracker™-labeled apoptotic targets and F4/80 staining) and in vivo models (e.g., knockout mice and administration of recombinant SECTM1A) (Wang et al., 2024) .

Raymond et al. 2022 introduce CharON (Caspase and pH Activated Reporter, Fluorescence ON), a genetically encoded fluorescent tool designed to track the process of apoptosis and efferocytosis in vivo, particularly in Drosophila embryos. CharON combines two components: pH-CaspGFP, a green-fluorescent reporter activated by caspase-3/7 cleavage during apoptosis and engineered to resist quenching in acidic environments, and pHlorina, a red fluorescent sensor that intensifies with decreasing pH, indicating corpse acidification inside phagolysosomes. This dual-reporter system allows for real-time visualization of dying cells (via green fluorescence) and their subsequent digestion by Mφ (via red fluorescence). By expressing CharON in Drosophila, it is possible to track individual Mφ as they migrated, engulfed apoptotic corpses, and digested them during embryonic development (Raymond et al., 2022).

1.7.4 Limitations of Existing Mφ Phagocytosis and Efferocytosis Platforms

Despite the wide array of assays developed to assess Mφ phagocytosis and efferocytosis, each method has inherent limitations that can affect the accuracy, physiological relevance, and interpretability of results. One of the most common challenges across many assays is the inability to clearly distinguish surface binding from internalization of phRodo-labelled particles or cells. Fluorescently labeled apoptotic cells or particles may adhere to Mφ membranes without being engulfed, potentially leading to overestimation of phagocytic activity unless specific controls are used, for example, mimicking a pH drop artificially with HCl or using microscopy to validate findings (Clark et al., 2019). Another limitation lies in the static nature of most experimental readouts. Many assays capture a single endpoint, typically after one to two hours of incubation, offering only a snapshot of the phagocytic or efferocytic process. This approach fails to capture the kinetics of phagocytosis or efferocytosis and overlooks its downstream events, such as phagosome maturation, lysosomal fusion, or degradation of engulfed material. A further concern is the physiological relevance of the particles used. Bead-based or synthetic particle assays, while convenient and reproducible, do not accurately mimic the complex surface and intracellular signals presented and derived by apoptotic cells. As a result, they may not engage the full spectrum of phagocytic receptors and signaling pathways involved in apoptotic cell clearance. pHrodo™-based assays, which rely on pH-sensitive fluorophores that emit fluorescence in acidic environments, provide a more specific readout of internalization. However, they are limited by their dependence on phagosome acidification. Mφ with impaired acidification, or experimental conditions that disrupt lysosomal function, may produce false-negative results. Additionally, low-level background fluorescence from pHrodo-labeled apoptotic cells can complicate the interpretation of results without a series of proper controls. Novel probes such as Annexin A5-pHrodo, which bind

phosphatidylserine on apoptotic cells, improve specificity but introduce new complexities. For example, Annexin A5 itself can inhibit efferocytosis at high concentrations, and the reliance on artificial labeling may not fully reflect *in vivo* apoptotic signaling (Miksa et al., 2009). *In vivo* models, such as the cardiac ischemia/reperfusion model used by Wang et al. (2024), offer unmatched physiological relevance but come with their challenges. These include low throughput, higher cost, and difficulty in isolating efferocytosis-specific outcomes from the broader complexity of tissue inflammation and immune responses. Despite its innovative capabilities, CharON (Raymond et al., 2022) does have several limitations. Technically, it relies on fluorescent signals that may overlap with other markers, and it is subject to photobleaching and phototoxicity during extended imaging. The tool requires genetic modification to express in model organisms, making its application in non-genetically tractable systems more complex. Quantifying dynamic events like corpse burden and signal ratios in live tissues can also be challenging. Biologically, the findings are based on *Drosophila*, which may not fully represent mammalian efferocytosis. Additionally, CharON tracks cell death and digestion but does not provide molecular insight into the downstream effects within Mφ or distinguish between different phagocyte types without additional markers. Finally, while it highlights heterogeneity in Mφ behavior, it does not identify the underlying causes of that variability, necessitating further mechanistic studies using complementary methods. What all these assays have in common is a lack of phenotypic characterization of the efferocyting cells. Incorporating this information could provide valuable insights into the molecular machinery driving efferocytosis and open new avenues for identifying therapeutic targets.

1.8 Rationale and Objective

Current knowledge of synovial Mφ subsets is primarily based on transcriptomic data, with a significant lack of information on their functional roles. There is a pressing need to investigate these subsets at the proteomic level and to perform functional analyses that go beyond gene expression. Moreover, existing functional Mφ assays provide limited insight, as they do not incorporate phenotypic information. This thesis shall bridge these gaps by combining functional assays with phenotypic profiling to achieve a more comprehensive understanding of synovial Mφ subsets.

1.9 Hypothesis

The objective leads to the following hypothesis of this thesis:

1. Developing integrated phenotype-function assays facilitates the characterization of human Mφ functions in health and disease, helping us identify candidate Mφ targets for pro-resolution drug development in IMIDs.
2. Different *in vitro* Mφ models exhibit distinct efferocytosis and iron recycling abilities, defining their applicability in gain-and-loss-of-function studies to discovery pro-resolution Mφ targets.
3. Human tissue Mφ subsets differ in efferocytosis and iron recycling capacities, influencing their roles in inflammation and pro-resolution in IMIDs.

Beyond the specific aims of this thesis, the work also contributes to a broader hypothesis pursued by our research group: that identifying the molecules and pathways regulating Mφ efferocytosis can reveal novel therapeutic targets in immune-mediated inflammatory diseases (IMIDs) and cancer.

1.10 Thesis Aims

1. **AIM 1 – Assay Establishment**
   Establish scalable assays that enable combined analysis of macrophage phenotypes and functions, integrating knowledge from human tissue Mφ atlases and CRISPR screens to identify functional regulators.
2. **AIM 2 – Invitro Mφ Platforms**
   Establish in-vitro macrophage platforms to study macrophage functions.
3. **AIM 3 – New Knowledge in Human Primary Mφ**
   Characterize surface phenotype and function (phagocytosis, iron pools) of human synovial tissue and synovial fluid Mф.

Project aims beyond the thesis

I. Human Atlas - Determine efferocytosis and iron metabolism of synovial tissue and synovial fluid Mφ.
II. Drug target discovery – Mφ efferocytosis regulators as potential drug targets in IMIDs and cancer.

2. Materials and Methods

2.1 Materials

2.1.1 Reagents and Consumables

Table 2-1 Reagents and consumables

ITEM	CATALOG NUMBER	VENDOR
LEUCOSEP 50ML RACKED STERILE, 25 PCS	227290	Greiner
FICOLL PAQUE PLUS, 6×500 ML	GE17-1440-03	GE (Thermo Fisher 11778538)
ACK LYSING BUFFER	A10492-01	Thermo Fisher Scientific GmbH
EASYSEP™ HUMAN MONOCYTE ISOLATION KIT	18001	STEMCELL Technologies
ROBOSEP™ BUFFER	20104	STEMCELL Technologies Germany GmbH
DPBS, NO CALCIUM, NO MAGNESIUM, 10×500ML	14190169 / 12037539	Gibco
ULTRAPURE EDTA	15575020	Thermo Fisher Scientific GmbH
GM-CSF	215-GM-050	R&D Systems
THERAPEAK™ X-VIVO™ 10	BEBP04-743Q	Lonza Cologne GmbH
NUNC MULTIDISHES WITH UPCELL SURFACE, 6 WELL	174901	Fisher Scientific GmbH
HUMAN IFN-GAMMA, 20 µG	rcyec-hifng	Invitrogen
LIPOPOLYSACCHARIDES FROM ESCHERICHIA COLI O55:B5	L4524-5MG	Sigma
HUMAN IL-4, PREMIUM GRADE, 25 µG	130-093-921	Miltenyi Biotec GmbH
DEXAMETHASONE	D4902-100MG	Sigma-Aldrich Chemie GmbH now Merck
IL-10	573204	BioLegend
RECOMBINANT HUMAN BMP-4 PROTEIN	314-BP-XXX-CF	Bio-Techne
HUMAN RECOMBINANT VEGF-165	78073.2	STEMCELL Technologies
STEMMACS™ CHIR99021	130-106-539	Miltenyi Biotec
HUMAN RECOMBINANT BFGF	78003	STEMCELL Technologies
HUMAN RECOMBINANT SCF	78062	STEMCELL Technologies
HUMAN RECOMBINANT IL-3 (CHO-EXPRESSED)	78194	STEMCELL Technologies
HUMAN RECOMBINANT IL-6	78050	STEMCELL Technologies
HUMAN RECOMBINANT DKK-1	78208	STEMCELL Technologies
HUMAN RECOMBINANT M-CSF, ACF	78150	STEMCELL Technologies
MTESRTM PLUS	100-0276	STEMCELL Technologies
STEMPRO MEDIUM	10639011	Thermo Fisher Scientific
HUMAN TRANSFERRIN	10652202001	Sigma-Aldrich Chemie GmbH now Merck
L-GLUTAMIC ACID	1743.1	ROTH
100X PENICILLIN STREPTOMYCIN	15307583	Fisher Scientific GmbH

L-ASCORBIC ACID	A5960-25G	Sigma-Aldrich Chemie GmbH now Merck
1-THIOGLYCEROL (MTG)	M6145-25ML	Sigma-Aldrich Chemie GmbH now Merck
IMDM WITH GLUTAMAX	31980048	Thermo Fisher Scientific GmbH
N2 SUPPLEMENT (100X)	17502048	Thermo Fisher Scientific
HAM'S F12 MEDIUM	P04-14550	PAN-Biotech GmbH
B27 SERUM-FREE SUPPLEMENT (50X)	17504044	Thermo Fisher Scientific
10% BOVINE SERUM ALBUMIN	A1595-50ML	Sigma-Aldrich Chemie GmbH now Merck
ROCK INHIBITOR Y-27632	72305	STEMCELL Technologies
PROPIDIUM IODIDE	F23001-LG	BioCat GmbH
IMATRIX-511	NP892-012	REPROCELL Europe Limited
GLUTAMIC ACID	1743.1	Roth
ASCORBIC ACID	A5960-25G	Sigma-Aldrich Chemie GmbH now Merck
GENTLE CELL DISSOCIATION REAGENT	100-0485	STEMCELL Technologies
HUMAN TRUSTAIN FCX™ (FC RECEPTOR BLOCKING SOLUTION)	422302	BioLegend
CELL STAINING BUFFER	420201	BioLegend
MACS® BSA STOCK SOLUTION	130-091-376	Miltenyi Biotec GmbH
AUTOMACS® RINSING SOLUTION	130-091-222	Miltenyi Biotec GmbH
MACSXPRESS WHOLE BLOOD NEUTROPHIL ISOLATION KIT	130-104-222	Miltenyi Biotec
DMEM/F12 GLUTAMAX	11554546	Fisher Scientific
FETAL BOVINE SERUM (FBS)	FBS-HI-11A	Capricorn Scientific GmbH
AMPHOTERICIN B	A2942-100ml	Sigma-Aldrich Chemie GmbH
PENICILLIN/STREPTOMYCIN (PEN/STREP)	PS-B	Capricorn Scientific GmbH
HEPES (1M)	15630080	Life Technologies GmbH
0.25% TRYPSIN-EDTA	25200072	Life Technologies GmbH
DMSO	A994.1	Carl Roth GmbH+Co. KG
NEUROCULT NS-A BASAL MEDIUM (HUMAN)	5750	Stem Cell Technologies
NEUROCULT NS-A PROLIFERATION SUPPLEMENTS – HUMAN (50ML)	5753	Stem Cell Technologies
EPIDERMAL GROWTH FACTOR (EGF)	AF-100-15	Peprotech
MURINE EGF (SUBSTITUTABLE FOR HUMAN EGF)	100-18B	Peprotech
FIBROBLAST GROWTH FACTOR (FGF)	315-09	Peprotech
PENICILLIN – STREPTOMYCIN (PENN/STREP)	N/A	N/A
LAMININ FROM ENGELBRETH-HOLM-SWARM MURINE SARCOMA BASEMENT MEMBRANE	L2020	Sigma-Aldrich
DELBECCO'S PHOSPHATE BUFFERED SALINE WITHOUT CALCIUM CHLORIDE, WITHOUT MAGNESIUM CHLORIDE (PBS)	2017-10	Gibco
ACCUTASE	A6964-100mL	Sigma-Aldrich
EBIOSCIENCE™ ANNEXIN V APOPTOSIS DETECTION KIT EFLUOR™ 450	88-8006-72	Fisher Scientific
RPMI 1640 MEDIUM, OHNE PHENOLROT	11835030	Fisher Scientific

µ-SLIDE 8 WELL HIGH CELL CULTURE CHAMBER SLIDE WITH 8 WELLS AND HIGH WALLS FOR HIGH-END MICROSCOPY	80806	IBDI
CELLMASK™ PLASMA MEMBRANE STAINS, ORANGE	C10045	Invitrogen
HOECHST 33342, TRIHYDROCHLORIDE, 10 ML	H3570	Fisher Scientific GmbH
PHRODO™ GREEN E. COLI BIOPARTICLES™ KONJUGAT FÜR DIE PHAGOZYTOSE	P35366	Fisher Scientific GmbH
PHRODO™ GREEN STP ESTER	P35369	Fisher Scientific GmbH
PHRODO™ RED, SUCCINIMIDYL ESTER	P36600	Fisher Scientific GmbH
BIOTRACKER FAR-RED LABILE FE2+ DYE	SCT037	Sigma Alderich
ESSENTIAL 8 MEDIUM	A1517001	Fisher Scientific GmbH
POLY-D-LYSINE	A3890401	Fisher Scientific GmbH
HUMAN IL-34, PEPROTECH 100UG	2000-34-100UG	Fisher Scientific GmbH
BIOLAMININ 111	LN111-02	Biolamina
TGFB1	100-21C-10	Fisher Scientific GmbH
HUMAN FRACTALKINE (CX3CL1) RECOMBINANT PROTEIN	300-31-20UG	Fisher Scientific GmbH
ANTI-ANTI	15240096	Fisher Scientific GmbH
LAMININ FROM ENGELBRETH-HOLM-SWARM MURINE SARCOMA BASEMENT MEMBRANE 1 MG/ML IN TRIS, BUFFERED NACL	L2020	Sigma Alderich
HYALURONIDASE	0000010-9000010H3506-100mg	Sigma Alderich

2.1.2 Equipment

Table 2-2 Equipment used

Name	Manufacturer
Heraeus Megafuge 16R centrifuge	Thermo Scientific
Centrifuge 5810R	Eppendorf
Heracell 150i CO2 incubator	Thermo Scientific
Binder CB170	Binder GmbH
Hera Safe KS 12	Thermo Scientific
EVOS XL core	Life Technologies
Precision GP 05	Thermo Scientific
TSX60086V/165VT0C37M	Thermo Scientific
Centrifuge 5418	Eppendorf
VACUSIP	Integra
Chromium Controller	10x Genomics
Qubit 4 Fluorometer	Invitrogen
FACSAriaTM Fusion	BD Biosciences
Luna-FL Dual Fluorescence Cell Counter	BioCat
"The Big Easy" EasySep™ Magnet	STEMCELL Technologies

Sony ID7000 multi-spectral flow cytometer	Sony biotechnology
Vilber Bio Sun Microprocessor controlled	Vilber
Incucyte S3 Live Cell Analysis Instrument	Satorius

2.1.3 Solutions

Table 2-3 Solution compositions

Name	Composition
100 mM Glutamic Acid	0.736g of Glutamic acid in 50 ml of PBS, pH adjusted to 7.5
500 mM Ascorbic Acid	2.2g in 25 ml of PBS
Stempro Medium	Stempro-34 SFM, 200 ug/mL Human Transferrin, 2 mM Glutamic Acid, 1x Pen Strep, 0.5 mM Ascorbic Acid, 0.45mM MTG
Serum-Free Differentiation Medium	75% IMDM with GlutaMAX, 25% F12, 1x N2 supplement, 1x B27 Supplement, 0.05% BSA, 1x Pen/Strep
FACS staining buffer	1:20 of autoMACS® Rinsing Solution with MACS® BSA Stock Solution
FACS blocking solution	FACS buffer 1:10 with *FcR Blocking Reagent, human*
Jurkat suspension buffer	D-PBS + 1mM HEPES

2.1.4 Antibody Table

Table 2-4 Antibody table

Marker	Fluorochrome	Vendor	Catalog number
B2M	PE-Cy7	Biolegend	316317
BAI1	AF647	R&D	FAB49692N-100
Cas9	AF 647	Cell signalling	7A9-3A3
CCR2	BV711	BD OptiBuild	747848
CD114	BUV615	BD OptiBuild	751179
CD11b	BV570	Biolegend	301325
CD11b	BB515	BD Horizon	564517
CD11b	BB515	Biolegend	
CD11b	AF700	Biolegend	
CD14	cFluorB548	Cytek	R7-20115
CD14	PE/fire 810	SONY	2596115
CD14	PE/Fire640	Biolegend	367154
CD146	R718	BD OptiBuild	752158
CD15	APC	Biolegend	323007
CD163	BUV563	BD OptiBuild	741402
CD172a/b	PerCPCy5.5	Biolegend	323811
CD192	BV421	Biolegend	357210
CD1c	BV650	BD OptiBuild	742749
CD206	BUV805	BD OptiBuild	742042
CD206	PE/fire 700	SONY	2205765

CD206	PE	Biolegend	321105
CD209	BB515	BD Horizon	564548
CD209	APC/Fire 750	Biolegend	330115
CD209	APC	SONY	2315025
CD209	APC Fire750	Biolegend	330115
CD26	BV480	BD OptiBuild	76532
CD274	BUV661	BD	741666
CD31	AF647	BD Pharmingen	561654
CD31	BUV395	BD Horizon	565290
CD33	PerCP Cy5.5	Biolegend	303414
CD34	BUV661	BD OptiBuild	750195
CD36	BV605	BD Horizon	563518
CD36	PerCPCy5.5	Biolegend	336223
CD38	BV711	Biolegend	303527
cd40	buv805	BD	742028
CD45	BUV496	BD OptiBuild	750179
CD45	PE/fire 810	SONY	1116435
CD45	BV750	Biolegend	368541
CD47	APC	Biolegend	323123
CD48	PE-CF594	BD Horizon	5627171
CD52	APC750	SONY	2180075
CD52	PerCP Cy5.5	SONY	2180045
CD54	BUV737	BD OptiBuild	741841
CD55	BV605	BD OptiBuild	742679
CD64	BV421	Biolegend	30519
CD64	BV510	BD OptiBuild	744975
CD64	Pacific Blue	SONY	2125085
CD68	AF647	SONY	2269095
CD68	APC/Fire 750	SONY	2269115
CD68	R718	BD Horizon	568070
CD68	PE	Biolegend	333807
CD68	R718	BD Horizon	568070
CD80	BV605	BD Horizon	563315
CD80	BUV395	BD Horizon	565210
CD80	BV650	Biolegend	305227
CD86	BUV615	BD	751042
CD90	BUV496	BD OptiBuild	741160
CD91	BUV661	BD OptiBuild	750155
CD91	BUV661	BD OptiBuild	750155
CX3CR1	R718	BD OptiBuild	752200
CXCR4	BV650	BD OptiBuild	740599
CXCR4	BUV395	BD Horizon	563924
FCER1alpha	R718	BD OptiBuild	752192
FOLR2	AF350	NOVUS	
FOLR2	PE	Biolegend	391703
HLA-DR	APC-Fire810	Biolegend	307674
HLA-DR	BV650	Biolegend	307649

HLA-DR	BUV395	BD	56794
HLA-DR	BV650	Biolegend	307649
Lyve1	AF750	NOVUS	NB100-725AF750
Lyve1	AF488	NOVUS	NB100-725AF488
MERTK	BV785	BD OptiBuild	748106
MERTK	PE	Biolegend	367608
Notch3	BV650	BD OptiBuild	745317
Podoplanin	BB700	BD OptiBuild	749715
SLC40a1	AF488		
SPP1	eFluor660	Invitrogen	
SSEA-4	VioGreen	Miltenyi	130-123-901
TIM-4	PE	Biolegend	354004
Tra-1-60	BUV395	BD Horizon	563878
Tra-1-60	AF488	Biolegend	330613
TREM-2	PE-Cy7	NOVUS	NBP1-07101PECY1

2.1.5 Cells

Table 2-5 Cell lines

Name	Type	Catalog No.	Manufacturer
StemRNA Human iPSC 771-3G	iPSC	RCRP005N	Stemgent™
6TF	iPSC	Shared from Jackson lab	(Dräger et al., 2022)
Jurkat T cells E6.1	Immortalized	Cryovial: 300223 Vital: 330223	CLS Cell Line Services
Monocytes	Primary	-	Blutbank Mannheim

2.1.6 Software and Tools

During the preparation of this thesis, various digital tools and software platforms were utilized to support data analysis, visualization, and manuscript preparation. For the analysis of conventional flow cytometry data, FlowJo was employed. Spectral flow cytometry data were processed using the SONY ID7000 software, which was used for spectral unmixing and autofluorescence correction; further detailed analyses were conducted using CellEngine. Confocal microscopy images were deconvoluted using Huygens software and subsequently analyzed with Fiji (ImageJ). GraphPad Prism was used for all statistical analyses (Table 2-6).

Table 2-6 Software used

NAME	DESCRIPTION OF USE	REFERENCE
FLOWJO	Analysis of FACS data	The flow cytometry results were analyzed using FlowJo™ v10.8.1 Software (BD Life Sciences).
FIJI (IMAGEJ) 2.3.0	Analysis of microscopy images	

HUYGENS SOFTWARE	Deconvolution of confocal microscopy images	Huygens Professional version [24.10] (Scientific Volume Imaging, The Netherlands, http://svi.nl).
GRAPHPAD 6.01	Graph preparation and statistical analysis	GraphPad Software, San Diego, California USA, www.graphpad.com.
CELL ENGINE	Multi-spectral flow cytoemty data analysis	CellEngine by CellCarta https://cellengine.com/#/
SONY ID7000 SOFTWARE	Multi-spectral flow cytometry data analysis	

OpenAI's ChatGPT (2024) was used during the thesis process for language and structure refinement, including grammar, clarity, and style improvements. No full paragraphs were generated by the tool, and it was not used for idea generation or content development. Additionally, ChatGPT and Perplexity were used as supplementary tools to aid in literature searches. Perplexity assisted with the identification of relevant academic sources during the literature review process. Mendeley was used as a reference management tool to organize citations and generate references in APA format.

OpenAI. (2024). *ChatGPT* (May 12 version 4.0) [Large language model]. https://chat.openai.com/

Perplexity. (2024). *Perplexity AI* [AI research assistant]. https://www.perplexity.ai/

Mendeley. (2024). *Mendeley Reference Manager* (Version 2.132.2) [Software]. https://www.mendeley.com/

2.2 Study Participants and Human Samples

2.2.1 Study Participants

Table 2-7 presents the study participants. The biological samples were obtained as biopsies at the Rheumatology Department of the Gulbenkian Institute for Molecular Medicine, Lisbon, Portugal, in collaboration with R. Teixeira, R. Barros, J. Polido-Pereira, and A. Calado. The study was conducted in accordance with ethical guidelines and was approved by the institutional ethics committee The study was approved by CAML Ethics Committee, Lisbon, Portugal (Reference N. 110/22).

Table 2-7 Study participants synovial biopsies, Lisbon, Portugal used for CITE Sequencing

Project ID	Sex	Age	Diagnosis
1	F	NA	Joint replacement surgery. Therapy leflunomide. Patient wash out the drug prior to surgery
2	F	61	Refractory RA change from anti-TNF
3	M	58	Refractory RA, change from MTX
4	F	66	MTX inadequate
5	M	67	Early RA

6	F	39	Early RA
7	M	29	Early RA
8	F	66	Early RA
9	M	68	Early RA
10	F	61	Early RA
11	F	58	csDMARD-inadequate
12	F	55	DMARD-inadequate (SSZ)
13	F	82	DMARD-inadequate
14	F	51	anti-TNF-inadequate
15	F	51	Remission RA
16	F	48	PDN/MTX-IR
17	M	77	Remission RA
18	F	53	anti-TNF-inadequate
19	F	51	Remission RA
20	F	32	anti-TNF-inadequate
21	F	59	Remission RA

2.2.2 Human Samples

2.2.2.1 Synovial Biopsies Portugal

Table 2-8 Rheumatoid Arthritis patient groups used for Cite Sequencing

Group	Total number sequenced
DMARD naive	6
csDMARD-inadequate	6
Remission	4
Anti-TNF/IL-6- inadequate	5
End stage disease	1

2.2.2.2 Synovial Fluid cells

Synovial fluid cells were collected, aliquoted, and cryopreserved with viability at two international rheumatology centers: University Medical Centre Ljubljana, Department of Rheumatology, Ljubljana, Slovenia, and Gulbenkian Institute for Molecular Medicine, Rheumatology Department, Lisbon, Portugal (see Table 2-6 for patient characteristics).

Table 2-9 Human synovial fluid sample details

Patient group	Sex	Age	Diagnosis	Therapy
1	Female	52	Polyarthritis Artherial hypertension, celiac diseases, kliver steatosis	Movalis (2016), depoMedrol intramuscular, then Movalis, Hyplaxy (2022), start MTX therapy March 2023, MTX stop because of adverse effects after 2 months (gingivitis, leukopenia, nausea), July 2023 start of therapy with Leflunomide (2023), **Arava, Naklofen** (2024)
2	unknown	68	Chronic erosive oligoarthritis	Arcoxia, **MTX**
3	unknown	49	Known hip OA (status post surgery), syndrome of chronic pain	Asthma therapy till 2012, intraarticular corticoid 2x, arthroscopic surgery - necrektomy and ablation of radial epicondyl, brufen, Analgin, paracetamol(2023)

2.2.2.3 PBMCs

For isolation of monocyte-derived macrophages (MDMs), buffy coats from healthy blood donors were ordered from the blood bank Mannheim. DRK-Blutspendedienst Baden-Württemberg/Hessen. Friedrich-Ebert-Straße 107, 68167 Mannheim. Buffy coats were not cooled and were not subjected to PCR testing.

2.3 Cell Isolations

2.3.1 Cell Isolations from Fresh Synovial Biopsies

Synovial tissues as collected during ultrasound-guided synovial biopsies or joint replacement surgery from patients with RA and osteoarthritis. Samples were transported to the laboratory in RPMI-medium and processed within 2 hours post-collection. Synovial biopsy fragments were dissociated using an optimized synovial tissue dissociation protocol published by Edalat S., Gerber R., et al. 2024, a publication which I co-authored. This protocol was derived from the method of (Donlin et al., 2018)

Briefly, synovial tissue fragments were placed on a 70 µm cell strainer and washed with D-PBS to remove potential non-synovial cell contaminants. Synovial biopsies were then minced into ~1 mm fragments in pre-warmed RPMI medium (glutamine, HEPES, without antibiotics or FBS) and digested and dissociated at 37°C using a combined enzymatic-mechanical approach. The enzymatic digestion mix contained 100 µg/ml Liberase (Roche) and 100 µg/ml DNAse I (Roche) in RPMI-1460 medium (glutamine, HEPES, without antibiotics or FBS). Minced tissue fragments were

transferred into the digestion solution using a wide-bore pipette tip, forceps, or scalpel, ensuring minimal tissue loss.

Tissue digestion was performed at 37°C in a water bath, ensuring a stable digestion temperature. The tissue fragments were continuously stirred for 30 minutes using a combination of ball- and cylinder-shaped magnetic stirrers. Fifteen minutes into digestion, mechanical dissociation was applied by passing the tissue fragments through a 16G needle ten times using a 1 ml syringe. Special care was taken to prevent needle clogging, which could result in tissue and cell loss. Enzymatic digestion was halted by 10% FBS in RPMI medium.

Minced tissue fragments were prepared in pre-warmed RPMI medium (glutamine, HEPES, without antibiotics or FBS).

Following digestion, the cell suspension was filtered through a 40 µm strainer pre-wet with 2 ml RPMI medium containing 10% FBS. An additional 1 ml of RPMI/10% FBS was used to wash the tube and maximize cell recovery. The remaining synovial tissue fragments were gently pressed against the strainer using a syringe plunger head to enhance the remaining cell release and enrich for synovial cells. The filtered single cell suspension was collected into a 15 ml Falcon tube, washed with 5 ml RPMI/10% FBS, and centrifuged at 300 x g for 10 minutes at RT.

Red blood cells were lysed using 1x Red Blood Cell Lysis buffer (Roche, prepared by diluting 10x RBC Lysis Buffer in nuclease-free water). Briefly, the cell pellet was resuspended in 0.5 ml RPMI/10% FBS and 1x RBC Lysis buffer (4.5 ml) was added to the cell suspension, followed by gentle vortexing for 5 seconds and incubation at RT for 2 minutes. The sample was then centrifuged at 300 x g for 10 minutes, and the supernatant was discarded. The cells were resuspended in D-PBS by gently flicking the pellet, resuspending in 10 ml PBS, and

The red blood cell-free pellet of synovial cells was washed with 10 ml D-PBS, centrifuged at 300 x g for 10 minutes, with a second centrifugation step at 300 x g for 2 minutes to remove any residual buffer.

To prepare a single-cell suspension suitable for scRNA-seq with 10xGenomics technology, cells were resuspended in 150 µl of 0.2% BSA-D-PBS (prepared by diluting 4 µl of 50 mg/ml BSA per 100 µl D-PBS). The cell viability and yield were determined using the Luna-FL dual fluorescence cell counter (Logos BioSystems) and Acridine Orange/Propidium Iodide cell labeling (ThermoFisher).

If debris or clumps were observed during cell counting, the cell suspension was filtered again through a 35 µm strainer into a 1.5 ml Eppendorf tube to prevent clogging of the 10X Genomics chips. The final cell concentration was adjusted to 700 cells/µl for loading on the 10X Genomics chips, for optimal loading efficiency and minimized clogging risk. For multispectral flow cytometry, cell concentration was set to $1x10^6$ cells/mL Cells were maintained on ice until processing with FACS sorting, multispectral flow cytometry or 10x Genomics protocol.

2.3.2 Cell Isolations from Fresh Synovial Fluid Cells

Cryopreserved synovial fluid samples were thawed in prewarmed 37 degrees RPMI 1640 medium and washed twice with DPBS. Cell concentration and viability were assessed using the Luna™ Automated Cell Counter. To reduce viscosity and digest extracellular matrix components, samples were incubated in a solution containing 500 µL of 0.5 µM hyaluronidase and 500 µL of DNase I (prepared as 10 µL/mL in DPBS) at 37 °C for 30 minutes in a water bath with continuous agitation. Following enzymatic digestion, cells were pelleted by centrifugation at 400 × g for 10 minutes,

followed by a second centrifugation step at 300 × g for 10 minutes to further purify the cell suspension.

2.3.3 Isolation of CD14+ Monocytes from Human Blood Samples

Peripheral Blood Mononuclear Cells (PBMCs) were isolated from buffy coats, which we obtained from Blutbank Mannheim. D-PBS + 2 mM EDTA was prepared by adding 2 mL of 0.5 M UltraPure EDTA to 500 mL of PBS. Seventeen mL of Ficoll Paque Plus was added to six Leucosep™ tubes per donor, followed by centrifugation at 1,000 x g for 30 seconds at room temperature. The remaining Ficoll above the separation membrane was aspirated. The buffy coats were transferred into a T75 cell culture flask and diluted to a total of 180 mL with PBS + 2mM EDTA, and 30 mL of the diluted blood was added per Leucosep™ tube at a 45° angle, to avoid disruption of the membrane. Tubes were centrifuged at 1,000 g for 10 minutes at RT with acceleration set to 1 and brake to 0. The serum phase was aspirated, and PBMCs were carefully collected from the interphase using a 5 mL pipette and pooled into four tubes per donor.

The PBMCs were washed by filling 50 mL Falcon tubes with PBS + 2mM EDTA, centrifuging at 250 x g for 10 minutes, and removing the supernatant with a pump. Pellets were pooled into two tubes, resuspended in PBS + 2mM EDTA, and centrifuged at 200 x g for 10 minutes. After supernatant removal, pellets were pooled into a single tube with 10 mL ACK lysing buffer and incubated for 7 minutes. The tubes were refilled with PBS + 2mM EDTA, centrifuged at 250 x g for 10 minutes, and supernatant removed. PBMCs were resuspended in 50 mL PBS + 2 mM EDTA and counted. The cells were spun down for 5 minutes at 700 rpm, adjusted to 5×10^7 cells/mL in RoboSep Buffer (STEMCELL), and transferred to FACS tubes. CD14+ monocyte enrichment was performed using the STEMCELL CD14 enrichment kit following the manufacturer's instructions. The solutions were added sequentially, mixed by pipetting, and incubated for 5 minutes. Magnetic beads were vortexed for 30 seconds before being added, and cells were incubated, resuspended in RoboSep Buffer, and placed in "The Big Easy" EasySep™ Magnet for 2.5 minutes. The PBMC-containing supernatant was transferred to a 15 mL Falcon tube while still positioned in the magnet and the FACS tube with beads was discarded after. CD14+ monocytes were counted, and if the yield exceeded 15%, samples were examined for platelet contamination under a microscope. Monocytes were palleted at 300 x g for 10 minutes, supernatant was removed, and residual liquid was aspirated.

Monocytes were resuspended at 1×10^6 cells/mL in XVIVO medium. For differentiation, 100 ng/mL GM-CSF was added to polarize towards M1-like Mφ, and 100 ng/mL M-CSF was added for M2-like Mφ polarizations. Three million cells (3 mL) were plated per well in a NUNC UpCell™ 6-well plate and incubated at 37°C, 5% CO_2 for six days without disturbance.

2.4 Human Cell Culture

2.4.1 Jurkat T cells

Jurkat T cells (JTs) were cultured in Roswell Park Memorial Institute (RPMI) 1640 medium supplemented with 10% fetal bovine serum (FBS) and 1X Penicillin/Streptomycin (Pen/Strep). To prepare the complete medium, 50 mL of FBS and 5 mL of Pen/Strep were added to a 500 mL bottle of RPMI 1640. Cells were maintained in T75 flasks at a density of 0.2–3.0 × 10^6 cells/mL in

suspension culture. The cell density was monitored regularly, ensuring it did not exceed 3.0×10^6 cells/mL to prevent cellular stress.

Cryopreservation

For cryopreservation, cells were collected and counted as described above. Cells were resuspended at a density of $4.0–5.0 \times 10^6$ cells/mL in culture medium supplemented with 10% dimethyl sulfoxide (DMSO). Aliquots of 1 mL were transferred into cryovials and stored in a CoolCell XL box at −80°C for no longer than 48 hours before transfer to liquid nitrogen for long-term storage.

Thawing of Cryopreserved Cells

Cryopreserved cells were thawed by first pre-warming RPMI-1640 medium in a 37°C water bath. Nine milliliters of warm medium were added to a Falcon tube. Cryovials were retrieved from liquid nitrogen and transported on dry ice to the culture facility. Cells were rapidly thawed in a 37°C water bath until partially thawed and immediately transferred into the Falcon tube containing warm medium. The suspension was centrifuged at 400 × g for 5 minutes, and the supernatant was aspirated. The cell pellet was resuspended in 1 mL of warm RPMI-1640 medium and transferred into a T75 flask containing 14 mL of fresh culture medium. Cells were then incubated under standard culture conditions.

2.4.2 Human Glioblastoma PBT-04FHTC

Plate coating

PBT-04 FHTC cells are adherent and maintained on coated 10 cm² culture dishes. To prepare the coating, Laminin (Engelbreth-Holm-Swarm murine sarcoma basement membrane, 1 mg/mL in Tris-buffered NaCl; Sigma-Aldrich, Cat. #L2020) is diluted 1:100 in PBS to create a 1× working solution. This solution should fully cover the surface of the tissue culture-treated plate or flask. For a 10 cm² dish, 5 mL of the 1× Laminin solution is applied. The plates are then incubated at 37 °C for at least one hour to facilitate Laminin polymerization.

Media preparation

To one bottle of NeuroCult NS-A Media (450ml), add one bottle of NeuroCult NS-A Proliferation Supplements – Human (50ml), Pen/Strep (5ml), 20 ug/ml epidermal growth factor (EGF) and 20 ug/ml Fibroblast growth factor (FGF). The prepared media was filter sterilized, and stored at 4° and used at a pre-warmed temperature of 37° C.

Establishing Cultures from Frozen Cells

To establish cultures from frozen cells, a 15 mL conical tube was prepared with 9 mL of room temperature phosphate-buffered saline (PBS). A cryo-vial containing frozen cells was rapidly thawed in the warming bath. The contents of the cryo-vial were gently transferred into the PBS-containing tube using a pipette. The suspension was then centrifuged at 400 × g for 4 minutes to pellet the cells. Following centrifugation, the supernatant was carefully aspirated to avoid disturbing the cell pellet, which may not always be clearly visible. The pellet was resuspended in 1 mL of complete Neurocult media, ensuring that the conical end of the tube was rinsed with media to maximize cell recovery. The resuspended cells were then plated in the coated tissue culture dish (10 cm or smaller). Cells were maintained in culture until they formed a confluent lawn before further dissociation and expansion.

Cells were maintained by replacing the media when splitting. When cells reached confluence or required passaging, the media was removed, and the cells were rinsed with PBS, which was then

aspirated. RT Accutase was added to completely cover the cells, and the plate was incubated at room temperature or 37°C until the cells detached (3–5 minutes). Detached cells were collected by adding PBS, transferred to a centrifuge tube, and spun at 400 × g for 4 minutes. The resulting cell pellet was resuspended in 1 mL of media, and 20 µL of the suspension was used for cell counting. Cells were then plated at a density of approximately 10,000 cells per cm² on freshly laminin-coated tissue culture plates or flasks. For cryopreservation, cells were resuspended in media supplemented with 10% DMSO.

2.5 Human iPSC Culture

2.5.1 StemRNA Human iPSC 771-3G cell line

The dishes were coated using the pre-mixing method. iMatrix 511 was diluted in DPBS to achieve a laminin concentration of 0.5 µg/cm² per well in a six-well plate. Specifically, 9.6 µL of laminin 511 was mixed with 2 mL of DPBS and then pipetted onto the culture dish. The volume was adjusted according to the size of the cell culture dishes. Laminin coating was performed either at 37 °C for 1 hour or at 4 °C overnight.

Cells were cultured on dishes pre-coated with Laminin-511 (2.4 µg/ml) in mTeSR™ Plus medium supplemented with a ROCK inhibitor (10 µM). Typically, within 24 to 48 hours post-seeding, the medium was replaced with mTeSR™ Plus without the ROCK inhibitor. Regions of spontaneous differentiation were manually removed by scratching under the microscope. The culture medium was changed daily, with occasional exceptions where a change was skipped when cell confluency was particularly low.

771 cell line splitting

Prior to splitting, iPSCs were washed three times with PBS. Depending on the experimental requirements, iPSCs were dissociated using one of the following methods:

- Gentle Cell Dissociation Reagent: Used when maintaining iPSC in clumps was desired. Briefly, Gentle Cell Dissociation Reagent was added to the wells and incubated at room temperature (RT) for 3–4 minutes and checked under the microscope. The cells were then washed twice with mTeSR™ Plus. To fully detach the cells, the wells were scraped, and then collected in a tube and centrifuged at 300 x g for 10 min at RT. The iPSCs were seeded dropwise following careful visual assessment of the confluency.

- Ez-Lift: Used to reduce the proportion of spontaneously differentiating cells. Briefly, iPSCs were washed once with Ez-Lift and incubated with Ez-Lift for 4 minutes at 37 °C. The plate was tapped from the bottom, followed by an additional 4-minute incubation at 37 °C. If necessary, incubation was extended in 2-minute intervals with tapping until satisfactory detachment was achieved. The cells were then collected and centrifuged (300 × g, 10 min, RT) before being seeded dropwise following careful assessment of confluency.

- Accutase: Used when single-cell dissociation was required. Cells were incubated with Accutase for 6–8 minutes at 37 °C. Following incubation, cells were collected in PBS at a volume three times that of the Accutase solution and centrifuged (300 × g, 10 min, RT). The iPSCs were then counted and seeded at the desired confluency.

771 Cell line iPSCs cryopreservation

Cells were detached using the appropriate dissociation method and resuspended in CryoStor, typically at a concentration of 1×10^6 or 2×10^6 cells/mL. In cases of clump detachment, two vials were used per six-well plate of culture.

2.5.2 6TF iPSC Cell Line

To prepare plates for 6TF-iPSC culture for iMicroglia differentiation, a double-coating procedure was carried out using Poly-D-Lysine (PDL) and truncated Vitronectin (VTN-N). For the initial PDL coating, a 1X borate buffer (BB) was prepared by diluting 2 mL of 20X BB stock in 38 mL of deionized water (dH_2O), yielding a total volume of 40 mL. This solution was sterile filtered, and 2 mL of PDL was added to the 38 mL of filtered 1X BB to prepare the coating solution. Each 10 cm² dish was coated with 6 ml of PDL solution and incubated at 37°C for 2 hours. Following incubation, the PDL solution was aspirated, and dishes were washed three times with sterile dH_2O. Subsequently, a second coating was performed using VTN-N diluted 1:50 in dPBS. For six dishes, 600 µL of VTN-N was mixed with 30 mL of dPBS, and 5 mL of this solution was added to each dish. The dishes were then incubated at room temperature for 1 hour.

To differentiate 6-TF iPSCs into iMicroglia, the culture medium was aspirated, and the iPSC colonies were rinsed once or twice with dPBS. To detach the cells, 700 µL of Accutase was added to each well, followed by a 7-minute incubation at 37°C. Afterward, 1 mL of dPBS was added directly into each well, and cells were gently dissociated by pipetting. The cell suspension was collected into a sterile Falcon tube, and wells were further washed with an additional 2 mL of dPBS, which was also added to the tube. The collected iPSC suspension was centrifuged at 300 × g for 10 minutes. The supernatant was discarded, and the cell pellet was resuspended in 1–2 mL of dPBS. Cells were counted using an automated cell counter / Trypan blue staining and then seeded at a density of 2×10^6 cells per dish in 10 mL of Essential 8 Medium supplemented with 1:100 RevitaCell and 2 µg/mL Doxycycline (1:1000).

2.5.3 Human iPSC to iMφ Differentiation

The differentiation of induced pluripotent stem cells (iPSCs) (771 cell line) into induced macrophages (iMφs) followed four distinct phases (Table 2-8):

Table 2-10 Distinct differentiation stages

Phase	Day	Stage of differentiation
1	0 -6	Mesoderm specification and induction of hemangioblast-like cells
2	6-10	Commitment of hemangioblasts to a hematopoietic cell lineage.
3	12-13	Maturation of hematopoietic cells
4	16-20	Differentiation of hematopoietic progenitors into iMφs.

The iMφ differentiation process followed the protocol described by Takata et al. (2017). iPSCs were cultured until they reached 60-80 % confluency. The first eight days of differentiation were carried out under hypoxic conditions (5 % CO_2, 5 % O_2). From day 0 to day 16, cells were maintained in Stempro Medium (Stempro-34 SFM supplemented with 200 µg/mL human transferrin, 2 mM glutamic acid, 1x penicillin-streptomycin, 0.5 mM ascorbic acid, and 0.45 mM MTG) with

media changes every other day. During this period, small molecules listed in Table 2-8 were added to the culture.

From day 16 to day 28, cells were transferred to a serum-free differentiation medium (SF-diff), which consisted of 75% IMDM with GlutaMAX, 25% F12, 1x N2 supplement, 1x B27 supplement, 0.05% BSA, and 1x penicillin-streptomycin. Media changes were performed every three days.

Floating cells began to appear from day 8 onward. These cells were collected by centrifugation (400 × g, 5 min), resuspended in fresh media, and returned to the differentiation dish. Additionally, from day 8, differentiation cultures were moved from hypoxic to normoxic conditions (5% CO_2). The differentiation protocol was adapted from Takata et al. (2017).

Table 2-11 Differentiation protocol

Day	Supplementation	Media	Cell returning
0	• 5 ng/mL BMP-4 • 50 ng/mL VEGF • 2 µM CHIR99021	Stempro medium	No
2	• 5 ng/mL BMP-4 • 50 ng/mL VEGF • 20 ng/mL FGF2	Stempro medium	No
4	• 15 ng/mL VEGF • 5 ng/mL FGF2	Stempro medium	No
6 - 10	• 50 ng/mL SCF • 10 ng/mL FGF2 • 20 ng/mL IL-3 • 10 ng/mL IL-6 • 10 ng/mL VEGF • 30 ng/mL DKK1	Stempro medium	From day 8
12 - 14	• 50 ng/mL SCF • 10 ng/mL FGF2 • 20 ng/mL IL-3 • 10 ng/mL IL-6	Stempro medium	Yes
16 - 28	• 50 ng/mL m-CSF	SF-diff medium	Yes

Post-differentiation culture

Cells we typically used straight from the differentiation protocol for experiments. If necessary, we transferred floating cells to the new culture dish, in SF-Diff supplemented with 50 ng/ml M-CSF with medium change twice a week.

2.5.4 6TF iPSC to iMicroglia Differentiation

The differentiation protocol was conducted in accordance with Dräger et al. (2022). Briefly, after seeding iPSCs, 10cm dishes were gently shaken in all directions to ensure even distribution of cells across the dish and dishes were incubated in cell culture incubator at 37°C and 5% CO2. From day 2 onwards the differentiating iPSCs were cultured in Advanced DMEM/F12 Medium supplemented with doxycycline and different cytokines. The medium was changed every other day for the duration of the iPSC-to-iMicroglia differentiation as presented in Table 2-9.

Table 2-12 iMicroglia differentiation media and cytokines

DAY	MEDIA COMPOSITION
0	Essential 8 Medium RevitaCell (1:100) 2 μg/ml Doxycycline (1:1000)
2	Advanced DMEM/F12 Medium 1x Anti-anti (1:100) 1x GlutaMAX (1:100) 2 μg/ml Doxycycline (1:1000) 100 ng/ml Human IL-34 (1:1000) 10 ng/ml Human GM-CSF (1:10.000)
4	Advanced DMEM/F12 Medium 1x Anti-anti (1:100) 1x GlutaMAX (1:100) 2 μg/ml Doxycycline (1:1000) 100 ng/ml Human IL-34 (1:1000) 10 ng/ml Human GM-CSF (1:10.000) 50 ng/ml Human M-CSF (1:2000) 50 ng/ml Human TGFB1 (1:2000)
6	Advanced DMEM/F12 Medium 1x Anti-anti (1:100) 1x GlutaMAX (1:100) 2 μg/ml Doxycycline (1:1000) 100 ng/ml Human IL-34 (1:1000) 10 ng/ml Human GM-CSF (1:10.000) 50 ng/ml Human M-CSF (1:2000) 50 ng/ml Human TGFB1 (1:2000)
8	Advanced DMEM/F12 Medium 1x Anti-anti (1:100) 1x GlutaMAX (1:100) 2 μg/ml Doxycycline (1:1000) 100 ng/ml Human IL-34 (1:1000) 10 ng/ml Human GM-CSF (1:10.000) 50 ng/ml Human M-CSF (1:2000) 50 ng/ml Human TGFB1 (1:2000) 50 ng/ml Human CX3CL1 (1:4000)

For the detachment of differentiated microglia, TrypLE Express was used. The required volume was 4 ml per 10 cm² dish. The culture medium was first aspirated, and cells were gently washed with PBS. TrypLE was then added to each dish, followed by a 10-minute incubation at 37°C to allow for enzymatic detachment. After incubation, 5 mL of D-PBS was added to each dish to neutralize the TrypLE, and the cells were gently detached and collected into a sterile Falcon tube. The dish was subsequently washed with an additional 5 –10 mL of PBS to ensure maximal cell recovery, and the wash was also added to the same tube. The collected cell suspension was centrifuged at 300 × g for 10 minutes, after which the supernatant was aspirated. The resulting cell pellet was resuspended in D-PBS and cell concentration was determined using an automated cell counter.

2.5.5 Differentiation of CD14+ Monocytes into Monocyte-Derived Macrophages (Mφ)

Up to day six post-monocyte isolation, the plates remained in the incubator without media changes or movement of the plate until processing to prevent detachment due to temperature drop. Cells were removed and left at room temperature for 20 minutes to one hour to facilitate lifting. Cells were collected, counted using Countess, and resuspended at 1×10^6 cells/mL. A required number of cells was polarized by adding the following factors: For M1 Mφ, 100 ng/mL GM-CSF, 50 ng/mL IFNγ, and 20 ng/mL LPS were added. For M2 Mφ, two alternative protocols were used: one with 100 ng/mL M-CSF, 50 ng/mL IL-4, and 50 ng/mL IL-10, and another with 100

ng/mL M-CSF, 50 ng/mL IL-10, and 100 nM Dexamethasone. After polarization, the cells were seeded into a fresh 6-well NUNC Up cell well plate at $1x10^6$. The cells were incubated for 24 hours to complete polarization.

2.6 Staining and FACS sorting

2.6.1 Antibody Panel Development

For the development of flow cytometry panels used for Mφ characterization, including MDMs and iMφs, marker selection was based on several decisive criteria. These included coverage of Mφ-specific markers, global leukocyte markers, tissue-residency-associated markers, as well as markers linked to pro-resolution and tissue-protective functions. Additionally, markers indicative of inflammatory responses and tissue infiltration were incorporated. For panels applied to primary synovial tissue cells and synovial fluid cells, additional markers specific to stromal and structural cell populations were included. The selection of these markers was informed by published literature as well as single-cell RNA sequencing (scRNA-seq) data generated within our research team.

Antibody selection was further guided by marker abundance on the cell surface. For highly expressed markers, dim fluorochromes were assigned, whereas bright fluorochromes were used for low-abundance markers to optimize signal resolution. To minimize spillovers and maintain a low complexity index, fluorochrome choices were carefully evaluated. In functional assays, such as the efferocytosis assay, the 488 nm laser was sparingly used to prevent signal spillover into the pHrodoGreen channel and ensure accurate readouts. Similarly, for iron uptake assays, channels surrounding the APC channel were avoided to prevent spillover effects and ensure reliable quantification. Additionally, specific markers for iron metabolism were incorporated. Furthermore, the panel was designed to allow for flexibility and easy adaptation based on emerging data from ongoing research within our team.

Antibodies were titrated on MDMs for Mφ, leucocyte and inflammation markers, FLS and Huvecs for structural cell markers. The starting point for titrations was titrations made on FACS Aira fusion.

2.6.2 General Staining Protocol

Cells were collected, pelleted by centrifugation, and washed once with FACS staining buffer (autoMACS® Rinsing Solution + MACS® BSA Stock Solution). After washing, cells were counted and resuspended at 100,000 cells per 45 µL of FACS staining buffer, followed by the addition of 5 µL FcX block (BioLegend) to minimize nonspecific binding. The suspension was incubated for 15 minutes at 4°C.

For antibody staining, a 50 µL antibody cocktail was prepared per sample, with an additional 10% volume to account for pipetting loss. The cocktail contained the required volumes of all antibodies, 10% Brilliant Stain Buffer (BD Biosciences) to stabilize tandem dyes, and FACS staining buffer to reach the final volume. After blocking, 50 µL of the antibody cocktail was added to each sample, bringing the final staining volume to 100 µL.

Samples were incubated at the appropriate at 4°C in the dark for 1h. After incubation, samples were washed 3 x and resuspended in FACS staining buffer + 10% brilliant stain buffer for measurement in SONY ID7000.

2.6.3 Flow cytometry - Fluorescence Activated Cell Sorting

The following protocol was used to collect, stain, and sort differentiated iMφs after Takata protocol to isolate a pure Mφ (CD45+, CD14+ and CD11b+/ double positive sort) population for later experiments.

Culture media containing floating cells from post-Takata iMφ plates were collected into a 15 mL Falcon tube. To wash the cells, 2 mL of 1X DPBS was added to each well, and the collected DPBS was combined with the media in the Falcon tube. SF-Diff plus M-CSF was added back to the plates and they were transferred back to the incubator.

The Falcon tubes containing the floating cells were spun down, and the total number of cells was determined using the Countess II cell counter with Trypan Blue staining. Cells were then centrifuged at 400 x g for 10 minutes at RT, and the supernatant was removed. The resulting cell pellet was resuspended in blocking buffer, which is prepared 1:5 FcR blocking reagent: staining buffer.

A total of $1x10^6$ cells were allocated for control samples, with 200,000 cells transferred into five separate 5 mL Falcon tubes for unstained control, single-stain control for CD45-APC, CD14-PE, CD11b-PE and single-stain control for viability dye. If necessary, the volume in each tube was adjusted to 100 µL using cell staining buffer. The remaining cells were transferred to a separate 5 mL Falcon tube for sorting. Cells were stained according to the specified scheme, using appropriate antibody volumes per 100 µL of cell staining buffer and 200,000 cells. For the sorting sample, antibody volumes were adjusted based on the total cell number (Table 2-10).

Table 2-13 Antibody volumes for FACS sorting

	CD45-APC	CD14-PE	CD11b-PE	Zombie NIR
Unstained	-	-	-	-
Single stained control 1	0.5 ul	-	-	
Single stain control 2	-	0.3 ul	-	-
Single stain control 3			0.3 ul	
Single stain control 4				0.1 ul
Multi Stain for Sorting calculated based on cell number				

Following the addition of antibodies, all tubes were incubated at 4°C for 30 minutes. After incubation, cells were centrifuged at 400 x g for 5 minutes, the supernatant was removed, and the pellet was resuspended in 3 mL of PBS, followed by another centrifugation at 400 x g for 5 minutes. This wash step was repeated twice. The control cell pellets were resuspended in 300 µL of cell staining buffer and transferred to FACS tubes, while sorting sample pellets were resuspended at 5 million cells/ml of cell staining buffer and transferred to FACS tubes through a filter cap for analysis. Celld were then sorted on FACSAriaTM Fusion (Becton Dickinson). After sorting, collection in 4°C SF-Diff media and confirming the purity of the CD45+ viable CD14+ CD11b+ and live cell population, the sorted cells were centrifuged and resuspended in SF-Diff + M-CSF. Finally, the cells were seeded into so-called post-Takata culture in 6-well NUNC Up-cell plates and incubated for recovery for 4–5 days before reseeding into experimental plates.

2.7 Induction of Cell Apoptosis and Apoptotic Cell Staining

2.7.1 Drug-induced Apoptosis

JTs were collected into a Falcon tube, spun down at 400 x g for 5mins, RT, and resuspended in their normal culture media at $1x10^6$ cells/mL. Cells were seeded into a 24 well-plate at 500k cells per well. JTs were treated at t= 6 hours, t = 4 hours and t = 3 hours with 7.5 µM Camptothecine at a concentration of 1 µm Staurosporine. After treatment incubation, cells were washed 3x with D-PBS, and spun down at 400 x g for 5 and minced at RT and resuspended in FACS staining buffer.

2.7.2 UV-radiation of Jurkat T cells

JTs were collected in Falcon tubes and centrifuged at 400 x g for 10 minutes at RT. The pallet was resuspended in RPMI 1640 Medium, no phenol red to avoid UV-reflection during radiation and the cell number was determined. Cells were resuspended at $1x10^6$ cells/mL and seeded into a 6-well plate, 2 mL/well. The plates were then transferred to the Vilber Bio Sun Microprocessor for radiation with required doses of UV-A and UV-B radiation. Cells were transferred back into the incubator.

2.7.3 UV-radiation of Human Glioblastoma PBT-04FHTC

For collecting, the media was removed, and the cells were rinsed with PBS, which was then aspirated. Accutase (RT) was added to completely cover the cells, and the plate was incubated at 37°C until the cells detached (3 to 5 minutes). Detached cells were collected by adding PBS, transferred to a centrifuge tube, and spun at 400 × g for 4 minutes. The resulting cell pellet was resuspended in 1 mL of PBS, and 20 µL of the suspension was used for cell counting. Cells were then resuspended in PBS and distributed in 6-well plates. The plates were then transferred to Vilber Bio Sun Microprocessor and treated at the required doses of UV-A and UV-B radiation. After UV radiation, cells were collected in a Falcon tube, spun down, and resuspended in their usual culture media.

2.7.4 Apoptotic cell staining with AnxV and 7AAD

Apoptotic cell fractions post-treatment were detected using the eBioscience Annexin V Apoptosis Detection Kit eFluor 450 was used according to the manufacturer's protocol. Briefly, JTs cells were collected after UV-radiation of apoptosis-inducing drug treatment, washed once with D-PBS, and resuspended in 1X Binding Buffer (contained in the KIT) at a density of 1–5 × 10^6 cells/mL. 5 µL of eFluor 450-conjugated Annexin V was added to 100 µL of the cell suspension, followed by incubation for 10–15 minutes at room temperature in the dark. After staining, cells were washed with 1X Binding Buffer, resuspended in 200 µL of 1X Binding Buffer, and, where applicable, 5 µL of 7-AAD was added to distinguish late apoptotic and necrotic cells. Samples were analyzed by flow cytometry or multi-spectral flow cytometry within 4 hours, maintaining them at 2–8°C and protected from light. All buffers contained calcium to ensure proper Annexin V binding, and chelating agents such as EDTA were avoided.

2.7.5 Labelling of apoptotic cells with pHrodoGreen

pHrodo™ Green STP Ester or pHrodo™ Red, Succinimidyl Ester were diluted in DMSO according to the manufacturer's protocol. Exposure of the dyes to light was avoided at all times. Apoptotic cells (JTs or glioblastoma cells) were detached if required and collected in a Falcon tube and spun down at 400G for 10 min, and washed 1x with PBS. Then, apoptotic cells were resuspended in Jurkat Suspension buffer (D-PBS + 1mM HEPES) at 1 x 10^6 cells/ mL (adopted from (Clark et al., 2019). Diluted pHrodo dyes were added at the required concentration and incubated for 45 min at RT in the dark. After incubation, the samples were washed 3x with 10 mL of Jurkat suspension buffer and suspended in Jurkat suspension buffer at required concentrations.

2.8 Discoverer Mφ

2.8.1 General Assay Set Up

The developed *Discovery Mφ* platform was used to determine Mφ functions, including efferocytosis, phagocytosis, and iron metabolism capacity of Mφ derived from several sources. Mφ were seeded into the experimental set-up, a 96-well plate. Attached Mφ are then stained with a multi-marker panel. For functional analysis, those Mφ are then either exposed to *E. coli* bioparticles to determine their efferocytosis capacity, to apoptotic cells to determine their efferocytosis capacity or to an iron tracker, to determine their iron metabolism capacity (Figure 2-1).

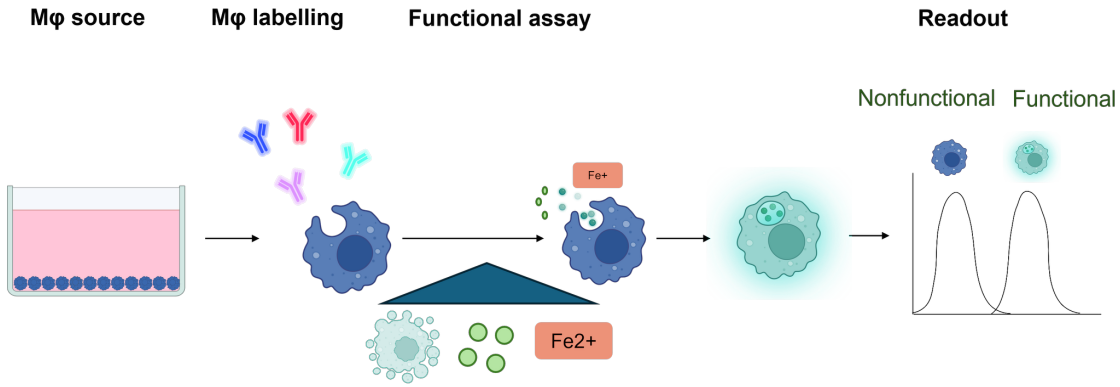

Figure 2-1 General assay set-up.

2.8.2 Spectral Flow Cytometry-based Efferocytosis Assay

General Considerations

- Phagocytes were pre-labeled with the antibodies against leukocyte and Mφ (e.g., CD45, CD14, CD11b, CD163 for iMφs), enabling differentiation between phagocytes and Jurkat T cells in cocultures.
- Efferocytosis inhibitors (eg. Cytochalasin D, Chloroquine, Flavopiridol and Bafilomycine) were re-added at every buffer changing step.
- Experimental plates containing phagocytes were centrifuged before each staining step to minimize cell loss.
- All staining steps were performed at 37°C to mimic physiological conditions, as 4°C incubation would inhibit efferocytosis.

• Different types of phagocytes can exhibit variable apoptotic cell uptake capacities; time-course measurements were performed as needed to distinguish time point of maximum apoptotic cell uptake.

Day 1

Phagocyte Seeding

Phagocytes were detached (if required), collected in a 15 mL or 50 mL Falcon tube, and centrifuged. Cells were counted and resuspended at a density of $1x10^6$ cells/mL in the appropriate culture medium: X-vivo (+ required polarization cytokines, see chapter 2.5.5) for MDMs or SF-Diff + M-CSF for iMφs. If no polarization was required cells were directly seeded. If polarized is required, this was done according to table 2-14 in the falcon tube and then seeded into fetal bovine serum (FBS)-coated 96-well flat-bottom plates (to allow Mφ detachment prior to measurement) at a density of 0.5 – 1 x 10^5 cells per well, with 1 x 10^5 cells.

Table 2-14 Cytokines used for Mφ polarizations

Cytokine, Corticosteroid	Polarization	Required concentration
IL-10	Anti-inflammatory	50 ng/ml
Dexamethasone	Anti-inflammatory	100 nM
TNF	Pro-inflammatory	20 ng/mL
IFNγ	Pro-inflammatory	50 nM

Phagocytes were polarized at a concentration of 1x10^6 cells/mL, then resuspended and seeded into FBS-coated 96-well plates. Plates were incubated at 37°C with 5% CO_2 for ~24 hours before further processing to allow recovery.

Induction of Apoptosis in Jurkat T Cells

Apoptosis was induced 13 hours (with 0.075 J/cm² UV-A and UV-B for JTs) before efferocytosis assays in accordance with the UV-induced apoptosis-induction protocol (chapter 2.7.2). Alternatively, apoptosis can be induced with 1 uM Staurosporine 3h before the efferocytosis assay Chapter 2.7.1).

Day 2

Treatment with phagocytosis/efferocytosis Inhibitors/Facilitators

If applicable, inhibitors or facilitators of phagocytosis/efferocytosis were added to required wells containing efferocytic cells before JT feeding. The following inhibitor/facilitator concentrations were used:

Table 2-15 Small molecules used for efferocytosis perturbation/ promotion studies

Compound	Mechanism	Concentration	Treatment pre-Jurkat addition
Cytochalasin D	Atkin polymerization inhibitor	10 µM	1h
Bafilomycine A1	specific inhibitor of the vacuolar-type H^+-ATPase (organelle acidification inhibitor)	100 nM	1h
Chloroquine	prevents acidification of the phagolysosome	100 nM	3h

Apoptotic supernatant	Expose phagocytes to released find-me signal released during apoptosis	15%	3h
Gas6	Bridging molecule between phagocytes and apoptotic cells (TAMs)	10 µM	24h
Protein S	Bridging molecule between phagocytes and apoptotic cells (TAMs)	5 µM	1h

Pre-labelling of phagocyted

Antibody Cocktail Preparation

For each experimental condition, 50 µL of antibody staining cocktail was prepared, consisting of the required antibody volumes, 10% BD Horizon Brilliant Stain Buffer (if using Brilliant Violet (BV) antibodies, to improve violet signal), and topped up with FACS staining buffer to a total volume of 50 µL. Cocktails were stored on ice in the dark. Viability (Zombie NIR) dye was added to the cocktail just before staining in a concentration of 1:2000 of total cocktail volume.

Blocking and Staining Procedure

- FBS-coated plates containing cultured phagocytes were centrifuged at 300 x g for 5 minutes, RT.
- Cells were then washed once with 100µl FACS staining buffer, and blocked with 5 µL FcX in 45 µL FACS buffer per well for 10 minutes at 37°C.
- The blocking solution was removed, and the antibody cocktail was added to the appropriate wells (50 µL per well). 50 µL of FACS staining buffer was added to control wells to have unstained controls for flow cytometry measurements.
- If inhibitors were used, they were re-added to according wells.
- Cells were incubated for 1 hour at 37°C in the dark (5% CO_2).

Note: Inhibitors/ facilitators were re-added, if required.

Labelling of apoptotic Jurkat T cells with pHrodoGreen

During phagocyte pre-labelling with antibodies, JT were collected, centrifuged at 400g for 10 minutes at RT, counted, and resuspended at $1x10^6$ cells/mL in Jurkat suspension buffer (D-PBS + 1 mM HEPES). Cells were stained with 5 µM pHrodoGreen (prepared from 10 µM pHrodoGreen in DMSO) for 45 minutes at room temperature in the dark.

Efferocytosis Assay

After 1 h of antibody incubation on phagocytic cells, 96 well-plates containing stained phagocytes were spun down and washed 2x with 100µL FACS staining buffer. After the second wash, 100 uL of Jurkat suspension buffer was added to each well.

Note: Efferocytosis/phagocytosis inhibitors/ facilitators were re-added into the required wells.

Jurkat Feeding

- Wash pHrodoGreen stained apoptotic JTs 3x with 10ml Jurkat suspension buffer (centrifugation after each washing step at 400 x g for 10 minutes, RT)
- 50 µL of Jurkat cell suspension containing the appropriate cell number (1:5 Mφ: JT ratio) was added to the required wells; control wells received 50 µL of Jurkat suspension buffer.

- 96-well plates containing now stained phagocytes + pHrodoGreen labelled JTs were gently swirled for even distribution.
- Plates were centrifuged at 400g for 1 minute to bring JTs into contact with efferocytic cells and incubated at 37°C, 5% CO_2 until measurement.
- For selected experiments, unengulfed JTs were removed after 30 minutes using a P200 pipette, and fresh Jurkat suspension buffer was added.
- Cells were incubated for a total efferocytosis period of 120-300 minutes until measurement on the multi-spectral flow cytometer SONY ID7000.

Note: Efferocytosis/ phagocytosis inhibitors/ facilitators were re-added, if required.

Multi-Spectral Flow Cytometry Analysis

Cells were resuspended with a multichannel p200 pipette. Phagocyte detachment was validated under the microscope. Analysis was performed using a SONY ID7000 multi-spectral flow cytometer. Plates were not cooled before or during measurement to maintain phagocytosis and efferocytosis functionality. Additional measurements were performed at 240 and 300 minutes post-apoptotic JTs addition for efferocytic cells requiring extended engulfment times.

2.8.3 Spectral Flow Cytometry Phagocytosis Assay

This assay may also be employed as a readout for phagocytosis. In this context, pHrodoGreen-labeled Escherichia coli particles are utilized as phagocytic targets in place of apoptotic JTs. All subsequent steps in the protocol, including washing procedures, staining, and flow cytometric analysis, remain unchanged.

2.8.4 Iron Metabolism Analysis

This assay setup can also be utilized to determine iron metabolism. By following the manufacturer's protocol for BioTracker Far-red Labile Fe2+ Dye, Sigma Aldrich, researchers can assess iron uptake and processing within cells. The workflow remains largely the same, with modifications tailored to incorporate iron-sensitive staining and analysis methods. In short, seeded Mφ, stained with an adjusted panel for iron metabolism assay, including antibodies against iron importers and the exporter ferroportin. To assess intracellular Fe^{2+} accumulation, cells were pretreated with 100 µM ferrous ammonium sulfate (FAS) in serum-free DMEM for 30 minutes before dye staining. The FAS solution was freshly prepared immediately before use. Measurement was done the same way as in efferocytosis and phagocytosis assay.

2.9 Assay validation using Confocal microscopy

2.9.1 Sample Preparation for Confocal Microscopy

Post Takata iMφs were seeded in density between 0.5-1 x10^5 per well into µ-Slide 8 Well polymer cover slip in SF-Diff + M-CSF, prior to the experiment. For negative efferocytosis/phagocytosis controls, wells were treated with 10 µM Cytochalasin D 1h pre-experiment and incubated at 37°C. After incubation, samples were stained with CellMask™ Plasma Membrane Stains orange, in a

1:1000 dilution, and Hoechst 33342, Trihydrochloride 1:500, were added and incubated for 10 min. After incubation, slides were washed 2x, and Jurkat suspension buffer was added.

For Phagocytosis assay: pHrodo™ Green *E. coli* Bioparticles™ Konjugat for Phagocytosis were diluted according to the manufacturer's protocol and added in a 1:10, iMφs: beads ratio. After 30 minutes of incubation at 37°C, images were acquired at intervals of 15 minutes.

For efferocytosis assay: apoptotic JTs (radiated with 0.075J/cm² and 13 hours post radiation incubation) were labelled with 5 µM pHrodoGreen were added at a ratio of 1:5 iMφs:pHrodoGreen Jurkat T-cells were added, and incubated for 30 min.

2.9.2 Confocal Microscopy

Images were taken on a Leica DMi8 Spinning Disk microscope with the confocal scanner CSU-X1. At ZMBH Heidelberg. Lasers: Laser: 405 nm - diode laser, 488 nm - 50 mW diode laser, 561 nm - 50 mW diode laser, 640 nm - Diode laser. We used the HC PL FLUOTAR 25x/0.8 IMM CORR objective and the Hamamatsu Orca Flash 4.0 LT (C11440-42U) camera. Pictures were acquired in 20 z-stacks at 1 um distance. Confocal microscopy was performed in cooperation with Tomasz Stadler (BioMedX Institute) and Dr. Holger Lorent (ZMBH Heidelberg).

2.10 Cite-Sequencing

2.10.1 Sorting Strategy of Synovial Cells

Prior to CITE-sequencing, total synovial cells were isolated from joint biopsy samples collected in Lisbon, Portugal, using the optimized protocol described by Edalat et al. Cell sorting was performed by Janine Lückgen and Maria Del Pilar Palacios, with decisions regarding sorting based on post-isolation cell counts. Specifically, samples with low cell numbers were processed directly for scRNA-seq and CITE-seq without prior sorting. Various sorting strategies were employed and iteratively refined throughout the project based on experimental findings. The decision-making process and applied sorting strategies are illustrated in Figure 2-2.

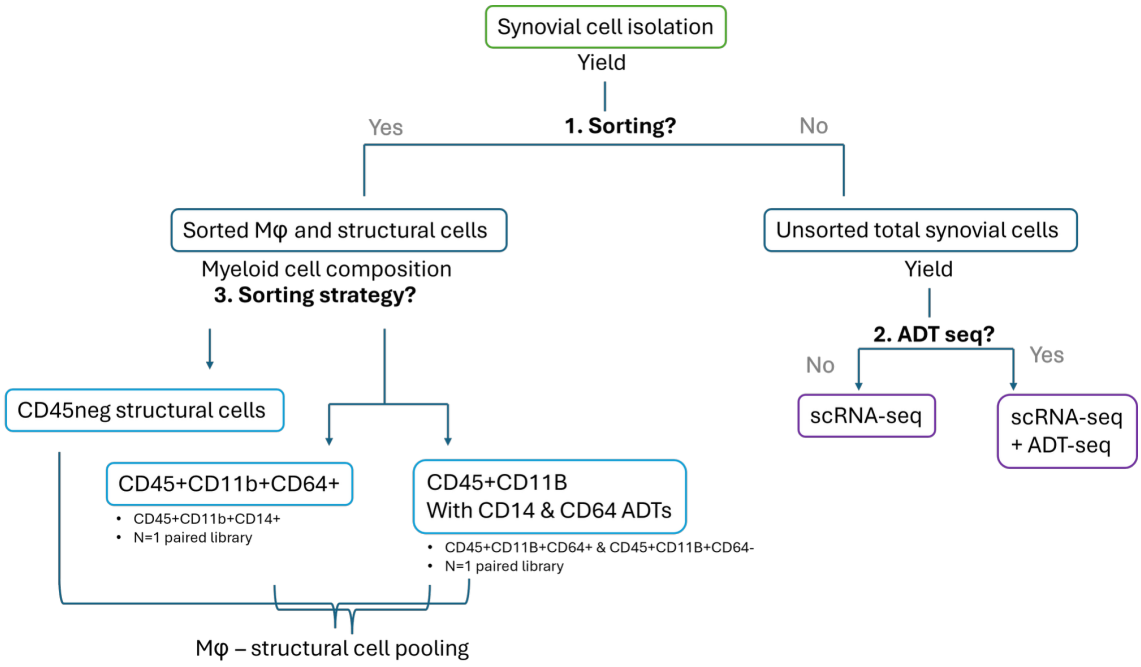

Figure 2-2 Decision tree, sorting strategy, and downstream analysis of synovial cells isolated from joint biopsies. Following total synovial cell isolation, the decision to proceed with fluorescence-activated cell sorting (FACS) was based on total cell yield. Samples with insufficient cell numbers were processed directly for single-cell RNA sequencing (scRNA-seq), and, when feasible, also included antibody-derived tag (ADT) profiling for CITE-sequencing. For samples with sufficient yield, initial sorting strategies were guided by the myeloid cell composition. In samples with low frequencies of $CD45^+$ cells, only $CD45^-$ cells were isolated. In samples enriched for $CD45^+$ cells, further selection was performed for macrophage populations using markers such as CD11b and CD64. As the project progressed, the sorting strategy was refined to isolate $CD45^-CD11b^+$ cells. Sorted populations were subsequently subjected to CITE-sequencing, including both transcriptomic (scRNA-seq) and protein (ADT) profiling.

2.11 Single-cell and Cell Surface Protein Library Preparation

Single-cell suspensions were processed using the Chromium Next GEM Single Cell 3' v3.1 with Cell Surface Protein (CSP) protocol, following the manufacturer's instructions (10x Genomics, CG000317 Rev C, 2021). Briefly, cells were labeled with barcoded antibodies targeting surface proteins, then encapsulated into Gel Bead-in-Emulsions (GEMs) using the Chromium Controller. Inside each GEM, cells were lysed, and reverse transcription occurred, capturing both mRNA and CSP tags. After GEMs were broken, cDNA was purified and amplified. Separate libraries were constructed for gene expression and CSP tags, which were quantified, pooled, and sequenced. This was performed by Janine Lückgen.

2.12 Data Analysis and Statistics

2.12.1 Analysis of Multispectral Flow Cytometry Data using Sony ID7000 Software

I used Sony ID7000™ software (Version 2.0.2) for sample unmixing, autofluorescence compensation and preliminary data analysis.

To accurately separate overlapping fluorescence signals, we employed spectral unmixing using the Sony ID7000 Spectral Cell Analyzer software (Version 2.0.2). This process involved recording the full emission spectra of each fluorochrome and computationally distinguishing their contributions to the detected signals.

First, Reference spectra were generated from singly antibody-labelled control samples using U ltracomp eBeads™ Kompensations-Beads (Invitrogen 01-2222-42), ensuring that each fluorophore's emission profile was accurately captured. These spectral profiles were then used to deconvolute the mixed signals in experimental samples. The unmixing algorithm assigned the appropriate contribution of each fluorophore to the overall detected fluorescence, correcting for spectral overlap and minimizing signal spillover.

Additionally, autofluorescence was accounted for by including unstained cell controls, allowing the software to subtract autofluorescence signals from the final unmixed data. This approach ensured a precise quantification of fluorescence intensities, leading to improved resolution and more reliable interpretation of multi-parameter flow cytometry data.

To correct for autofluorescence, we utilized the Autofluorescence Finder tool in the Sony ID7000 Spectral Cell Analyzer software. This tool enabled the detection and subtraction of autofluorescence, minimizing its impact on fluorescence signal quantification. Initially, unstained control samples were analyzed to identify inherent autofluorescence signals. Using virtual filters across multiple wavelengths, particularly in the ultraviolet and violet ranges where autofluorescence is more pronounced, distinct autofluorescent populations were identified. These populations were then gated, and their spectral signatures were recorded to serve as reference spectra. During spectral unmixing, these reference spectra were incorporated to computationally separate autofluorescence from fluorochrome-specific signals. This method allowed for a more accurate representation of true fluorescence, improving signal resolution and data reliability. By implementing this adjustment, autofluorescence interference was minimized, ensuring precise quantification of fluorescence signals from labeled markers.

2.12.2 Unsupervised Analysis of Multi-Spectral Flow Cytometry Data

After unmixing and autofluorescence adjustment in the SONY ID7000 software, flow cytometry data was further processed using CellEngine (Primity Bio). Unsupervised analysis was performed to identify population distributions and fluorescence intensity patterns. Compensation, transformation, and quality control were conducted within CellEngine using default or user-defined parameters.

To explore cellular heterogeneity, Uniform Manifold Approximation and Projection (UMAP) was applied for dimensionality reduction, allowing visualization of distinct cell populations based on marker expression. Hierarchical clustering and heatmaps were generated to assess relationships between populations and their marker co-expression profiles. Mean fluorescence intensity (MFI) values were computed for key markers, and comparisons were performed to evaluate expression differences across conditions.

2.12.3 Image Processing and Deconvolution

Raw fluorescence microscopy images were processed using Huygens Professional software (version 24-10), Scientific Volume Imaging, Hilversum, Netherlands) for deconvolution. The images were corrected for background noise and deconvolved using the Classic Maximum Likelihood

Estimation (CMLE) algorithm with a signal-to-noise ratio (SNR) set according to image acquisition conditions. To ensure consistency, identical deconvolution settings were applied across all images within the same experimental condition. Processed images were further analyzed using ImageJ/Fiji.

2.12.4 Analysis of CITE-seq Data

CITE sequencing data was analyzed by our external bioinformatician Helena Crowell using R. In short, Gene expression (GEX) and antibody capture (CSP) data were read and imported. The GEX data were formatted into a SingleCellExperiment object, with CSP data included as an alternative experiment (altExp). Low-quality cells were filtered based on quality control metrics. Feature selection and Leiden clustering were performed using a shared nearest neighbor (SNN) graph. Potential doublets were identified and removed using scFblFinder. Selected features were used for batch correction via Harmony integration. Dimensionality reduction was performed using UMAP, followed by SNN graph-based Leiden clustering. Cluster abundances, dimensionality reduction embeddings, and differentially expressed genes were visualized. Cells were stratified into stromal, myeloid, and other immune cell types for more targeted analysis. Each group was reprocessed and visualized using the same procedures as above. Clusters were annotated, and both GEX and CSP data were visualized by cluster, patient, condition, and sorting strategy.

2.12.5 Statistical Analysis

All statistical analyses outside Cell Engine were performed using GraphPad Prism (version 10, GraphPad Software, San Diego, CA, USA). Descriptive statistics were used to summarize the data, and results are presented as mean ± standard deviation (SD) or mean ± standard error of the mean (SEM), as appropriate. Normality was assessed using the Shapiro-Wilk test. Comparisons between two groups were conducted using an unpaired two-tailed t-test. For comparisons involving multiple groups, one-way or two-way analysis of variance (ANOVA) was performed. The significance level of $p < 0.05$ was considered statistically significant.

3. Results

3.1 Discoverer Mφ Enables the Analysis of Mφ Phenotypes and Functions Across Different Tissues, Pathologies, and Perturbations

To enable the systematic analysis of Mφ phenotypes and functions across diverse tissues, pathological contexts, and experimental perturbations, I developed the *Discoverer Mφ* Assay. This medium-throughput platform enables temporal profiling of Mφ functional states through data acquisition at defined time points. The assay is partially automated, featuring automated data collection, and is designed for scalability. Its versatility lies in its compatibility with a broad range of Mφ subtypes derived from multiple sources, and the modularity of its phenotyping panels, which can be readily tailored to specific experimental objectives. Moreover, the assay supports the assessment of multiple key Mφ functions, including efferocytosis, phagocytosis, and iron metabolism, and permits dynamic tracking of functional changes in response to perturbations. Beyond assessing Mφ surface marker-linked phenotypes, the *Discoverer Mφ Assay* enables the development, optimization, and fine-tuning of functional and phenotypic readouts for perturbation studies using tool compounds or genetic perturbations, such as functional CRISPR screens.

A key strength of the assay lies in its capacity to simultaneously resolve immunophenotypic and functional characteristics of target cells (e.g, Mφ) at the single-cell level, yielding multiparametric data per cell. While originally developed for Mφ, the assay is adaptable to other cell types due to its low complexity fluorochrome panels. These panels are designed within a green-red fluorescence window, allowing broad compatibility with commonly used fluorescent reporters and readouts. This design enables flexible antibody selection and functional assays across diverse cell types, enhancing the assay's utility in multi-omics workflows and broader immunological studies.

3.1.1 Discoverer Mφ – Design

In the first step, I developed and optimized a prototype *Discoverer Mφ* assay focusing on the phagocytosis and efferocytosis Mφ readouts. The *Discoverer Mφ* assay started with Mφ seeding in a 96-well plate under different experimental conditions. Next, Mφ were prelabeled with a 25 to 30 antibody panel against general Mφ markers (CD68, CD11b, CD14, CD64), markers indicative of trMφ (FOLR2, TREM2, TIMD4, CD163, CD206), markers indicative of tiMφ (CCR2), inflammation linked markers (CD48, CD86, CD80, CD274), efferocytosis receptors (MERTK) and the global leukocyte marker CD45 enabling detailed immunophenotyping. Different tool molecules were added during defined assay steps in accordance with the experimental design.

Subsequently, pHrodo™ Green-labeled *E. coli* bioparticles (for phagocytosis assays) or pHrodo™ Green-prelabeled apoptotic cells (for efferocytosis assays) were incubated with antibody-prelabeled Mφ. pHrodo™ Green is a pH-sensitive fluorophore that exhibits increased fluorescence intensity in acidic environments. Upon internalization of the bioparticles or apoptotic cells from the extracellular milieu (pH ~7.2) into Mφ, phagosomes are formed, which subsequently fuse with lysosomes to create phagolysosomes. Within these compartments, the pH decreases to approximately 5.0 and can reach as low as 4.5 during degradation processes (Westman & Grinstein,

2021), thereby enhancing the fluorescence of pHrodo™ Green (Lindner et al., 2020). This fluorescence increase serves as a quantitative readout for particle internalization and progression into the acidic intracellular compartment (Figure 3-1).

By combining targeted and carefully selected antibody labeling with pHrodo-based functional assessment, *Discoverer Mφ* enables concurrent phenotypic and functional profiling of phagocytic cells in a single experiment, using the multispectral flow cytometer SONY ID7000.

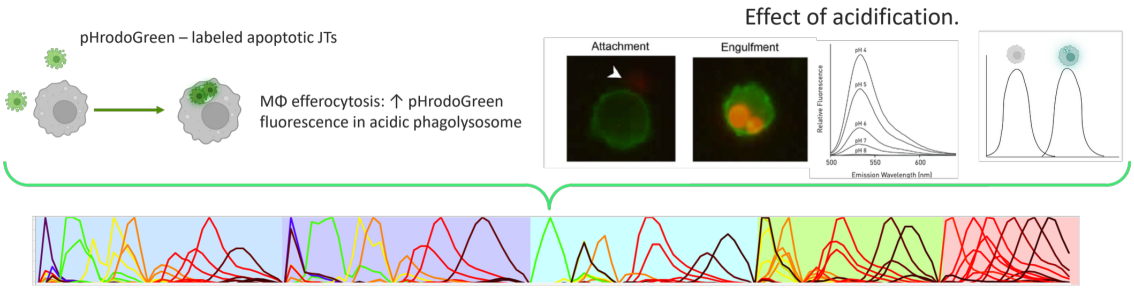

Figure 3-1 Assay principle. Created with BioRender, SONY ID7000 panel design tool.

Initially, I explored high-content imaging using the Incucyte platform to quantify efferocytosis, motivated by its ability to provide kinetic, spatially resolved readouts in live-cell assays (Clark et al., 2019). This approach utilized pHrodo™ Red-labeled apoptotic JTs, which was titrated (Appendix A-a) as targets for engulfment by Mφ. However, under our experimental conditions, the assay failed to generate a robust or interpretable signal. Specifically, pHrodo™ Red fluorescence measured in wells containing both Mφ and labeled apoptotic cells was comparable to control wells containing only pHrodoRed-labeled JTs. These observations suggested a lack of discrimination between engulfed and non-engulfed cells, raising concerns about assay sensitivity and specificity.

Nevertheless, I acknowledge that this result does not definitively reflect a limitation of the Incucyte platform itself. It remains plausible that efferocytosis did not occur to a detectable extent under these conditions, and that the low signal was a true biological outcome rather than a technical failure. Contributing factors may include suboptimal Mφ activation (in this case, M2-like Mφ polarized from MDMs) or inadequate apoptotic cell to phagocytic cell ratios. At the time, we did not perform complementary imaging (e.g., confocal microscopy) to confirm whether engulfment had taken place. Thus, we cannot entirely exclude the possibility that the assay underperformed due to ineffective efferocytosis rather than inadequate detection.

A critical technical challenge was the inability to efficiently remove non-internalized JTs after co-culture. Since pHrodo™ Red fluorescence is pH-dependent, residual apoptotic JTs adhering to Mφ or present in the medium could contribute to a background signal. As shown in our HCl-treated control (Appendix A-b), Jurkat cells exposed to acidic pH exhibited strong fluorescence, further supporting the idea that extracellular acidification or residual unengulfed targets may mask specific signals from internalized apoptotic cells (Appendix A-c,d).

A key limitation of this approach was the lack of phenotypic resolution, as the Incucyte system used in our experiments was equipped with only two lasers and corresponding detection channels, restricting analysis to the functional readout and a single Mφ surface marker. Given these limitations, both experimental and interpretational, it was concluded that the Incucyte platform was not suitable for reliably quantifying efferocytosis under our assay conditions and needs. The inability to confidently distinguish between internalized and non-internalized apoptotic cells, coupled with the lack of phenotypic information on Mφ, led us to discontinue this approach.

I subsequently transitioned to multispectral flow cytometry (SONY ID7000), which offered significantly higher sensitivity, robust internalization readouts via pHrodo™ Green fluorescence, and the added advantage of simultaneous high-dimensional phenotyping of phagocytic cells. The flow cytometry platform ultimately enabled a reliable and multiplexed characterization of efferocytic capacity, overcoming several limitations encountered in the initial imaging-based approach.

The multi-spectral flow cytometry approach was initially developed and optimized to evaluate both phagocytic and efferocytic capacities of Mφ. The procedure begins with seeding Mφ into a 96-well plate, followed by staining with a high-parameter panel comprising 25-30 markers for comprehensive Mφ characterization. After staining and washing steps, chemical inhibitors, if applicable, are added, followed by an additional incubation period prior to functional analysis.

3.1.2 Design and Optimization of a Multi-Parameter Assay for Investigating Mφ Function and Efferocytic Pathways

To develop a versatile assay applicable across diverse experimental goals, including human tissue Mφ characterization, drug and CRISPR perturbation studies, and functional readout development, I systematically evaluated and optimized multiple assay parameters. A central objective in the assay design was to enable mechanistic insights into Mφ function, particularly in the context of phagocytosis and efferocytosis. The design of the assay was thus designed to closely track the sequential mechanistic steps of phagocytosis and efferocytosis under physiologically relevant conditions as close as possible.

For the efferocytosis assay, specific focus was placed on optimizing the 'find-me' and 'eat-me' signals presented by apoptotic cells. This included fine-tuning the extent of PS exposure on the surface of JTs by selecting an appropriate cell death inducer. In parallel, I assessed the expression of Mφ surface proteins and receptors known to interact with apoptotic cell ligands to confirm their potential involvement in efferocytic uptake. Particularly, the expressions of MERTK, CD163, TIMD4, TREM2, FOLR2 and CD206 (Mehrotra & Ravichandran, 2022; Moon et al., 2020) were tested based on published literature.

Several additional experimental variables were optimized, including the composition and concentration of the antibody panel used for Mφ phenotyping, labeling conditions for Mφ, and incubation times for apoptotic cell uptake and subsequent degradation. Furthermore, a panel of pharmacological inhibitors was tested to evaluate their ability to modulate efferocytosis, allowing for functional perturbation of the pathway. An overview of the key optimization steps and assay parameters is provided in Figure 3-2.

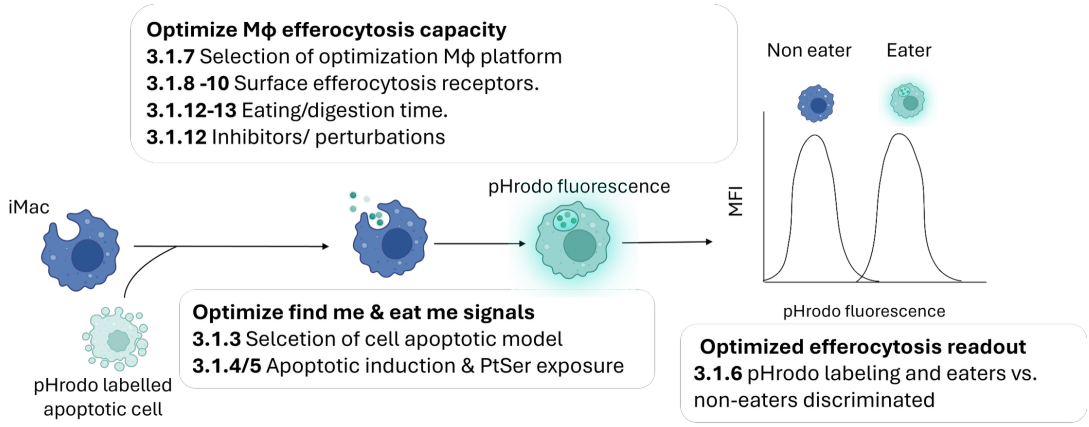

Figure 3-2 Required assay optimization steps. Bold numbers indicate chapters. *Created with BioRender*.

3.1.3 Selection of Apoptotic Target Cell Model

Jurkat T cells (JTs) (ATCC TIB-152), a human T lymphocyte-derived cell line, were selected as the apoptotic cell model for the efferocytosis assay due to their extensive use in efferocytosis research, which facilitates direct comparison with previously published studies (Elliott & Ravichandran, 2010). JTs are considered a gold standard in *in vitro* efferocytosis assays because they exhibit a well-characterized and reproducible apoptotic phenotype, are readily accessible, and are easily manipulated in culture. While other cell lines, such as PBMCs, can also undergo apoptosis and be engulfed by phagocytes, they are more variable in cell composition and culture and less frequently used in efferocytosis models, which would limit the comparability and reproducibility of the assay. JTs have been shown to be efficiently engulfed by various phagocytic cell types, including Mφ, reinforcing their utility in studying apoptotic cell clearance in vitro (Kraynak et al., 2022;Ballerie et al., 2019).

3.1.4 Drug-Induced Apoptosis Induction: Staurosporine Identified as Optimal Candidate

The gold standard for inducing apoptosis in JTs for efferocytosis assays involves the use of apoptosis-inducing agents such as staurosporine or camptothecin (Sanchez-Alcar et al., 2000; Ullal & Pisetsky, 2010). Staurosporine induces apoptosis by broadly inhibiting protein kinases, leading to mitochondrial dysfunction, cytochrome c release, caspase activation, ROS generation, and downregulation of anti-apoptotic proteins, ultimately triggering programmed cell death (Ullal & Pisetsky, 2010). Camptothecin induces apoptosis in JTs by inhibiting DNA topoisomerase I, leading to DNA damage and activation of the intrinsic apoptotic pathway. This process involves mitochondrial cytochrome c release and caspase activation, resulting in programmed cell death (Sanchez-Alcar et al., 2000)

To minimize potential pro-inflammatory effects caused by necrotic cells on phagocytes, my objective was to enrich JTs in the early stages of apoptosis. Specifically, I aimed to achieve a high proportion of early apoptotic cells relative to necrotic cells. Early apoptotic cells are characterized by maximal externalization of PS on the outer leaflet of the plasma membrane. Additionally, PS serves as a key ligand for efferocytic receptors on phagocytes. Its externalization on the surface of apoptotic cells functions as an "eat-me" signal, facilitating recognition and subsequent engulfment by phagocytes through receptor-mediated pathways (Ravichandran & Lorenz, 2007).

To determine the optimal inducer and incubation time, I employed Annexin V (AnxV) staining, which detects PS exposure, in combination with 7-Aminoactinomycin D (7AAD), a DNA intercalating dye that penetrates cells with compromised membranes. This allowed discrimination of distinct cell populations via flow cytometry using a FACS Aria Fusion system. Early apoptotic cells were identified as $AnxV^{pos}$ and $7AAD^{neg}$, indicating high PS exposure with intact membrane integrity. Late apoptotic cells were double-positive for both AnxV and 7AAD but displayed reduced AnxV signal, consistent with compromised membranes and diminishing PS externalization. Necrotic cells were identified as AnxV-negative and 7AAD-positive, while viable cells were negative for both markers (Gating strategy presented in Figure 3-3a).

Treatment with 1 µM staurosporine for 4 hours resulted in a significantly higher proportion of $AnxV^{+}$/7-AAD^{-} early apoptotic JTs proportion (62.5%) as compared to 4-hour treatment with 7.5 µM camptothecin (43.03 % early apoptotic cells). However, 7.5 µM camptothecin treatment led to a notable increase in the early apoptotic cell fraction, when incubated for 6 hours, (58%) which was comparable to that observed with 4-hour treatment of cells with 1 µM staurosporine (Figure

3-3b). PS surface exposure as determined by the AnxV mean fluorescence intensity (MFI), was significantly greater in 4h staurosporine treated JTs compared to 6h camptothecin-treated JTs (1474.33 a.u. versus 463.67 a.u., p=0.0001, Figure 3-3c).

Based on these findings, staurosporine was identified as the most suitable apoptosis-inducing agent for our experimental requirements, as it elicited the highest proportion of $AnxV^+/7AAD^-$ early apoptotic cells in the 4 hour condition, induces the highest phosphatidyl serine exposure on JTs surfaces and demonstrated a more rapid induction of apoptosis, particularly evident at the 4h treatment time point, accelerating experimental workflows.

After identifying staurosporine as the optimal apoptosis-inducing agent, the experimental conditions for staurosporine-induced apoptosis in JTs were further optimized, with particular focus on the duration of exposure. As shown in Figure 3-3d, among tested treatment times (3 hours, 4 hours and 6 hours), treatment with 1 µM staurosporine for 3 hours resulted in the highest proportion of Annexin $V^+/7\text{-}AAD^-$ early apoptotic cells (58.48%), accompanied by a relatively low percentage of Annexin $V^+/7\text{-}AAD^+$ late apoptotic (16.3%) and Annexin $V^-/7\text{-}AAD^+$ necrotic cells (3.5%). When analyzing Annexin V MFI, a proxy for PS surface exposure, 4-hour staurosporine treatment yielded the highest PS exposure (488.3 a.u.), compared to 359 a.u. observed at 3 hours (Figure 3-3e).

Consequently, a 3-hour treatment with 1 µM staurosporine was selected as the optimal condition for inducing apoptosis in JTs for downstream applications, such as Mφ efferocytosis assays. This condition maximized the yield of early apoptotic cells while maintaining relatively high PS exposure, only slightly lower than that observed at 4 hours.

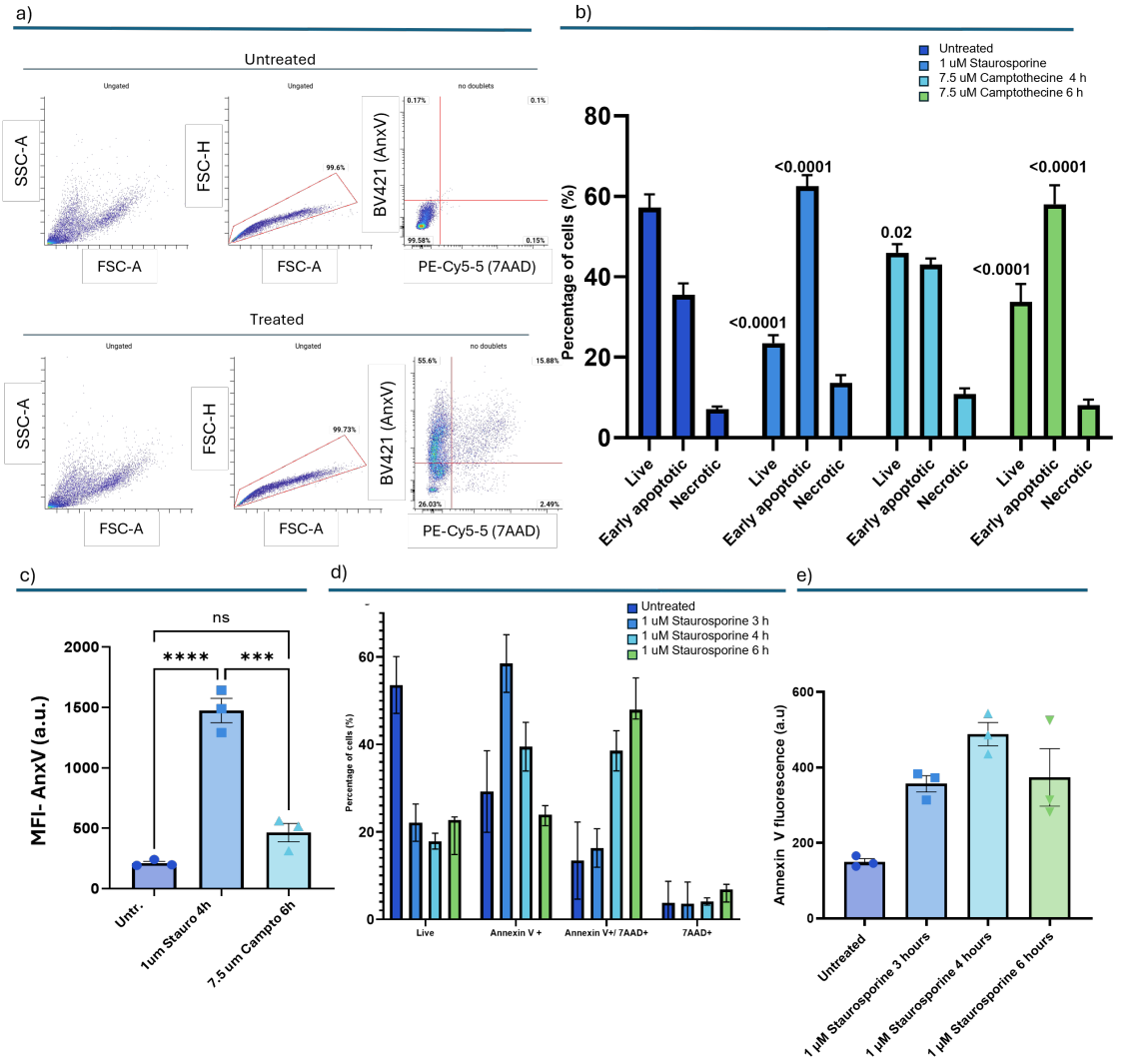

Figure 3-3 Drug-induced apoptosis induction. a) Gating strategy used in Annexin V/7-AAD apoptosis assay to identify cell populations: live cells (Annexin V^-/7-AAD^-), early apoptotic cells (Annexin V^+/7-AAD^-), late apoptotic cells (Annexin V^+/7-AAD^+), and necrotic cells (Annexin V^-/7-AAD^+). BV421 = Annexin V staining, PE Cy-5.5 = 7AAD signal. b) Percentage of live, early apoptotic, late apoptotic, and necrotic Jurkat T cells after treatment with apoptosis-inducing drugs: Staurosporine (1 µM, 4 h), and Camptothecin (7.5 µM, 4 h and 6 h). One-way Anova, n=3. c) Direct comparison of apoptotic response between Staurosporine (1 µM, 4 h) and Camptothecin (7.5 µM, 6 h). d) Titration of Staurosporine (1 µM) treatment for 3h, 4h, and 6h, showing the highest phosphatidylserine exposure at 3 h. Data are presented as mean ± SEM of n = 3). Statistical analysis was performed using one-way ANOVA. e) Annexin V exposure upon 1 µM staurosporin exposure for 3h, 4h, and 6h. Data shown as MFI ± SEM. BV421 Brilliant Violet 421; PE-Cy5.5 Phycoerythrin-Cyanine5.5, Stauro Staurosporine, Campto camptothecin, MFI mean fluorescence intensity

3.1.5 UV-radiation Efficiently Induced Apoptosis in Jurkat T cells

I established a UV-induced apoptosis assay to generate drug-free apoptotic cell supernatants, as drug-based apoptosis models are unsuitable for studying Mφ responses due to potential interference from residual drugs. First, I optimized the apoptosis-inducing conditions including UV radiation dose, exposure duration, and post-exposure incubation time to achieve consistent and reproducible induction of early apoptosis. These conditions led to a high percentage of early apoptotic cells characterized by PS exposure on the cell surface. UV radiation induces apoptosis through mechanisms such as DNA damage, oxidative stress, and activation of death receptor pathways,

culminating in caspase activation and cell death (Nakvasina et al., 2023). The resulting supernatants contain a diverse array of "find-me" signals that attract and potentially prime Mφ, allowing for a physiologically relevant model of apoptotic cell communication. Moreover, UV-induced PS exposure has been proposed as a potential therapeutic strategy in skin cancer (Shurin et al., 2009).

To achieve the highest possible PS exposure on the cell surface and the greatest proportion of early apoptotic cells, characterized by Annexin V-positive and 7-AAD-negative staining, I tested a range of UV radiation doses, from 0.025 J/cm² to 0.2 J/cm², using both UV-A and UV-B wavelengths and harvesting and assessing AnxV and 7AAD signal after different time points (10h, 13h and 16h post radiation).

These experiments demonstrated that a dose of 0.075 J/cm² of combined UV-A/UV-B radiation, followed by a 13-hour post-exposure incubation period, resulted in the highest surface exposure of PS (AnxV signal) on JTs. This condition yielded the greatest MFI of Annexin V binding (MFI AnxV = 2261 a.u., Figure 3-4a) and the highest proportion of early apoptotic cells (53,3%), defined as Annexin V-positive and 7-AAD-negative, compared to late apoptotic (2.45%) or necrotic populations (19,57%) (Figure 3-4b). This optimized UV-induced apoptosis condition was then benchmarked against staurosporine-induced apoptosis, a commonly used gold standard. UV radiation induced an even higher level of PS exposure as measured by AnxV binding signal (0.075 J/cm² UV: 22261 vs. 1984 in staurosporine condition; Figure 3-4b). Notably, the fraction of early apoptotic cells under UV treatment was even higher than that observed with staurosporine, with a lower proportion of late apoptotic and necrotic cells, suggesting a more favorable apoptotic profile for downstream applications (53,3% vs. 38.34%, Figure 3-4d).

Based on these results, UV-induced apoptosis induction with a dose of 0.075 J/cm² was performed in the following efferocytic experiments.

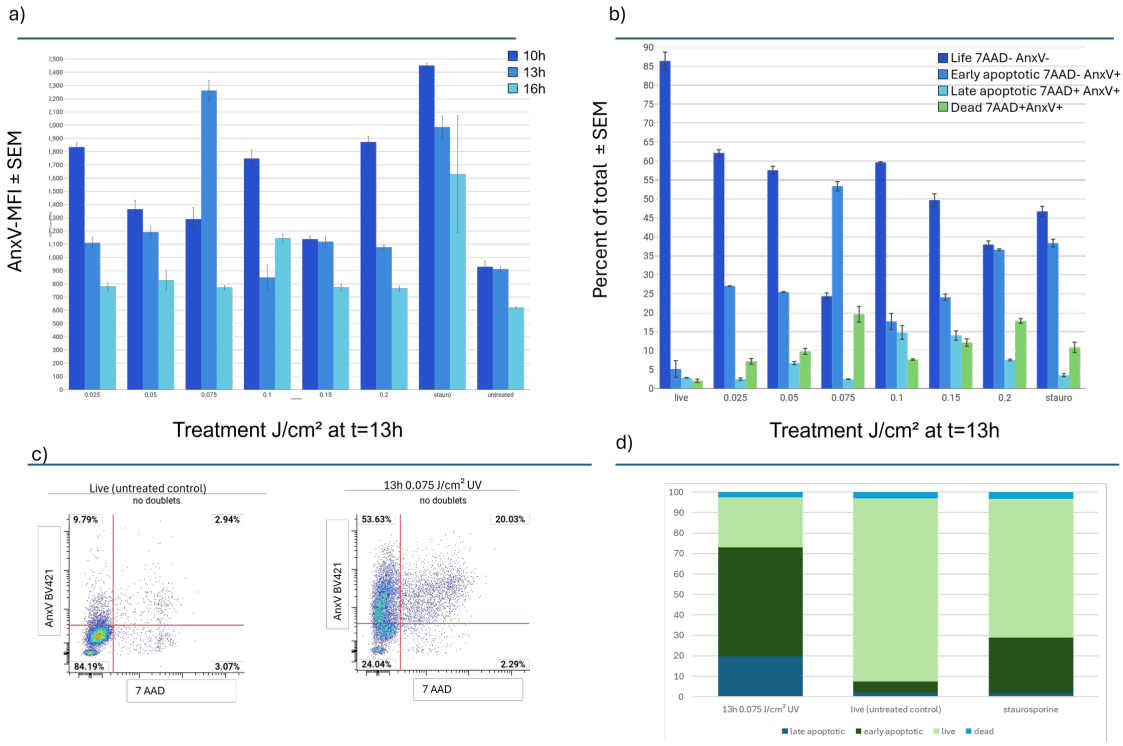

Figure 3-4 Optimizing UV-induced apoptosis of Jurkat T cells. Annexin V/7-AAD apoptosis assay. a) Mean fluorescence intensity (MFI) of Annexin V binding on Jurkat T cells exposed to varying doses of UV radiation (x-axis). Following UV exposure, cells were incubated for 10–16 hours prior to analysis. Unstained cells and staurosporine-treated cells served

as negative and positive controls, respectively. *n* = 3. b) Distribution of apoptotic populations (live, early apoptotic, late apoptotic/necrotic) across UV radiation doses at 13 hours post-exposure. c) Representative dot plots comparing untreated control cells and cells treated with 0.075 J/cm² UV radiation. d) Comparison of UV-induced (0.075 J/cm²) and staurosporine-induced apoptosis in Jurkat T cells. Proportions of live, early apoptotic, late apoptotic, and necrotic cells are shown as percentages of total cells. *n* = 3. Analysis done with CellEngine.

3.1.6 Titration of pHrodoGreen Dye to Track Apoptotic Cell Acidification

To monitor apoptotic corpse engulfment by phagocytes, I employed pHrodoGreen staining of apoptotic cells, a pH-sensitive dye that increases in fluorescence as pH decreases. This dye was selected over pHrodoRed due to compatibility with our existing staining panel, which contains multiple red-emitting fluorophores. Using pHrodoRed would have resulted in excessive spectral overlap. Additionally, according to the manufacturer (Thermo Fisher Scientific), pHrodoGreen has a narrower emission peak compared to pHrodoRed, reducing spillover into adjacent detection channels.

The goal of this experiment was to determine an optimal concentration of pHrodoGreen for labeling apoptotic JTs, enabling reliable tracking of pH changes associated with their uptake and internalization into the acidic phagolysosome (pH ~4.5–5) from the extracellular environment (pH ~7.2). I tested a titration range from 100 nM to 10 µM pHrodoGreen. JTs were labeled with each concentration and subjected to pH adjustment. The resulting fluorescent signal was measured by multi-spectral flow cytometry.

Titration results (Figure 3-5a) showed that concentrations between 1 µM and 10 µM yielded optimal separation between labeled and unlabeled JTs. At these concentrations, pHrodoGreen fluorescence was sufficiently bright to distinguish labeled apoptotic cells from background and antibody-derived signals used to phenotype the phagocytes. Importantly, the signal remained sensitive to subtle variations in uptake efficiency. From this range, 5 µM pHrodoGreen was identified as the optimal concentration for labeling JTs in a separate experiment. This concentration provided a robust signal for detecting apoptotic cell uptake and confirmed their subsequent acidification upon internalization into the phagolysosome (Figure 3-5b). 5 µM pHrodoGreen labelled JTs were used for following efferocytosis experiments.

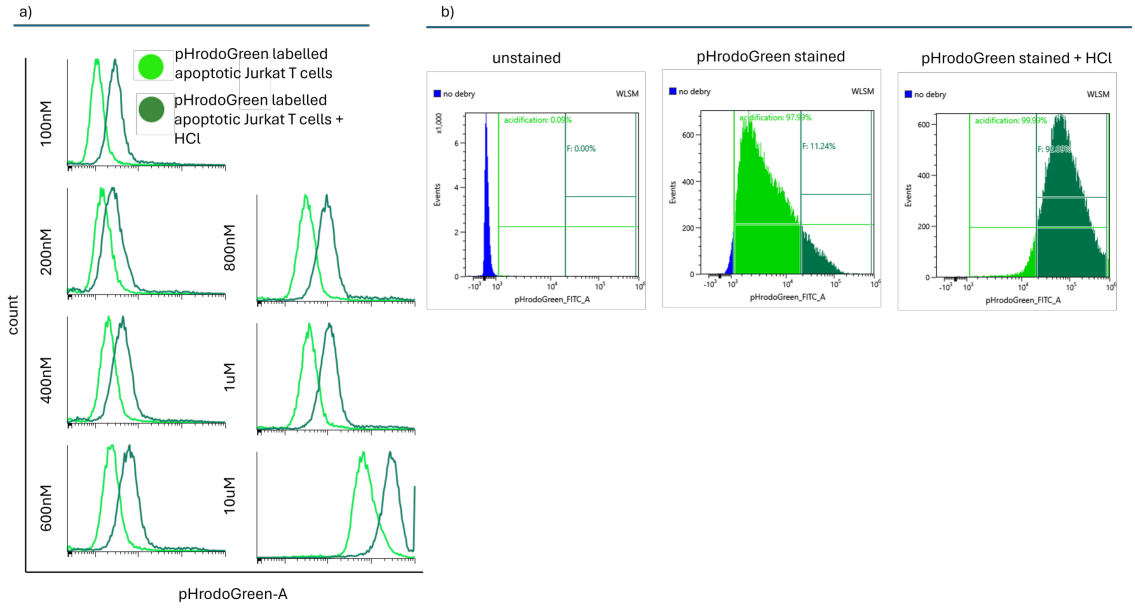

Figure 3-5 pHrodoGreen titration on apoptotic Jurkat T cells. a) pHrodoGreen fluorescence intensity upon staining with pHrodoGreen dye concentrations pf 100nM, 200nM, 400nM, 600nM, 800nM, 1000nM and 10000nM. Graphs represent

pHrodGreen labelled apoptotic Jurkat T cells (light green) and pHrodoGreen LaBelle apoptotic Jurkat T cells + HCl to mimic acidic environment within the phagolysosme (pH4.5-5) (dark green) b) apoptotic Jurkat T cells stained with a concentration of 5 µM pHrodoGreen dye. Samples were acquired, unmixed, and autofluorescence-adjusted on the SONY ID7000 and analyzed using CellEngine. *N=2.*

3.1.7 Selection of Mφ Platforms for Studies of Mφ Functions and Phenotypes

scRNA-seq studies have revealed the broad transcriptional diversity of human tissue Mφ subsets. However, their functional roles remain largely elusive and are primarily inferred from transcriptomic data. For example, synMφ from both healthy individuals and patients with RA express high levels of genes associated with efferocytosis. Yet, there are currently no established assays that enable direct tracking of efferocytosis in these cells (Alivernini et al., 2020).

Access to and the quantity of primary tissue Mφ are often limited, which precludes assay development and optimization using these valuable cells.

To address this gap, a variety of in vitro Mφ models have been developed. These models support the development of new Mφ assays, facilitate the study of Mφ biology, and aid in the identification of novel molecular targets for Mφ-targeted therapies. Findings from in vitro systems can then be validated in primary human Mφ through focused, hypothesis-driven experiments.

Core Aims of the *Discoverer-Mφ* Platform:

1. Enable multiparameter functional and phenotypic characterization of primary human Mφ isolated from human organs/tissues, with a primary focus on synovial tissue and synovial fluid-derived Mφ.
2. Characterize and compare various in vitro Mφ platforms with primary Mφ to identify the most suitable models for gain and loss-of-function studies targeting diverse Mφ phenotypes and functions.
3. Optimize phenotypic and functional Mφ readouts for perturbation studies, including chemical tool molecules and CRISPR-based perturbations (single and pooled CRISPR screens).

Peripheral blood $CD14^+$ monocytes are an accessible source for generating monocyte-derived macrophages (MDMs) in vitro. These cells can be polarized using various cytokine combinations to simulate distinct features of primary human Mφ, particularly those of tiMφ. However, MDMs reflect trMφ biology only to a limited extent. trMφ often arise from yolk sac progenitors during embryogenesis and are maintained locally throughout adulthood. These embryonically derived trMφ are distinct from tiMφ, which are primarily derived from circulating monocytes.

To better replicate the characteristics of trMφ in vitro, we established induced pluripotent stem cell (iPSC)-derived macrophage (iMφ) platforms. iMφ recapitulate several features of trMφ, and the iPSC-to-iMφ differentiation protocols mimic yolk sac hematopoiesis. The advantages and disadvantages of different Mφ platforms used for studying Mφ biology and target discovery are summarized in Table 3-1.

Given our research focus on trMφ pathobiology, we established and optimized the *Discoverer Mφ* platform using the iMφ model. iMφ not only reflect key characteristics of trMφ but can also be generated in sufficient quantities. Moreover, iPSCs are amenable to large-scale genetic perturbation studies, such as those using CRISPR technologies(Singh et al., 2024).

To generate iMφ, we followed the protocol described by Takata et al., 2017 and colleagues.

Table 3-1 Advantages and disadvantages of selected Mφ models.

Mφ model selection	Tissue-derived	Monocyte-derived Mφ	iPSC derived Mφ
Accessibility	Very limited	Good	Unlimited
Capacity for genome editing	Limited	Limited	Easier
Association	Tissue-resident like	Circulating	Tissue resident-like

3.1.8 Panel with low complexity index and spillover allows discrimination of Mφ subtypes and connects to functionality

The Mφ immunophenotyping antibody panel was designed to comprehensively cover a range of biologically relevant targets. These included Mφ-specific markers, pan-leukocyte, tissue-residency-associated markers, and markers linked to Mφ infiltration, inflammation, pro-resolution, and tissue-protective functions. This strategic panel composition enabled us to assess Mφ identity and functional state across multiple axes, including phenotype, localization, and activation status. For the efferocytosis panel study, the antibody panel was extended to include markers associated with efferocytosis (MERTK, TIMD4, FOLR2), incorporating antibodies against proteins previously implicated in this process (Table 3-2).

Table 3-2 Mφ marker phenotyping panel

MARKER	FUNCTION
CD45	Global leukocyte marker
CD64	tissue residency/ trMφ marker
TIMD4	
MERTK	
TREM2	
FOLR2	
CD163	
CD206	
CD11B	Global Mφ marker
CD14	
CD68	
HLA-DR	Antigen presentation and Mφ activation
CD40	
CD48	Immunoregulation
CD86	
CD80	
CD274	
CD38	linked to Mφ inflammation
CD36	lipid metabolism
CCR2	tiMφ marker

Additional panels were developed to investigate further Mφ-associated targets and to include functional readouts, such as indicators of iron metabolism (CD91, SLC40a1, CD71) (Appendix E-

d). Furthermore, to facilitate analysis of the synovial tissue microenvironment, antibodies targeting non-myeloid structural cells were included (e.g., antibodies for fibroblast markers, endothelial cell markers, etc.) (Appendix E-e).

The flexibility and versatility of our panel design were enabled by careful fluorochrome selection criteria. These were driven by the need to: 1. maximize marker coverage within available detector space, 2. minimize spectral overlap, and 3. preserve channel availability for functional probes. A key principle guiding fluorochrome assignment was to match fluorochrome brightness to antigen density. Highly expressed and abundant markers such as CD45 and CD14 were assigned to dimmer fluorochromes, thereby reserving the brightest dyes for low-abundance or weakly expressed targets (Figure 3-6a).

Furthermore, widely used markers (e.g., CD11b, CD45) are commercially available in a broad range of fluorochrome conjugates. This allowed us to assign such markers to less commonly used or more spectrally unique dyes (“exotic” channels), providing greater flexibility in panel construction. Conversely, less common markers with limited fluorochrome options, such as FOLR2, were allocated to more standard and brighter channels such as PE, even though PE exhibits relatively higher spectral spillovers. This strategic balancing of brightness, availability, and spectral behavior was crucial to maximizing panel performance.

To evaluate the performance of spectral unmixing in the spectral flow cytometry setup, I analyzed the R^2 matrix derived from single-stained controls using the Sony ID7000 spectral analyzer. This matrix quantifies spectral spillover (non-orthogonality) between fluorophores, which is a critical determinant of panel quality.

Our core antibody panel comprises 23 different fluorophores. The average R^2 value across all fluorophore pairs was 0.093, indicating low overall spectral spillover. The median R^2 was 0.011, suggesting that most fluorophores exhibited minimal interference with others. The minimum R^2 value reached ~0.000004, representing near-perfect spectral separation in certain fluorophore combinations (Figure 3-6b).

Among the 23 fluorophores analyzed, PE displayed the highest overall spillover, particularly into PE-Fire 810 (R^2 = 0.34). Despite this relatively high value, it remained within the acceptable threshold for panel performance and did not compromise downstream analysis. Notably, AF488 exhibited the lowest overall spillover, making it an optimal choice for channels requiring minimalinterference. This informed us of our decision to assign AF488 to the functional pHrodoGreen readout, which is particularly sensitive to spectral contamination.

Regarding the choice of pHrodoGreen, the selection was influenced by the limited number of commercially available conjugations. We prioritized fluorophores that minimized spillover into pH-sensitive channels while ensuring compatibility with the remaining antibody panel.

a)

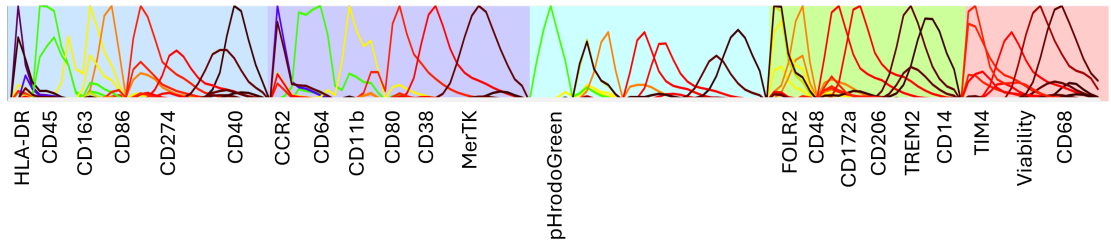

b)

Marker	Fluorochrome	Sum	HLA-DR BUV395	CD45 BUV496	CD163 BUV563	CD86 BUV615	CD274 BUV661	CD40 BUV805	CCR2 BV421	CD64 BV510	CD11b BV570	CD80 BV650	CD38 BV711	MERTK BV785	pHrodoGreen AF488	FOLR2 PE	CD48 PE-CF594	CD172a PE-Cy5	CD206 PE-Fire700	TREM-2 PE-Cy7	CD14 PE-Fire810	TIM4 APC	viability Zombie-NIR	CD68 APC-Fire750
HLA-DR	BUV395	0.2		0.02	0.01	0.00	0.00	0.15	0.01	0.00	0.00	0.00	0.00	0.00	0.00	0.00	0.00	0.00	0.00	0.00	0.01	0.00	0.00	0.00
CD45	BUV496	0.5	0.02		0.03	0.00	0.01	0.00	0.01	0.29	0.00	0.01	0.01	0.00	0.00	0.00	0.01	0.01	0.01	0.01	0.02	0.01	0.01	0.01
CD163	BUV563	0.7	0.01	0.03		0.24	0.00	0.00	0.00	0.01	0.17	0.01	0.03	0.02	0.00	0.10	0.01	0.01	0.02	0.01	0.01	0.01	0.01	0.02
CD86	BUV615	0.6	0.00	0.00	0.24		0.03	0.00	0.00	0.00	0.08	0.01	0.02	0.02	0.01	0.01	0.09	0.00	0.01	0.01	0.00	0.00	0.01	0.02
CD274	BUV661	0.8	0.00	0.01	0.00	0.03		0.00	0.00	0.01	0.02	0.15	0.02	0.02	0.01	0.01	0.01	0.02	0.00	0.02	0.04	0.43	0.00	0.00
CD40	BUV805	0.4	0.15	0.00	0.00	0.00	0.00		0.00	0.00	0.02	0.02	0.00	0.07	0.00	0.01	0.01	0.02	0.02	0.00	0.01	0.01	0.00	0.02
CCR2	BV421	0.2	0.01	0.01	0.00	0.00	0.00	0.00		0.02	0.01	0.00	0.00	0.12	0.00	0.00	0.01	0.01	0.01	0.01	0.01	0.00	0.00	0.01
CD64	BV510	0.6	0.00	0.29	0.01	0.00	0.01	0.00	0.02		0.02	0.00	0.02	0.00	0.00	0.01	0.01	0.03	0.03	0.02	0.03	0.01	0.01	0.02
CD11b	BV570	0.9	0.00	0.00	0.17	0.08	0.02	0.02	0.01	0.02		0.01	0.03	0.01	0.01	0.29	0.07	0.01	0.02	0.02	0.05	0.01	0.02	0.03
CD80	BV650	0.5	0.00	0.01	0.01	0.01	0.15	0.02	0.00	0.00	0.01		0.04	0.01	0.01	0.01	0.01	0.00	0.01	0.03	0.05	0.07	0.01	0.02
CD38	BV711	0.4	0.00	0.01	0.03	0.02	0.02	0.00	0.00	0.02	0.03	0.04		0.03	0.01	0.02	0.03	0.01	0.00	0.02	0.06	0.00	0.05	0.00
MERTK	BV785	0.5	0.00	0.00	0.02	0.02	0.02	0.07	0.12	0.00	0.01	0.01	0.03		0.01	0.02	0.03	0.04	0.04	0.01	0.03	0.01	0.00	0.01
pHrodoGreen	AF488	0.1	0.00	0.00	0.00	0.01	0.01	0.00	0.00	0.00	0.01	0.01	0.01	0.01		0.00	0.00	0.01	0.01	0.00	0.00	0.00	0.00	0.01
FOLR2	PE	1.0	0.00	0.00	0.10	0.01	0.01	0.01	0.00	0.01	0.29	0.01	0.02	0.02	0.00		0.14	0.00	0.00	0.00	0.34	0.01	0.01	0.01
CD48	PE-CF594	0.5	0.00	0.01	0.01	0.09	0.01	0.01	0.01	0.01	0.07	0.01	0.03	0.03	0.00	0.14		0.04	0.00	0.01	0.03	0.00	0.01	0.02
CD172a	PE-Cy5	0.6	0.00	0.01	0.01	0.00	0.02	0.02	0.01	0.03	0.01	0.00	0.01	0.04	0.01	0.00	0.04		0.25	0.00	0.00	0.10	0.01	0.01
CD206	PE-Fire700	0.5	0.00	0.01	0.02	0.01	0.00	0.02	0.01	0.03	0.02	0.01	0.00	0.04	0.01	0.00	0.00	0.25		0.02	0.00	0.00	0.00	0.00
TREM-2	PE-Cy7	0.5	0.00	0.01	0.01	0.01	0.02	0.00	0.01	0.02	0.02	0.03	0.02	0.01	0.00	0.00	0.01	0.00	0.02		0.22	0.01	0.00	0.07
CD14	PE-Fire810	0.9	0.01	0.02	0.01	0.00	0.04	0.01	0.01	0.03	0.05	0.05	0.06	0.03	0.00	0.34	0.03	0.00	0.00	0.22		0.02	0.01	0.00
TIM4	APC	0.7	0.00	0.01	0.01	0.00	0.43	0.01	0.00	0.01	0.01	0.07	0.00	0.01	0.00	0.01	0.00	0.10	0.00	0.01	0.02		0.01	0.00
viability	Zombie-NIR	0.6	0.00	0.01	0.01	0.01	0.00	0.00	0.00	0.01	0.02	0.01	0.05	0.00	0.00	0.01	0.01	0.01	0.00	0.00	0.01	0.01		0.47
CD68	APC-Fire750	0.7	0.00	0.01	0.02	0.02	0.00	0.02	0.01	0.02	0.03	0.02	0.00	0.01	0.01	0.01	0.02	0.01	0.00	0.07	0.00	0.00	0.47	

Figure 3-6 Panel design. a) Exemplary Mφ panel for functional efferocytosis and phagocytosis readout. b) R^2 matrix of Mϕ panel for functional efferocytosis and phagocytosis readout. *Created with SONY ID7000 template.*

Further optimization of the panel could include re-evaluating fluorophore combinations with high R^2 values, adjusting detector configurations, or implementing computational corrections to improve unmixing accuracy.

3.1.9 Accurate Discrimination of Engulfed Versus Free-Floating Jurkat T Cells in Efferocytosis Experiments

In the context of efferocytosis assays involving a mixed population of JTs and Mφ, a critical challenge arises from the incomplete or non-performed removal of non-engulfed JTs cells. In experiments in which JTs were removed, despite extensive washing steps, some JTs remain freely floating within the culture, and additional washes might have led to detachment and unintended loss of adherent Mφ. Consequently, there is a need for an alternative strategy to reliably discriminate between free-floating JTs and those that are either attached to or engulfed by Mφ.

This distinction is essential, particularly when analyzing pHrodoGreen signals. pHrodo-positive signals originating from internalized JTs indicate true efferocytosis events, while signals from external, non-engulfed JTs may produce false positives. Thus, to accurately quantify efferocytosis, it is critical to establish a gating strategy that distinguishes between these populations.

To enable this, Mφ were pre-labelled with a panel containing the pan-leukocyte marker CD45 and Mφ identifying CD14 and CD11b, allowing for clear identification and discrimination from JTs during flow cytometric analysis. Cells were first gated based on viability dye (Zombie NIR) exclusion and CD45 expression. Specifically, CD45-negative and viability dye-high events were excluded from the analysis to remove dead cells and non-target populations (Figure 3-7a and 3-7b).

Several assay controls were implemented to validate and optimize the gating strategy. Unstained Mφ or antibody-prelabelled Mφ were incubated with either unlabeled (Figure 3-7c), or pHrodo-Green-labelled JTs, both in the presence and absence of co-culture (Figure 3-7c). These controls helped define fluorescence thresholds and signal characteristics for positive versus negative populations. Additionally, JTs labelled with pHrodoGreen were analyzed both in the absence and presence of hydrochloric acid (HCl), simulating the acidic milieu of phagolysosomes. This allowed further refinement of gating parameters to detect the pHrodo signal shift during engulfment events.

The final gating strategy enabled reliable discrimination between Mφ and JTs and allowed further sub-gating of Mφ into phagocytic (‘eater’) and non-phagocytic (“non-eater”) subsets based on internalized pHrodoGreen-positive JTs (Figure 3-7e). This approach ensured precise quantification of efferocytosis while minimizing false-positive signal attribution.

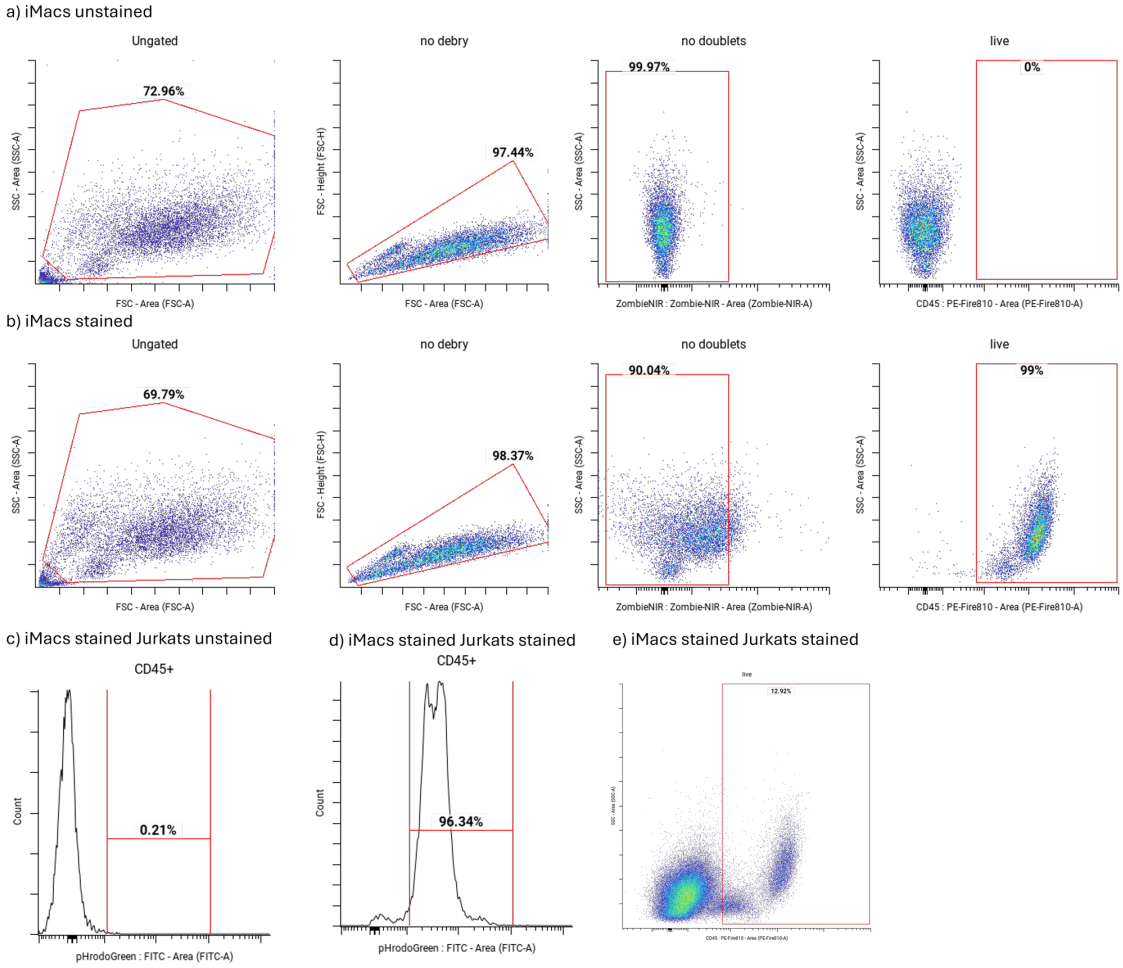

Figure 3-7 Gating strategy of mixed macrophage and Jurkat T cell populations in efferocytosis experiment. a) Gating of unstained induced macrophages (iMφ) based on forward scatter area (FSC-A) and side scatter area (SSC-A) to exclude debris. Doublets were excluded using FSC-A vs. FSC-height (FSC-H). A negative gate for the viability dye Zombie NIR

was then set on debris- and doublet-excluded iMφ. Viable cells (Zombie NIR-negative) were further gated for CD45 expression. b) Gating performed on unstained iMφ was applied to stained iMφ to identify the macrophage population. c) Negative gating of pHrodo Green signal was established using iMφ-stained plus unstained Jurkat T cells. d) Positive gating for pHrodo Green signal was defined using iMφ-stained + pHrodo Green-labeled Jurkat T cells. e) The overall gating strategy enables discrimination between iMφ and Jurkat T cells. *n = 3. Samples were acquired, unmixed, and autofluorescence-adjusted on the SONY ID7000 and analyzed using CellEngine.*

3.1.10 iPSC-Derived Mφ Express Efferocytosis-Associated Markers Across Harvests, Making it a Suitable Platform for Assay Optimizations

To establish an optimal setup for efferocytosis platform development, optimization, and future phenotypic and functional studies, we assessed the iPSC-to-iMφ differentiation protocol published by Takata et al. (2017) and evaluated its suitability for our experimental needs. Upon completion of the differentiation protocol from iPSCs to induced iMφ, a confluent adherent cell layer remains at the bottom of the culture well. This adherent layer can be sustained in SF-Diff medium supplemented with M-CSF for up to 21 days, continuously producing non-adherent, floating cells, including iMφ (~89 % Mφ in total floating cells) (Figure 3-8). These floating cells can be collected at regular intervals, and iMφ populations can be subsequently isolated through fluorescence-activated cell sorting (FACS; see Appendix C & D) to obtain a highly purified iMφ fraction (72.8%). Incorporation of the FACS step is essential to eliminate contaminating non-Mφ differentiated cell types, which may otherwise confound downstream analyses.

Prolonged maintenance of the adherent layer beyond the originally described differentiation protocol, with repeatable harvesting of iMφ for up to 21 days, has been successfully established in our laboratory as part of Work Package 2 (Dr. Carolina Gamez, Tomasz Stadler). This represents a methodological extension to the original protocol published by Takata et al. (2019).

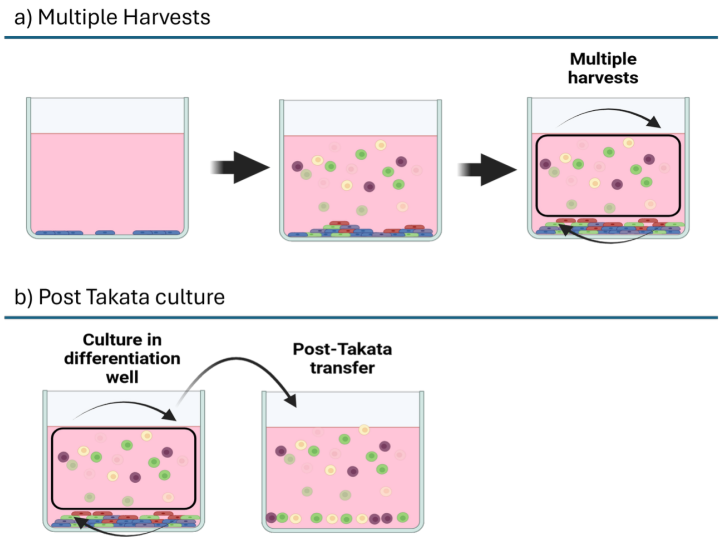

Figure 3-8 iPSC to iMφ differentiation and multiple harvests strategy a) Induced macrophages (iMφ) are derived from human induced pluripotent stem cells (iPSCs) through a 28-day differentiation protocol. Starting around day 25, the adherent "mother" cell layer at the bottom of the culture wells begins to release non-adherent, floating cells into the supernatant. These floating cells, which include newly differentiated iMφ, are maintained in culture. Beginning on day 28 - coinciding with the completion of the differentiation protocol - floating cells are collected at defined time points and subjected to fluorescence-activated cell sorting (FACS) based on CD45, CD14, CD11b, and viability markers to obtain a purified iMφ population. The adherent mother layer remains intact and continues to generate new floating cells over time. b) Sorted iMφ are reseeded into fresh culture plates and maintained for up to three weeks before experimental use, with medium (SF-Diff supplemented with M-CSF) changed three times per week. When the mother layer yields a sufficient

number of new floating cells, the harvesting and sorting procedure is repeated, enabling multiple rounds of iMφ isolation from a single differentiation batch.

As this platform was utilized to optimize the efferocytosis assay, I validated the relevance of our iMφ model in the context of efferocytosis and assessed the expression of key surface markers previously implicated in the efferocytosis process. Using a newly developed Mφ phenotyping panel and multispectral flow cytometry, I comprehensively characterized the marker profile of freshly sorted (viable, CD45+ CD11b+ CD14+) iMφ on day 28 of differentiation. As illustrated in the histograms comparing stained versus unstained iMφ (Figure 3-9a), the iMφ exhibited robust expressions of MERTK, FOLR, CD14, CD163 and TREM2, all of which have been reported to play roles in efferocytosis. TIMD-4 (important phagocytosis marker) expression was detectable, albeit at lower levels. CD206 showed minimal signal above background, with only a slight peak shift. These findings were further corroborated by heatmap analysis across three biological replicates (n = 3), supporting consistent marker expression patterns among iMφ (Figure 3-9b).

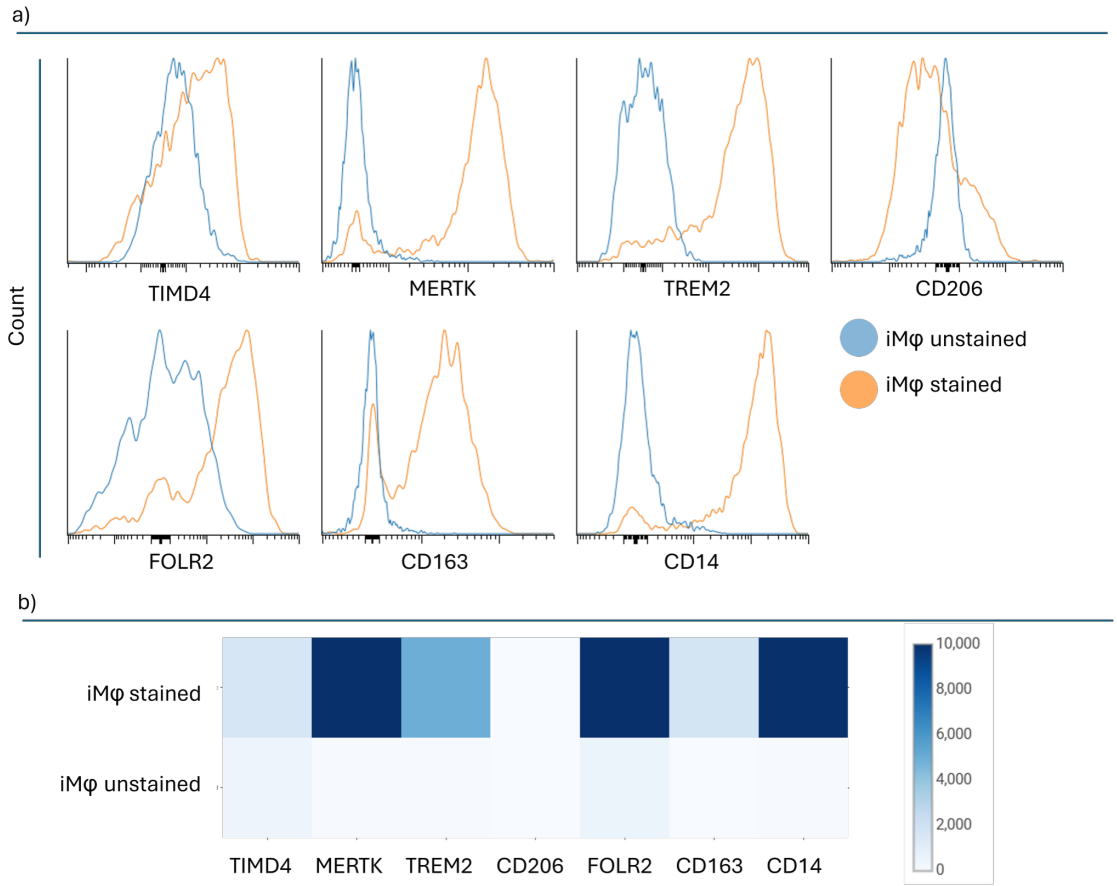

Figure 3-9 Evaluation of efferocytosis marker expression on sorted iMφ using multi-spectral flow cytometry. Cells were pre-gated to exclude debris, doublets, non-viable and CD45 negative cells. a) Representative histograms comparing unstained (blue) versus stained (orange) induced macrophages (iMφ). Robust expressions of MERTK, TREM2, FOLR2, CD163, and CD14 were observed, while CD206 and TIMD4 showed low to minimal expression. (*n = 1)*. b) Heatmap of marker expression across the same panel in independent biological replicates (*n = 3*). Heatmap displays median fluorescence intensity of n=3. Data acquisition was performed on a SONY ID7000 cytometer with spectral unmixing and autofluorescence correction. Downstream analysis was conducted using CellEngine.

To assess the consistency of efferocytosis marker expression across differentiation protocols, the experiment was replicated using an independently derived Mφ differentiation. Additionally, to evaluate the robustness of marker expression across different harvests, floating cells were collected from above the adherent mother layer on day 28 of differentiation. These cells were sorted

for CD45$^+$, CD11b$^+$, CD14$^+$, and viability to isolate iMφ, which were then seeded into a post-differentiation culture. On day 42, two weeks after completion of the differentiation protocol, newly generated floating cells were again harvested, sorted using the same gating strategy, and seeded into a parallel post-differentiation culture. Both cell populations were subsequently analyzed in parallel on day 46 of the protocol. The same staining panel as previously described was applied in this experiment, except for TIMD4, which was omitted due to institutional constraints on reagent availability. As shown in Figure 3-10, MERTK expression remained robust in the second harvest, indicating stable expression across differentiation batches. TREM2 expression exhibited a slight reduction but remained detectable. CD206 expression was unchanged in between harvests, relative to previous measurements, although a modest increase in signal intensity was observed, potentially reflecting improved staining efficiency. In contrast, FOLR2 expression was reduced in the second harvest, while CD163 and CD14 expression levels remained consistent with the initial differentiation (Figure 3-10). It remains unclear whether the observed reduction in certain markers in the second harvest is attributable to the extended duration these cells remained above the adherent mother layer before collection, or to the longer post-harvest culture period in the first harvest. As these variables were not independently controlled, the precise contribution of time spent away from the mother layer to marker stability cannot be definitively determined. Ideally, this could be addressed through experiments assessing multiple harvests with matched durations post-isolation; however, such a design was not feasible within the current study due to constraints in time, funding, and available personnel.

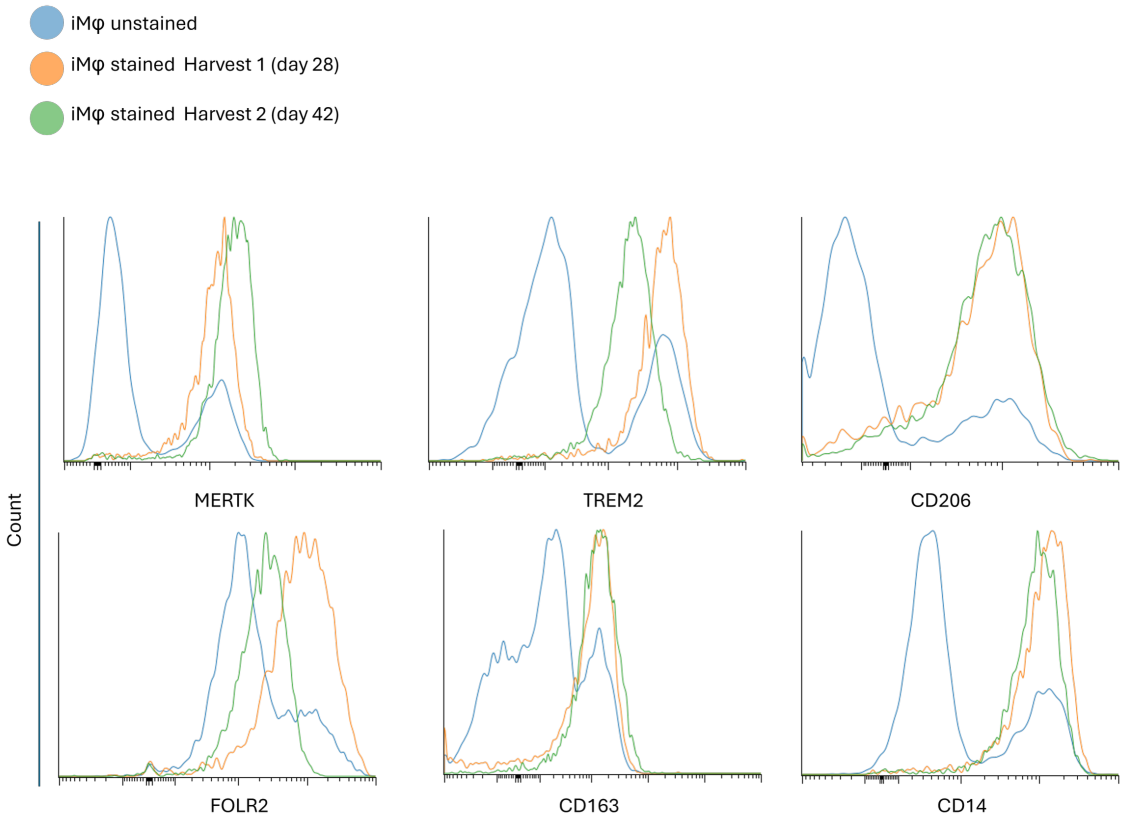

Figure 3-10 Multi-spectral flow cytometry analysis of efferocytosis-associated marker expression in sorted iMφ across independent differentiation harvests. iMφ were pre-gated to exclude debris, doublets, non-viable cells and CD45 negative cells. iMφ were independently differentiated and harvested at two timepoints: Harvest 1 (orange), collected on day 28 and maintained in post-differentiation culture until analysis, and Harvest 2 (green), collected on day 42. All samples were stained and analyzed on day 46 using a multi-spectral flow cytometer. Unstained control from Harvest 1 is shown in blue.

Marker expression profiles are overlaid to compare efferocytosis-associated phenotypes between harvests. Slight decrease in TREM2 and FOLR2 expression from Harvest one to Harvest two. Robust expression of CD206, CD14, CD163 and MERTK. N=4. Data acquisition was performed on a SONY ID7000 cytometer with spectral unmixing and autofluorescence correction. Downstream analysis was conducted using CellEngine.

The expression of markers not directly related to efferocytosis is presented in Appendix D. Additional markers detected include CD40, CD86, and CD274, which are associated with immunoregulation and antigen presentation. Notably, CCR2 (a marker linked to tissue infiltration) is absent in both harvests, supporting the tissue-resident phenotype of the iMφ model. Interestingly, CD48, a marker involved in inflammatory regulation, was not expressed in the first harvest but appeared in the second. This may indicate a slight shift toward a more pro-inflammatory phenotype in the latter population.

These findings demonstrate that the iMφ platform is well-suited for our intended applications, as key efferocytosis markers**,** including MERTK, TREM2, CD206, and CD163**,** are consistently expressed. While some variation was observed between different harvests, the overall marker profile remained stable, indicating robustness across differentiation batches and post-differentiation time points. This supports the platform's suitability for downstream functional efferocytosis assays and future phenotypic studies.

3.1.11 Optimization of Apoptotic Cell Exposure Times to Phagocytes - Eating Times. Assay allows Tracking Dynamic Range of Efferocytosis.

To quantitatively assess the dynamics of efferocytosis, including the rate of apoptotic cell uptake, the digestion time window, and the fluorescence intensity of the pHrodoGreen signal, was measured at defined time intervals over 2 hours of JTs cell efferocytosis. In this experiment, pHrodoGreen-labeled apoptotic JTs cells were co-cultured with antibody-prelabeled iMφs. Data acquisition was performed at 15, 30-, 60-, 90-, and 120-minutes following JTs addition. All cells were included in the analysis, meaning JTs remained in the wells throughout the measurement process. To distinguish iMφ with their potentially attached or engulfed apoptotic JTs from free, not iMφ-bound JTs, pre-gating was performed using CD45 signal. This signal is only positive on iMφ, as JTs have not been stained with the antibody cocktail.

Over time, a progressive increase in pHrodoGreen fluorescence intensity was observed in the CD45+ fraction (Figure 3-11a), with the most pronounced shift occurring between 60 and 90 minutes. This increase could be attributed either to the successive uptake of one or multiple apoptotic JTs or to the intracellular localization of engulfed corpses into the phagolysosome within iMφs, where acidification occurs. Furthermore, the data indicates that the pHrodoGreen signal reaches saturation after 90 minutes, as no further fluorescence increase was detected thereafter. This plateau is further corroborated by Figure 3-11b.

To further dissect the dynamics of Mφ pHrodoGreen signal changes during JTs' efferocytosis, I employed small molecule inhibitors known to interfere with distinct stages of efferocytosis. Experiments were conducted in the presence and absence of these inhibitors, and pHrodoGreen fluorescence signals were recorded over multiple time points. Specifically, Cytochalasin D (CytoD), an inhibitor of actin polymerization that blocks phagocytic cup formation, was used (Clark et al., 2019). These experiments demonstrated a marked reduction in pHrodoGreen signal in CytoD-

treated Mφ beginning at 60 minutes post-JT addition (Figure 3-11b). This finding implies that the pronounced increase in pHrodoGreen signal in CD45+CD14+ Mφ at 90 minutes primarily reflects phagolysosomal acidification of apoptotic JTs.

As additional controls, the $CD45^-$ cell population, representing the apoptotic, pHrodoGreen-labeled JTs, was gated and analyzed for pHrodoGreen fluorescence (Appendix F). No shift in fluorescence intensity was observed within the $CD45^-$ fraction over time, indicating that the pHrodoGreen signal increase observed in the $CD45^+$ Mφ population is attributable to phagocytic uptake and subsequent acidification within the phagolysosomal compartment. Furthermore, wells containing only pHrodoGreen-labeled JTs (without iMφ) were analyzed at baseline (t = 15 min) and after 120 minutes to assess whether progressive apoptosis and cell death or extracellular acidification could account for increased pHrodoGreen signal. No measurable increase in fluorescence was detected under these conditions, thereby excluding the possibility that apoptotic JTs alone contribute to the observed fluorescence changes due to extracellular medium acidification or continued cell death (Appendix Fb).

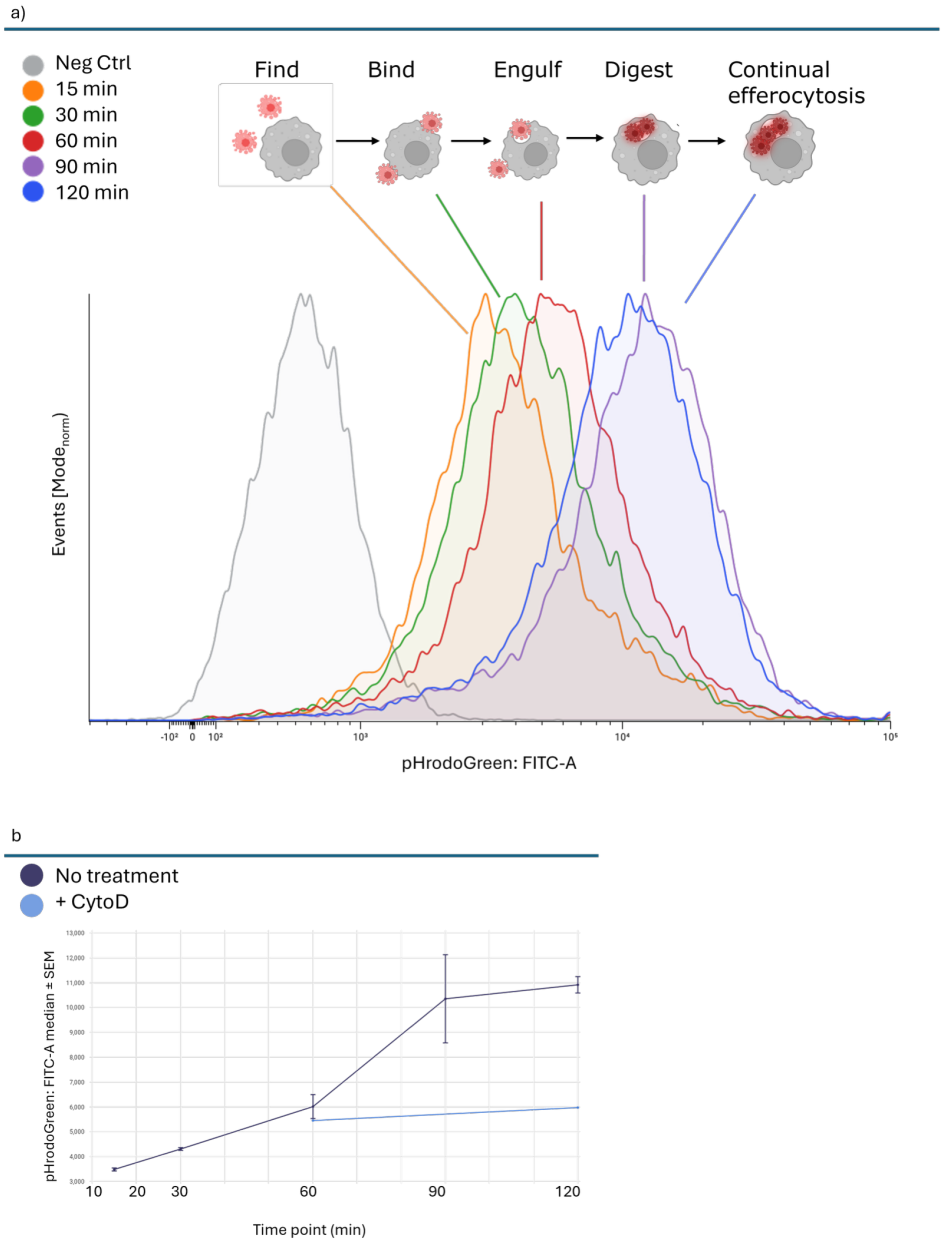

Figure 3-11 Macrophage efferocytosis dynamics over time. a) Efferocytosis assay: Viable $CD45^+CD14^+$ interstitial macrophages (iMφ) were analyzed over time for phagocytosis of apoptotic Jurkat T cells labeled with pHrodo™ Green. Staining panel presented in Appendix Ea. Debris, doublets, and Jurkat cells were excluded from the analysis. Histograms represent the increase in pHrodo™ Green fluorescence signal at 15, 30, 60, 90, and 120 minutes, as measured on the SONY ID7000 analyzer. Jurkat T cells were not removed from the co-culture during the time course. *N = 2* b) Comparison of efferocytosis kinetics in $CD45^+CD14^+$ macrophages treated with or without 10 µM Cytochalasin D, an inhibitor of actin polymerization. pHrodo™ Green fluorescence signal was used to assess internalization over time. *N =2.* Antibody panel details are provided in Appendix C. Data acquisition was performed using the SONY ID7000 software with unmixing and autofluorescence correction. Downstream analysis was conducted using Cell Engine. Data shown are representative of *N = 2* independent experiments.

To demonstrate that the dynamics of efferocytosis are robust and reproducible across different iMφ differentiation runs, we include data from an independent iPSC-to-iMφ differentiation experiment performed under identical experimental conditions (Figure 3-12a). The rationale for this replication was to verify that the observed kinetics of pHrodoGreen signal accumulation, used as a readout for efferocytosis, are not specific to a single differentiation batch but represent a consistent functional behavior of iMφ, which is crucial for potential utilization in a CRISPR screen. This assurance is crucial for the reliability and reproducibility of the assay across experiments and users.

Importantly, this experiment included additional extended time points beyond 120 minutes to refine the temporal resolution of pHrodoGreen signal saturation in efferocyting iMφ. No further increase in pHrodoGreen fluorescence was observed after 120 minutes post the addition of pHrodo-labelled apoptotic Jurkat T cells. This defines a stable signal window, crucial for downstream assay applications. This window likely represents the point at which most engulfed Jurkat T cells have reached the acidic phagolysosomal compartment, where pHrodo becomes maximally fluorescent - and before significant signal degradation occurs due to fluorochrome breakdown or recycling of phagosomes. Thus, this 120-240 min window offers an optimal period to quantify efferocytosis robustly and reproducibly without signal variability due to ongoing phagocytic events or dye instability.

We also observed a higher MFI of pHrodoGreen in the second differentiation experiment (Figure 3-12) compared to the first run (Figure 3-11). These differences might have been observed due to an expanded antibody panel (see expanded panel presented in Appendix E-c vs original panel presented in Appendix E-a), which introduced additional fluorochromes and required compensation adjustments. The expanded panel included markers (e.g. CD80, CD86, CD40, CD274, CD38 & CD172a) to characterize subpopulations and assess phenotypic shifts during efferocytosis, providing more granular data on the efferocyting population. This expanded panel caused a higher baseline fluorescence of stained iMφ as compared to previous experiments adding up on pHrodoGreen signal.

Further evidence that the fluorescence increase over time is due to acidification is provided in Figure 3-12b, which includes pHrodoGreen-labelled JT controls. These JTs, maintained in a neutral environment (Jurkat suspension buffer pH ~7.2), displayed fluorescence intensity of 2641 a.u., supporting the interpretation that acidification becomes apparent from 60 minutes onward in the efferocytosing iMφ (which reach ~3919.9 ± 99 a.u. at 60 min, Figure 3-12a).

Upon addition of HCl to the JT-only condition, the pHrodoGreen fluorescence increased dramatically to approximately 14,000 a.u., whereas the maximum fluorescence observed in the efferocytosis condition plateaued at around 6861 a.u. It is important to emphasize that this comparison is not quantitative, but rather qualitative. The acid-treated JT control represents endpoint acidifica-

tion in a bulk population (500,000 cells), which is not directly comparable to the number of apoptotic JTs internalized by iMφ during efferocytosis, where each Mφ typically engulfs only a few cells. Additionally, the phagolysosomal environment in iMφ is dynamic and regulated, in contrast to the abrupt and extreme acidification caused by HCl. Furthermore, because the pHrodoGreen-labelled apoptotic JTs are enclosed within phagolysosomes in iMφ, factors such as light scattering, spectral interference, and signal dampening from surrounding cellular components may reduce fluorescence intensity. In contrast, JTs in acid are measured in suspension without such structural or environmental barriers, which likely allows for a clearer, stronger signal.

While the HCl-treated condition provides a useful positive control to confirm pHrodoGreen responsiveness to low pH, it does not reflect the biological complexity of the intracellular environment. In macrophages, acidification occurs alongside fluorochrome degradation, signal quenching, and dynamic trafficking of the phagosome, all of which can modulate the overall pHrodo signal.

Finally, the pH in the HCl-treated JT condition was likely lower than the physiological pH typically found in phagolysosomes. However, because these samples must be measured immediately after HCl addition to prevent total cell degradation, it is not feasible to re-adjust or confirm the pH prior to spectral flow cytometry analysis. Despite these limitations, the HCl-treated JTs provide a valuable reference point for assessing the maximum fluorescence potential of pHrodoGreen under highly acidic conditions and support the interpretation that fluorescence increase in Mφ is primarily driven by acidification.

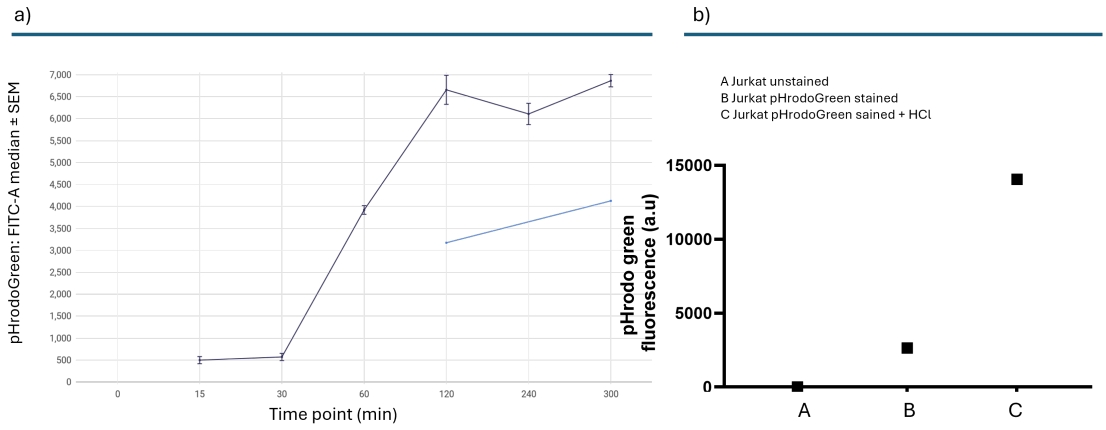

Figure 3-12 Tracking macrophage efferocytosis over time – time window of stable efferocytosis signal in macrophages following Jurkat T cell (JT) addition. a) Spectral flow cytometry efferocytosis assay and assay controls. pHrodo™ Green fluorescence intensity was measured iMφ co-cultured with pHrodo™ Green-labeled apoptotic Jurkat T cells over time (minutes), comparing untreated macrophages in the absence (n=4, dark blue) or presence (light blue) of 10 µM Cytochalasin D (n = 1). b) Jurkat T cell-only experimental controls (n = 1) included the following conditions: A unstained Jurkat T cells, B Jurkat T cells stained with pHrodo™ Green, and C pHrodo™ Green-stained Jurkat T cells treated with HCl to mimic the acidic environment of the phagolysosome. Samples were acquired on the Sony ID7000 spectral flow cytometer. Spectral unmixing and autofluorescence adjustments were performed using Sony ID7000 software. Data were further analyzed using CellEngine.

3.1.12 Proof of Principle: Tracking Mφ Efferocytosis with Discoverer Mφ Using Small Molecule Efferocytosis Inhibitors

To further deconvolute the capacity of *Discoverer Mφ* to monitor the efferocytosis process, I employed a set of well-characterized efferocytosis inhibitors. These compounds were selected based

on extensive literature evidence demonstrating their effectiveness in disrupting distinct stages of efferocytosis (Figure 3-13a).

Cytochalasin D (Cyto D) is a potent inhibitor of actin polymerization; it binds to the barbed (plus) end of actin filaments, thereby blocking filament elongation and disrupting cytoskeletal dynamics necessary for phagocytic cup formation and engulfment of apoptotic cells (Das et al., 2014). In the presence of Cyto D, apoptotic cells can still bind to the Mφ surface, but their internalisation is effectively prevented. Chloroquine disrupts the maturation of the phagolysosome by blocking the fusion of phagosomes with lysosomes (Bhat & Hickey, 2000). Consequently, while Mφ treated with chloroquine can still engulf apoptotic cells, the acidic environment required to activate the pHrodoGreen fluorescence does not form, resulting in no detectable fluorescence shift. Flavopiridol, a CDK9 inhibitor, has been shown to impair continual efferocytosis by interfering with RNA Polymerase II pause release, thereby limiting the transcriptional program necessary for sequential engulfment events (Tufan et al., 2024). As a result, Mφ exposed to flavopiridol internalize fewer Jurkat T cells, which leads to reduced pHrodo fluorescence intensity.

My experimental findings are summarized in Figure 3-13 b and c. With measurements recorded 240 minutes post-JT addition after Jurkat T cells were removed after 90 minutes (efferocytic "eating time"). The strongest pHrodoGreen fluorescence signal (blue) was observed in Mφ that were not exposed to any inhibitor, indicating efficient efferocytosis under control conditions. Treatment with Cyto D resulted in a substantial decrease in fluorescence, reflecting impaired efferocytic uptake. Among the three inhibitors tested, chloroquine produced the most pronounced reduction in fluorescence, consistent with its inhibition of phagolysosomal acidification. Flavopiridol had the weakest inhibitory effect under our experimental conditions. This milder effect is likely due to the continued, albeit reduced, engulfment and transport of apoptotic cells to phagolysosomes, where pHrodoGreen can still be activated by the acidic environment. However, since flavopiridol restricts the number of apoptotic cells processed per Mφ, the overall signal remains lower than in untreated controls.

These findings provide strong evidence for the capability of *Discoverer Mφ* to sensitively and robustly track Mφ efferocytosis and distinguish between different mechanistic stages affected by pharmacological inhibition.

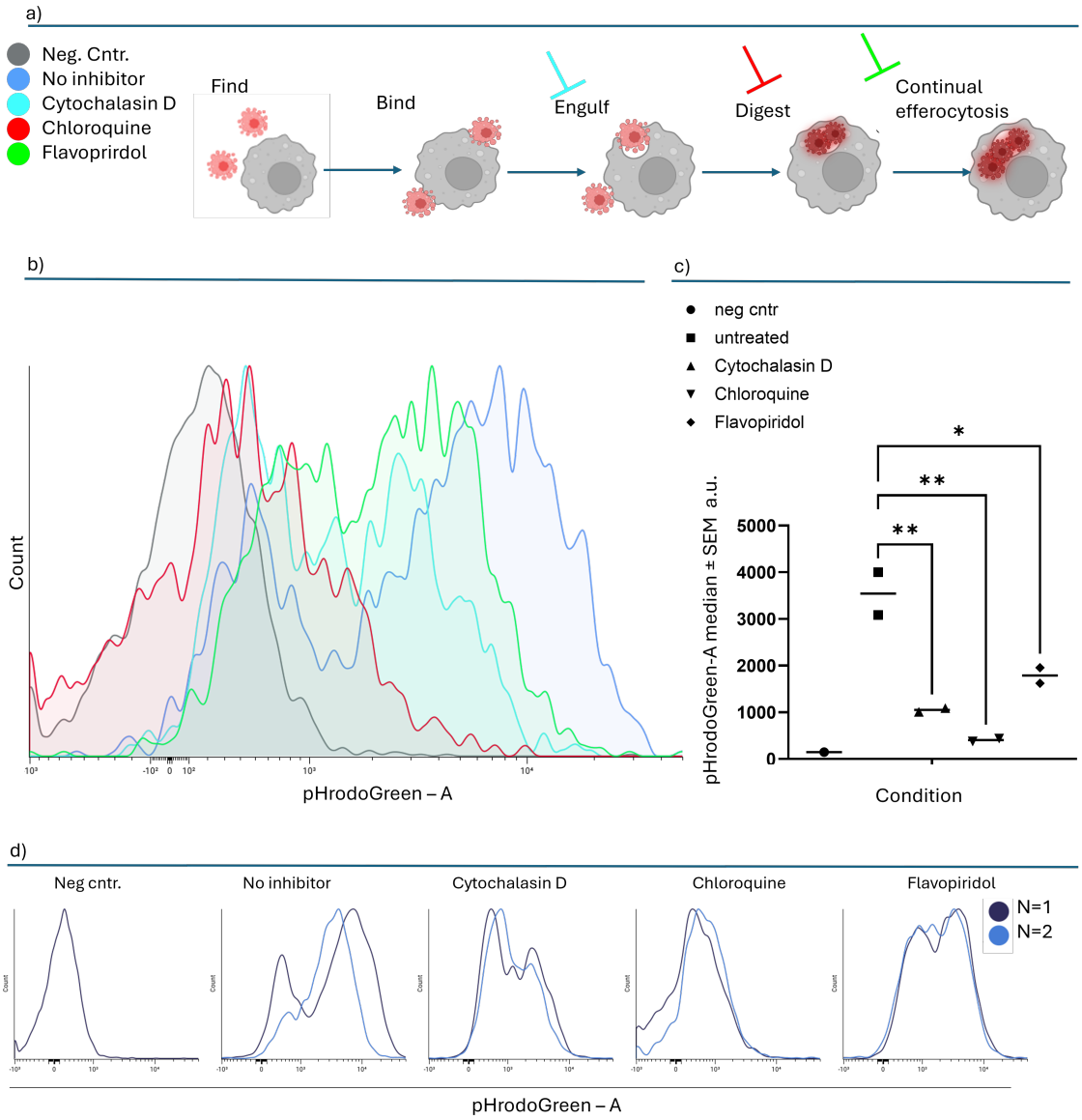

Figure 3-13 Literature-reported efferocytosis inhibitors demonstrate the capability of Discoverer Mφ to track macrophage efferocytosis. Schematic illustration of experimental conditions and the mechanisms of efferocytosis inhibitors. Grey: negative control (iMφ stained with macrophage panel, co-cultured with unstained Jurkat T cells); dark blue: positive control (stained iMφ + 5 µM pHrodo™ Green-labeled Jurkat T cells, no inhibitor); light blue: Cytochalasin D (10 µM, inhibitor of actin polymerization); red: Chloroquine (100 nM, inhibitor of phagolysosomal fusion and acidification); green: Flavopiridol (10 µM, CDK9 inhibitor, blocks continual efferocytosis). b) Histogram showing pHrodo™ Green fluorescence intensity in macrophages following treatment with each inhibitor. Data are pregated to exclude debris and doublets, and gated on viable $CD45^{+}CD14^{+}$ cells. c) Dot plot summarizing median pHrodo™ Green fluorescence intensity across all treatment groups. Statistical significance: $p < 0.05$, $p < 0.001$. d) Overlay histogram of replicate numbers (n = 2) across inhibitor and control conditions. Samples were acquired on a SONY ID7000 spectral flow cytometer, unmixed, and corrected for autofluorescence. Data were analyzed using CellEngine, and statistical analyses were performed using GraphPad Prism v10.2.3, Ordinary one-way Anova N = 2 independent biological replicates.

3.1.13 Proof of Principle - Confocal Microscopy Confirms Spectral Flow Cytometry Results. Mφ Fluorescence Increases upon Efferocytosis of Apoptotic Jurkat T cells.

Spectral flow cytometry provides strong evidence for efferocytosis, as indicated by increased pHrodoGreen fluorescence intensity; however, due to its lack of spatial resolution, it cannot definitively confirm that the fluorescence originates from internalized apoptotic JTs. To address this limitation and verify that the fluorescence increase results from the engulfment of apoptotic JTs followed by phagosomal acidification, confocal microscopy was employed. As shown in Figure 3-14, pHrodoGreen-labeled apoptotic JTs were clearly localized within the phagolysosome of efferocytosing iMφs at 120 minutes post co-incubation. Notably, a marked increase in pHrodoGreen fluorescence was observed in the internalized Jurkat T cells (Figure 3-14c), consistent with the data obtained using the SONY ID7000 spectral flow cytometer (Figure3-14b).

To further validate that the fluorescence increase depends on active efferocytosis, Cyto D, was used to block the engulfment process. In the presence of Cyto D, spectral flow cytometry revealed a striking reduction in pHrodoGreen signal (Figure 3-14b, histogram: red line) compared to the untreated control (green line). Similarly, confocal microscopy showed no internalization of apoptotic Jurkat T cells and no increase in pHrodoGreen fluorescence intensity under these conditions (Figure 3-14a). Together, these results support and complement the findings obtained with the *Discoverer Mφ* system, providing direct spatial and functional evidence that the observed pHrodoGreen signal increase in macrophages is indeed associated with efferocytosis.

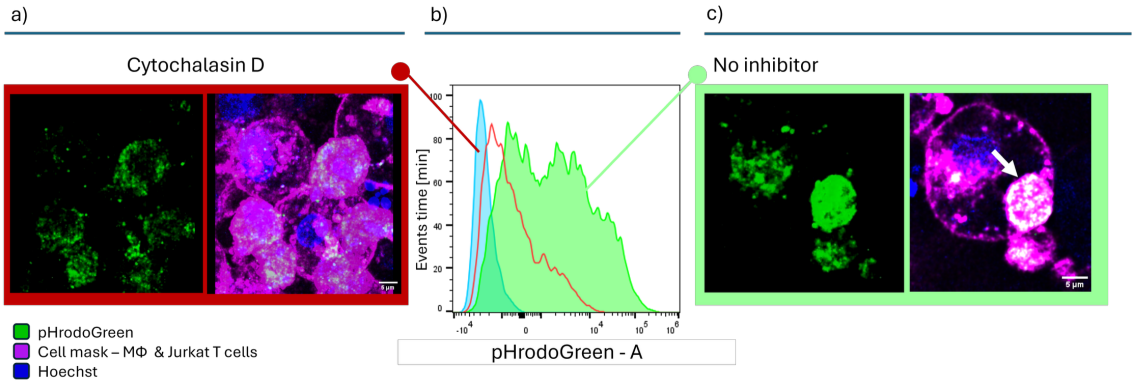

Figure 3-14 Confocal microscopy as a proof of principle for the spectral flow cytometry-based efferocytosis assay. Efferocytosis of UV-irradiated, pHrodoGreen-labeled apoptotic Jurkat T cells by iMφ was assessed using both confocal microscopy and spectral flow cytometry. Jurkat T cells were labeled with pHrodoGreen (5 µM), and iMφs were counterstained with Hoechst (nuclear staining, 1:500) and CellTracker Orange (1:1000). Cells were co-cultured at a 1:5 iMφ:Jurkat ratio, and efferocytosis was allowed to proceed for 240 minutes. Non-engulfed or non-attached Jurkat T cells were removed after a 30-minute incubation ("eating time"). a) For the Cytochalasin D (CytoD) condition, iMφs were pre-treated with 10 µM Cytochalasin D for 1 hour prior to Jurkat T cell addition. To maintain effective inhibition of phagocytosis, Cytochalasin D was re-added immediately after Jurkat addition. b) Spectral flow cytometry analysis was performed using the SONY ID7000 cytometer. iMφs were stained with a macrophage-specific surface marker panel. Histogram overlay shows: Blue: Negative control: pre-labeled iMφs co-cultured with unlabeled apoptotic Jurkat T cells (no pHrodoGreen). Red: Cyto D-treated: pre-labeled iMφs co-cultured with pHrodoGreen-labeled apoptotic Jurkat T cells + 10 µM Cyton D. Green: Untreated control, pre-labeled iMφs co-cultured with pHrodoGreen-labeled apoptotic Jurkat T cells (active efferocytosis). A marked reduction in pHrodoGreen signal was observed in the Cyto D condition compared to the untreated control, confirming inhibition of efferocytosis. c) Representative confocal microscopy image of the untreated control condition shows pHrodoGreen-positive apoptotic Jurkat T cells localized within the iMφs, indicating successful engulfment and

phagosomal acidification. No internalized fluorescence was observed in the Cyto D condition. Confocal imaging was performed using a Leica TCS SP5 confocal microscope. Image analysis and interpretation were conducted in collaboration with Tomasz Stadler. Spectral flow cytometry experiments were performed in biological duplicates (n=2). Confocal microscopy was performed on seven spots per well, with one representative field shown, scale bar = 5 µM.

3.1.14 Discoverer Mφ Can Detect Phagocytosis Capacity in iMφ

To establish a reliable phagocytosis readout, I tested our established iMφ model for its phagocytic capacity and evaluated the applicability of Discoverer Mφ to monitor this process. As shown in Figure 3-15a, a shift in pHrodoGreen fluorescence intensity indicates phagocytic activity. The pHrodoGreen-positive population - gated based on the iMφ-only condition (left panel) - was 6.34% in the Cyto D-treated condition and 14.19% in the untreated control.

Interestingly, in the corresponding dot plots (Figure 3-15b), an increase in SSC-A was observed in pHrodoGreen-positive events. This suggests increased granularity upon engulfment of pHrodoGreen-labeled *E. coli* particles, supporting the feasibility of tracking phagocytosis using this approach. These results point to either a modest phagocytic capacity of iMφ or suboptimal experimental conditions for the Discoverer Mφ assay.

To further support the phagocytic potential of iMφ, a confocal microscopy-based phagocytosis assay was performed. This assay confirmed that iMφ exhibit phagocytic activity. These microscopy data are part of Tomasz Stadler's thesis and are not included in the present work.

Importantly, this preliminary experiment was conducted primarily to assess whether pHrodoGreen fluorescence intensity could be reliably tracked using our current setup. As no pre-labelling of iMφ was performed and gating was based solely on FFC/SSC to exclude debris and doublets, the experiment should be considered a pilot. Further optimization, such as refined gating strategies, optimized co-culture times and pre-labelling, will be necessary to enhance data quality and reproducibility. Following this initial validation step, I proceeded with experiments focusing on efferocytosis, which constitutes the main objective of this study.

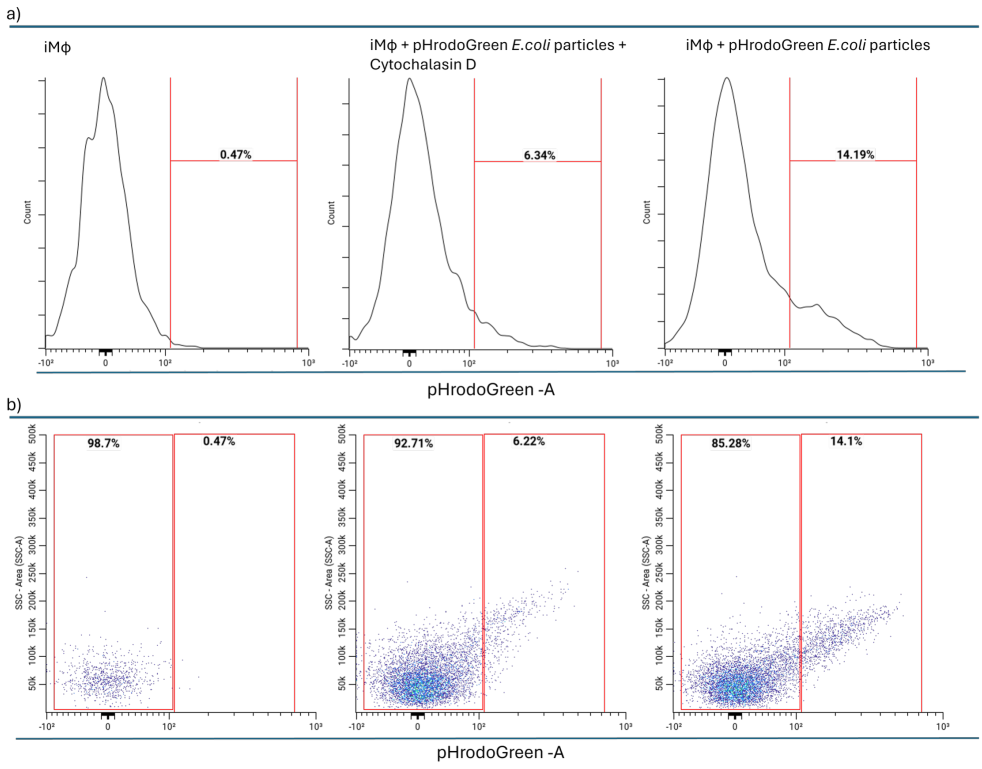

Figure 3-15 Phagocytosis assay on iMφ using spectral flow cytometry. Histograms indicating pHrodoGreen fluorescence of iMφ only, iMφ + 10uM Cytochalasin D + pHrodoGreen *E.coli* bioparticles and iMφ + pHrodoGreen labelled *E.coli* bioparticles. Corresponding Dot plot below histogram. Samples were acquired on the SONY ID7000 flow cytometer, unmixed, and corrected for autofluorescence, n=1.

3.1.15 Discoverer Mφ Applicable to Detect Iron Metabolism in Mφ and Allows Phenotyping of Iron Metabolism Associated Markers

Dysregulated iron metabolism is increasingly recognized as a key contributor to the pathogenesis of inflammation and tissue damage in RA. Mφ, as pivotal regulators of tissue iron homeostasis, are central to this process (Zhao et al., 2023b). We hypothesized that re-establishing iron homeostasis may mitigate inflammatory responses and promote tissue repair. Accordingly, targeting aberrant iron metabolism pathways represents a potentially promising therapeutic strategy for inflammatory diseases.

To investigate iron trafficking dynamics in Mφ, we modified the *Discoverer Mφ* platform to incorporate iron-linked immunophenotypic and functional readouts, resulting in the development of the *Discoverer Mφ-IRON* assay. The assay was conceptualized and designed in partnership with Janine Lückgen, with both its establishment and subsequent experimental applications carried out in collaboration with her.

A distinguishing feature of the *Discoverer Mφ-IRON* assay is its ability to assess the intracellular labile iron pool in Mφ. This was accomplished by integrating the Labile Iron Tracker Far-Red fluorescent dye. The antibody panel was refined by swapping fluorochromes on existing antibodies and expanding the panel to include markers for surface receptors involved in iron transport, specifically CD71 (transferrin receptor), CD91 (LRP1), SLC40A1 (ferroportin), and CD163, as detailed in Appendix E-e.

For experimental conditions, Mφ were cultured either in standard medium (X-vivo, Lonza) or supplemented with ferric ammonium citrate (FAS) at a final concentration of 100 µM, which was added one hour ptior to adding the iron tracker (Figure 3-16).

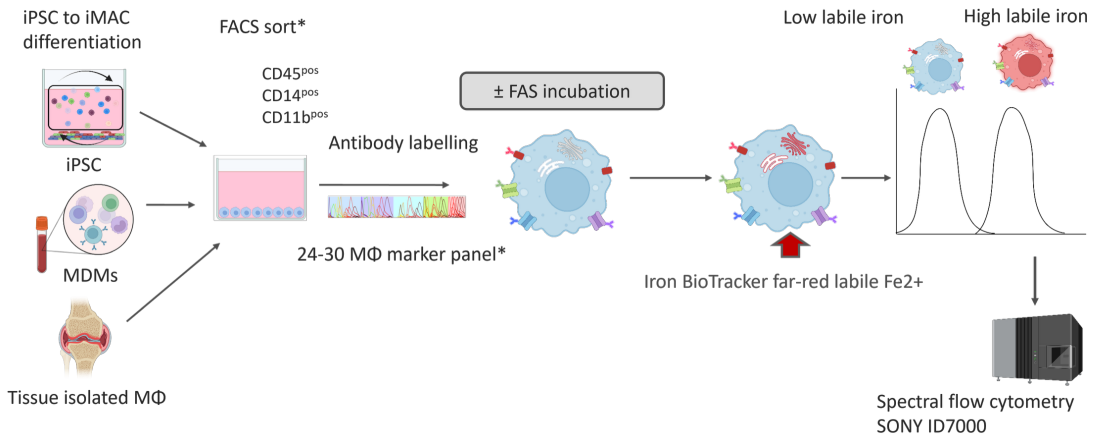

Figure 3-16 Discoverer Mφ – IRON assay concept**.** Representative assay schematic. Primary human synovial fluid cells and model *in vitro* macrophage s were utilized. The assay runs in a 96-well plate format from seeding to reading on Sony ID7000 spectral analyzer. Cells were labelled with an adapted macrophage marker targeting antibody panel, incorporating antibodies against direct and indirect iron transporters. Culture media were enriched or not for extracellular iron using ferric ammonium sulfate (FAS) supplementation., Finally, cells were stained with Iron BioTracker™ Far-Red, a fluorescent probe specific for labile Fe^{2+}. Samples were analyzed on the SONY ID7000 spectral analyser.

The data presented in Figure 3-17 shows that M1-like Mφ exposed to iron showed a moderate level of iron accumulation, consistent with the known tendency of pro-inflammatory Mφ to retain iron. In comparison, M2a Mφ polarized with dexamethasone and IL-10 accumulated slightly lower iron levels under the same conditions. Similarly, M2b Mφ polarized with IL-10 and IL-4 showed comparable iron levels to the dexamethasone/IL-10 condition. When pre-incubated with FAS, iron levels increased in both M1 and M2 populations, indicating active iron import. The effect of FAS treatment was particularly strong in M2 Mφ polarized with IL-10 and IL-4, which showed the highest iron levels across tested conditions (Figure 3-17b,c). To further analyze marker expression and correlate with measured labile iron contents, each cell type was compared to the unstained control (Appendix J). This analysis revealed that markers commonly expressed across all polarization conditions included CD14, CD45, CD64, CD206, HLA-DR, CD209, and Trem2. MERTK expression was observed only in M2-polarized cells. Markers involved in iron import, such as CD71 (transferrin receptor) and CD91 (heme–haptoglobin transporter), were expressed across all polarizations. In contrast, the iron exporter SLC40A1 was not expressed in any polarization state. CD163 also appeared to be absent, although this is likely due to an issue with the antibody used.

To investigate the role of Mφ polarization in iron uptake, key surface markers associated with iron metabolism were analyzed across different Mφ phenotypes. The resulting heatmap (Fig. 3-17d) illustrates the differential expression of these markers in M1 Mφ, M2a Mφ (stimulated with IL-10 and dexamethasone), and M2b Mφ (stimulated with IL-10 and IL-4). A notable increase in CD71 (transferrin receptor) expression was observed in M2-polarized Mφ, particularly under IL-10/IL-4 stimulation, indicating a heightened capacity for transferrin-bound iron uptake in these cells. CD91, a receptor involved in the endocytosis of heme-iron complexes, also showed elevated expression in M2 conditions, further supporting their enhanced iron-handling capabilities.

These surface marker patterns were corroborated by a complementary experiment measuring intracellular iron content, which revealed the highest levels in M2b Mφ, moderate levels in M2a, and the lowest in M1. This distribution aligns closely with the expression levels of CD71 and CD91 and highlights the increased iron uptake capacity of M2b Mφ (Figure 3-17d). These findings reinforce the established role of M2 Mφ, particularly those activated by IL-10 and IL-4, in tissue repair, inflammation resolution, and iron recycling. Conversely, the minimal iron accumulation observed in M1 Mφ is consistent with their primary function in host defense rather than in metabolic regulation or tissue remodeling (Gaetano et al., 2010).

Furthermore, CD206, another marker associated with endocytosis and scavenging functions, was upregulated in M2 Mφ, further supporting their enhanced iron-handling capacity. In contrast, M1 Mφ displayed comparatively lower levels of these iron uptake markers, aligning with their primary role in microbial defense rather than tissue repair.

Markers such as CD14, HLA-DR, and CD45 were broadly expressed across all phenotypes, reflecting general Mφ activation and immune function. Additional upregulation of TREM2, MERTK, and FOLR2 in M2-polarized cells may indicate their involvement in anti-inflammatory signaling pathways and the promotion of homeostasis.

Collectively, these data suggest that Mφ polarization significantly influences iron uptake pathways, with M2 Mφ exhibiting a phenotype more conducive to iron acquisition and recycling. This aligns with their functional role in resolving inflammation and maintaining tissue homeostasis.

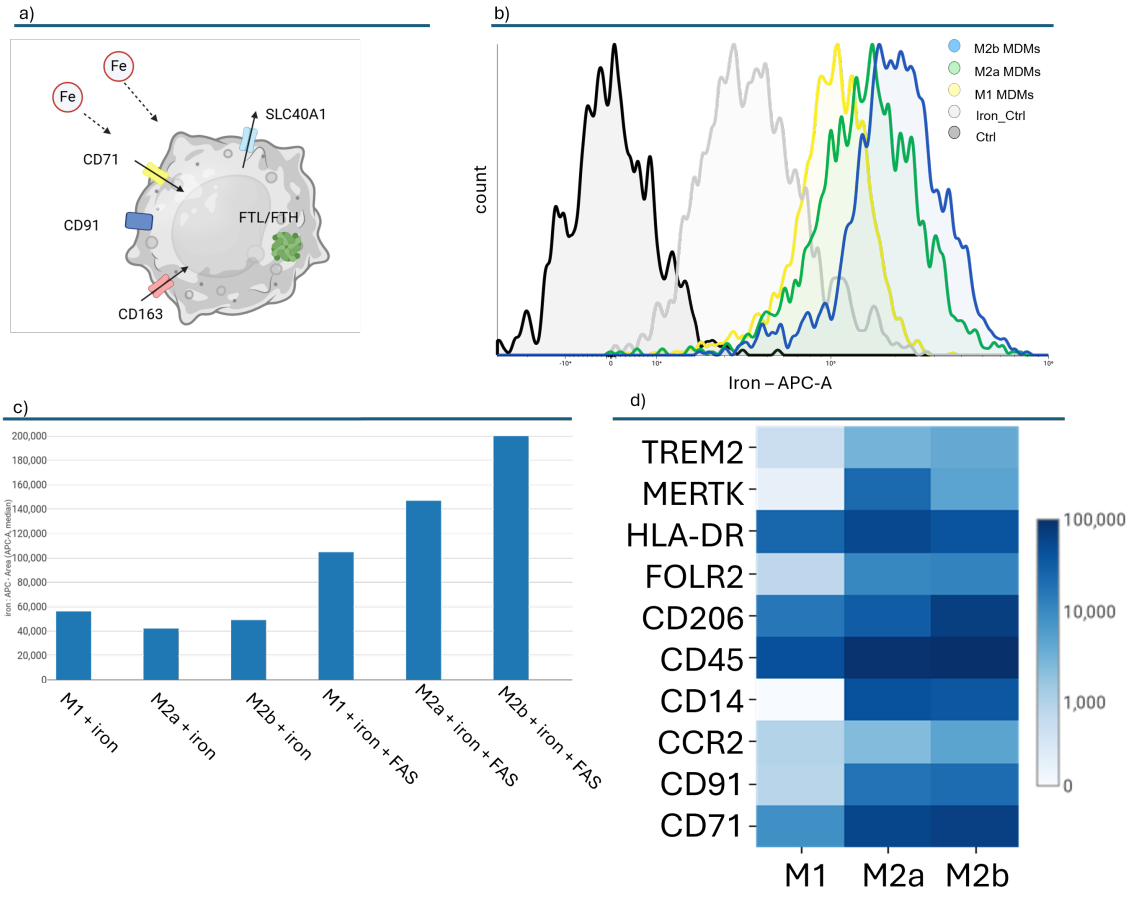

Figure 3-17 Proof-of-principle for iron metabolism assay in macrophage subtypes. a) Expression of iron importers (CD71, CD91, CD163) and the iron exporter SLC40A1 across macrophage subtypes. b) Histogram of APC-A signal indicating intracellular labile iron content. Conditions include: black (unstained control), grey (Iron BioTracker only (no FAS)), yellow M1-like macrophages (FAS + Iron BioTracker), green (M2a-like macrophages (IL-10 + dexamethasone, FAS + Iron BioTracker)), blue-green (M2b-like macrophages (IL-4 + IL-10, FAS + Iron BioTracker)). 1h incubation. All samples were pre-gated for debris, doublet exclusion, viability, and $CD45^{+}CD14^{+}CD64^{+}$ cell populations. Normalized to mode. c) Bar plot summarizing APC signal intensity corresponding to intracellular labile iron levels across conditions (n=2). d) Heatmap showing differential expression of iron-transporters and macrophage surface marker expression across monocyte-derived macrophage (MDM) subtypes of $CD45^{+}CD14^{+}CD64^{+}$ population. Only markers displayed that are expressed (based on stained vs unstained, heatmaps presented in Appendix J), n=2. Heatmap scaled to x. Samples were acquired using the SONY ID7000 flow cytometer, unmixed, and autofluorescence-corrected using SONY ID7000 software. Histogram, bar plot, heatmap created with CellEngine.

After broadly testing and establishing efferocytosis readout on *Discoverer Mφ* with iPSC-derived Mφ and primary human monocyte-derived Mφ, we developed additional readouts of Mφ functions and tested other Mφ in vitro models to understand the versatility of *Discoverer Mφ* as a tool for Mφ function-phenotype analyses. The *Discoverer Mφ* platform is not only suitable for assessing Mφ efferocytosis capacity but also enables the evaluation of phagocytic activity and the quantification of labile iron pools.

3.2 Discoverer Mφ Enables Differential Analysis on Different Cell Platforms, Across Various Readouts and Perturbations

3.2.1 Discoverer Mφ identifies highest efferocytosis capacity in iPSC derived Mφ and reveals efferocytosis driving surface markers

To better match *in vitro* Mφ models with relevant functional surface marker profiles, I assessed the applicability of *Discoverer Mφ* across other commonly used polarization conditions. Specifically, I evaluated human monocyte-derived macrophages (MDMs) generated from two healthy donors, polarized into M1-like (GM-CSF, LPS, IFNγ) and M2-like (M-CSF, IL-10, Dexamethasone) phenotypes. These were compared to iMφ under identical experimental conditions (Figure 3-18a).

To characterize the efferocytosis-related and general immunophenotypic features of each subset, I analyzed surface markers using spectral flow cytometry. Markers were grouped into functional categories: inflammation-linked, lipid metabolism-associated, immune activation, antigen presentation, general leukocyte and Mφ markers, and efferocytosis/tissue-resident Mφ (trMφ) features. Only marker signatures consistently observed across both donor replicates were included for interpretation.

As presented in the heatmap (Figure 3-18a), M1-like Mφ (D1, D2) exhibited strong enrichment for inflammatory and immune activation markers including CCR2, CD274 (PD-L1), CD38, CD86, HLA-DR, and CD40, reflecting a robust pro-inflammatory surface profile. These cells lacked or showed minimal expression of efferocytosis and trMφ-associated markers.

In contrast, M2-like Mφ (D1, D2) demonstrated high expression of CD36 (associated with lipid metabolism), along with several efferocytosis/trMφ-related markers including CD206, CD163, TREM2, and FOLR2. TIMD4 and MERTK were modestly more enriched in D2 compared to D1, suggesting minor donor-specific variation; however, both donors showed consistently higher expression of these markers relative to M1-like Mφ.

iMφ displayed broad and consistent expression of efferocytosis and trMφ markers (TIMD4, MERTK, TREM2, FOLR2, CD163, CD206), often at the highest levels among all subsets. Notably, CD48 was markedly elevated in iMφ and largely absent from both M1- and M2-like Mφ, providing distinguishing feature of the iMφ model. This distinct expression pattern, especially for key efferocytosis markers such as TIMD4, MERTK, and TREM2, was further evident in high-resolution histogram plots (Figure 3-18b).

Overall, iMφ share substantial phenotypic overlap with M2-like Mφ in terms of efferocytosis and tissue residency features yet remain distinguishable through unique markers such as CD48. M1-like Mφ retain a distinct pro-inflammatory and antigen-presenting surface signature with minimal reparative marker expression. Importantly, inter-donor variability in MDM subsets was limited, supporting the robustness and reproducibility of these polarization protocols.

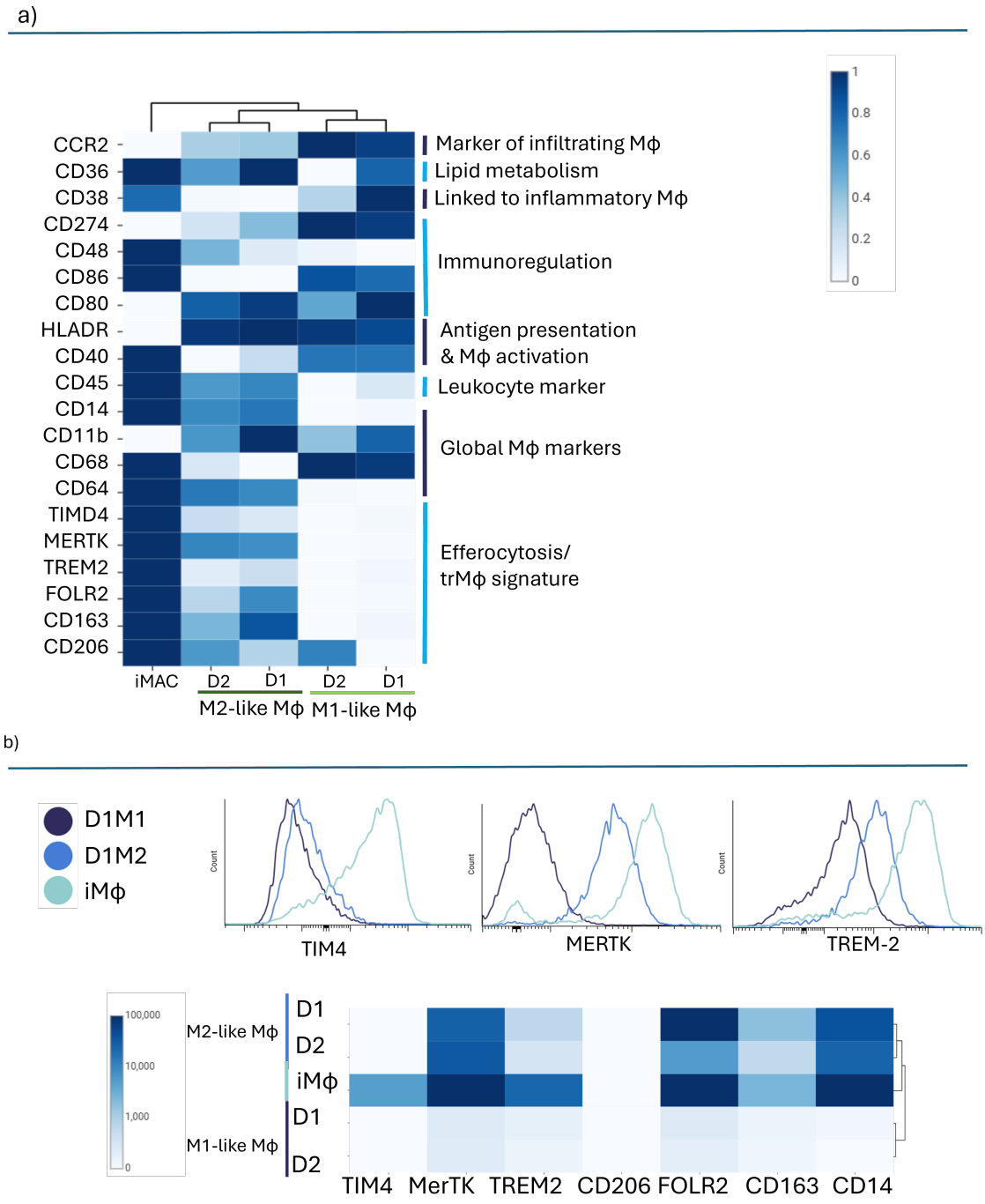

Figure 3-18 Comparative immunoprofiling of differentially polarized MDM and iMφ in *in vitro* platforms. Heatmap showing surface marker expression profiles across macrophage (Mφ) platforms, including monocyte-derived macrophages (MDMs) from two donors (D1: donor 1; D2: donor 2) and induced macrophages (iMφ). Surface markers were grouped into functional categories, including: efferocytosis and tissue-resident macrophage (trMφ) markers; global Mφ markers; global leukocyte markers; macrophage activation and antigen-presenting cell (APC) markers; inflammation- and immune activation-associated markers; lipid metabolism-related markers; and tissue-infiltrating signatures. Data were derived from viable $CD45^+$ cells, pre-gated to exclude debris, doublets, and dead cells (see Appendix H for gating strategy). N = 4 samples. Expression values were scaled and normalized to a 0–1 range. Original dot plots and unstained controls are provided in Appendix G. b) Higher-resolution heatmap view focusing on efferocytosis and tissue-residency-associated marker subsets. Corresponding histograms illustrate expression differences in key surface markers identified in the heatmap. Samples were acquired using a SONY ID7000 spectral flow cytometer, unmixed and corrected for autofluorescence using SONY ID7000 software. Data analysis including heatmap and histogram generation was conducted in CellEngine.

Quantitative analysis of efferocytosis using the *Discoverer Mφ* profiling system revealed significant heterogeneity in the efferocytic capacity across distinct in vitro Mφ platforms. Among the evaluated subtypes, M1-like Mφ exhibited minimal pHrodoGreen fluorescence following co-incubation with apoptotic pHrodoGreen-labeled Jurkat T cells, indicative of poor to no efferocytic activity (Figure 3-19a,b). The temporal kinetics of pHrodoGreen signal accumulation in M1-like Mφ was markedly slower than in both M2-like Mφ and iMφ, further supporting their limited capacity for apoptotic cell uptake (Figure 3-19b). Notably, pharmacological disruption of actin polymerization using CytoD did not significantly affect the already low fluorescence signal in M1-like Mφ, suggesting an inherent deficiency in efferocytic competence within this subset, independent of cytoskeletal rearrangement (Figure 3-19c).

Conversely, M2-like Mφ demonstrated significantly elevated pHrodoGreen fluorescence intensity upon co-culture with apoptotic Jurkat T cells, with a robust and accelerated signal increase over time relative to M1-like Mφ. The efferocytic response in M2-like Mφ was notably diminished by CytoD treatment (Appendix I), confirming actin-dependent internalization and highlighting their comparatively higher phagocytic efficiency.

Among all tested Mφ phenotypes, iMφ displayed the greatest pHrodoGreen fluorescence intensity, indicative of the highest efferocytosis capacity (Figure 13-19b). The fluorescence signal in iMφ reached a plateau more rapidly than in other subtypes, underscoring unique and efficient efferocytic kinetics that distinguish this Mφ platform.

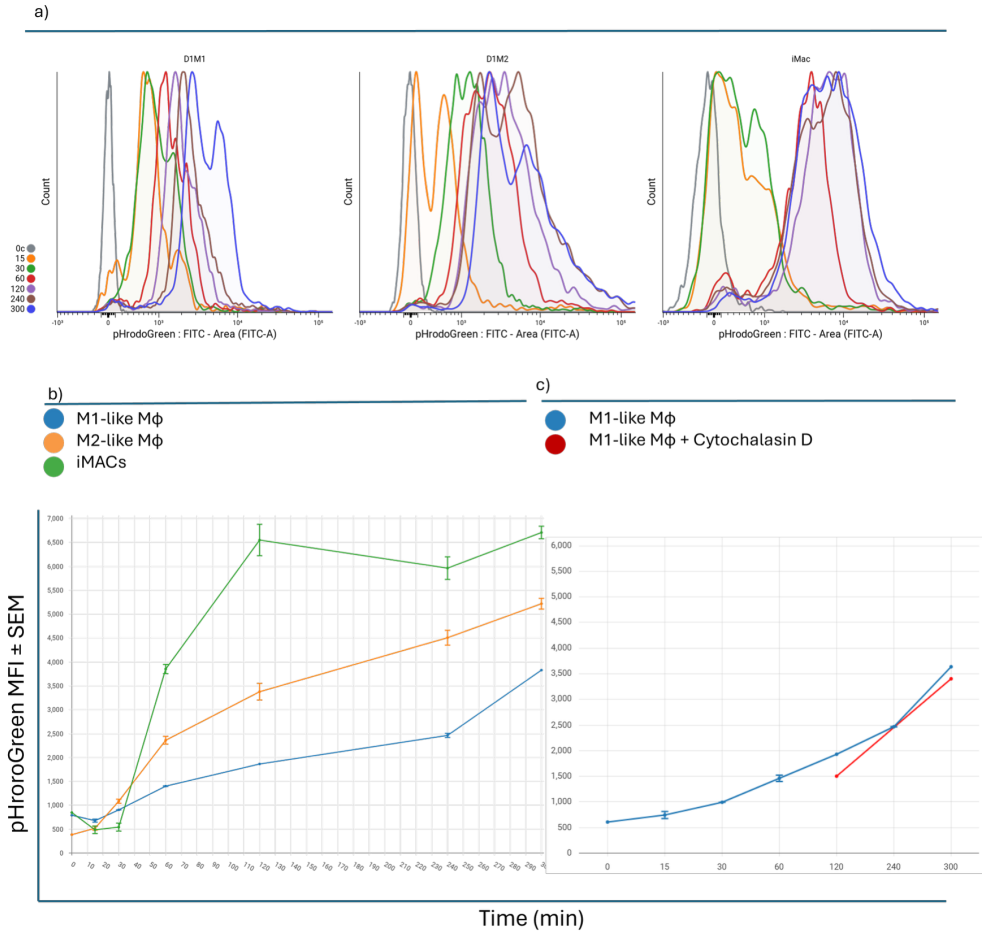

Figure 3-19 Capacity for efferocytosis of apoptotic Jurkat T cells across in vitro macrophage platforms. a) Representative pHrodo™ Green fluorescence peak shifts in gated live CD45⁺ macrophages from different macrophage models over time, indicating uptake of pHrodo™ Green-labeled apoptotic Jurkat T cells. A progressive increase in peak fluorescence was

observed in both M1 and M2 macrophages. iPSC-derived macrophages (iMφ) exhibited a marked fluorescence shift between 60 and 120 minutes, suggesting rapid efferocytosis followed by signal saturation. *(n = 4 per condition)* b) Quantification of efferocytosis kinetics measured as median pHrodo™ Green fluorescence intensity over time. M1 macrophages (blue) showed the slowest uptake, M2-like macrophages (orange) displayed intermediate kinetics, while iMφs (green) demonstrated the fastest and most robust increase in fluorescence. *(n = 4 per timepoint per macrophage type* c) Comparison of pHrodo™ Green fluorescence in untreated M1 macrophages (blue) versus M1-like macrophages pre-treated with 10 µM Cytochalasin D, an actin polymerization inhibitor, and exposed to apoptotic Jurkat T cells. Cytochalasin D treatment significantly impaired efferocytosis capacity. *(n = 4 per condition)*. Data were acquired using the SONY ID7000 spectral flow cytometer, unmixed and autofluorescence-corrected using SONY ID7000 software. Data analysis, including histogram and plot generation, was performed with CellEngine.

Taken together, these findings demonstrate that M2-Mφ possess a notable capacity for efferocytosis, further supported by their elevated expression of efferocytosis-associated receptors (Figure 3-18b). In contrast, M1 Mφ appeared largely incapable of engulfing apoptotic JTs, which correlated with their limited expression of key efferocytosis-related receptors. These results underscore the ability of *Discoverer Mφ* to reveal both functional and phenotypic divergence between Mφ subtypes, enabling inference of their potential roles, including, but not limited to, immunoregulatory and tissue homeostatic functions. Moreover, these findings highlight the differential applicability of in vitro Mφ platforms for studying distinct aspects of efferocytic and regulatory behavior.

3.2.2 Discoverer Mφ Reveals Maximum to High Efferocytosis Capacity in iMφ Making them Ideal Candidates for Perturbation Studies

To investigate whether distinct polarization conditions modulate the efferocytic capacity of iMφ, we subjected iMφ to classical (M1; IFN-γ + TNF-α) and alternative (M2; IL-10 + Dexamethasone) polarization stimuli. We hypothesized that efferocytosis would be enhanced in iMφ treated with IL-10 and Dexamethasone, and suppressed following IFN-γ and TNF-α treatment.

The ability of model Mφ to dynamically increase or decrease their efferocytosis capacity is critical for enabling gain- and loss-of-function studies involving genetic or pharmacological perturbations. In this context, we established iMφ as a tractable model of trMφ suitable for efferocytosis-targeted investigations.

Supporting this model, differentially polarized human MDMs exhibited distinct capacities to engulf apoptotic JTs, highlighting the influence of cytokine microenvironment on efferocytic function.

Interestingly, when assessing key efferocytosis-associated surface markers, TIMD4, TREM2, and MERTK, across the polarization in iMφ conditions, I observed minimal to no change in their expression levels (Figures 3-12a,b). This suggests that modulation of efferocytic activity in polarized iMφ may occur independently of changes in the expression of these canonical receptors.

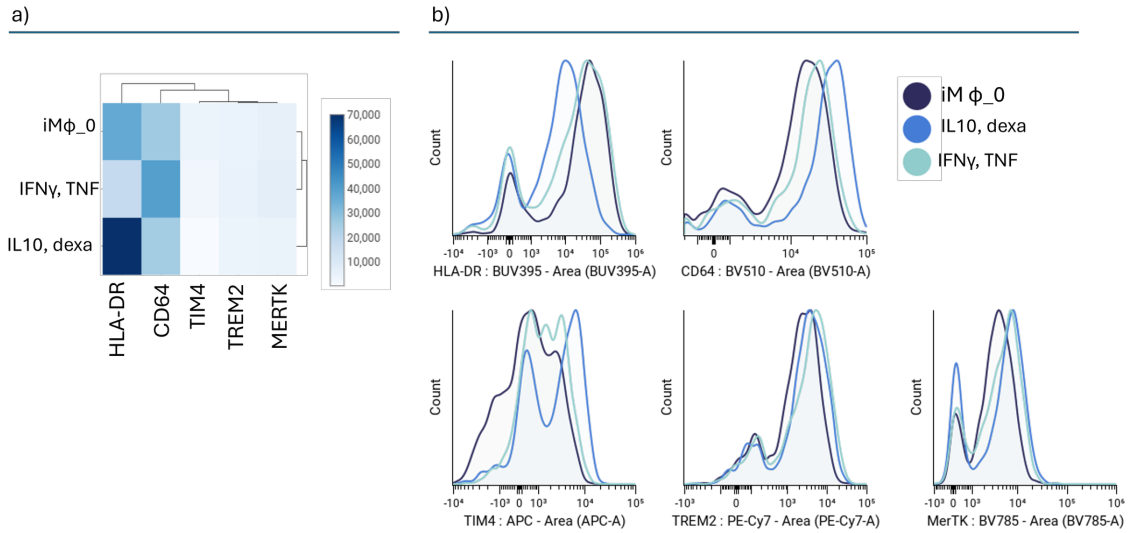

Figure 3-20 Expression of efferocytosis-associated surface markers in differentially polarized iMφ. a) Heatmap comparing the expression of key efferocytosis-related surface markers across distinct iMφ polarization states: non-polarized iMφ, M1-like iMφ (polarized with IFN-γ + TNF-α), and M2-like iMφ (polarized with IL-10 + Dexamethasone. Only markers with detectable expression (determined by comparison to unstained controls; see Appendix X) were included. Heatmap was generated from CD45^{+} viable cells following exclusion of debris and doublets. Color intensity represents raw median fluorescence intensity (MFI). n = 2. b) Representative histogram overlays of marker expression in each polarization condition, normalized to mode. Histograms show positively expressed markers, as determined by comparison to unstained controls (Appendix K). All samples were acquired using the SONY ID7000 spectral flow cytometer. Data were unmixed, autofluorescence-corrected using ID7000 software, and analyzed in CellEngine. Data are representative of N = 2 replicates.

To investigate whether M1 and M2 polarizing cytokines affect the efferocytosis capacity of iMφ, pHrodo™ Green fluorescence intensity was measured in iMφ 120 minutes after target addition. Spectral flow cytometry analysis of the pHrodo Green signal revealed no significant differences in efferocytosis capacity across the different experimental conditions. These findings suggest that iMφ possess an intrinsically high efferocytosis capacity, which could not be significantly enhanced or suppressed by M1 or M2 polarizing cytokines under our experimental conditions (Figure 3-21a,b). However, it is possible that longer exposure durations to the polarizing cytokines may be required to induce detectable changes in efferocytosis capacity, and future experiments could explore this variable to further elucidate the modulatory potential of M1/M2 cytokine environments.

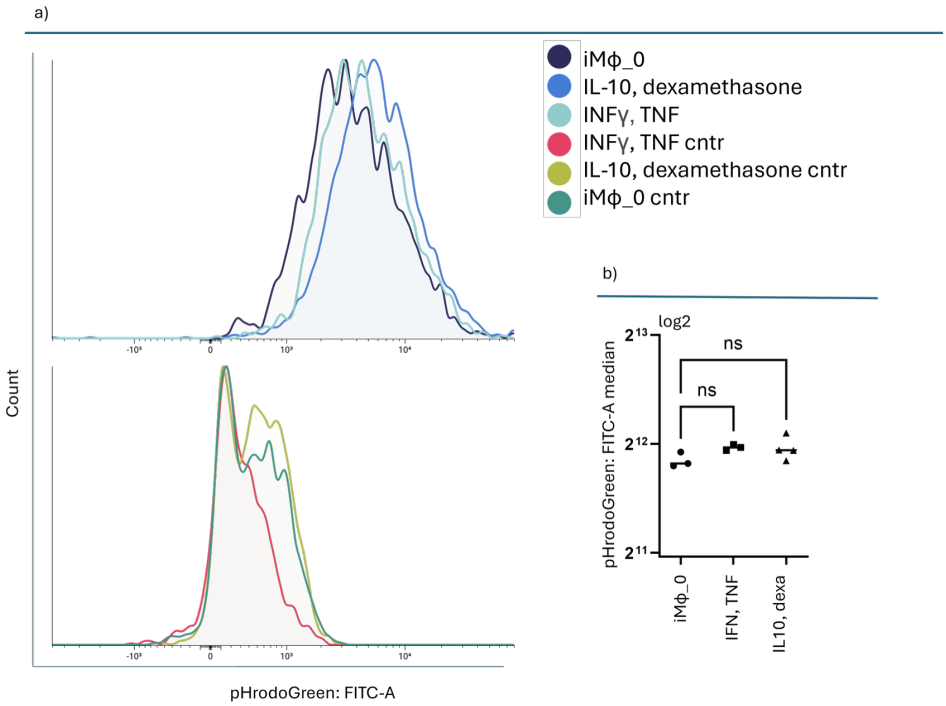

Figure 3-21 Efferocytosis capacity of iMφ under different polarization conditions. a) Representative histogram overlay of pHrodo™ Green fluorescence signal intensities in iPSC-derived macrophages (iMφ) polarized for 24 hours with either IL-10 and dexamethasone (anti-inflammatory/M2-like), IFN-γ and TNF (pro-inflammatory/M1-like), or left unpolarized (iMφ_0). Apoptotic Jurkat T cells labeled with pHrodo™ Green were added at a 1:5 ratio (macrophages to apoptotic cells). Data were acquired 120 minutes after addition, without removal of apoptotic cells prior to measurement. The histogram illustrates efferocytosis activity under different polarization states. b) Quantification of efferocytosis capacity based on median fluorescence intensity of pHrodo™ Green signal across the three polarization conditions (n = 4). Statistical analysis was performed using ordinary one-way ANOVA followed by pairwise comparisons. All samples were acquired on a SONY ID7000 spectral flow cytometer, unmixed, and corrected for autofluorescence using SONY ID7000 Software. Data were analyzed using CellEngine and statistical analysis was performed in GraphPad Prism.

From this data the question arose whether the intrinsically high efferocytosis capacity of iMφ could be further enhanced or suppressed. To answer this and thus assess whether iMφ are suitable for studies investigating perturbation or inhibition of efferocytosis through gain- and loss-of-function approaches, we evaluated a panel of pharmacological inhibitors targeting key efferocytosis pathways, alongside molecules known to enhance efferocytosis (including Protein S1). Protein S1 promotes efferocytosis by acting as a bridging molecule that binds to PS on apoptotic cells and engages TAM family receptors (Tyro3, Axl, and MerTK) on Mφ, thereby facilitating the engulfment process. As shown in Figure 3-22 a and b, untreated cells and cells treated with Protein S1 exhibited the highest efferocytosis capacity across all polarization states, significantly exceeding that of the negative control (no inhibitor or promotor control) ($p < 0.0001$).

Treatment with CytoD, chloroquine, bafilomycin A1, and flavopiridol resulted in a marked reduction in efferocytosis capacity compared to untreated conditions ($p < 0.0001$). CytoD, which inhibits actin polymerization, disrupts the cytoskeletal rearrangements necessary for apoptotic cell engulfment. Chloroquine and bafilomycin A1 impair lysosomal acidification and maturation, interfering with phagosome-lysosome fusion and degradation of engulfed material. Flavopiridol, a broad-spectrum cyclin-dependent kinase inhibitor, suppresses transcriptional programs required for sustained efferocytic activity. Among the inhibitors tested, chloroquine and bafilomycin exerted the most pronounced inhibitory effects. Flavopiridol, in contrast, exhibited the least inhibition of ef-

ferocytosis, which is consistent with its mechanism of action as it is primarily targeting transcriptional regulation required for sustained, but not initial, efferocytic activity. Notably, all inhibitors demonstrated comparable efficacy across Mφ polarization states, indicating a general vulnerability of efferocytosis to disruption of these cellular processes.

In contrast, treatment with Protein S1 preserved high efferocytosis capacity, comparable to that observed in untreated cells. Protein S1 functions as a bridging molecule between PS on apoptotic cells and efferocytosis receptors on phagocytes, facilitating recognition and uptake. The maintained or slightly enhanced efferocytosis observed upon Protein S1 treatment is likely due to more efficient receptor-ligand interactions. Statistical analysis confirmed significant differences among treatment groups ($p < 0.0001$), with a modest but significant increase in Protein S1-treated iMφ IL-10/dexamethasone compared to wild-type iMφ ($p < 0.05$).

These findings infer that iMφ have a high basal efferocytosis activity, which can be inhibited, making iMφ a well-suited in vitro Mφ model for loss-of-function mechanistic and target discovery studies of efferocytosis. Pharmacological blockade of actin dynamics, lysosomal function, and transcriptional regulation robustly impaired efferocytosis, providing valuable positive controls as well as tools for dissecting the molecular underpinnings of this critical process for maintaining human tissue homeostasis.

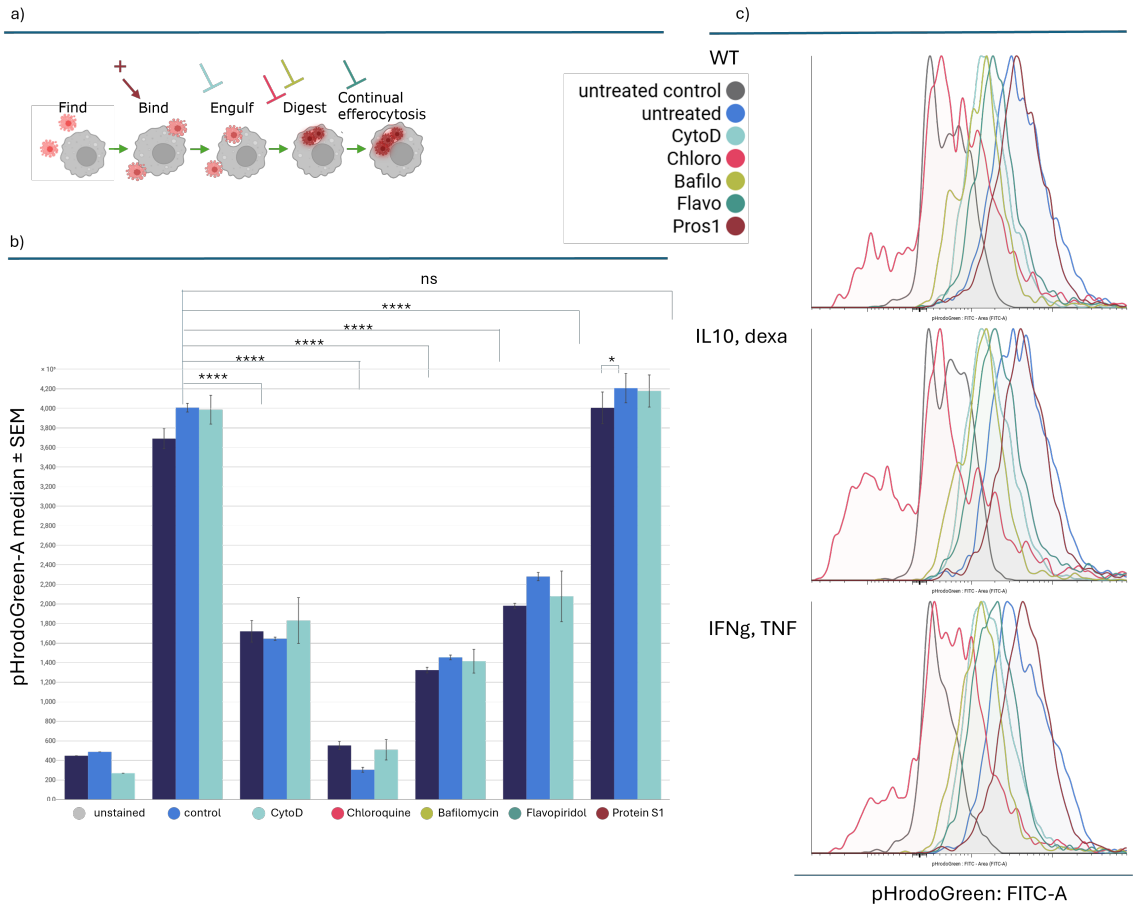

Figure 3-22 Pharmacological modulation of efferocytosis in iMφ under different polarization conditions. a) Schematic illustration of efferocytosis stages targeted by different inhibitors and promoters. Protein S1 (brown) was used to promote the binding phase; Cytochalasin D (pink) to block the engulfment phase; chloroquine (turkeys) and bafilomycin A1 (green) to impair phagolysosome formation and function; and flavopiridol (dark green) to interfere with continual efferocytosis. Untreated control (blue) and unstained control (pre-labeled iMφ + unlabeled Jurkat) (grey) were used as controls and comparators. b) Quantification of efferocytosis capacity following treatment with inhibitors or Protein S1 across different polarization conditions. A highly significant reduction in efferocytosis signal was observed with all inhibitors compared to

paired untreated controls. No significant enhancement of efferocytosis by Protein S1 was detected under most experimental conditions, except for a modest increase in iMφ treated with IL-10 + dexamethasone. Each experimental condition represents n = 4 biological replicates. Statistical analysis: ordinary one-way ANOVA for inhibitor/promoter comparisons to untreated controls, and two-way ANOVA for comparisons between cytokine treatments and inhibitor/promoter effects. Results were considered significant at $p < 0.05$. ****$p < 0.0001$, *$p < 0.05$. c) Representative histograms showing the effects of inhibitors on pHrodo Green fluorescence peak shifts in iMφ under different polarization conditions. Data were gated on viable $CD45^+$ single cells (debris and doublets excluded). Data acquisition was performed on a SONY ID7000 spectral analyzer with unmixing and autofluorescence correction using SONY ID7000 software. Data analysis was conducted using CellEngine.

When examining the expression of efferocytosis-associated surface markers, treatment with n CytoD altered the expression of several markers, likely due to disruption of cytoskeletal dynamics affecting receptor trafficking and membrane localization (Figure 3-23a). In contrast, treatment with other inhibitors, such as chloroquine, bafilomycin A1, and flavopiridol, which primarily interfere with intracellular processing pathways (e.g., endosomal acidification or lysosomal degradation), induced only slight changes in surface marker expression patterns in iMφ, both in the presence and absence of polarizing cytokines. Protein S1 slightly increased the expression of MERTK, and the expression of the other efferocytosis markers remained stable, supporting the findings demonstrated in the previous figure 3-22. Together these findings suggest that receptor expression is differentially regulated depending on whether cytoskeletal trafficking or intracellular degradation pathways are disrupted.

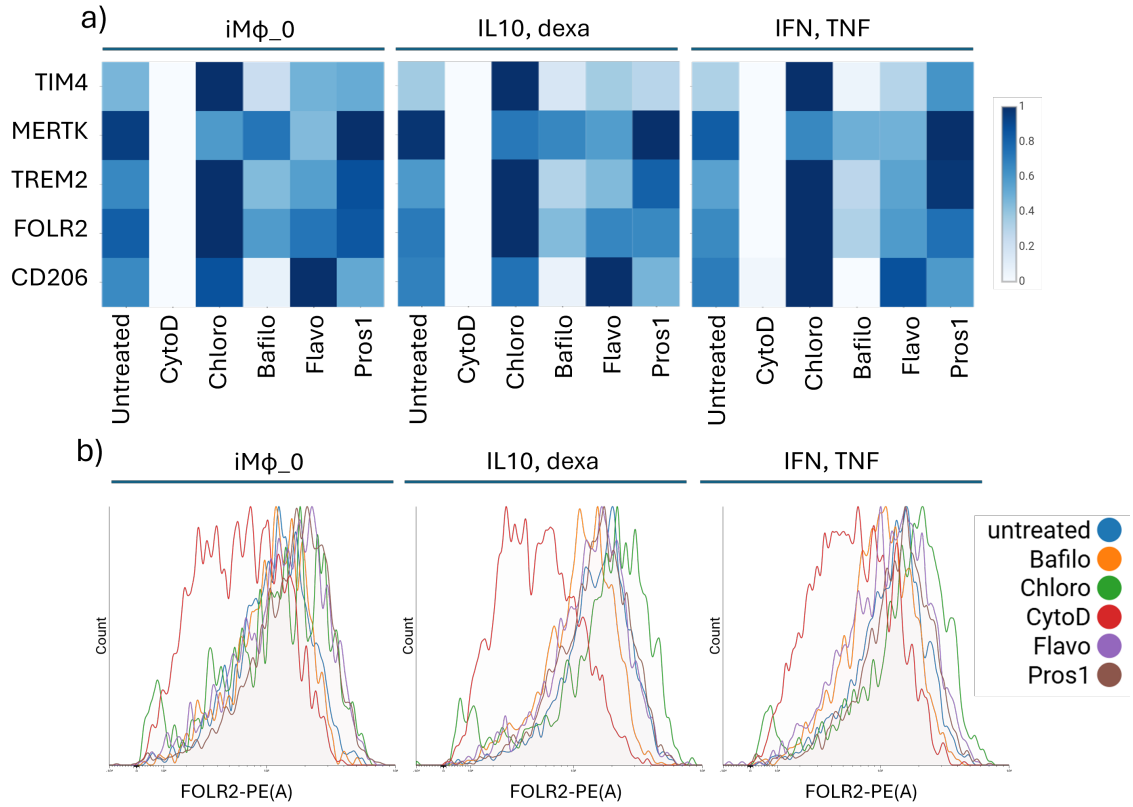

Figure 3-23 Impact of cytokine polarization and efferocytosis modulators on efferocytosis-linked surface marker expression in iMΦ. CytoD: 10 µM Cytochalasin D; Chloro: 100 nM Chloroquine; Bafilo: 10 µM Bafilomycin A1; Flavo: 10 µM Flavopiridol; Pros1: 5 µM Protein S1.a) Heatmap showing expression levels of key efferocytosis-related surface markers across iMΦ treated with two different cytokine polarization conditions (M1 and M2) in the presence or absence of efferocytosis modulators. Heatmaps were generated from $CD45^+$ viable cells, normalized to one, with scaling representing raw marker expression intensities. Data represent n = 4 biological replicates per experimental condition. b) Representative histograms showing FOLR2 expression across different treatment conditions and efferocytosis modulators. Histograms for all markers presented in the heatmap are available in Appendix K. Data were obtained from gated viable $CD45^+$ single

cells, with debris and doublets excluded. Samples were acquired using a Sony ID7000 spectral analyzer with the DISCOVERER M assay. Spectral unmixing and autofluorescence correction were performed using Sony ID7000 software. Data analysis was conducted with CellEngine.

3.2.3 iPSC-Derived Microglia might be Better Suited *In Vitro* Mφ Platform for Gain-of-Efferocytosis Studies

Given that the efferocytosis capacity of iMφ could not be further augmented beyond their intrinsically high baseline levels, these cells may be suboptimal for investigating gain-of-function perturbations in efferocytosis studies. Consequently, we sought to identify alternative in vitro Mφ models with a more modifiable efferocytic phenotype and evidence of compatibility with large-scale CRISPR-based screening platforms. To this end, we successfully optimized the differentiation of 6-transcription factor (6-TF) iPSCs into induced microglia-like cells (iMicroglia), building on the original protocol in collaboration with Dr. Nélio Oliveira and the laboratory of Prof. Bill Skarnes (The Jackson Laboratory, US). As part of this optimization, we evaluated the impact of cytokine conditioning by incubating iMicroglia with either GM-CSF (following the original protocol) or substituting M-CSF during the final 24 hours prior to initiating the efferocytosis assay.

Preliminary characterization of iMicroglia revealed a distinct efferocytosis-associated surface marker profile compared to iMφ (Figure 3-24a, b). Specifically, expression of markers such as MERTK, CD206, and CD14 were detected in iMicroglia, while CD163 and TREM2 were absent. Functional assessment using the *Discoverer Mφ* efferocytosis assay demonstrated a limited capacity of iMicroglia to engulf apoptotic Jurkat T cells relative to iMφ under comparable experimental conditions (Figure 3-24c). Notably, only iMicroglia conditioned with M-CSF exhibited detectable efferocytosis activity, with approximately 30–40% of cells showing pHrodo-positive uptake. Furthermore, this residual efferocytosis activity was completely abrogated by chloroquine treatment, which suppressed pHrodo fluorescence signal (Figure 3-24c), indicating that lysosomal acidification remains critical for detection of engulfed apoptotic targets in this model.

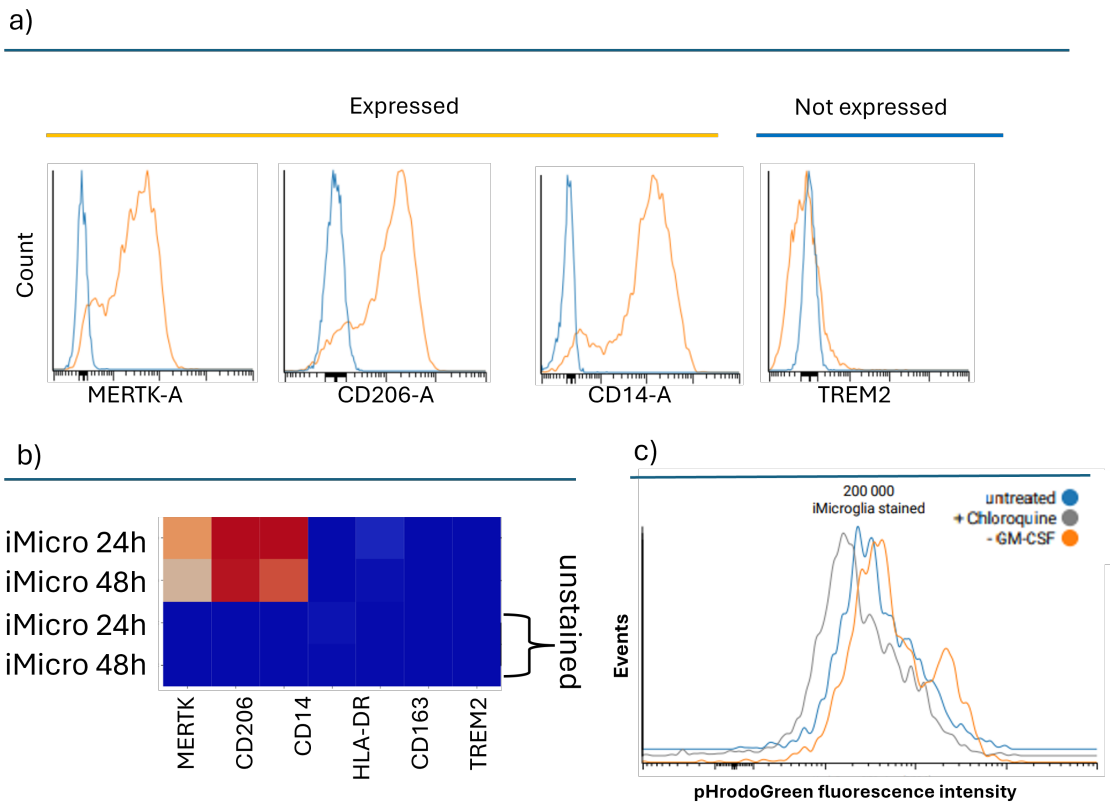

Figure 3-24 Characterization of efferocytosis marker expression and efferocytic activity in iMicroglia. a) Expression of efferocytosis-linked surface markers in iMicroglia, comparing unstained cells (blue) versus stained iMicroglia labeled with the adjusted antibody panel (orange).b) Heatmap showing differential surface marker expression in unstained (bottom two rows) and antibody-labeled (top two rows) iMicroglia following GM-CSF withdrawal and replacement with M-CSF for either 24 or 48 hours. Heatmap conditions represent mean fluorescence intensity values, normalized across the full data range, scaled to one. c) Representative histograms of pHrodo™ Green fluorescence intensity in live $CD14^+CD206^+$ iMicroglia (blue) after addition of apoptotic pHrodo™-labeled Jurkat T cells. Cells were either maintained under standard GM-CSF conditions or cultured without GM-CSF but with M-CSF replacement for the last 24 hours (orange). Cells treated with chloroquine (10 µM, grey) are shown to highlight inhibition of efferocytic activity. Samples were acquired using a SONY ID7000 spectral analyzer; spectral unmixing and autofluorescence correction were performed with SONY ID7000 software. Cells were pre-gated to exclude debris and doublets, and viability gating and $CD14^+CD206^+$ selection were applied prior to analysis. Data were analyzed using CellEngine. N = 2 biological replicates per experimental condition.

These preliminary findings suggest that iMicroglia may represent a more suitable in vitro Mφ platform than iMφ for investigating strategies aimed at enhancing efferocytosis. However, further validation and optimization of this model are necessary before it can be applied to large-scale perturbation studies. These efforts are ongoing within our broader research project but fall outside the scope of the current PhD thesis.

To assess the suitability of Discoverer-derived iMicroglia for quantifying the engulfment of cancer cells, a pilot experiment was conducted in which iMicroglia were exposed to apoptotic glioblastoma cells labeled with pHrodoGreen. As shown in Figure 3-25a, a moderate increase in pHrodoGreen fluorescence was detected relative to both the CytoD-treated negative control and a non-cancer cell control. Notably, when compared to iMicroglia incubated with pHrodoGreen-labeled JTs, the glioblastoma condition elicited a higher fluorescence intensity and a more substantial peak shift. These preliminary findings suggest that iMicroglia may exhibit a preferential efferocytic response toward glioblastoma cells, indicating potential target specificity in their phagocytic activity. However, as this was a preliminary experiment, additional controls and replicates are required to rule out alternative explanations for the observed differences in pHrodoGreen signal.

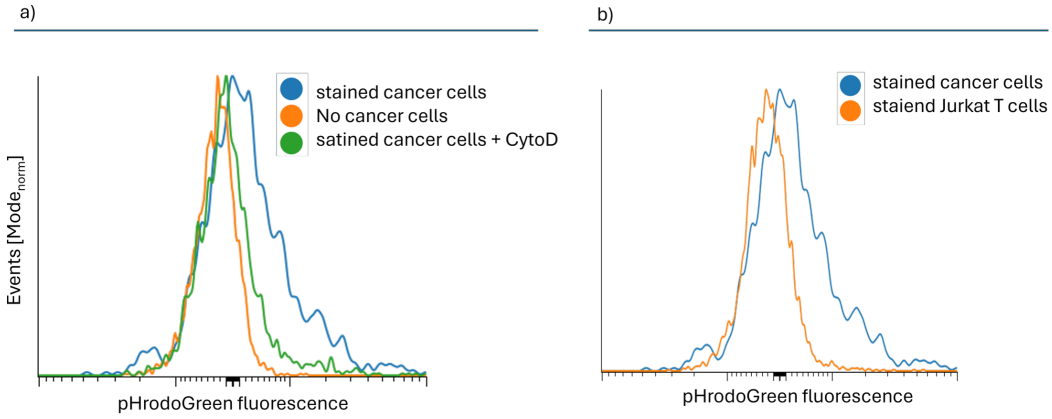

Figure 3-25 Pilot glioblastoma efferocytosis experiment on iMicroglia cells. Representative pHrodo™ Green fluorescence peak shifts in gated live $CD14^+CD206^+$ iMicroglia. a) Minimal peak shift of efferocytosis condition (blue) containing stained iMicroglia incubated with pHrodoGreen labelled apoptotic glioblastoma cells as compared to negative control (orange) containing stained iMicroglia, no apoptotic cancer cells and inhibitor-treated condition (green) containing stained iMicroglia incubated with pHrodoGreen labelled apoptotic glioblastoma cells plus 10uM Cytochalasin D. b) Comparison of iMicroglia cells incubated with pHrodoGreen labelled Glioblastoma cells (blue) compared with pHrodoGreen labelled apoptotic Jurkat T cells reveals more distinct peak shift in glioblastoma condition. Samples were acquired using a SONY ID7000 spectral analyzer; spectral unmixing and autofluorescence correction were performed with SONY ID7000 software. Cells were pre-gated to exclude debris and doublets, and viability gating and $CD14^+CD206^+$ selection were applied prior to analysis. Data were analyzed using CellEngine. N = 2 biological replicates per experimental condition.

3.3 Discoverer Mφ Data Integration Creates New Knowledge in Functional Phenotypization of Synovial Cells

Following extensive validation across functional readouts, phenotyping antibody panels, and in vitro Mφ platforms, we proceeded to employ the *Discoverer Mφ* system to generate new insights into human tissue Mφ diversity using valuable patient-derived biospecimens. With a focus on pro-resolution target discovery in IMIDs, we selected RA as a prototype disease model to study the phenotypic and functional heterogeneity of Mφ populations within the synovium.

To build a comprehensive understanding of tissue biology during IMID remission and flare states, we are integrating multiple advanced technologies, including CITE-sequencing (CITE-seq), spectral flow cytometry, CosMx spatial transcriptomics, and large-scale multiomics data integration (Figure 3-26).

Synovial macrophages (synMφ) and structural cells are being isolated from synovial tissue and synovial fluid samples collected from arthritis patients presenting with various forms of arthritis (e.g., osteoarthritis, RA) and across different disease activity states (remission, active RA, and end-stage disease requiring joint replacement), as well as varying treatment responses (including cDMARD-naïve patients, cDMARD-inadequate responders, and anti-TNF therapy-resistant RA cases). Biospecimens are obtained via ultrasound-guided synovial biopsy, arthrocentesis, or joint replacement surgery. To date, we have collected 39 synovial tissue samples and 20 synovial fluid samples from arthritis patients.

Processing and analysis of the biospecimens have involved multiple complementary methodologies. The majority of human synovial tissue biopsies were processed and CITE-seq libraries generated by Janine Lückgen. Maria del Pilar Palacios Cisneros and Mojca Frank Bertoncelj contributed by dissociating synovial biopsies and creating CITE-seq libraries for a subset of patient samples. For synovial tissues obtained during joint replacement surgery, the PTA research team conducted intensive overnight experiments encompassing tissue dissociation, fluorescence-activated cell sorting (FACS), CITE-seq library preparation, and spectral flow cytometry. Bioinformatic analysis of the CITE-seq data was performed by Helena R. Crowell, with data annotation and interpretation carried out by Mojca Frank Bertoncelj.

My contributions to the experimental work on human synovial tissue included the optimization of antibody concentrations for FACS sorting and CITE-sequencing, tissue processing, and the complete spectral flow cytometry workflow. This encompassed the design and optimization of multi-spectral flow cytometry panels for phenotyping synovial Mφ, stromal, and structural cells, the establishment and execution of functional assays (including assay set-up optimization and experimental execution), as well as subsequent data analysis and interpretation.

In this PhD thesis, I present a subset of data from the synovial CITE-seq analyses, focusing primarily on synovial Mφ but also partially addressing structural cell populations. These transcriptomic data were aligned with multicolor spectral flow cytometry analyses of synovial tissue and synovial fluid cells from patients with inflammatory arthritis, using the *Discoverer Mφ* platform (Figure 3-26). By integrating CITE-seq with *Discoverer Mφ*-based phenotyping and functional assays, we were able to uncover differential abundances, phenotypes, and functional characteristics of diverse synMφ and structural cell subsets across various arthritis types, disease activity states, and therapeutic response categories.

Many of these cellular subsets are currently definable primarily (and often exclusively) by their distinct transcriptional signatures. The integration of transcriptomic, surface protein, and functional data enables the identification of specific synovial Mφ and structural cell populations (Who?), elucidation of their functional roles (What?), and association with clinical metadata such as disease activity, therapeutic response, and remission status. Ultimately, this multidimensional approach supports the construction of a comprehensive multi-omics map of human synovial tissue in both remission and active arthritis, providing a valuable resource for the scientific community and informing future research and therapeutic development initiatives.

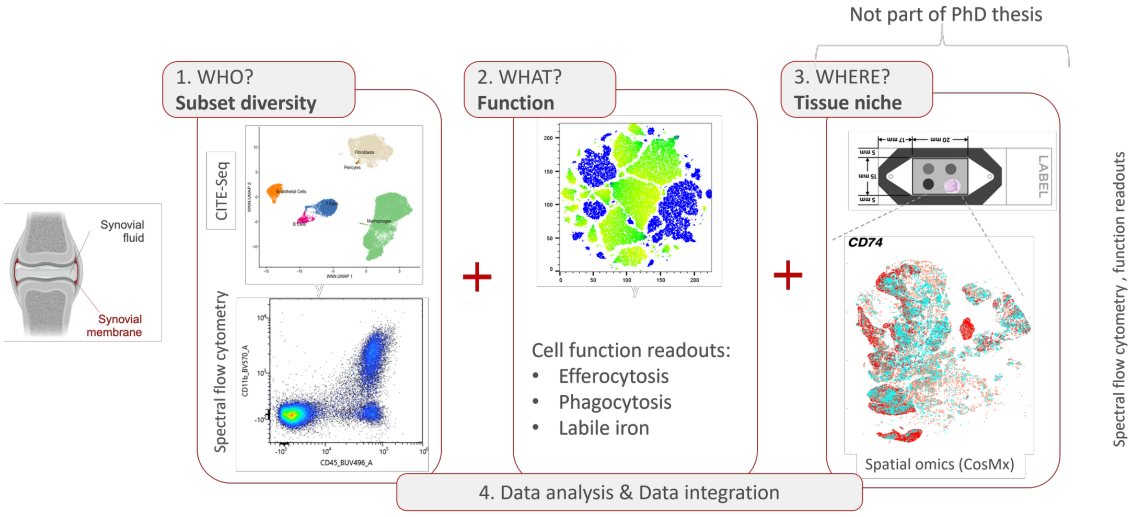

Figure 3-26 Integrative analysis of synovial CITE-seq, spectral flow cytometry, and spatial transcriptomics datasets. Combined single-cell and spatial analyses were performed to identify the diversity of synovial macrophage (synMφ) and structural cell subsets (Who?), define their phenotypic and functional characteristics (What?), and assign their spatial localization and cellular neighborhoods within synovial tissue (Where?). These analyses were conducted across different rheumatoid arthritis (RA) activity states, treatment response categories, and arthritis types.

3.3.1 CITE-Seq Uncovers Synovial Cell Diversity

Figure 3-27 presents a comprehensive multi-omics analysis of synMφ in RA, combining single-cell RNA sequencing (scRNA-seq), antibody-derived tag (ADT) profiling, and surface marker phenotyping. As shown in Figure 3-27a UMAP plot displays the integrated scRNA-seq data from 167,650 synovial cells isolated from 21 RA patient synovial tissues with DMARD-naïve RA (n=6, 28,6% contributed cells), RA inadequately responding to csDMARDs (n=6, 28,6 % contributed cells), Anti-TNF/IL-6 inadequate responsers (n=5 23,8 % contributed cells) and RA in remission (n=4, 19% contributed cells). Total synovial cells were derived from unsorted samples (n=9) and sorted samples (n=14). In sorted samples, we enriched for $CD45^-$ structural cells (n=1 samples) and myeloid cells sorted as $CD45^+CD11B^+$ (n=5 biopsies), $CD45^+CD11B^+CD64^+$ (n=7 biopsies), $CD45^+CD11B^+CD14^+$ (n=1 biopsy), and $CD45^+CD11B^+CD64^-$ (n=1 biopsy). Thus, the proportion of different main synovial cell populations on the UMAP (Figure 3-27a) is skewed toward dominance of structural and myeloid cells, whereas lymphoid cells originate primarily from non-sorted

tissue samples. In general, we detected all key synovial cell populations, including a distinct fibroblast-like synoviocyte (FLS) population, two endothelial cell clusters, pericytes/mural cells, lymphoid clusters consisting of T cells and natural killer (NK) cells, B cells, an avascular cluster consisting of endothelial cells and mural cells, and a myeloid cluster consisting of synMφ and neutrophils. In the next step, we performed *in silico* sorting of myeloid cells to enable more granular sub-clustering of Mφ subsets, as illustrated in Figure 3-27b. Principal clusters were identified based on the top enriched cluster-specific genes and informed by prior reference synovial scRNA-seq datasets (Alivernini et al., 2020; Edalat et al., 2024). Sub clustering of myeloid cells revealed four transcriptionally distinct Mφ populations, along with a cluster of NAMPT$^+$ IFITM2$^+$ synovial neutrophils. The identified synMφ populations included: (1) trMφ, characterized by high expression of FOLR2, MERTK, and SLC40A1 (yellow cluster); (2) a Mφ subset with low FOLR2 but high TREM2 and SPP1 expression (dark pink cluster); and (3-4) two distinct subsets of infiltrating CCR2$^+$ Mφ. The infiltrating CCR2$^+$ Mφ were further distinguished based on gene expression profiles, with one subset enriched for CLEC10A (light pink cluster) and the other for IL1B and SLC11A1 (green cluster).

Notably, SLC40A1 (encoding the iron exporter ferroportin) and SLC11A1 (encoding the iron importer DMT1), genes involved in iron homeostasis, were specifically enriched in the FOLR2high tissue-resident and IL1B^{high} infiltrating Mφ subsets, respectively. These findings suggest a compartmentalization of iron metabolism functions across different synMφ populations within the synovial tissue. Further investigation using the Discoverer Mφ-IRON assay will provide deeper insights into iron transporter signatures and iron metabolic pathways in these synovial Mφ subsets.

scRNA-seq data, visualized in the heatmap in Figure 3-27c, further revealed high expression of genes encoding complement components (C1QA, C1QB, C1QC) alongside other key markers (SELENOP, CD163, GLIPR1) previously associated with synovial tissue residency (Alivernini et al., 2020), specifically within the tissue-resident FOLR2^{high}, MERTK^{high}, and SLC40A1^{high} Mφ subsets. Consistent with findings from Mφ profiling platforms, FOLR2$^+$ cells also displayed elevated expression of CD163, MERTK, TIMD4, and CD14, further supporting their classification as tissue-resident synovial Mφ.

Within the synMφ populations, the FOLR2$^+$ TREM2^{low} SPP1^{high} cluster displayed the highest expression of TIMD4, TREM2, and MARCO, markers closely linked to tissue residency. In contrast, the CCR2$^+$ CLEC10A$^+$ subcluster exhibited the highest expression of EREG, a gene associated with inflammation and fibrosis. These findings mirror the model of Trzebanski et al. (2024) who described a monocyte-derived dendritic cells progenitors (MDP) derived monocytes/Mφ population in a murine model (whole BM isolated from C57BL/6 WT animals). In their study, CLEC10A expression was enriched in CD319$^+$ classical monocytes, which originate from MDPs and were shown to contribute preferentially to Mφ populations with dendritic-cell-like features, including high MHC-II expression and antigen-presenting capacity. Notably, although these monocytes co-expressed CCR2, their functional fate was distinct from that of granulocyte-monocyte progenitors-derived (inflammatory) monocytes (Trzebanski et al., 2024). The presence of CLEC10A suggests that this subset may serve a specialized role in immune regulation or antigen presentation within the inflamed synovium. Thus, the identification of CLEC10A$^+$ Mφ in human synovial tissue supports a model in which monocyte ontogeny shapes Mφ heterogeneity and function in chronic inflammatory environments.

Finally, the CCR2$^+$ IL1B$^+$ SLC11A1$^+$ subcluster showed strong expression of FCN1, LYZ, and MPEG1, genes linked to inflammatory responses and immune activation.

As shown in Figure 3-27d, transcriptomic profiles and ADT signatures largely corresponded with the transcriptomic profiles of surface markers across transcriptionally defined synovial Mφ subsets. Several key Mφ markers, including FOLR2, CD163, CD74, CCR2, CD52, CD48, and CX3CR1, were robustly validated at the protein level (Figure 3-27d). Integration of CITE-seq data further enabled the identification of surface markers distinguishing specific synMφ subsets. Finally, transcriptomic and ADT-based Mφ sub clustering were aligned, as summarized in Table 3-3 and Figure 3-27e.

Table 3-3 Clusters identified in scRNAseq vs. ADT-based clusters

Cluster	scRNA-based clusters	ADT-based clusters
1	$FOLR2^{high}MERTK^{high}SLC40a1^{high}$	$FOLR2^{high/med}\,CCR2^{neg}$
2	$FOLR2^{low}TREM2^{high}SPP^{high}$	$FOLR2^{dim}CCR2^{dim}CX3CR1^{neg}$
3	$CCR2^{+}CLEC10A^{+}$	CCR2+CD74+
4	$CCR2^{+}IL1B^{+}SLC40A1^{+}$	$CCR2+CD74^{neg}$

This alignment of protein and transcriptomic data supports both unbiased exploration and targeted functional analyses of subset-specific synovial Mφ phenotypes and functions, thereby advancing our understanding of their roles in RA pathogenesis.

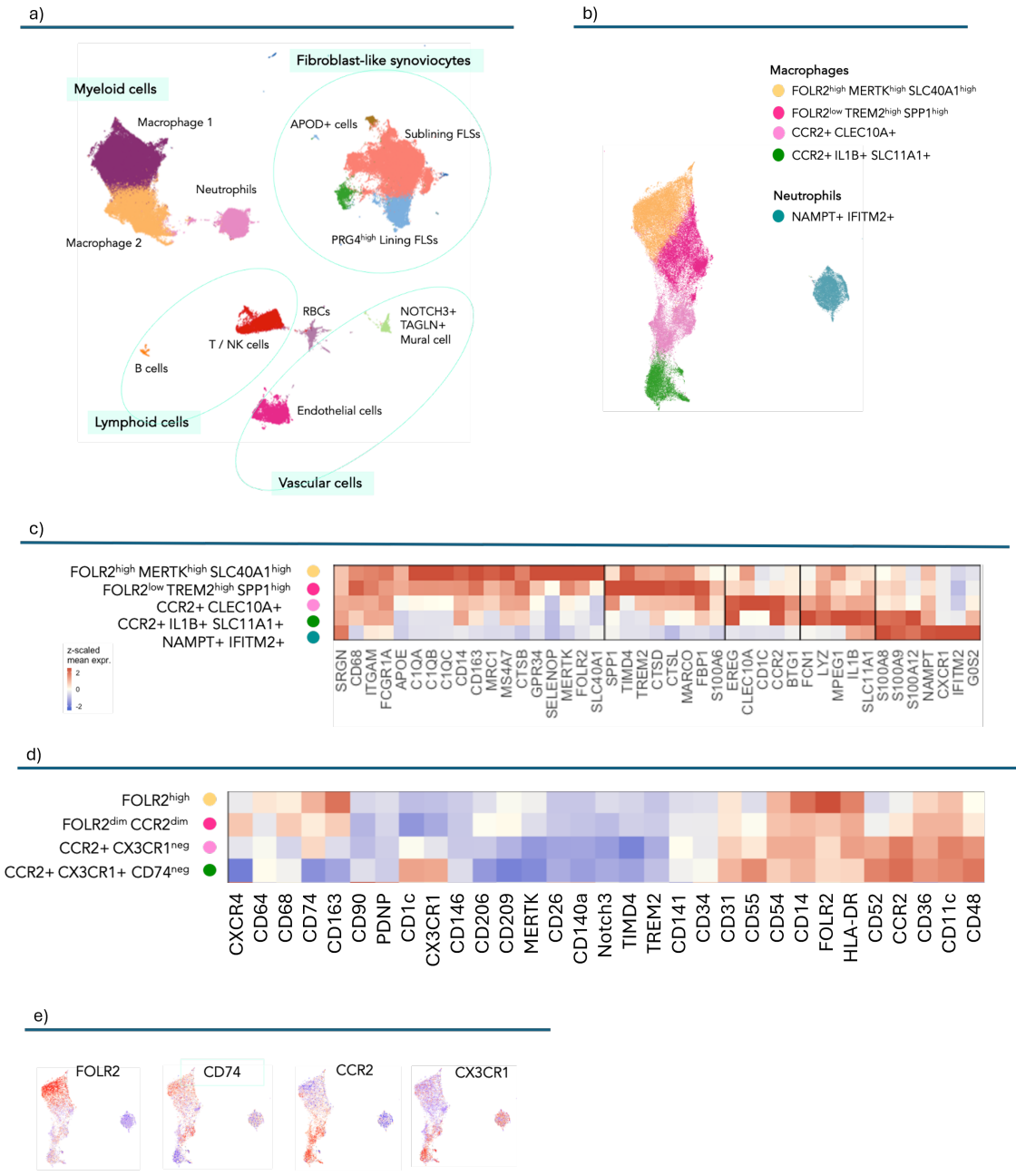

Figure 3-27 Multi-Omics Profiling – CITE-Sequencing of Human Synovial Macrophages in Rheumatoid Arthritis. Synovial cells were isolated fresh during synovial tissue dissociation (CITE Edalat) and labelled with CITE-Seq and sorting antibodies (in a subset of samples that underwent sorting). Next, scRNA-seq and ADT libraries were generated (10x Genomics, 3′ v3.1 chemistry) and sequenced on the Illumina NovaSeq 6000 platform (paired-end reads, with minimum coverage of 50,000 RNA and 5,000 ADT reads per cell). a) UMAP plot showing integrated scRNA-seq data from 167,650 synovial cells from 21 patients with DMARD-naïve RA (n=6), csDMARD-inadequate (n=6) and Anti-TNF/IL-6 inadequate responders-inadequate (n=5) responders, as well as RA patients in remission (n=4). See Table 2-8 for cell quantity per patient group. b) Synovial myeloid cells were *in silico* sorted and further subclustered into four distinct macrophage (Mφ) clusters and one neutrophil cluster. c) Heatmap of top enriched genes across synovial myeloid cell clusters. Gene expression was calculated across all cells in each subcluster in pseudo bulk. d) ADT signatures for selected macrophage surface marker genes shown on heatmaps, as determined by synovial cell CITE-Seq (n =16 samples). e) The aligned transcriptomics and ADT classifications of synovial macrophage clusters. Data were created by Janine Lückgen, Mojca

Frank Bertoncelj, and Maria del Pilar Palacios Cisneros. Samples were acquired in partnership with the teams of Vasco Romao and Joao Eurico Fonseca, University of Lisbon, Lisbon, Portugal, as well as in collaboration with Georg Schett, University Clinic Erlangen, Germany. Bioinformatics data analysis was performed by Helena R. Crowell, with data annotation and interpretation by Mojca Frank Bertoncelj.

3.3.2 Spectral Flow Cytometry

Spectral flow cytometry analysis was conducted on freshly isolated synovial cells (Edalat et al., 2024), allowing for a high-resolution identification of diverse structural and myeloid cell populations within the synovial tissue compartments. The antibody panel for spectral flow cytometry was designed to comprehensively capture diverse synovial Mφ populations, with parallel adaptations of the antibody panel for analysis of synovial structural cells. The selection of surface markers targeted in the spectral flow cytometry antibody panels was based primarily on our synovial scRNA-seq atlas by Edalat et al. (2024), which I coauthored. Additionally, the antibody panel was further fine-tuned in accordance with synovial Mφ scRNA-seq finidings from Alivernini S et al., (2020) as well as synovial CITE-Seq data by Zhang et al (2023). The panel markers global leukocyte/myeloid cell/Mφ markers as well as markers linked to various Mφ phenotypes, including tissue residency, pro-resolution, pro-inflammatory, tissue infiltrating phenotypes. Structural cell markers included endothelial cell, mural cell/pericyte and FLS markers (Table 3-4).

Table 3-4 Surface markers to characterize total synovial cells

Characteristics	Marker
Global leukycyte, myeloid cells, macrophages	CD45, CD54, CD64, CD11b, CD14, CD68
Tissue residency linked	FOLR2, TIMD4, (SLC40A1)
Pro-resolution linked	CD163, MERTK, CD206, TREM2, CD209
Inflammation linked/ infiltration linked	CD114, CD52, CD48, SPP1, CX3CR1, CCR2
Antigen presentation-linked	HLA-DR
Iron transporters	CD71, CD91, SLC40A1
Lipid metabolism	CD36
Non-Mφ marker	CD31, CD34, CD26, Notch3, Podoplanin, CD90, CD55, CD146

A pilot Discoverer Mφ-based analysis was performed on total synovial cells isolated from the synovial tissue of an osteoarthritis (OA) patient undergoing joint replacement surgery (Figure 3-28). By plotting CD45 against CD14 expression, three main populations were clearly distinguished: $CD45^-$ structural cells, $CD45^+CD14^+$ Mφ, and $CD45^+CD14^-$ non-Mφ leukocytes (Figure 3-28a). Further sub-classification of synovial macrophages (synMφ) using the Discoverer Mφ antibody panel identified three key populations: $CCR2^+FOLR2^-$ infiltrating synovial macrophages (tiMφ), $FOLR2^+CCR2^-$ tissue-resident synovial Mφ, and an intermediate population of $CCR2^+FOLR2^+$ synMφ (Figure 3-28b). Consistent with previous findings (Zhang *et al.*, *Nat. Immunity*, 2019), OA synovium demonstrated a relative enrichment of trMφ over tiMφ.

Detailed phenotypic profiling revealed that $CCR2^+FOLR2^-$ tiMφ expressed elevated levels of CD48, a marker associated with pro-inflammatory activity. In contrast, $FOLR2^+CCR2^-$ trMφ exhibited high expression of markers linked to tissue residency and immunoregulatory functions, including CD163, MERTK, CD206, TREM2, TIM4, and CD209. Additional markers such as CD14,

HLA-DR, and CD54 were also enriched in the trMφ cluster. These findings support a model in which trMφ contribute to tissue-protective and homeostatic roles within the OA synovium.

Strikingly, the spectral flow cytometry data closely mirrored observations from our synovial CITE-sequencing dataset, identifying the same three Mφ subpopulations: FOLR2^{+}CCR2^{-} trMφ, FOLR2^{+}CCR2^{+} intermediate Mφ, and CCR2^{+}FOLR2^{-} tiMφ.

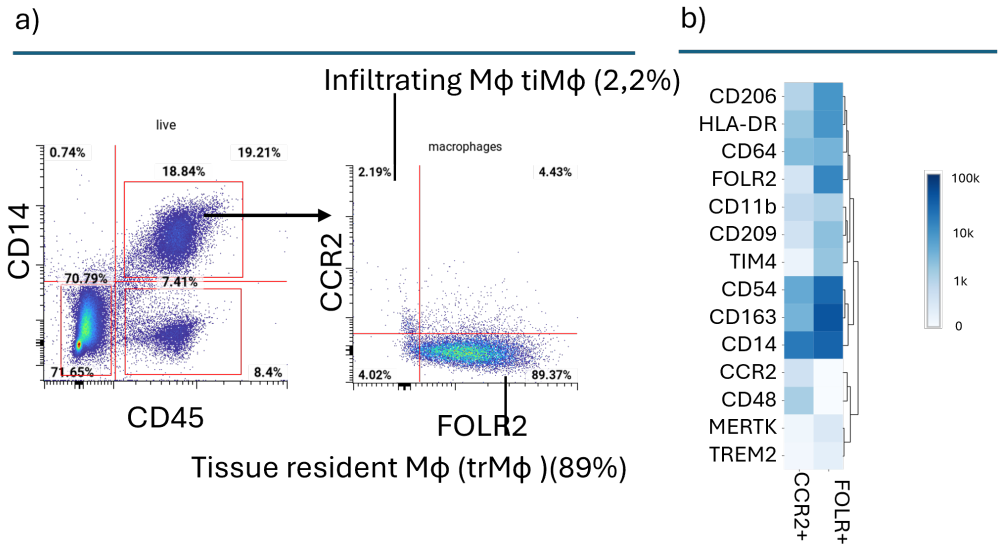

Figure 3-28 Spectral flow cytometry analysis of synovial macrophages in OA synovium. Total live, unsorted synovial cells were analyzed. Debris, doublets, and dead cells were excluded using forward and side scatter gating, singlet discrimination, and ZombieNIR viability staining. a) Live ZombieNIR-negative synovial cells were gated based on CD45 and CD14 expression to identify CD45− structural cells, CD45+CD14+ macrophages (Mφ), and other CD45+CD14− leukocytes. CD45+CD14+ macrophages were further gated based on FOLR2 and CCR2 surface expression to define three macrophage subsets, including FOLR2+CCR2− tissue-resident macrophages and CCR2+FOLR2− infiltrating macrophages. (b) Heatmap comparing marker expression profiles of FOLR2+CCR2− and CCR2+FOLR2− synovial macrophage subsets. Expression values were normalized using z-score transformation across markers. The heatmap scale represents z-score values of marker expression intensity. Samples were acquired on a SONY ID7000 spectral flow cytometer with autofluorescence adjustment and spectral unmixing applied (SONY ID700 software). Data analysis was performed using Cell Engine. Representative data shown from one biological replicate (n = 1).

These findings are further corroborated by our previously published study (Edalat et al., 2024), in which integrated single-cell RNA sequencing (scRNA-seq) data from 25 synovial tissue samples derived from patients with various forms of inflammatory arthritis revealed 12 transcriptionally distinct subclusters within the Mφ and myeloid dendritic cell compartment. Consistent with our current observations, FOLR2^high subclusters displayed the highest expression of canonical Mφ marker genes, including *CD14, CD68, TREM2, CD163, TIMD4, MERTK, MRC1* (CD206), and *CD209*. In contrast, elevated expression of *CD48* was observed in CCR2^{+} macrophage subclusters, in line with an infiltrating monocyte-derived Mφ phenotype.

As part of the validation strategy described in Edalat et al. (2024), I conducted multispectral flow cytometry experiments to phenotypically characterize synovial cell populations and independently validate the main immune and stromal cell clusters identified by scRNA-seq. Synovial tissue samples, two in total were obtained via ultrasound-guided wrist biopsies from patients with early rheumatoid arthritis and processed by Janine Lückgen in collaboration with our partners at the University of Lisbon, Portugal. Following tissue dissociation, cells were fixed and stained with a comprehensive antibody panel targeting key leukocyte (CD45), myeloid (CD14), lymphoid (CD3, CD4,

CD8, CD19), and stromal (CD31, PDPN) surface markers. Data acquisition was performed using the Sony ID7000 spectral flow cytometer.

Flow cytometric analysis confirmed the presence of major synovial immune populations, including $CD45^+CD14^+$ Mφ, $CD45^+CD19^+$ B cells, and $CD45^+CD3^+$ T cells, with the latter further subdividing into $CD4^+$ and $CD8^+$ subsets. Moreover, $CD45^-$ stromal cells segregated into two discrete populations: $CD31^+$ ($PECAM1^+$) endothelial cells and $PDPN^+$ synovial fibroblasts (Figure 3-29)

In summary, the spectral flow cytometry analysis not only validated the major transcriptionally defined cell clusters reported in Edalat et al. (2024) but also provided strong orthogonal support for the synovial cell populations identified in our current scRNA-seq dataset. Together, these complementary approaches underscore the reproducibility and robustness of synovial cell identity assessments across transcriptomic and proteomic single-cell platforms.

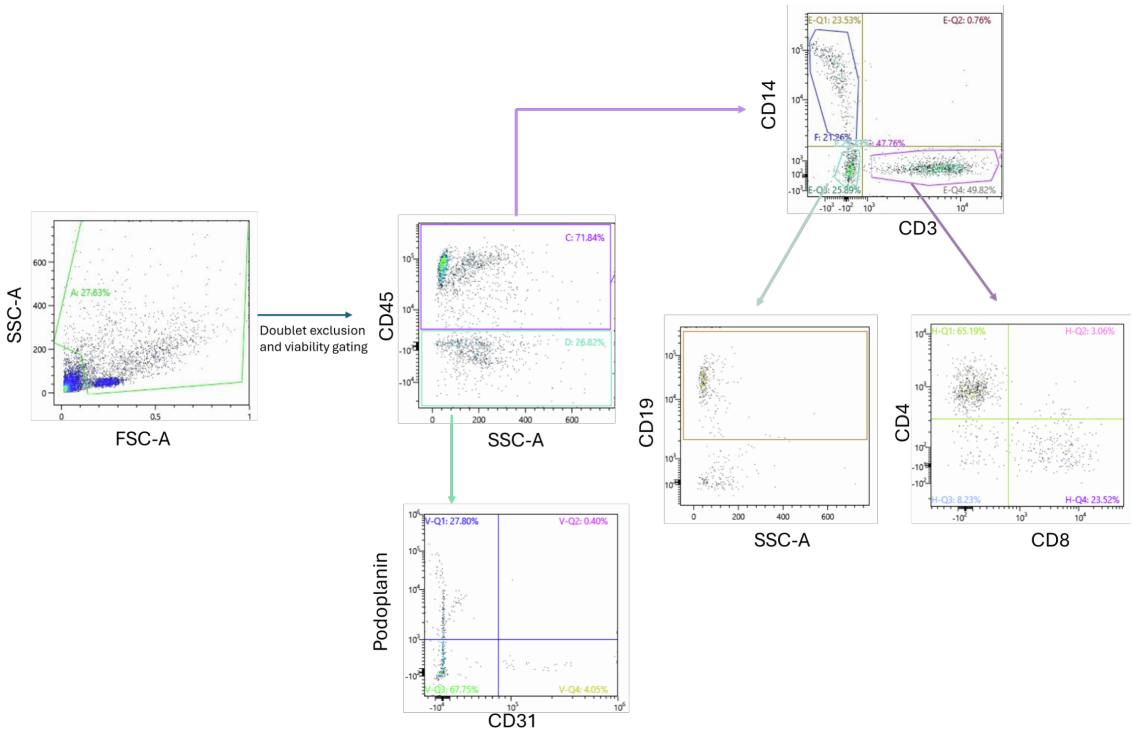

Figure 3-29 Spectral flow cytometry analysis of freshly isolated synovial tissue cells. Synovial cells were isolated from a wrist biopsy and fixed before staining with a multispectral antibody panel targeting surface markers for leukocytes (CD45), myeloid cells (CD14), lymphocytes (CD3, CD4, CD8, CD19), and structural cells (CD31, PDPN). Analysis with the Sony ID7000 spectral cytometer identified two main compartments based on CD45 expression. The $CD45^+$ immune cell population included $CD14^+$ macrophages, $CD19^+$ B cells, and $CD3^+$ T cells, which were further subdivided into $CD4^+$ and $CD8^+$ subsets. The $CD45^-$ population comprised $CD31^+$ endothelial cells and $PDPN^+$ synovial fibroblasts. Data analysis was performed using Sony ID7000 software. *N*=2; one representative example is shown. Adapted from Edalat et al., 2024, already published data.

3.4 Synovial Mφ exhibit E. coli Particle Binding Capacity. A Pilot Experiment for Functional Analysis of Human Tissue Mφ.

As part of our continued work using *Discoverer Mφ*-based immunophenotyping of primary human synovial structural cells and Mφ, we performed a pilot assay aimed at incorporating functional phagocytosis readouts into ex vivo synovial cell analysis. Fresh synovial cells were isolated from

joint tissue obtained during total joint replacement surgery from two RA patients. Cells were immediately stained with antibody panels, incubated for 30 minutes at 37°C with *pHrodo™ Green*-labeled *E. coli* bioparticles at a 1:10 cell-to-particle ratio, and analyzed using a Sony ID7000 spectral flow cytometer.

$CD45^+CD14^+$ Mφ were seeded directly into plates and fed with particles immediately after isolation, without a pre-adherence phase. This likely limited their ability to attach to the well surface and form a stable cytoskeletal architecture conducive to phagocytosis. Additionally, the *pHrodo™ Green* bioparticles were not removed by washing prior to cytometric analysis. This prevented the exclusion of free or loosely associated beads and made it difficult to distinguish true internalization events from external attachment, especially in highly adhesive structural cell populations.

Indeed, fluorescence signal analysis showed minimal *pHrodo™ Green* signal in $CD45^+CD14^-$ leukocytes (Figure 3-30b, purple) as compared to the no- E.coli particles control (Figure 3-30a), consistent with their expected low phagocytic capacity. In $CD45^-CD14^-$ cells (Figure 3-30b blue) FLS, higher pHrodoGreen signal was detected. However, based on FSC/SSC characteristics and the known adhesive nature of FLS, we suspect this signal reflects non-specific adhesion and/or bead aggregation within the structural cell gate, rather than active uptake. Signal intensity in this population did not exceed 10^5 fluorescence units.

The subset of $CD45^+CD14^+$ Mφ exhibited elevated *pHrodo™ Green* fluorescence (between 10^4 to 10^5 units), indicating likely particle internalization. This supports some functional activity in the Mφ compartment. However, Mφ without pHrodoE.coli particles already display high fluorescence intensity, which indicated high autofluorescence of Mφ interfering with pHrodoGreen signal. Additionally, the overall magnitude and frequency of this response were lower than expected.

Several factors contributed to this reduced phagocytic readout. First, a pronounced shift in cell viability was observed across the entire sample, suggesting compromised cell health during isolation or incubation, which may have impaired overall functional responsiveness. Second, as mentioned, Mφ were not given time to adhere before exposure to particles, potentially affecting uptake. Third, the short 30-minute incubation window may have captured only early particle binding stages, potentially missing later internalization and acidification phases, especially given that the precise timing of signal acquisition relative to incubation completion was not tightly controlled. Fourth, due to the low number of viable cells retrieved from RA synovial tissue, it was not feasible to run parallel experimental conditions or include appropriate technical controls (e.g., time-course, wash vs. no-wash, or viability-enhancing conditions). This underscores the exploratory nature of the study.

Finally, the use of synovial tissue from RA patients, whose Mφ may exhibit chronic activation, phenotypic skewing, or impaired phagocytic capacity, adds an important biological variable. RA-associated inflammation has been shown to alter Mφ function, which may further explain the limited response observed here. Therefore, while this pilot study demonstrates conceptual feasibility of integrating functional readouts into spectral cytometry-based immunophenotyping, it also highlights key technical and biological limitations.

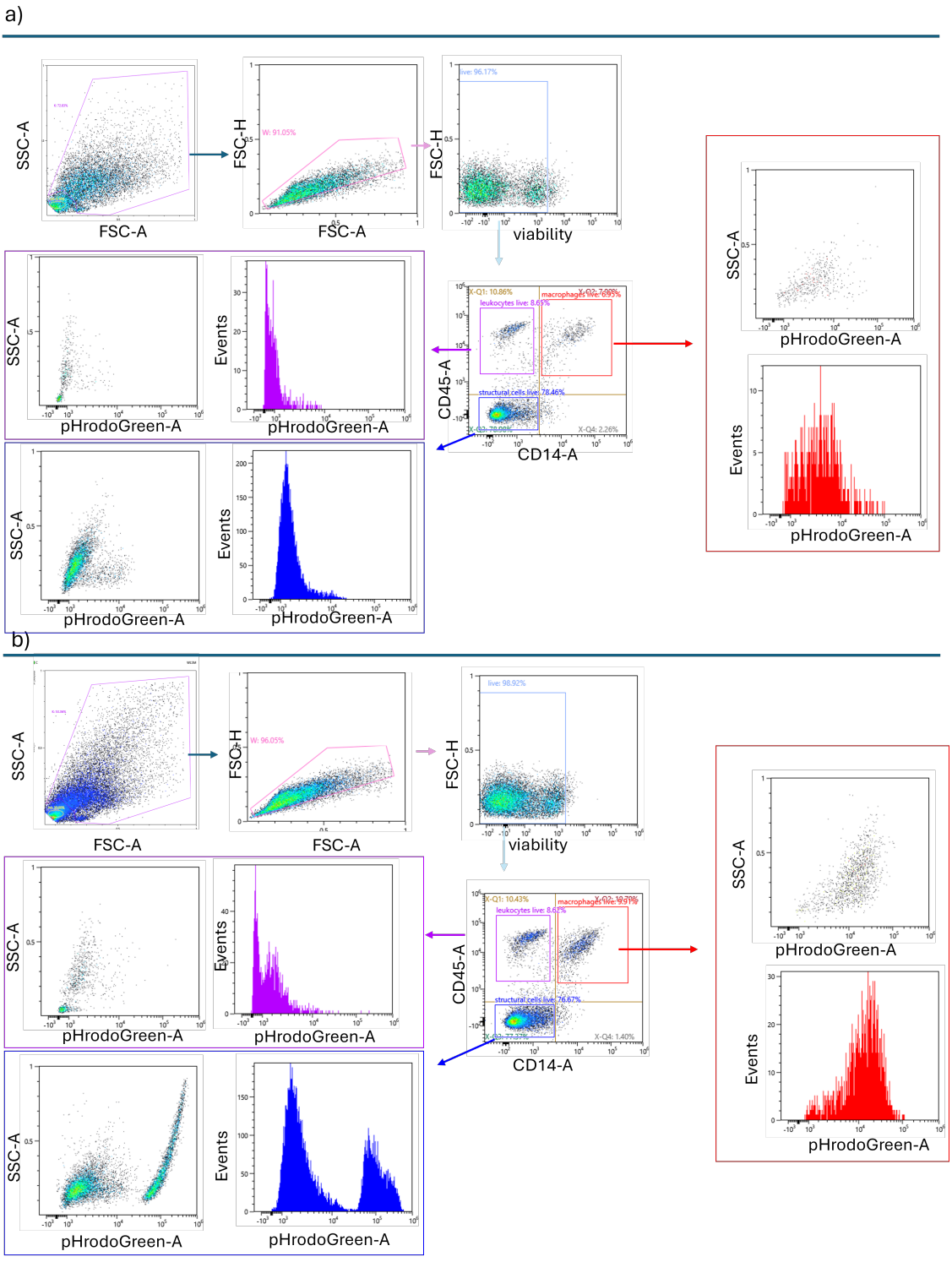

Figure 3-30 Pilot spectral flow cytometry analysis of synovial macrophages in RA synovium to assess phagocytic capacity using *Discoverer Mφ*. Total live, unsorted synovial cells from rheumatoid arthritis (RA) patients were analyzed. Following pre-labeling with surface antibody panels and washing, *pHrodo™ Green E. coli* bioparticles were co-incubated with the cells at 37 °C for 30 minutes. Samples were then immediately analyzed on a SONY ID7000 spectral flow cytometer. Debris, doublets, and dead cells were excluded through forward and side scatter (FSC/SSC) gating, singlet discrimination, and Zombie NIR viability staining. a) Negative control condition: no *pHrodo™ Green* bioparticles added, used to establish baseline fluorescence. b) Phagocytosis condition: *pHrodo™ Green E. coli* bioparticles were added to assess uptake. Live Zombie NIR-negative synovial cells were gated based on CD45 and CD14 expressions to identify three major populations: $CD45^-$ structural cells (blue), $CD45^+CD14^+$ macrophages (red), and $CD45^+CD14^-$ non-macrophage leukocytes (purple). All three populations were subsequently plotted for their *pHrodo™ Green* fluorescence intensity to assess bioparticle uptake.

3.4.1.1 Experimental Considerations and Planned Refinements

To address these limitations and improve assay robustness, we propose the following optimizations for future experiments:

1. **Macrophage Pre-Adherence**
   Allow $CD45^+CD14^+$ macrophages to adhere for 1–2 hours prior to bioparticle incubation to better mimic physiological conditions and promote functional uptake.
2. **Wash Step Post-Incubation**
   Introduce gentle washing after incubation to remove unbound beads, reduce background noise, and clarify signal specificity.
3. **Time-Course Analysis with Controlled Readout**
   Implement precise readout timing and analyze additional timepoints (e.g., 15, 30, 60, 120 minutes) to differentiate early binding from later internalization and acidification phases
4. **Bead-Only Controls and FSC/SSC Calibration**
   Include bead-only controls and monitor scatter profiles to detect and gate out bead aggregates, particularly within $CD45^-$ structural cell gates.
5. **Enhanced Structural Cell Phenotyping**
   Use additional markers (e.g., CD90 or PDNP) to more precisely identify and gate fibroblast-like synoviocytes.
6. **Viability Optimization**
   Modify tissue digestion, reduce manipulation time, and potentially include survival factors to preserve the viability and functionality of isolated cells.
7. **Healthy Donor Synovial Tissue**
   Include synovial samples from healthy or non-inflammatory donors (e.g., trauma or OA patients) to establish baseline phagocytic performance, distinguish disease-related defects, and validate the assay.
8. **Positive Control Cell Lines**
   Use phagocytosis-competent controls (e.g., our established iMφ) to benchmark assay performance and interpret signal ranges.
9. **Cell Enrichment or Pooling**
   Enrich for macrophage populations or pool tissue from multiple donors to increase viable cell numbers and enable parallel experimental conditions.

This pilot study provides critical technical and biological insights for the development of a synovial phagocytosis assay. While some functional activity was observed in Mφ, the experimental limitations, including lack of adherence time, absence of bead removal, low cell viability, short incubation duration, and disease-altered cell functionality, collectively limited the robustness of the data. Future iterations incorporating the outlined refinements will improve assay specificity and reliability, supporting a deeper investigation of phagocytic function in synMφ across health and disease.

3.5 Discoverer Mφ Uncovers Iron Metabolism in Fresh RA Synovial Mφ

CITE-seq analysis uncovered that various synMφ subsets display distinct gene expression profiles related to iron metabolism. As illustrated in Figure 3-31a, trMφ characterized by high levels

of FOLR2, MERTK, and SLC40A1, formed one cluster, while a separate group marked by low FOLR2, high TREM2, and elevated SPP expression showed the strongest expression of SLC40A1, the gene encoding the iron exporter ferroportin. Conversely, tiMφ expressing CCR2, IL1B, and SLC11A1, or alternatively, CCR2-negative and CLEC10A-positive cells, displayed the lowest SLC40A1 expression. In contrast, SLC11A1, which codes for the iron importer DMT1, was most abundantly expressed in tiMφ and minimally expressed in trMφ, suggesting an inverse relationship in iron import/export regulation among these Mφ populations.

To support these transcriptomic observations with protein-level and functional evidence, multispectral flow cytometry was employed using paired synovial cell suspensions from rheumatoid arthritis (RA) patients. These were the same donor tissues utilized in parallel phagocytosis assays (presented in Figure 3-30). Mφ were identified as $CD45^+CD14^+$ and further categorized based on CCR2 and FOLR2 surface expression. In contrast to OA synovium, RA samples showed a predominance of $CCR2^+$ Mφ. These are segregated into $CCR2^+FOLR2^-$ tiMφ (comprising roughly 21.2% of Mφ) and a $CCR2^+FOLR2^+$ double-positive subset (approximately 44%), the latter representing an intermediate phenotype. Notably, the proportion of $FOLR2^+CCR2^-$ trMφ was significantly lower in RA samples compared to OA donors (14%).

Iron transporter expression and labile Fe^{2+} levels were next examined within $CCR2^+FOLR2^+$ and $CCR2^+FOLR2^-$ subpopulations (Figure 3-31b). As presented in Figure 3-31c, the $CCR2^+FOLR2^+$ subset exhibited slightly higher surface expression of SLC40A1 and reduced levels of CD71 (transferrin receptor), mirroring gene expression data. However, the overall expression is quite low, which becomes obvious when comparing total stained cells to the unstained control (Figure 3-31d). When labile intracellular Fe^{2+} was assessed using a far-red iron-sensitive dye after ferric ammonium sulfate (FAS) treatment, both subsets showed similar Fe^{2+} levels, with a slight increase observed in the $FOLR2^+$ group. However, due to the small number of events captured, these findings are considered preliminary and will need validation in future experiments with additional synovial samples.

Overall, this proof-of-concept study highlights the capacity of the *Discoverer Mφ* platform to simultaneously assess labile intracellular iron content and phenotype-specific expression of iron-handling proteins in defined Mφ subsets.

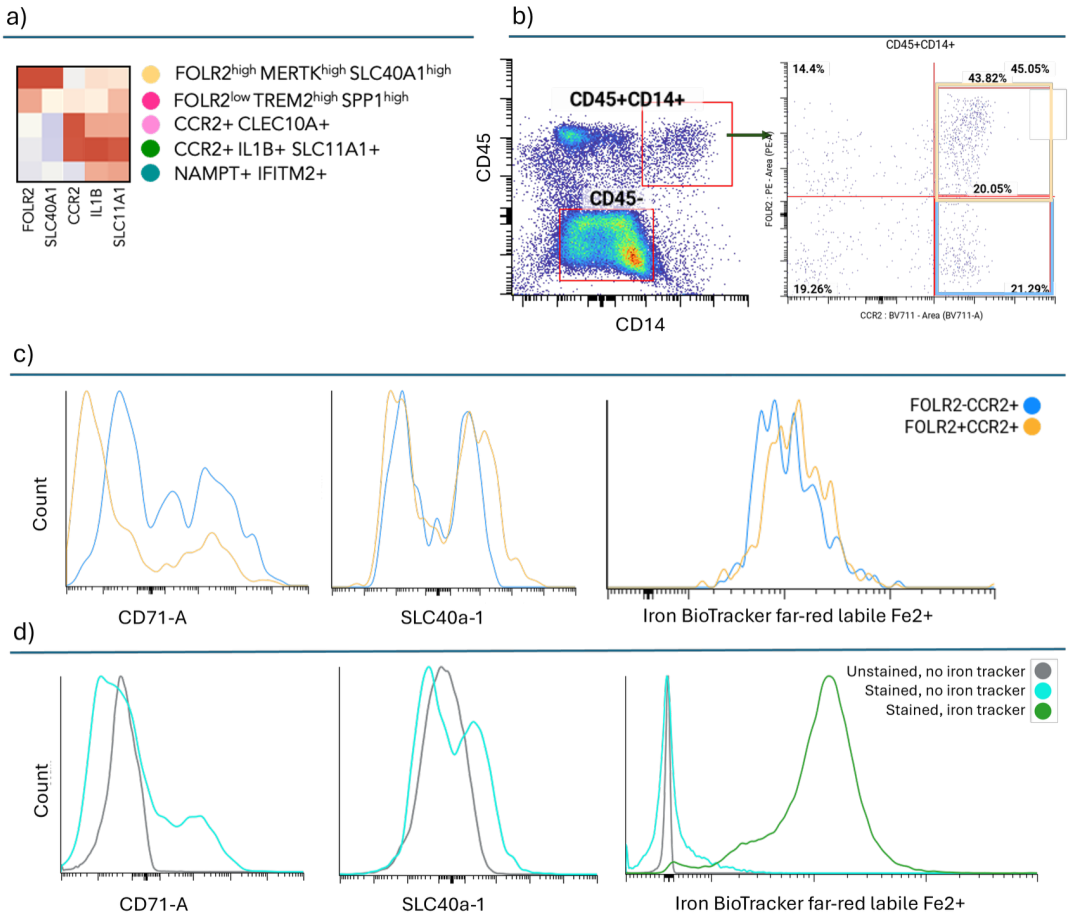

Figure 3-31 Iron transporter expression and labile iron content of synovial macrophages derived from RA synovium.

a) CITE-seq analysis of synovial macrophage subsets reveals distinct expression patterns of iron metabolism–related genes. b–d) Pilot spectral flow cytometry assessment of intracellular Fe^{2+} levels and iron transporter expression in synovial macrophages from RA patients using the DISCOVERER Mφ platform. Live, unsorted synovial cells were isolated from rheumatoid arthritis (RA) patient samples. Following surface staining with an iron-related antibody panel and washing, cells were treated with ferric ammonium sulfate (FAS) and then incubated with an iron tracker dye. Samples were immediately analyzed on a SONY ID7000 spectral flow cytometer. Debris, doublets, and dead cells were excluded using FSC/SSC gating, singlet discrimination, and Zombie NIR viability staining (n = 2). b) Macrophages were identified as $CD45^{+}CD14^{+}$ cells and further subdivided into $CCR2^{+}FOLR2^{+}$ and $CCR2^{+}FOLR2^{-}$ subsets. c) Comparative histograms showing surface expression of CD71 (transferrin receptor; iron importer) and SLC40A1 (ferroportin; iron exporter) between $FOLR2^{+}CCR2^{+}$ (orange) and $FOLR2^{-}CCR2^{+}$ (blue) macrophage populations. d) Histograms from doublet-excluded cell populations comparing: unstained total synovial cells (grey), stained synovial cells without FAS or tracker (turquoise), and stained cells treated with FAS and iron tracker (green), to assess transporter expression and iron tracker signal. Data acquisition was performed using the SONY ID7000; spectral unmixing and autofluorescence compensation were carried out using SONY ID7000 software, and downstream analysis was completed in CellEngine.

3.5.1 Synovial Fluid Mφ Suitable to Deepen Functional and Phenotypic Knowledge

For future functional analyses on primary human synMφ we will use synovial fluid samples in addition to synovial tissue samples from patients with various types of arthritis. Given the challenges in obtaining synovial tissue, we aimed to fine-tune the *Discoverer Mφ* assay for application on more accessible synovial fluid samples. Synovial fluid cells were collected, aliquoted, and cryopreserved with viability at two international rheumatology centers: University Medical Centre

Ljubljana, Department of Rheumatology, Ljubljana, Slovenia and Gulbenkian Institute for Molecular Medicine, Rheumatology Department, Lisbon, Portugal (see Table 2-9 for patient characteristics).

Our experimental design comprised the following sequential steps:

1. Optimization of synovial fluid cell preparation for spectral flow cytometry.
2. Immunophenotyping of synovial fluid samples to identify macrophage-containing samples.
3. Application of the *Discoverer Mφ* assay to perform combined immunophenotype-function analysis of synovial fluid macrophages.

In the initial experiment, we selected synovial fluid cells from three patients with Polyarthritis (Patient group 1) chronic erosive arthritis (patient group 2) and known hip osteoarthritis (patient group 3). Cells were thawed and processed into single-cell suspensions using hyaluronidase and DNase I. To identify appropriate patient groups for functional studies, samples from one, two and three were analyzed.

Multispectral flow cytometry revealed that synovial fluid cells predominantly comprised $CD45^+$ leukocytes, with a smaller fraction of $CD45^-$ cells likely representing synovial structural cells. The composition of leukocyte populations varied between the three donors. Notably, Patient Group 3 exhibited the highest proportion of leukocytes. Across all patient groups, neutrophils were the most abundant leukocyte subtype, identified as CD15+ cells.

When comparing leukocyte subsets, synovial fluid from Patient Group 3 with OA displayed the highest frequency of $CD45^+CD14^+$ Mφ (Figure 3-32a). Further analysis revealed that this patient also exhibited the highest abundance of $CCR2^+FOLR2^-$ Mφs (Figure 3-32b).

These results demonstrate that the *Discoverer Mφ* assay effectively enables detailed immunophenotyping of synovial fluid cells and highlights substantial inter-donor variability in both total leukocyte composition and Mφ subsets.

Based on these findings, samples from Patient Group 3 will be prioritized for future functional analyses. We are currently expanding synovial fluid analyses across our collected cohort and concurrently optimizing functional readouts on samples enriched in Mφ.

Once fine-tuned, the *Discoverer Mφ* assay will be used for combined functional and immunophenotypic analyses of synovial Mφ from both fluid and tissue sources. These analyses will cover

key macrophage functions, including phagocytosis, efferocytosis, and iron metabolism, with the goal of building a comprehensive function-phenotype map of synovial Mφ in human joints.

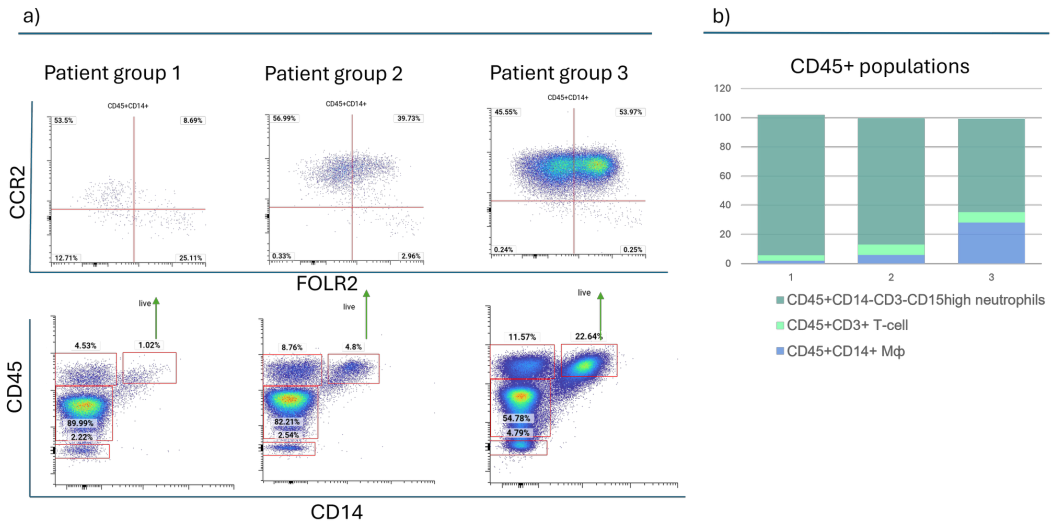

Figure 3-32 Pilot immunophenotyping analysis of human synovial fluid cells from arthritis patients using the *Discover Mφ* assay and spectral flow cytometry. Viable synovial fluid cells were thawed and enzymatically treated with hyaluronidase and DNase I to generate single-cell suspensions. Cells were subsequently labeled with a multidimensional antibody panel for spectral flow cytometry-based immunophenotyping. a) Gating strategy used to identify major synovial fluid cell populations. CD45 and CD14 expression were used to distinguish leukocytes ($CD45^+$), monocytes/macrophages ($CD45^+CD14^+$), and $CD45^-$ structural cells. Further discrimination of macrophage subsets was achieved using CCR2 and FOLR2, allowing the identification of infiltrating monocytes/macrophages ($CCR2^+FOLR2^-$) and tissue-resident macrophages ($CCR2^-FOLR2^+$). Additional details on the gating strategy are provided in [Appendix M]. b) Distribution of immune cell populations within the $CD45^+$ leukocyte compartment across synovial fluid samples from three donors (N = 3; donor characteristics in Table 2-9). $CD45^{high}CD14^+$ monocytes/macrophages are indicated in blue, CD45highCD14$^-$ $CD3^+$ T cells in light green, and $CD45^{med}$ $CD14^-$ $CD3^-$ $CD15^{high}$ neutrophils in dark green. Representative CD3 and CD15 expression plots are shown in Appendix 6-9.

3.6 Summary

The *Discoverer Mφ a*ssay is a versatile, medium -throughput platform that enables simultaneous analysis of Mφ phenotypes and functions within a single 96-well plate, supporting unbiased and targeted studies across tissues and disease models, facilitating mechanistic insights, CRISPR screen optimization, and multi-omics integration, while remaining adaptable for applications beyond Mφ research (Figure 3-33).

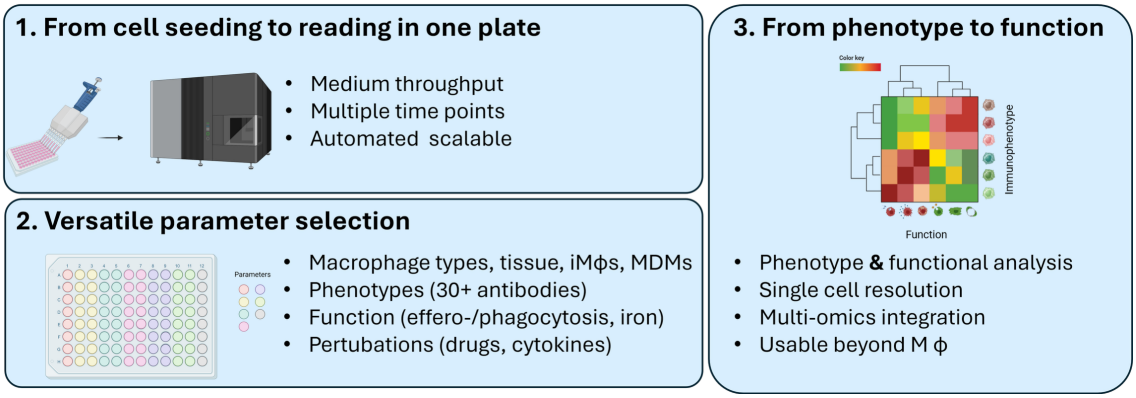

Figure 3-33 Discoverer Mφ summary

4. Discussion

4.1 Overview / Summary of Key Findings

In my PhD thesis, I developed and validated *Discoverer Mφ*, a novel spectral flow cytometry-based assay that enables integrated phenotypic and functional analysis of Mφ, with a focus on Mφ tissue clearing and homeostatic functions, including efferocytosis, phagocytosis, and iron metabolism-linked readouts.

By enabling the simultaneous analysis of Mφ functions and surface markers, *Discoverer Mφ* bridges the current methodological gap in assigning functions to distinct human Mφ populations identified through single-cell omics approaches. Conversely, *Discoverer Mφ* enables an unbiased functional classification of human Mφ across a range of functions, followed by the identification of functionally divergent subsets through surface marker signatures.

It is reasonable to consider that different Mφ subsets exhibit a continuum of capacities for a given function, potentially ranging from minimally to maximally capable of performing that function. As a direct consequence, distinct primary or in vitro-generated Mφ subsets will serve as more-or-less suitable models for gain or loss-of-function perturbation experiments, whether genetic (CRISPR) or drug-based. My experiments demonstrated that *Discoverer Mφ* can successfully guide the selection of suitable Mφ models for a given function readout and gain/loss of function experiments. Specifically, iMφ exhibited superior efferocytosis capacity compared to M2- polarized MDMs, while M1-polarized MDMs were not efferocyting. Furthermore, iMφ robustly expressed the canonical efferocytosis receptors, such as MERTK and TIMD-4, which were not or minimally detectable in M1-polarized MDMs. This indicated that iMφ closely mimicked trMφ phenotype, which is consistent with transcriptomic studies and the stem cell origin of iMφ (Lee et al., 2018; Ginhoux & Guilliams, 2016). Furthermore, this study demonstrates that iMφ are well-suited for efferocytosis inhibition assays. Using the *Discoverer Mφ* platform, I observed a robust and reproducible reduction in efferocytic capacity in response to treatments with inhibitors previously described in the literature. Conversely, preliminary data from pilot studies using iMicroglia suggest that microglia exhibit a comparatively lower baseline efferocytic activity than iMφ, indicating their potential utility in gain-of-function efferocytosis studies. Taken together, the *Discoverer Mφ* platform is well-positioned to support both gain and loss-of-function approaches for dissecting the molecular mechanisms governing efferocytosis.

The *Discoverer Mφ* platform enables precise optimization of complex experimental conditions, making it particularly well-suited for phenotypic and functional CRISPR screening in Mφ. By systematically refining key assay parameters, such as the incubation time between Mφ and apoptotic cells, as well as optimizing pHrodo-Green labeling conditions for maximal peak separation, I was able to enhance assay sensitivity. These adjustments allowed for the detection of even subtle changes in pHrodo-Green fluorescence intensity, thereby ensuring that the efferocytosis assay is robust and sensitive enough to support high-resolution CRISPR-based perturbation studies.

Furthermore, *Discoverer Mφ* facilitates functional characterization of primary synMφ from RA patients, aligning with single-cell transcriptomic evidence of pro-resolving and inflammatory Mφ populations (Alivernini et al., 2020; Culemann et al., 2019).

A key strength of the *Discovery Mφ* assay lies in its flexible, modular antibody panel, which can be easily adapted to suit diverse biological questions. Designed for spectral flow cytometry principles, the panel balances low spillover, minimal complexity, and sufficient spectral space to include functional probes (e.g., pHrodoGreen for efferocytosis, iron-sensitive dyes like IronTracker for labile iron tracking). This tunability allows rapid repositioning of markers to explore specific axes of Mφ biology, such as co-staining for iron metabolism-related transporters (e.g., TFR1, FPN, DMT1) or immune resolution markers linked to efferocytosis (e.g., MERTK, AXL, TIMD4). The panel's versatility extends beyond Mφ. Its structure can accommodate markers for other myeloid cells, stromal cells, and even tumor cells, enabling multiparametric analysis of cellular interactions within complex co-culture or tissue-derived systems. Moreover, the use of fluorochrome-efficient marker choices and scalable gating strategies enables live cell sorting of phenotypically and functionally defined subpopulations. These sorted subsets can then be subjected to targeted downstream analyses, such as bulk or single-cell RNA-seq, proteomics, or metabolic assays, offering a bridge between surface phenotype, functional state, and molecular signature.

4.2 Comparison with Existing Methods and Findings

Current functional assays for phagocytosis and efferocytosis largely rely on simplified assays, based on pHrodo-labeled particles and apoptotic cells, often analyzed via confocal microscopy or bulk flow cytometry (Clark et al., 2019). While these methods provide basic uptake data, they fall short in providing multiplexed readouts that can identify which Mφ subsets are functionally active.

Bravo et al. (2023) and Clark et al. (2019) used high-content imaging and Incucyte platforms to monitor efferocytosis in real time; however, these methods lacked phenotypic resolution and provided limited kinetic precision. I initially explored similar experimental approaches, including tracking efferocytosis tracking using the Incucyte system and conventional flow cytometry based on pHrodoGreen fluorescence increase. These experiments were stopped because of their insufficient sensitivity and temporal resolution for capturing the nuanced dynamics of efferocytosis robustly measured in *Discoverer Mφ*. Similarly, Stöhr et al. (2018) introduced Annexin A5-pHrodo, to label apoptotic cells to track efferocytosis as a more physiological probe, yet these approaches are typically limited to single-endpoint analysis and cannot deconvolve the heterogeneity within Mφ populations.

Discoverer Mφ advances the field by integrating dynamic functional analysis with surface marker profiling using spectral flow cytometry. This allows real-time analysis of Mφ functions (e.g. efferocytosis) while also capturing protein marker expression patterns that define efferocytosis-competent subsets (e.g., $MERTK^{+}CD206^{+}$). Moreover, the optimization of "eating" and "removal" times enables kinetic resolution, which is often missing from static assays. To my best knowledge, *Discoverer Mφ* is the first assay to combine subset-level resolution with functional readouts across multiple Mφ platforms, including iMφ, MDMs, and ex vivo primary human tissue Mφ. This assay is also broadly re-purposable to other cell types and other fluorescence-linked function readouts.

4.3 Implications for Macrophage Biology

My research provides critical functional validation of Mφ traits that have previously been inferred from single-cell transcriptomic analyses. For instance, the study by Alivernini et al. (2020) identified a subset of $CD206^{+}MerTK^{+}$ Mφ that predominated in healthy and remission-phase RA synovial tissue, as opposed to inflamed tissue. These Mφ were characterized as pro-resolving, enriched for phagocytic and efferocytic gene signatures, and expressed key markers such as TIMD4, CD163, AXL, MERTK, and Gas6.

Consistent with these transcriptomic insights, I observed high surface expression of MerTK and other efferocytosis-associated markers (e.g., CD206, TIMD-4) in $FOLR2^{+}$ tissue-resident synovial Mφ derived from osteoarthritic (OA) synovium. To functionally validate these observations, I employed the *Discovery Mφ* assay using iMφ, which confirmed robust expression of key phagocytic and efferocytic markers, including the $MerTK^{+}CD206^{+}$ described by Alivernini et al. Together with TIMD4, TREM2, FOLR2, CD163 phenotypes. Moreover, the higher efferocytic activity of iMφ correlates with their enhanced expression of receptors such as MerTK, CD206 and TIMD-4, known regulators of apoptotic cell clearance (Zhou et al., 2021; Park et al., 2015). Importantly, these $MerTK^{+}CD206^{+}$ iMφ demonstrated the highest efferocytic capacity in vitro, surpassing monocyte-derived macrophages (MDMs) in both M1 and M2-like polarizations in performance. MDMs polarized toward an M1-like state exhibited a markedly different profile: they lacked expression of FOLR2 and CD206, displayed minimal to no efferocytosis, and instead showed a pro-inflammatory surface signature, including upregulation of CD48, CD80, and CD86.

These results begin to bridge the gap between phenotypic identity and functional behavior, highlighting the importance of subset-specific efferocytosis capacity in Mφ biology.

The inclusion of iron metabolism-linked signature in *Discoverer Mφ* further adds a critical dimension to understanding homeostatic Mφ functions. Mφ are central to systemic and local iron homeostasis, and dysregulated iron metabolism is a feature of many inflammatory and malignant diseases (Soares & Hamza, 2016; Winn et al., 2020). Our findings show that iron-linked transporters and intracellular labile Fe2+ concentrations (upon exposing Mφ to iron reach environment) vary across differentially polarized monocyte-derived Mφ. These results suggest that functional iron-handling capacity might differ among distinct primary human Mφ subsets whose characteristics can be partially replicated with distinct *in vitro* polarized Mφ states. Indeed, our scRNAseq data from human synovial tissues in remission and active, treatment naïve/inadequately responding RA, show that synovial $FOLR2^{high}$ $MERTK^{high}$ tissue resident and CCR2 IL1b infiltrating Mφ are differentially enriched in the expression of iron-linked transporters, including SLC40A1, CD163 and SLC11A1. To further scRNA-seq data, we conducted pilot spectral flow cytometry experiments in synovial Mφ from synovial tissues, obtained from two RA and one OA patient undergoing joint replacement surgery. These data demonstrate that $FOLR2^{+}$ subsets exhibit higher expression of SLC40A1 compared to their $FOLR2^{-}$ counterparts. Conversely, CD71 (TFRC) expression appeared to be elevated in the $FOLR2^{-}$ subset. Due to the phagosomal localization of SLC11A1 in Mφ, it was not feasible to validate its expression using the *Discoverer Mφ* platform. Unfortunately, no suitable antibody was available for SLC11A2 (DMT1), a closely related transporter to SLC11A1, which is expressed on the plasma membrane and mediates the uptake of non-transferrin-bound iron.

Regarding CD163 and CD91, no significant differences in expression were observed between subsets. However, the low frequency of Mφ populations within the RA synovium may have limited our ability to detect potential differences, likely due to insufficient cell numbers.

Thus, *Discoverer Mφ* provides a novel functional validation to single-cell transcriptomic data from synovial tissue in inflammatory arthritis (Edalat et al., 2024; Tański et al., 2021), and can facilitate studies on the role of iron dysregulation in chronic inflammation and autoimmunity.

4.4 Application to Disease Models: RA and Beyond

4.4.1 Discoverer Mφ in fresh OA and RA tissue

In RA, Mφ contribute to chronic inflammation in the synovial tissue. Specifically, inflamed synovial tissues are characterized by an overrepresentation of pro-inflammatory tissue-infiltrating tiMφ, and a depletion or dysfunction of trMφ (McInnes & Schett, 2011; Alivernini et al., 2020).

Alivernini et al. (2020) utilized scRNAseq to identify transcriptionally distinct Mφ populations in RA synovial tissues across different arthritis activity states. MerTK^{+}CD206^{+} Mφ were enriched in efferocytosis-related genes (e.g., MerTK, Axl, Timd4, Gas6) and regulatory markers (e.g., VSIG4, NR4A2) and were associated with maintenance of clinical remission, while inflammatory CCR2^{+} Mφ (MerTK^{-}CD206^{-}) predominated in active disease. By analyzing immunophenotypes of synovial Mφ with spectral flow cytometry, I demonstrated the presence of tissue-resident-FOLR2+CCR2-, “transitional” FOLR2+CCR2-, and infiltrating CCR2+FOLR2- Mφ subsets in synovial samples from OA and RA patients. In line with published studies, OA synovial sample was dominated by FOLR2+ Mφ, and RA synovia were populated by FOLR2+CCR2- and CCR2+FOLR2- Mφ. Combined efferocytosis and immunophenotyping experiments on synovial Mφ are beyond the scope of this PhD thesis but within the scope of my post-PhD project. However, my results showed that FOLR2^{high}, CCR2^{neg} CD206^{high} MERTK^{+} tissue resident-like iMφ exhibit near maximal efferocytosis capacity under our experimental conditions, whereas CCR2^{high}, FOLR2^{neg} CD206^{low} MERTK^{neg} infiltrating-like M1-polarized MDMs do not efferocyte. These findings support the hypothesis that defective apoptotic cell clearance by inflammatory Mφ subsets contributes to the persistence of inflammation in RA (Sangaletti et al., 2021; Mehrotra & Ravichandran, 2022).

Linking efferocytosis capacity with Mφ subsets in active RA and remission, could identify Mφ subsets as targets for efferocytosis-facilitating therapies. In RA, unresolved inflammation results in continuous neutrophil recruitment, antigen presentation, and tissue destruction. Improving efferocytosis, especially in specific Mφ subsets, could help restore resolution pathways and break the cycle of chronic inflammation. Candidate drugs enhancing MERTK signaling, specialized lipid mediator (e.g. resolvin) secretion or efferocytosis, e.g., efferocytosis-targeting nanoparticles (Kraynak et al., 2022), could be tested using *Discoverer Mφ* or could be evaluated to assess efferocytosis capacity at the whole population as well as Mφ subset level.

In addition to efferocytosis, the capability of *Discoverer Mφ* to measure iron metabolism-linked readouts can provide further insight into RA pathophysiology. Disrupted Mφ iron handling contributes to synovial inflammation, oxidative stress, and systemic hypoferremia seen in anemia of chronic disease (Tański et al., 2021; Soares & Hamza, 2016). By measuring surface expression of iron transporters (e.g., Ferroportin, CD71), my data support the notion that iron metabolism is

skewed in disease-associated Mφ, and that this skewing is subset-specific. Recent research evidence linked ferroptosis and iron dysregulation to RA progression and immune cell dysfunction (Liu et al., 2024).

Beyond its relevance to autoimmune diseases, *Discoverer Mφ* also offers promising applications in the cancer field, particularly in understanding Mφ-tumor interactions. In this context, I evaluated the platform's suitability for quantifying the engulfment of UV-irradiated pHrodoGreen-labelled apoptotic glioblastoma cells into iPSC-derived microglia (iMicroglia). The results demonstrated a modest but distinct increase in pHrodoGreen fluorescence in Microglia compared to Cytochalasin D-treated iMicroglia and engulfment of JTs targets, suggesting a preferential uptake of glioblastoma cells by iMicroglia.

This observation hints at a possible cell target specificity of efferocytosis responses by tissue-adapted Mφ or microglia, aligning with previous findings in taMφ and their selective interactions with apoptotic tumor cells. For instance, Qiu et al. (2023) and Astuti et al. (2024) demonstrated that efferocytosis of apoptotic tumor cells can drive Mφ reprogramming toward an immunosuppressive, tumor-promoting phenotype. The enhanced uptake of glioblastoma cells observed in my experiments may reflect early stages of this reprogramming process, consistent with the immunosuppressive polarization reported in TAMs in glioblastoma and other solid tumors (Cendrowicz et al., 2021).

Moreover, this result connects to the broader concept demonstrated in the Introduction: while efferocytosis is a pro-resolving mechanism in inflammatory diseases, in cancer, it can paradoxically support immune evasion and resistance of cancer to therapy. Galluzzi et al. (2021) and Morana et al. (2022) highlighted that signals derived from apoptotic tumor cells can skew Mφ function, particularly when efferocytosis is coupled with release of tolerogenic mediators such as IL-10 or expression of checkpoints like MerTK, which can be tested in future research applying *Discoverer Mφ.*

By enabling the functional quantification of such interactions, *Discoverer Mφ* provides a powerful platform to dissect the specificity, magnitude, and downstream consequences of cancer cell engulfment across Mφ subsets. This capability could be extended to co-culture systems, therapeutic testing (e.g., MerTK or AXL inhibitors), or engineered iMicroglia/iMφ models to better understand TAM plasticity in the glioblastoma/cancer microenvironment.

Moreover, iron metabolism is increasingly implicated in cancer progression and therapy resistance (Candelaria et al., 2021). By enabling functional detection of iron export and uptake in Mφ with simultaneous iron transporter analysis, Discoverer *Mφ* paves the path to investigate taMφ iron metabolism in the tumor niche, an area currently under explored.

4.4.2 Transcriptomic Profiling of Synovial Macrophage Subsets

To complement phenotypic and functional analyses, transcriptomic profiling was performed on sorted synMφ subsets using bulk RNA sequencing. This provided deeper molecular insights into the Mφ compartment in RA, validated marker-based gating strategies, and contextualized functional potential across subsets.

We have combined CITE-sequencing (scRNA-seq + antibody-derived tag (ADT) profiling) and spectral flow cytometry-based surface marker phenotyping to build a high-resolution map of Mφ heterogeneity in the synovial tissue microenvironment of actively inflamed and quiescent RA joints. The CITE-seq map contains 167,000 synovial single-cell profiles, with a primary focus on

myeloid and structural synovial cell populations. Structural cells included fibroblast-like synoviocytes, endothelial cells, and mural cells/pericytes, whereas the myeloid compartment consisted of diverse Mφ subsets and IFITM2^{+}NAMPT^{+} neutrophils. These neutrophils, also observed in Edalat et al. (2024), represent a specialized, previously under characterized, IFITM^{+} population enriched in inflamed tissue.

Utilizing scRNA-seq profiles, we identified four distinct Mφ subclusters, accompanied by a separate cluster of IFITM2^{+}NAMPT^{+} neutrophils. Within the Mφ compartment, a key distinction emerged between FOLR2^{+} trMφs and infiltrating CCR2^{+} Mφ. Two FOLR2^{+} subsets were observed: one expressing FOLR2^{high}, MERTK^{high}, and SLC40A^{high}, and another FOLR2^{low}, TREM2^{high}, and SPP1^{+}. Likewise, two CCR2^{+} subsets were defined: CCR2^{+}CLEC10A^{+} and CCR2^{+}IL1B^{+}SLC11A1^{+}. Interestingly, the CCR2^{+}CLEC10A^{+} subset displayed a transcriptional profile distinct from the CCR2^{+}IL1B^{+}SLC11A1^{+} cluster. In particular the CLEC10A expression, has recently been linked to a monocyte population of monocyte-dendritic cell progenitor (MDP) origin in mice, characterized by enhanced antigen presentation and DC-like features (Trzebanski et al., 2024). In contrast to granulocyte derived CCR2^{+} monocytes, which are primed for inflammatory responses, this paper shows that MDP-derived CLEC10A^{+} monocytes exhibited regulatory or tolerogenic potential and were shown to seed specific trMφ populations under steady-state and post-inflammatory conditions. The presence of this subset in synovial tissue suggests that monocyte ontogeny may shape Mφ heterogeneity even within inflamed environments, potentially influencing the balance between inflammation and resolution. This ontogeny-aligned functional divergence may underlie distinct roles of CCR2^{+} Mφ subsets in synovitis and offers a conceptual framework for interpreting Mφ plasticity in tissue inflammation.

Gene expression analysis of these in silico-sorted Mφ subsets revealed that the FOLR2^{+} populations exhibited higher expression of genes associated with phagocytosis and efferocytosis (e.g., TIMD4, CD163, SRGN, CD14), as well as CX3CR1, consistent with a tissue-patrolling, homeostatic role.

This pattern is consistent with earlier transcriptomic studies in RA and other forms of arthritis (Edalat et al., 2024; Alivernini et al., 2020; Zhang et al., 2023). Alivernini et al. identified nine phenotypically distinct Mφ clusters across 32,000 single-cell transcriptomes of synovial Mφ, which grouped into four core subpopulations: FOLR2^{high}, TREM2^{high}, HLA^{high}, and CD48^{high}. Of these, FOLR2^{high} and TREM2^{high} Mφ, which co-express MerTK and CD206, were enriched in patients in clinical and ultrasound-defined remission and exhibited signatures linked to lipid mediator biosynthesis, immune regulation (e.g., VSIG4, ALDH1A1), and fibroblast-supportive functions. Conversely, inflammatory MerTK^{neg}CD206^{neg} subsets, including SPP1^{+}CD48^{+} and ISG15^{+}HLA^{high}, dominated in treatment-naïve and refractory RA and were associated with antigen presentation, interferon response, and pro-inflammatory cytokine production.

These findings are further supported by our previously published study (Edalat et al., 2024), which applied integrated scRNA-seq to 25 synovial tissue samples from patients with various forms of inflammatory arthritis, revealing 12 distinct Mφ and myeloid DC subclusters. Notably, FOLR2^{high} subclusters in that dataset consistently expressed the highest levels of Mφ markers, including CD14, CD68, TREM2, CD163, TIMD4, MERTK, MRC1 (CD206), and CD209, markers typically associated with tissue-resident or homeostatic Mφ identities. This aligns closely with the current study's identification of FOLR2^{high}MERTK^{+} Mφ as a core tissue-resident population, further characterized by expression of the iron exporter SLC40A1 and a lack of CCR2 expression. Edalat et al. further defined functional modules of trMφ with iron recycling (LYVE1^{+}SLC40A1^{+}) and matrix sensing (FOLR2^{+}COLEC12^{high}) activities, underscoring their diversity and specialized functions.

Our transcriptomic analysis further reveals elevated expression levels of complement system genes (C1QA, C1QB, and C1QC) within FOLR2$^+$ cell subsets. These findings are consistent with those reported by Alivernini et al. (2021), who demonstrated increased expression of scavenger receptor and complement-associated genes, including C2, C1QA, C1QB, C1QC, CD59, DEFB1, and CFD, in MERTK$^+$ subsets.

The convergence of these findings across independent datasets strengthens the evidence for a dichotomy between resident and recruited macrophage lineages in RA synovium and reinforces the biological significance of FOLR2 and CCR2 as potential markers for functionally distinct Mφ phenotypes. Notably, Zhang et al. (2023) provided a comprehensive single-cell atlas of over 314,000 synovial cells, stratifying RA synovitis into six inflammatory phenotypes or cell-type abundance phenotypes, each characterized by distinct cellular compositions and enriched cell states. Their analysis highlighted the dynamic nature of synovial inflammation and the role of specific Mφ subsets, including MERTK$^+$HBEGF$^+$ and SPP1$^+$ Mφ, in defining particular inflammatory states such as CTAP-M. The SPP1$^+$ subset in particular overlapped with Alivernini's CD48^{high} Mφ, and was associated with NAMPT, IL1B, and TNFAIP6 expression. These insights reinforce the relevance of Mφ diversity in shaping the tissue microenvironment and predicting treatment response.

Also in our study, we applied ADT profiling. We selected antibodies based on Edalat's and Alivernini's findings. Protein expression studies confirmed several of the transcriptomic differences. Differential expression of FOLR2, CD163, CD74, CCR2, CD52, CD48, CX3CR1, and SPN (CD14) were robustly validated at the protein level. Matching protein expression profiles with scRNA seq maps revealed that FOLR2, CD74, CCR2 and CX3CR1 could be used to Flow Cytometry sort the four transcriptionally identified Mφ subsets, which could be utilized for downstream functional analysis of those subsets. However, we noted variability in antibody performance, as not all TotalSeq reagents yielded robust signals.

As described previously, we performed multi-spectral flow cytometric analysis of OA synovial cells. Multi-spectral cytometry confirmed elevated expression of CD14, CD68, TREM2, CD163, TIMD4, MERTK, MRC1 (CD206), and CD209 in the FOLR2$^+$ subpopulation, as well as increased levels of CD48 and CCR2 in the CCR2$^+$ inflammatory subset. These flow-based phenotypic findings independently validated our transcriptomic observations and supported a functionally distinct role for each Mφ subset in tissue homeostasis versus inflammation.

Together, these multi-omics findings support a refined model of synovial Mφ compartmentalization, where subsets are distinguished not only by surface phenotype and developmental origin but also by metabolic function, particularly in iron handling. This molecular stratification complements the functional profiling offered by *Discoverer Mφ*, providing a foundation for mechanistic investigations and therapeutic targeting of specific Mφ states in RA.

4.5 Technical Limitations and Challenges

While *Discoverer Mφ* represents a significant methodological advance in integrated Mφ phenotyping and functional profiling, several limitations must be acknowledged to contextualize its capabilities and guide future improvements.

First, the assay is based on an *in vitro* setup, which, although optimized for reproducibility and control, does not fully replicate the complexity of tissue environments. The absence of stromal and immune cell interactions, such as those provided by fibroblasts or T cells, limits the biological

context in which Mφ naturally operate. Paracrine signaling from these cell types is known to strongly influence Mφ behavior, and its absence may lead to oversimplified interpretations of efferocytic or iron-handling capacity.

A further limitation relates to the model apoptotic cells used in the assay. JTs were selected for their reproducibility and compatibility with pHrodo-based labeling. However, this model may not faithfully represent the heterogeneity of apoptotic cell signals in tissue, including differences in “eat-me” or “don’t-eat-me” markers and membrane compositions. While the use of these models enables assay standardization, they do not fully mimic the immunogenicity or clearance signals of primary apoptotic cells. Future studies using patient-derived apoptotic targets would provide greater physiological relevance, although logistical challenges remain.

Tissue access was also a major limiting factor in this thesis. Although phenotypic profiling of synovial Mφ was successfully performed using freshly digested human tissue, it was not feasible to run efferocytosis assays on these cells so far. Limited tissue availability, variability in Mφ yield, and unpredictable cell ratios within the synovial compartment made it difficult to consistently isolate sufficient numbers of viable Mφ for functional assays. This limitation is particularly relevant in RA research, where the abundance and composition of synMφ vary widely between patients and biopsy sites. Additionally, the high clinical value of tissue samples prevented antibody titration directly on tissue-derived cells. Instead, titrations were performed on MDMs or cell lines, which do not fully represent the expression profiles or autofluorescence characteristics of synovial Mφ. Some markers of interest were not expressed on the titration platforms, limiting their optimal inclusion in the tissue staining panel.

Technical sensitivity also presents challenges, particularly with the use of pHrodo Green for detecting efferocytosis. While pHrodo provides a sensitive and intuitive readout of phagolysosomal acidification, its signal is highly dependent on precise experimental conditions. Small deviations in temperature, cell number, buffer pH, or timing (delay of experiments) can lead to considerable variability in fluorescence intensity. Consequently, direct comparison between independently conducted experiments is difficult, and quantitative comparisons are only meaningful when conditions are tightly matched within the same experiment. This restricts the assay’s suitability for longitudinal or cross-experiment comparisons unless normalization strategies are rigorously applied.

The application of spectral flow cytometry, particularly utilizing the Sony ID7000 platform, facilitates comprehensive high-dimensional phenotypic profiling. However, this advanced technology introduces considerable analytical complexity. At present, there are no universally standardized workflows for critical processes such as autofluorescence correction, gating strategies, or panel design optimization specific to this system. As a result, data analysis remains partially user-dependent and prone to inter-operator variability, a challenge that is especially pronounced when working with primary tissue samples that possess inherent background autofluorescence. As one of the early adopters of the newly launched ID7000 platform, I was engaged in parallel learning and optimization efforts in collaboration with the manufacturer. While this collaborative process contributed valuable insights into the system’s capabilities, it also resulted in procedural delays and preventable errors that might have been mitigated had the technology and its analytical pipelines been more mature and widely established.

Further development of community guidelines and data processing pipelines for spectral cytometry will be essential to improve reproducibility and standardization.

In addition, the iMφ model, while powerful for functional assay, requires a lengthy differentiation process of approximately 30 days. This makes it time-consuming, expensive, and sensitive to

cumulative technical errors such as contamination or drift in cytokine responsiveness. These factors can limit scalability and reproducibility, particularly when comparing across different experimental batches.

So far, I have primarily used apoptotic JTs in the assay. However, these cells may not be suitable for all Mφ types. For example, iMicroglia cells exhibited poor uptake of JTs, which could be due to their similar cell sizes. When running the assay on confocal microscopy, we observed that JTs are roughly the same size as iMicroglia, this may hinder efficient engulfment. Additionally, efferocytosis might be cell type-specific and limited to phagocytes typically found in the brain. Supporting this idea, iMicroglia cells showed a significantly greater increase in fluorescence when apoptotic glioblastoma cells were used instead.

It is important to recognize that *Discoverer Mφ* is inherently correlative in its current form. Although it robustly links surface marker expression with efferocytic and iron-handling behavior, it does not establish causality. For example, high MerTK expression is associated with enhanced efferocytosis, but the direct regulatory role of MerTK cannot be inferred without perturbation studies. As outlined in the aims of this thesis, future integration with CRISPR-based functional genomics screens will be essential to identify causal regulators and signaling networks governing Mφ functions.

In addition to the inherent limitations of the *Discoverer Mφ* platforms, our CITE-seq data also presents certain constraints. One major challenge arises from the variability in cell sorting strategies across different patient samples, which complicates direct comparisons. Because the majority of cells included in the CITE-seq analysis came from non-sorted samples (n = 9), the overall cell distribution is skewed. In the sorted samples (n = 14), we specifically enriched for $CD45^-$ structural cells and $CD45^+$ myeloid cells, which included various subsets. As a result, structural and myeloid cells are overrepresented in UMAP, while lymphoid populations mainly originate from the non-sorted samples. Still, we were able to detect all major synovial cell types, including FLS, endothelial cells, pericytes, T cells, B cells, NK cells, and myeloid cells such as synovial macrophages and neutrophils.

Initially, samples were sorted based on $CD45^+$ $CD11b^+$ $CD64^+$ markers, yielding a relatively pure Mφ population. However, upon identification of a novel $CD64^-$ Mφ subset on spectral flow cytometry, the gating strategy was revised to include all $CD45^+$ $CD11b^+$ cells. While this broader approach captures a more heterogeneous myeloid compartment, including both Mφ and neutrophils, it introduces complexity in downstream analysis due to mixed cell populations. Despite these challenges, this revised strategy was necessary to achieve sufficient sample sizes (n-numbers). Consequently, meticulous and consistent annotation was essential to ensure accurate cell type identification and comparative analysis across the dataset.

4.6 Future Directions and Therapeutic Outlook

The *Discoverer Mφ* assay establishes a robust platform for advancing our understanding of Mφ functional diversity and provides a blueprint for multiple translational applications. This includes clinical biomarker development, therapeutic screening, and high-dimensional systems biology approaches.

Longitudinal sampling of synovial tissue or peripheral blood in RA patients, both before and after therapy, offers a promising avenue for determining whether dynamic changes in Mφ efferocytosis

or iron metabolism predict therapeutic outcomes. Given the central role of Mφ-driven resolution in IMIDs, functional Mφ profiling could enable precision medicine by stratifying patients for targeted, pro-resolving interventions. For example, efferocytic capacity and ferroportin-mediated iron export could serve as biomarkers of therapeutic responsiveness or disease remission.

The Mφ subsets identified via CITE-seq in this study can be FACS-isolated for downstream *in vitro* functional assays, including efferocytosis, phagocytosis, and iron metabolism. These assays could assign distinct functional capacities to transcriptionally defined subsets. Additionally, integrating lipidomics (e.g., specialized pro-resolving mediators [SPMs] via e.g. LEGENDplex) and metabolomics will provide deeper insight into the immunometabolic programs of Mφs across different RA disease stages. Combining these functional data with the *Discoverer Mφ* assay creates a multidimensional platform for delineating macrophage heterogeneity and plasticity in RA.

Discoverer Mφ can also function as a screening tool for therapeutic discovery. Our group is actively investigating small molecules and biologics that enhance efferocytosis, such as MerTK agonists and resolvins, as potential interventions. A key future direction involves the optimization of pooled CRISPR knockout screening in iMicroglia, with a focus on efferocytosis and differentiation-related phenotypes.

For this purpose, a custom-pooled guide RNA (gRNA) library targeting 765 experimentally and computationally prioritized Mφ genes has been developed in our team, guided by human cross-tissue single-cell RNA atlases. The library includes 100 non-targeting controls. Preliminary experiments have successfully generated $CD14^{+}MERTK^{+}$ iMicroglia with high viability. Spectral flow cytometry data indicate that 30 - 40% of these cells are capable of efferocytosis, as measured by pHrodoGreen-labeled apoptotic JTs. Further validation, including functional blockade and orthogonal readouts, is underway.

An extensive biobank of $mKate2^{+}$ Cas9-expressing 6-TF iPSCs has been established. Titration experiments confirmed an optimal multiplicity of infection (MOI ≈ 0.3) for maintaining gRNA diversity during large-scale screening. Importantly, the iMicroglia differentiation protocol (~8 days) is substantially shorter and less proliferative than conventional iMφ protocols, offering improved feasibility for maintaining representation in pooled CRISPR screens. This platform has high potential for identifying novel regulators of human microglial differentiation and efferocytic competence.

Beyond CRISPR, *Discoverer Mφ* can be integrated with spatial transcriptomics, high-dimensional lipidomics (e.g., SPM profiling), and immune co-culture models (e.g., with synovial fibroblasts or T cells). This would provide systems-level insights into Mφ-mediated resolution mechanisms, aligning with the therapeutic framework proposed by Kraynak et al. (2022), who used phosphatidylserine-coated nanoparticles to reprogram Mφ in inflamed tissues,a concept directly testable using this assay.

While this thesis primarily applies *Discoverer Mφ* to RA as a model of IMIDs, its utility extends to cancer biology, particularly in studying taMφ. Despite their clinical relevance, taMφ functional plasticity remains poorly understood due to the lack of scalable, multiparametric assays linking phenotype to function.

Discoverer Mφ provides a unique platform to fill this gap, allowing simultaneous quantification of efferocytosis, iron metabolism, and phagocytosis. This is particularly relevant in tumors, where apoptotic cancer cells exploit Mφ efferocytosis to dampen inflammation and promote immune tolerance. Using this assay, it becomes possible to investigate how tumor-derived factors modulate TAM function, identify surface markers of immunosuppressive phenotypes, and dissect the signaling pathways involved in immune evasion.

Additionally, *Discoverer Mφ* allows real-time detection of phenotypic and functional shifts in taMφ following cancer cell engulfment, which can be coupled with cytokine profiling and lipidomics to explore how efferocytosis shapes the TME. This has implications for understanding cancer progression and therapeutic resistance.

A particularly novel aspect of *Discoverer Mφ* is its capacity to interrogate Mφ iron metabolism at single-cell resolution. We have demonstrated feasibility in tracking iron uptake (e.g., via transferrin receptor 1, TFR1) and storage, with potential to assess labile iron pools and iron export (e.g., ferroportin, FPN). This enables dissection of iron-driven Mφ plasticity, a key component in shaping immune responses in cancer.

Emerging research suggests that tumors exhibit “iron addiction,” upregulating TFR1 and suppressing FPN to enhance intracellular iron availability, thereby promoting proliferation and angiogenesis. In parallel, tumors often deprive taMφ of iron, altering their function. Using *Discoverer Mφ*, we can experimentally manipulate these iron dynamics. For example, recent evidence (Zhang et al., 2024) suggests that iron oxide nanoparticle supplementation (e.g., ferumoxytol) can reprogram M2-like TAMs toward a pro-inflammatory phenotype. Our platform is ideally suited to test such hypotheses and identify therapeutic strategies targeting iron metabolism to restore antitumor immunity.

4.7 Conclusion

This thesis set out to explore the functional diversity of human Mφs in inflammatory disease, with a central hypothesis that integrating phenotypic and functional readouts would reveal subset-specific differences in efferocytosis and iron metabolism, key processes in immune regulation and tissue homeostasis. The development and application of the *Discoverer Mφ* assay have substantiated this hypothesis by enabling scalable, multidimensional assessment of Mφ activity at single-cell resolution.

In alignment with Aim 1, I successfully established a modular assay platform that couples surface phenotyping with functional metrics such as phagocytosis, iron uptake/storage, and efferocytosis.

In fulfillment of Aim 2, we developed and validated *in vitro* human Mφ platforms, including induced pluripotent stem cell (iPSC)-derived Mφs and primary RA-derived Mφs, to enable controlled dissection of functional states. These models demonstrated reproducible capacity for efferocytosis and can now serve as a basis for high-throughput perturbation studies (e.g., pooled CRISPR, small-molecule screening).

In support of Aim 3, our phenotypic and preliminary functional characterization of primary synovial tissue derived Mφ from RA patients revealed Mφ subsets heterogeneity in phenotype indicating distinct functional properties. These features were subset-specific and aligned with transcriptional signatures identified through CITE-seq, supporting the second hypothesis: that distinct Mφ subsets play differential roles in IMID pathogenesis and resolution, depending on their effector functions.

Moreover, this work contributes to the broader hypothesis pursued by our research group: that defining the molecular regulators of Mφ efferocytosis and iron metabolism can uncover novel therapeutic targets for IMIDs and cancer. The *Discoverer Mφ* assay now provides a powerful framework to test this at scale. For instance, we demonstrated the feasibility of integrating this platform with lipidomics, cytokine profiling, and CRISPR screening to map Mφ response programs across disease contexts and perturbations.

Looking forward, *Discoverer Mφ* has clear translational potential. It can be deployed to functionally stratify patients, assess therapeutic responsiveness, and identify Mφ-targeted immunomodulators. In oncology, its application to taMφ may reveal how efferocytosis and iron availability shape immune suppression and tumor progression, while in IMIDs, it could help identify resolution-promoting subsets amenable to therapeutic activation.

In conclusion, the work presented in this thesis demonstrates that combining phenotypic and functional Mφ profiling not only elucidates the diversity of Mφ roles in health and disease but also lays the groundwork for developing Mφ-centered therapeutic strategies across immune-mediated conditions.

5. References

Adkar, S. S., & Leeper, N. J. (2024). Efferocytosis in atherosclerosis. In *Nature Reviews Cardiology*. Nature Research. https://doi.org/10.1038/s41569-024-01037-7

Alivernini, S., MacDonald, L., Elmesmari, A., Finlay, S., Tolusso, B., Gigante, M. R., Petricca, L., Di Mario, C., Bui, L., Perniola, S., Attar, M., Gessi, M., Fedele, A. L., Chilaka, S., Somma, D., Sansom, S. N., Filer, A., McSharry, C., Millar, N. L., … Kurowska-Stolarska, M. (2020). Distinct synovial tissue macrophage subsets regulate inflammation and remission in rheumatoid arthritis. *Nature Medicine*, *26*(8), 1295–1306. https://doi.org/10.1038/s41591-020-0939-8

Arandjelovic, S., & Ravichandran, K. S. (2015). Phagocytosis of apoptotic cells in homeostasis. In *Nature Immunology* (Vol. 16, Issue 9, pp. 907–917). Nature Publishing Group. https://doi.org/10.1038/ni.3253

Arosio, P., Ingrassia, R., & Cavadini, P. (2009). Ferritins: A family of molecules for iron storage, antioxidation and more. In *Biochimica et Biophysica Acta - General Subjects* (Vol. 1790, Issue 7, pp. 589–599). https://doi.org/10.1016/j.bbagen.2008.09.004

Badran, O., Cohen, I., & Bar-Sela, G. (2024). The Impact of Iron on Cancer-Related Immune Functions in Oncology: Molecular Mechanisms and Clinical Evidence. In *Cancers* (Vol. 16, Issue 24). Multidisciplinary Digital Publishing Institute (MDPI). https://doi.org/10.3390/cancers16244156

Baeten, D., Kruithof, E., De Rycke, L., Boots, A. M., Mielants, H., Veys, E. M., & De Keyser, F. (2005). Infiltration of the synovial membrane with macrophage subsets and polymorphonuclear cells reflects global disease activity in spondyloarthropathy. *Arthritis Res Ther*. https://doi.org/10.1186/ar1501)ht

Ballerie, A., Lescoat, A., Augagneur, Y., Lelong, M., Morzadec, C., Cazalets, C., Jouneau, S., Fardel, O., Vernhet, L., Jégo, P., & Lecureur, V. (2019). Efferocytosis capacities of blood monocyte-derived macrophages in systemic sclerosis. *Immunology and Cell Biology*, *97*(3), 340–347. https://doi.org/10.1111/imcb.12217

Baumann, I., Kolowos, W., Voll, R. E., Manger, B., Gaipl, U., Neuhuber, W. L., Kirchner, T., Kalden, J. R., & Herrmann, M. (2002). Impaired Uptake of Apoptotic Cells Into Tingible Body Macrophages in Germinal Centers of Patients With Systemic Lupus Erythematosus. *ARTHRITIS & RHEUMATISM*, *46*(1), 191–201. https://doi.org/10.1002/art.10027

Benn, M. C., Pot, S. A., Moeller, J., Yamashita, T., Fonta, C. M., Orend, G., Kollmannsberger, P., & Vogel, V. (2023). *How the mechanobiology orchestrates the iterative and reciprocal ECM-cell cross-talk that drives microtissue growth*. https://www.science.org

Bravo, D. D., Shi, Y., Sheu, A., Liang, W.-C., Lin, W., Wu, Y., Yan, M., & Wang, J. (2023). A Real-Time Image-Based Efferocytosis Assay for the Discovery of Functionally Inhibitory Anti-MerTK Antibodies. *The Journal of Immunology*, *210*(8), 1166–1176. https://doi.org/10.4049/jimmunol.2200597

Brown, G. C. (2024). Cell death by phagocytosis. In *Nature Reviews Immunology* (Vol. 24, Issue 2, pp. 91–102). Nature Research. https://doi.org/10.1038/s41577-023-00921-6

Brown, R., Richardson, K. L., Kabir, T. D., Trinder, D., Ganss, R., & Leedman, P. J. (2020). Altered Iron Metabolism and Impact in Cancer Biology, Metastasis, and Immunology. In *Frontiers in Oncology* (Vol. 10). Frontiers Media S.A. https://doi.org/10.3389/fonc.2020.00476

Brown, S., Heinisch, I., Ross, E., Shaw, K., Buckley, C. O., & Savill, J. (2002). Apoptosis disables CD31-mediated cell detachment from phagocytes promoting binding and engulfment. *Nature*, *418*(6894), 200–203. https://doi.org/10.1038/nature00811

Buckley, C. D., Gilroy, D. W., Serhan, C. N., Stockinger, B., & Tak, P. P. (2013). The resolution of inflammation. In *Nature Reviews Immunology* (Vol. 13, Issue 1, pp. 59–66). https://doi.org/10.1038/nri3362

Camaschella, C., Nai, A., & Silvestri, L. (2020). Iron metabolism and iron disorders revisited in the hepcidin era. In *Haematologica* (Vol. 105, Issue 2, pp. 260–272). Ferrata Storti Foundation. https://doi.org/10.3324/haematol.2019.232124

Candelaria, P. V., Leoh, L. S., Penichet, M. L., & Daniels-Wells, T. R. (2021). Antibodies Targeting the Transferrin Receptor 1 (TfR1) as Direct Anti-cancer Agents. In *Frontiers in Immunology* (Vol. 12). Frontiers Media S.A. https://doi.org/10.3389/fimmu.2021.607692

Cao, H., Schroeder, B., Chen, J., Schott, M. B., & McNiven, M. A. (2016). The endocytic fate of the transferrin receptor is regulated by c-Abl kinase. *Journal of Biological Chemistry*, *291*(32), 16424–16437. https://doi.org/10.1074/jbc.M116.724997

Cendrowicz, E., Sas, Z., Bremer, E., & Rygiel, T. P. (2021). The role of macrophages in cancer development and therapy. In *Cancers* (Vol. 13, Issue 8). MDPI. https://doi.org/10.3390/cancers13081946

Chanmee, T., Ontong, P., Konno, K., & Itano, N. (2014). Tumor-associated macrophages as major players in the tumor microenvironment. In *Cancers* (Vol. 6, Issue 3, pp. 1670–1690). https://doi.org/10.3390/cancers6031670

Chao, M. P., Weissman, I. L., & Majeti, R. (2012). The CD47-SIRPα pathway in cancer immune evasion and potential therapeutic implications. In *Current Opinion in Immunology* (Vol. 24, Issue 2, pp. 225–232). https://doi.org/10.1016/j.coi.2012.01.010

Chen, S., Saeed, A. F. U. H., Liu, Q., Jiang, Q., Xu, H., Xiao, G. G., Rao, L., & Duo, Y. (2023). Macrophages in immunoregulation and therapeutics. In *Signal Transduction and Targeted Therapy* (Vol. 8, Issue 1). Springer Nature. https://doi.org/10.1038/s41392-023-01452-1

Chung, B., Chaston, T., Marks, J., Srai, S. K., & Sharp, P. A. (2009). Hepcidin decreases iron transporter expression in vivo in mouse duodenum and spleen and in vitro in THP-1 macrophages and intestinal Caco-2 cells. *Journal of Nutrition*, *139*(8), 1457–1462. https://doi.org/10.3945/jn.108.102905

Clark, R., Usselmann, L., Brown, M. R., Goeppert, A. U., & Corrigan, A. (2019). A flexible high content imaging assay for profiling macrophage efferocytosis. *Journal of Immunological Methods*, *473*. https://doi.org/10.1016/j.jim.2019.112636

Coulis, G., Jaime, D., Guerrero-Juarez, C., Kastenschmidt, J. M., Farahat, P. K., Nguyen, Q., Pervolarakis, N., Mclinden, K., Thurlow, L., Movahedi, S., Hughes, B. S., Duarte, J., Sorn, A., Montoya, E., Mozaffar, I., Dragan, M., Othy, S., Joshi, T., Hans, C. P., … Armando Villalta, S. (2023). *Single-cell and spatial transcriptomics identify a macrophage population associated with skeletal muscle fibrosis*. https://www.science.org

Coussens, L. M., & Werb, Z. (2002). Inflammation and cancer. In *Nature* (Vol. 420, Issue 6917, pp. 860–867). https://doi.org/10.1038/nature01322

Crowson, C. S., Liao, K. P., Davis, J. M., Solomon, D. H., Matteson, E. L., Knutson, K. L., Hlatky, M. A., & Gabriel, S. E. (2013). Rheumatoid arthritis and cardiovascular disease. In *American Heart Journal* (Vol. 166, Issue 4). Mosby Inc. https://doi.org/10.1016/j.ahj.2013.07.010

Culemann, S., Grüneboom, A., Nicolás-Ávila, J. Á., Weidner, D., Lämmle, K. F., Rothe, T., Quintana, J. A., Kirchner, P., Krljanac, B., Eberhardt, M., Ferrazzi, F., Kretzschmar, E., Schicht, M., Fischer, K., Gelse, K., Faas, M., Pfeifle, R., Ackermann, J. A., Pachowsky, M., … Krönke, G. (2019). Locally renewing resident synovial macrophages provide a protective barrier for the joint. *Nature*, *572*(7771), 670–675. https://doi.org/10.1038/s41586-019-1471-1

Dalli, J., & Serhan, C. N. (2017). Pro-resolving mediators in regulating and conferring macrophage function. In *Frontiers in Immunology* (Vol. 8, Issue NOV). Frontiers Media S.A. https://doi.org/10.3389/fimmu.2017.01400

Das, S., Owen, K. A., Ly, K. T., Park, D., Black, S. G., Wilson, J. M., Sifri, C. D., Ravichandran, K. S., Ernst, P. B., & Casanova, J. E. (2011). Brain angiogenesis inhibitor 1 (BAI1) is a pattern recognition receptor that mediates macrophage binding and engulfment of Gram-negative bacteria. *Proceedings of the National Academy of Sciences of the United States of America*, *108*(5), 2136–2141. https://doi.org/10.1073/pnas.1014775108

De Schepper, S., Verheijden, S., Aguilera-Lizarraga, J., Viola, M. F., Boesmans, W., Stakenborg, N., Voytyuk, I., Smidt, I., Boeckx, B., Dierckx de Casterlé, I., Baekelandt, V., Gonzalez Dominguez, E., Mack, M., Depoortere, I., De Strooper, B., Sprangers, B., Himmelreich, U., Soenen, S., Guilliams, M., … Boeckxstaens, G. (2018). Self-Maintaining Gut Macrophages Are Essential for Intestinal Homeostasis. *Cell*, *175*(2), 400-415.e13. https://doi.org/10.1016/j.cell.2018.07.048

Distéfano-Gagné, F., Bitarafan, S., Lacroix, S., & Gosselin, D. (2023). Roles and regulation of microglia activity in multiple sclerosis: insights from animal models. In *Nature Reviews Neuroscience* (Vol. 24, Issue 7, pp. 397–415). Springer Nature. https://doi.org/10.1038/s41583-023-00709-6

Donlin, L. T., Rao, D. A., Wei, K., Slowikowski, K., McGeachy, M. J., Turner, J. D., Meednu, N., Mizoguchi, F., Gutierrez-Arcelus, M., Lieb, D. J., Keegan, J., Muskat, K., Hillman, J., Rozo, C., Ricker, E., Eisenhaure, T. M., Li, S., Browne, E. P., Chicoine, A., … Guthridge, J. (2018). Methods for high-dimensonal analysis of cells dissociated from cyropreserved synovial tissue. *Arthritis Research and Therapy*, *20*(1). https://doi.org/10.1186/s13075-018-1631-y

Doran, A. C., Yurdagul, A., & Tabas, I. (2020). Efferocytosis in health and disease. In *Nature Reviews Immunology* (Vol. 20, Issue 4, pp. 254–267). Nature Research. https://doi.org/10.1038/s41577-019-0240-6

Dräger, N. M., Sattler, S. M., Huang, C. T. L., Teter, O. M., Leng, K., Hashemi, S. H., Hong, J., Aviles, G., Clelland, C. D., Zhan, L., Udeochu, J. C., Kodama, L., Singleton, A. B., Nalls, M. A., Ichida, J., Ward, M. E., Faghri, F., Gan, L., & Kampmann, M. (2022). A CRISPRi/a platform in human iPSC-derived microglia uncovers regulators of disease states. *Nature Neuroscience*, *25*(9), 1149–1162. https://doi.org/10.1038/s41593-022-01131-4

Drakesmith, H., Nemeth, E., & Ganz, T. (2015). Ironing out Ferroportin. In *Cell Metabolism* (Vol. 22, Issue 5, pp. 777–787). Cell Press. https://doi.org/10.1016/j.cmet.2015.09.006

Drilon, A., Rekhtman, N., Arcila, M., Wang, L., Ni, A., Albano, M., Van Voorthuysen, M., Somwar, R., Smith, R. S., Montecalvo, J., Plodkowski, A., Ginsberg, M. S., Riely, G. J., Rudin, C. M., Ladanyi, M., & Kris, M. G. (2016). Cabozantinib in patients with advanced RET-rearranged non-small-cell lung cancer: an open-label, single-centre, phase 2, single-arm trial. *The Lancet Oncology*, *17*(12), 1653–1660. https://doi.org/10.1016/S1470-2045(16)30562-9

Duffield, J. S., Forbes, S. J., Constandinou, C. M., Clay, S., Partolina, M., Vuthoori, S., Wu, S., Lang, R., & Iredale, J. P. (2005). Selective depletion of macrophages reveals distinct, opposing roles during liver injury and repair. *Journal of Clinical Investigation*, *115*(1), 56–65. https://doi.org/10.1172/JCI200522675

Edalat, S. G., Gerber, R., Houtman, M., Lückgen, J., Teixeira, R. L., Palacios Cisneros, M. del P., Pfanner, T., Kuret, T., Ižanc, N., Micheroli, R., Polido-Pereira, J., Saraiva, F., Lingam, S., Burki, K., Burja, B., Pauli, C., Rotar, Ž., Tomšič, M., Čučnik, S., … Frank Bertoncelj, M. (2024). Molecular maps of synovial cells in inflammatory arthritis using an optimized synovial tissue dissociation protocol. *IScience*, *27*(6). https://doi.org/10.1016/j.isci.2024.109707

Elliott, M. R., & Ravichandran, K. S. (2010). Clearance of apoptotic cells: Implications in health and disease. In *Journal of Cell Biology* (Vol. 189, Issue 7, pp. 1059–1070). https://doi.org/10.1083/jcb.201004096

Elliott, M. R., Zheng, S., Park, D., Woodson, R. I., Reardon, M. A., Juncadella, I. J., Kinchen, J. M., Zhang, J., Lysiak, J. J., & Ravichandran, K. S. (2010). Unexpected requirement for ELMO1 in clearance of apoptotic germ cells in vivo. *Nature*, *467*(7313), 333–337. https://doi.org/10.1038/nature09356

Flannagan, R. S., Canton, J., Furuya, W., Glogauer, M., & Grinstein, S. (2014). The phosphatidylserine receptor TIM4 utilizes integrins as coreceptors to effect phagocytosis. *Molecular Biology of the Cell*, *25*(9), 1511–1522. https://doi.org/10.1091/mbc.E13-04-0212

Freire-de-Lima, C. G., Yi, Q. X., Gardai, S. J., Bratton, D. L., Schiemann, W. P., & Henson, P. M. (2006). Apoptotic cells, through transforming growth factor-β, coordinately induce anti-inflammatory and suppress pro-inflammatory eicosanoid and NO synthesis in murine macrophages. *Journal of Biological Chemistry*, *281*(50), 38376–38384. https://doi.org/10.1074/jbc.M605146200

Gaetano, C., Massimo, L., & Alberto, M. (2010). Control of iron homeostasis as a key component of macrophage polarization. In *Haematologica* (Vol. 95, Issue 11, pp. 1801–1803). https://doi.org/10.3324/haematol.2010.030239

Galy, B., Conrad, M., & Muckenthaler, M. (2024). Mechanisms controlling cellular and systemic iron homeostasis. In *Nature Reviews Molecular Cell Biology* (Vol. 25, Issue 2, pp. 133–155). Nature Research. https://doi.org/10.1038/s41580-023-00648-1

Gardai, S. J., McPhillips, K. A., Frasch, S. C., Janssen, W. J., Starefeldt, A., Murphy-Ullrich, J. E., Bratton, D. L., Oldenborg, P. A., Michalak, M., & Henson, P. M. (2005). Cell-surface calreticulin initiates clearance of viable or apoptotic cells through trans-activation of LRP on the phagocyte. *Cell*, *123*(2), 321–334. https://doi.org/10.1016/j.cell.2005.08.032

Gheibi Hayat, S. M., Bianconi, V., Pirro, M., & Sahebkar, A. (2019). Efferocytosis: molecular mechanisms and pathophysiological perspectives. In *Immunology and Cell Biology* (Vol. 97, Issue 2, pp. 124–133). John Wiley and Sons Inc. https://doi.org/10.1111/imcb.12206

Ginhoux, F., & Guilliams, M. (2016). Tissue-Resident Macrophage Ontogeny and Homeostasis. In *Immunity* (Vol. 44, Issue 3, pp. 439–449). Cell Press. https://doi.org/10.1016/j.immuni.2016.02.024

Gomez Perdiguero, E., Klapproth, K., Schulz, C., Busch, K., Azzoni, E., Crozet, L., Garner, H., Trouillet, C., De Bruijn, M. F., Geissmann, F., & Rodewald, H. R. (2015). Tissue-resident macrophages originate from yolk-sac-derived erythro-myeloid progenitors. *Nature*, *518*(7540), 547–551. https://doi.org/10.1038/nature13989

Gordon, S. (2016). Phagocytosis: An Immunobiologic Process. In *Immunity* (Vol. 44, Issue 3, pp. 463–475). Cell Press. https://doi.org/10.1016/j.immuni.2016.02.026

Greenberg, M. E., Sun, M., Zhang, R., Febbraio, M., Silverstein, R., & Hazen, S. L. (2006). Oxidized phosphatidylserine-CD36 interactions play an essential role in macrophage-dependent phagocytosis of apoptotic cells. *Journal of Experimental Medicine*, *203*(12), 2613–2625. https://doi.org/10.1084/jem.20060370

Greenberg, S. (1999). *Phagocytosis : the host*. JAI Press.

Gude, D. R., Alvarez, S. E., Paugh, S. W., Mitra, P., Yu, J., Griffiths, R., Barbour, S. E., Milstien, S., & Spiegel, S. (2008). Apoptosis induces expression of sphingosine kinase 1 to release sphingosine-1-phosphate as a “come-and-get-me” signal. *The FASEB Journal*, *22*(8), 2629–2638. https://doi.org/10.1096/fj.08-107169

Guilliams, M., Thierry, G. R., Bonnardel, J., & Bajenoff, M. (2020). Establishment and Maintenance of the Macrophage Niche. In *Immunity* (Vol. 52, Issue 3, pp. 434–451). Cell Press. https://doi.org/10.1016/j.immuni.2020.02.015

He, L., Jhong, J. H., Chen, Q., Huang, K. Y., Strittmatter, K., Kreuzer, J., DeRan, M., Wu, X., Lee, T. Y., Slavov, N., Haas, W., & Marneros, A. G. (2021). Global characterization of macrophage polarization mechanisms and identification of M2-type polarization inhibitors. *Cell Reports*, *37*(5). https://doi.org/10.1016/j.celrep.2021.109955

Hegarty, L. M., Jones, G. R., & Bain, C. C. (2023). Macrophages in intestinal homeostasis and inflammatory bowel disease. In *Nature Reviews Gastroenterology and Hepatology* (Vol. 20, Issue 8, pp. 538–553). Nature Research. https://doi.org/10.1038/s41575-023-00769-0

Herre, J., Marshall, A. S. J., Caron, E., Edwards, A. D., Williams, D. L., Schweighoffer, E., Tybulewicz, V., Reis E Sousa, C., Gordon, S., & Brown, G. D. (2004). Dectin-1 uses novel mechanisms for yeast phagocytosis in macrophages. *Blood*, *104*(13), 4038–4045. https://doi.org/10.1182/blood-2004-03-1140

Hickman, E., Smyth, T., Cobos-Uribe, C., Immormino, R., Rebuli, M. E., Moran, T., Alexis, N. E., & Jaspers, I. (2023). Expanded characterization of in vitro polarized M0, M1, and M2 human monocyte-derived macrophages: Bioenergetic and secreted mediator profiles. *PLoS ONE*, *18*(3 March). https://doi.org/10.1371/journal.pone.0279037

Hoeffel, G., & Ginhoux, F. (2015). Ontogeny of tissue-resident macrophages. In *Frontiers in Immunology* (Vol. 6, Issue SEP). Frontiers Research Foundation. https://doi.org/10.3389/fimmu.2015.00486

Hou, J., Karin, M., & Sun, B. (2021). Targeting cancer-promoting inflammation — have anti-inflammatory therapies come of age? In *Nature Reviews Clinical Oncology* (Vol. 18, Issue 5, pp. 261–279). Nature Research. https://doi.org/10.1038/s41571-020-00459-9

Italiani, P., & Boraschi, D. (2014). From monocytes to M1/M2 macrophages: Phenotypical vs. functional differentiation. In *Frontiers in Immunology* (Vol. 5, Issue OCT). Frontiers Media SA. https://doi.org/10.3389/fimmu.2014.00514

Jaumouillé, V., & Grinstein, S. (2016). Molecular Mechanisms of Phagosome Formation. *Microbiology Spectrum*, *4*(3). https://doi.org/10.1128/microbiolspec.mchd-0013-2015

Karimova, A. F., Khalitova, A. R., Suezov, R., Markov, N., Mukhamedshina, Y., Rizvanov, A. A., Huber, M., Simon, H. U., & Brichkina, A. (2025). Immunometabolism of tumor-associated macrophages: A therapeutic perspective. In *European Journal of Cancer* (Vol. 220). Elsevier Ltd. https://doi.org/10.1016/j.ejca.2025.115332

Kim, K. K., Dotson, M. R., Agarwal, M., Yang, J., Bradley, P. B., Subbotina, N., Osterholzer, J. J., & Sisson, T. H. (2018). Efferocytosis of apoptotic alveolar epithelial cells is sufficient to initiate lung fibrosis. *Cell Death and Disease*, *9*(11). https://doi.org/10.1038/s41419-018-1074-z

Kinchen, J. M., & Ravichandran, K. S. (2008). Phagosome maturation: Going through the acid test. In *Nature Reviews Molecular Cell Biology* (Vol. 9, Issue 10, pp. 781–795). https://doi.org/10.1038/nrm2515

Knab, K., Chambers, D., & Krönke, G. (2022). Synovial Macrophage and Fibroblast Heterogeneity in Joint Homeostasis and Inflammation. In *Frontiers in Medicine* (Vol. 9). Frontiers Media S.A. https://doi.org/10.3389/fmed.2022.862161

Kojima, Y., Volkmer, J. P., McKenna, K., Civelek, M., Lusis, A. J., Miller, C. L., Direnzo, D., Nanda, V., Ye, J., Connolly, A. J., Schadt, E. E., Quertermous, T., Betancur, P., Maegdefessel, L., Matic, L. P., Hedin, U., Weissman, I. L., & Leeper, N. J. (2016). CD47-blocking antibodies restore phagocytosis and prevent atherosclerosis. *Nature*, *536*(7614), 86–90. https://doi.org/10.1038/nature18935

Komai, T., Inoue, M., Okamura, T., Morita, K., Iwasaki, Y., Sumitomo, S., Shoda, H., Yamamoto, K., & Fujio, K. (2018). Transforming growth factor-β and interleukin-10 synergistically regulate humoral immunity via modulating metabolic signals. *Frontiers in Immunology*, *9*(JUN). https://doi.org/10.3389/fimmu.2018.01364

Kourtzelis, I., Hewitson, J., & Roger, T. (2021). Editorial: Macrophage Plasticity in Sterile and Pathogen-Induced Inflammation. In *Frontiers in Immunology* (Vol. 12). Frontiers Media S.A. https://doi.org/10.3389/fimmu.2021.823023

Kraynak, C. A., Huang, W., Bender, E. C., Wang, J. L., Hanafy, M. S., Cui, Z., & Suggs, L. J. (2022). Apoptotic body-inspired nanoparticles target macrophages at sites of inflammation to support an anti-inflammatory phenotype shift. *International Journal of Pharmaceutics*, *618*. https://doi.org/10.1016/j.ijpharm.2022.121634

Kubasch, A. S., Peterlin, P., Cluzeau, T., Götze, K. S., Sockel, K., Teipel, R., Jentzsch, M., Attalah, H., Sebert, M., Chermat, F., Gloaguen, S., Puttrich, M., Cross, M., Schneider, M., Kayser, S., Schipp, D., Giagounidis, A., Tirado-Gonzalez, I., Descot, A., … Ades, L. (2023). Efficacy and safety of bemcentinib in patients with advanced myelodysplastic neoplasms or acute myeloid leukemia failing hypomethylating agents- the EMSCO phase II BERGAMO trial. *Leukemia*, *37*(11), 2309–2313. https://doi.org/10.1038/s41375-023-02029-1

Lahey, K. C., Gadiyar, V., Hill, A., Desind, S., Wang, Z., Davra, V., Patel, R., Zaman, A., Calianese, D., & Birge, R. B. (2022). Mertk: An emerging target in cancer biology and immuno-

oncology. In *International Review of Cell and Molecular Biology* (Vol. 368, pp. 35–59). Elsevier Inc. https://doi.org/10.1016/bs.ircmb.2022.04.004

Lauber, K., Bohn, E., Kröber, S. M., Xiao, Y., & Blumenthal, S. G. (2003). Apoptotic Cells Induce Migration of Phagocytes via Caspase-3-Mediated Release of a Lipid Attraction Signal. *Cell*, 717–730.

Lee, C. Z. W., Kozaki, T., & Ginhoux, F. (2018). Studying tissue macrophages in vitro: are iPSC-derived cells the answer? In *Nature Reviews Immunology* (Vol. 18, Issue 11, pp. 716–725). Nature Publishing Group. https://doi.org/10.1038/s41577-018-0054-y

Lei, G., Zhuang, L., & Gan, B. (2024). The roles of ferroptosis in cancer: Tumor suppression, tumor microenvironment, and therapeutic interventions. In *Cancer Cell* (Vol. 42, Issue 4, pp. 513–534). Cell Press. https://doi.org/10.1016/j.ccell.2024.03.011

Li, M., He, L., Zhu, J., Zhang, P., & Liang, S. (2022). Targeting tumor-associated macrophages for cancer treatment. In *Cell and Bioscience* (Vol. 12, Issue 1). BioMed Central Ltd. https://doi.org/10.1186/s13578-022-00823-5

Liang, W., & Ferrara, N. (2021). Iron Metabolism in the Tumor Microenvironment: Contributions of Innate Immune Cells. In *Frontiers in Immunology* (Vol. 11). Frontiers Media S.A. https://doi.org/10.3389/fimmu.2020.626812

Lindner, B., Burkard, T., & Schuler, M. (2020). Phagocytosis assays with different pH-sensitive fluorescent particles and various readouts. *BioTechniques*, *68*(5), 245–250. https://doi.org/10.2144/BTN-2020-0003

Liu, Y., Liang, J., Sha, Z., & Yang, C. (2024). Inhibition of Oxidative Stress-Induced Ferroptosis Can Alleviate Rheumatoid Arthritis in Human. *Journal of Immunology Research*, *2024*. https://doi.org/10.1155/2024/9943747

Liu, Y., Luo, X., Chen, Y., Dang, J., Zeng, D., Guo, X., Weng, W., Zhao, J., Shi, X., Chen, J., Dong, B., Zhong, S., Ren, J., Li, Y., Wang, J., Zhang, J., Sun, J., Xu, H., Lu, Y., … Pan, Y. (2024). Heterogeneous ferroptosis susceptibility of macrophages caused by focal iron overload exacerbates rheumatoid arthritis. *Redox Biology*, *69*. https://doi.org/10.1016/j.redox.2023.103008

McInnes, I. B., & Gravallese, E. M. (2021). Immune-mediated inflammatory disease therapeutics: past, present and future. In *Nature Reviews Immunology* (Vol. 21, Issue 10, pp. 680–686). Nature Research. https://doi.org/10.1038/s41577-021-00603-1

Mehrotra, P., & Ravichandran, K. S. (2022). Drugging the efferocytosis process: concepts and opportunities. In *Nature Reviews Drug Discovery*. Nature Research. https://doi.org/10.1038/s41573-022-00470-y

Mehta, N. U., & Reddy, S. T. (2015). Role of hemoglobin/heme scavenger protein hemopexin in atherosclerosis and inflammatory diseases. In *Current Opinion in Lipidology* (Vol. 26, Issue 5, pp. 384–387). Lippincott Williams and Wilkins. https://doi.org/10.1097/MOL.0000000000000208

Meyerstein, D. (2021). Re-examining Fenton and Fenton-like reactions. In *Nature Reviews Chemistry* (Vol. 5, Issue 9, pp. 595–597). Nature Research. https://doi.org/10.1038/s41570-021-00310-4

Miksa, M., Komura, H., Wu, R., Shah, K. G., & Wang, P. (2009). A novel method to determine the engulfment of apoptotic cells by macrophages using pHrodo succinimidyl ester. *Journal of Immunological Methods*, *342*(1–2), 71–77. https://doi.org/10.1016/j.jim.2008.11.019

Misharin, A. V., Morales-Nebreda, L., Reyfman, P. A., Cuda, C. M., Walter, J. M., McQuattie-Pimentel, A. C., Chen, C. I., Anekalla, K. R., Joshi, N., Williams, K. J. N., Abdala-Valencia, H., Yacoub, T. J., Chi, M., Chiu, S., Gonzalez-Gonzalez, F. J., Gates, K., Lam, A. P., Nicholson, T. T., Homan, P. J., … Perlman, H. (2017). Monocyte-derived alveolar macrophages drive lung fibrosis and persist in the lung over the life span. *Journal of Experimental Medicine*, *214*(8), 2387–2404. https://doi.org/10.1084/jem.20162152

Moon, B., Lee, J., Lee, S. A., Min, C., Moon, H., Kim, D., Yang, S., Moon, H., Jeon, J., Joo, Y. E., & Park, D. (2020). Mertk Interacts with Tim-4 to Enhance Tim-4-Mediated Efferocytosis. *Cells*, *9*(7). https://doi.org/10.3390/cells9071625

Moon, B., Yang, S., Moon, H., Lee, J., & Park, D. (2023). After cell death: the molecular machinery of efferocytosis. In *Experimental and Molecular Medicine* (Vol. 55, Issue 8, pp. 1644–1651). Springer Nature. https://doi.org/10.1038/s12276-023-01070-5

Morana, O., Wood, W., & Gregory, C. D. (2022). The Apoptosis Paradox in Cancer. In *International Journal of Molecular Sciences* (Vol. 23, Issue 3). MDPI. https://doi.org/10.3390/ijms23031328

Morioka, S., Maueröder, C., & Ravichandran, K. S. (2019). Living on the Edge: Efferocytosis at the Interface of Homeostasis and Pathology. In *Immunity* (Vol. 50, Issue 5, pp. 1149–1162). Cell Press. https://doi.org/10.1016/j.immuni.2019.04.018

Moro, H., Bamba, Y., Nagano, K., Hakamata, M., Ogata, H., Shibata, S., Cho, H., Aoki, N., Sato, M., Ohshima, Y., Watanabe, S., Koya, T., Takada, T., & Kikuchi, T. (2023). Dynamics of iron metabolism in patients with bloodstream infections: a time-course clinical study. *Scientific Reports*, *13*(1). https://doi.org/10.1038/s41598-023-46383-7

Moshayedi, S., Tasorian, B., & Almasi-Hashiani, A. (2022). The prevalence of osteoporosis in rheumatoid arthritis patient: a systematic review and meta-analysis. *Scientific Reports*, *12*(1). https://doi.org/10.1038/s41598-022-20016-x

Mosser, D. M., Hamidzadeh, K., & Goncalves, R. (2021). Macrophages and the maintenance of homeostasis. In *Cellular and Molecular Immunology* (Vol. 18, Issue 3, pp. 579–587). Springer Nature. https://doi.org/10.1038/s41423-020-00541-3

Muckenthaler, M. U., Rivella, S., Hentze, M. W., & Galy, B. (2017). A Red Carpet for Iron Metabolism. In *Cell* (Vol. 168, Issue 3, pp. 344–361). Cell Press. https://doi.org/10.1016/j.cell.2016.12.034

Multhoff, G., Molls, M., & Radons, J. (2012). Chronic inflammation in cancer development. In *Frontiers in Immunology* (Vol. 2, Issue JAN). https://doi.org/10.3389/fimmu.2011.00098

Myers, K. V., Amend, S. R., & Pienta, K. J. (2019). Targeting Tyro3, Axl and MerTK (TAM receptors): Implications for macrophages in the tumor microenvironment. In *Molecular Cancer* (Vol. 18, Issue 1). BioMed Central Ltd. https://doi.org/10.1186/s12943-019-1022-2

Nakaya, M., Tanaka, M., Okabe, Y., Hanayama, R., & Nagata, S. (2006). Opposite effects of Rho family GTPases on engulfment of apoptotic cells by macrophages. *Journal of Biological Chemistry*, *281*(13), 8836–8842. https://doi.org/10.1074/jbc.M510972200

Nakvasina, M. A., Holyavka, M. G., Artyukhov, V. G., Radchenko, M. S., & Lidokhova, O. V. (2023). Mechanisms of UV-induced human lymphocyte apoptosis. In *Biophysical Reviews* (Vol. 15, Issue 5, pp. 1257–1267). Springer Science and Business Media Deutschland GmbH. https://doi.org/10.1007/s12551-023-01142-w

Norris, P. C., Skulas-Ray, A. C., Riley, I., Richter, C. K., Kris-Etherton, P. M., Jensen, G. L., Serhan, C. N., & Maddipati, K. R. (2018). Identification of specialized pro-resolving mediator clusters from healthy adults after intravenous low-dose endotoxin and omega-3 supplementation: a methodological validation. *Scientific Reports*, *8*(1). https://doi.org/10.1038/s41598-018-36679-4

Pan, Y., Yu, Y., Wang, X., & Zhang, T. (2020). Tumor-Associated Macrophages in Tumor Immunity. In *Frontiers in Immunology* (Vol. 11). Frontiers Media S.A. https://doi.org/10.3389/fimmu.2020.583084

Park, B., Lee, J., Moon, H., Lee, G., Lee, D. H., Hoon Cho, J., & Park, D. (2015). Co-receptors are dispensable for tethering receptor-mediated phagocytosis of apoptotic cells. *Cell Death and Disease*, *6*(5). https://doi.org/10.1038/cddis.2015.140

Park, D., Tosello-Trampont, A. C., Elliott, M. R., Lu, M., Haney, L. B., Ma, Z., Klibanov, A. L., Mandell, J. W., & Ravichandran, K. S. (2007). BAI1 is an engulfment receptor for apoptotic cells upstream of the ELMO/Dock180/Rac module. *Nature*, *450*(7168), 430–434. https://doi.org/10.1038/nature06329

Park, S. Y., Kang, K. B., Thapa, N., Kim, S. Y., Lee, S. J., & Kim, I. S. (2008). Requirement of adaptor protein GULP during stabilin-2-mediated cell corpse engulfment. *Journal of Biological Chemistry*, *283*(16), 10593–10600. https://doi.org/10.1074/jbc.M709105200

Perrot, C. Y., Karampitsakos, T., & Herazo-Maya, J. D. (2023). Monocytes and macrophages: emerging mechanisms and novel therapeutic targets in pulmonary fibrosis. In *American Journal of Physiology - Cell Physiology* (Vol. 325, Issue 4, pp. C1046–C1057). American Physiological Society. https://doi.org/10.1152/ajpcell.00302.2023

Pfeifhofer-Obermair, C., Tymoszuk, P., Petzer, V., Weiss, G., & Nairz, M. (2018). Iron in the tumor microenvironment-connecting the dots. In *Frontiers in Oncology* (Vol. 8, Issue NOV). Frontiers Media S.A. https://doi.org/10.3389/fonc.2018.00549

Philpott, C. C., & Jadhav, S. (2019). The ins and outs of iron: Escorting iron through the mammalian cytosol. In *Free Radical Biology and Medicine* (Vol. 133, pp. 112–117). Elsevier Inc. https://doi.org/10.1016/j.freeradbiomed.2018.10.411

Post SM, Malaney P, Zhang X, Aitken MJL, Mak PY, Ruvolo VR, Yasuhiro T, Kozaki R, Chan LE, Ostermann LB, Konopleva M, Carter BZ, DiNardo C, Andreeff MD, Khoury JD, & Ruvolo PP. (2022). AXL/MERTK inhibitor ONO-7475 potently synergizes with venetoclax and overcomes venetoclax resistance to kill F LT 3-ITD acute myeloid leukemia. *Acute Myeloid Leukemia*.

Qiu, H., Shao, Z., Wen, X., Liu, Z., Chen, Z., Qu, D., Ding, X., & Zhang, L. (2023a). Efferocytosis: An accomplice of cancer immune escape. In *Biomedicine and Pharmacotherapy* (Vol. 167). Elsevier Masson s.r.l. https://doi.org/10.1016/j.biopha.2023.115540

Qiu, H., Shao, Z., Wen, X., Liu, Z., Chen, Z., Qu, D., Ding, X., & Zhang, L. (2023b). Efferocytosis: An accomplice of cancer immune escape. In *Biomedicine and Pharmacotherapy* (Vol. 167). Elsevier Masson s.r.l. https://doi.org/10.1016/j.biopha.2023.115540

Ravichandran, K. S., & Lorenz, U. (2007). Engulfment of apoptotic cells: Signals for a good meal. In *Nature Reviews Immunology* (Vol. 7, Issue 12, pp. 964–974). https://doi.org/10.1038/nri2214

Raymond, M. H., Davidson, A. J., Shen, Y., Tudor, D. R., Lucas, C. D., Morioka, S., Perry, J. S. A., Krapivkina, J., Perrais, D., Schumacher, L. J., Campbell, R. E., Wood, W., & Ravichandran, K. S. (2022). *Live cell tracking of macrophage efferocytosis during Drosophila embryo development in vivo*. https://www.science.org

Richeldi, L., du Bois, R. M., Raghu, G., Azuma, A., Brown, K. K., Costabel, U., Cottin, V., Flaherty, K. R., Hansell, D. M., Inoue, Y., Kim, D. S., Kolb, M., Nicholson, A. G., Noble, P. W., Selman, M., Taniguchi, H., Brun, M., Le Maulf, F., Girard, M., … Collard, H. R. (2014). Efficacy and Safety of Nintedanib in Idiopathic Pulmonary Fibrosis. *New England Journal of Medicine*, *370*(22), 2071–2082. https://doi.org/10.1056/nejmoa1402584

Rishi, G., Huang, G., & Subramaniam, V. N. (2021). Cancer: The role of iron and ferroptosis. In *International Journal of Biochemistry and Cell Biology* (Vol. 141). Elsevier Ltd. https://doi.org/10.1016/j.biocel.2021.106094

Sanchez-Alcar, J. A., Ault, J. G., Khodjakov, A., & Schneider, E. (2000). Increased mitochondrial cytochrome c levels and mitochondrial hyperpolarization precede camptothecin-induced apoptosis in Jurkat cells. In *Cell Death and Differentiation* (Vol. 7). www.nature.com/cdd

Sangaletti, S., Botti, L., Gulino, A., Lecis, D., Bassani, B., Portararo, P., Milani, M., Cancila, V., De Cecco, L., Dugo, M., Tripodo, C., & Colombo, M. P. (2021). SPARC regulation of PMN clearance protects from pristane-induced lupus and rheumatoid arthritis. *IScience*, *24*(6). https://doi.org/10.1016/j.isci.2021.102510

Schaer, D. J., Schaer, C. A., Buehler, P. W., Boykins, R. A., Schoedon, G., Alayash, A. I., & Schaffner, A. (2006). *CD163 is the macrophage scavenger receptor for native and chemically modified hemoglobins in the absence of haptoglobin*. https://doi.org/10.1182/blood-2005-03

Schett, G., & Neurath, M. F. (2018). Resolution of chronic inflammatory disease: universal and tissue-specific concepts. In *Nature Communications* (Vol. 9, Issue 1). Nature Publishing Group. https://doi.org/10.1038/s41467-018-05800-6

Seitz, H. M., Camenisch, T. D., Lemke, G., Shelton Earp, H., & Matsushima, G. K. (2007). Macrophages and Dendritic Cells Use Different Axl/Mertk/Tyro3 Receptors in Clearance of Apoptotic Cells 1. In *The Journal of Immunology* (Vol. 178). http://journals.aai.org/jimmunol/article-pdf/178/9/5635/1240257/zim00907005635.pdf

Serhan, C. N., & Levy, B. D. (2018). Resolvins in inflammation: Emergence of the pro-resolving superfamily of mediators. In *Journal of Clinical Investigation* (Vol. 128, Issue 7, pp. 2657–2669). American Society for Clinical Investigation. https://doi.org/10.1172/JCI97943

Serhan, C. N., Yang, R., Martinod, K., Kasuga, K., Pillai, P. S., Porter, T. F., Oh, S. F., & Spite, M. (2009). Maresins: Novel macrophage mediators with potent antiinflammatory and proresolving actions. *Journal of Experimental Medicine*, *206*(1), 15–23. https://doi.org/10.1084/jem.20081880

Shurin, M. R., Potapovich, A. I., Tyurina, Y. Y., Tourkova, I. L., Shurin, G. V., & Kagan, V. E. (2009). Recognition of live phosphatidylserine - labeled tumor cells by dendritic cells: A

novel approach to immunotherapy of skin cancer. *Cancer Research*, *69*(6), 2487–2496. https://doi.org/10.1158/0008-5472.CAN-08-2611

Singh, A., Chakraborty, S., Wong, S. W., Hefner, N. A., Stuart, A., Qadir, A. S., Mukhopadhyay, A., Bachmaier, K., Shin, J.-W., Rehman, J., & Malik, A. B. (2022). *Nanoparticle targeting of de novo profibrotic macrophages mitigates lung fibrosis*. https://doi.org/10.1073/pnas

Singh, A., Smedley, G. D., Rose, J. G., Fredriksen, K., Zhang, Y., Li, L., & Yuan, S. H. (2024). A high efficiency precision genome editing method with CRISPR in iPSCs. *Scientific Reports*, *14*(1). https://doi.org/10.1038/s41598-024-60766-4

Smith, M. D. (2011). The Normal Synovium. In *The Open Rheumatology Journal* (Vol. 5).

Smolen, J. S., Aletaha, D., Barton, A., Burmester, G. R., Emery, P., Firestein, G. S., Kavanaugh, A., McInnes, I. B., Solomon, D. H., Strand, V., & Yamamoto, K. (2018). Rheumatoid arthritis. *Nature Reviews Disease Primers*, *4*. https://doi.org/10.1038/nrdp.2018.1

Soares, M. P., & Hamza, I. (2016). Macrophages and Iron Metabolism. In *Immunity* (Vol. 44, Issue 3, pp. 492–504). Cell Press. https://doi.org/10.1016/j.immuni.2016.02.016

Stöhr, R., Deckers, N., Schurgers, L., Marx, N., & Reutelingsperger, C. P. (2018). AnnexinA5-pHrodo: a new molecular probe for measuring efferocytosis. *Scientific Reports*, *8*(1). https://doi.org/10.1038/s41598-018-35995-z

Summers, R. J., Jain, J., Vasileiadi, E., Smith, B., Stout, M., Kelvin, J., Wang, X., Frye, S. V, Earp, H. S., Tyner, J. W., Dreaden, E., DeRyckere, D., & Graham, D. K. (2021). Therapeutic Targeting of Mertk and BCL-2 in T-Cell and Early T-Precursor Acute Lymphoblastic Leukemia. *Blood*, *138*(Supplement 1), 1184–1184. https://doi.org/10.1182/blood-2021-151726

Tajbakhsh, A., Gheibi hayat, S. M., Movahedpour, A., Savardashtaki, A., Loveless, R., Barreto, G. E., Teng, Y., & Sahebkar, A. (2021). The complex roles of efferocytosis in cancer development, metastasis, and treatment. In *Biomedicine and Pharmacotherapy* (Vol. 140). Elsevier Masson s.r.l. https://doi.org/10.1016/j.biopha.2021.111776

Takata, K., Kozaki, T., Lee, C. Z. W., Thion, M. S., Otsuka, M., Lim, S., Utami, K. H., Fidan, K., Park, D. S., Malleret, B., Chakarov, S., See, P., Low, D., Low, G., Garcia-Miralles, M., Zeng, R., Zhang, J., Goh, C. C., Gul, A., … Ginhoux, F. (2017). Induced-Pluripotent-Stem-Cell-Derived Primitive Macrophages Provide a Platform for Modeling Tissue-Resident Macrophage Differentiation and Function. *Immunity*, *47*(1), 183-198.e6. https://doi.org/10.1016/j.immuni.2017.06.017

Tang, M., Chen, Z., Wu, D., & Chen, L. (2018). Ferritinophagy/ferroptosis: Iron-related newcomers in human diseases. In *Journal of Cellular Physiology* (Vol. 233, Issue 12, pp. 9179–9190). Wiley-Liss Inc. https://doi.org/10.1002/jcp.26954

Tański, W., Chabowski, M., Jankowska-Polańska, B., & Jankowska, E. A. (2021). *Iron metabolism in patients with rheumatoid arthritis*.

Theurl, I., Aigner, E., Theurl, M., Nairz, M., Seifert, M., Schroll, A., Sonnweber, T., Eberwein, L., Witcher, D. R., Murphy, A. T., Wroblewski, V. J., Wurz, E., Datz, C., & Weiss, G. (2009). Regulation of iron homeostasis in anemia of chronic disease and iron deficiency anemia: Diagnostic and therapeutic implications. *Blood*, *113*(21), 5277–5286. https://doi.org/10.1182/blood-2008-12-195651

Truman, L. A., Ford, C. A., Pasikowska, M., Pound, J. D., Wilkinson, S. J., Dumitriu, I. E., Melville, L., Melrose, L. A., Ogden, C. A., Nibbs, R., Graham, G., Combadiere, C., & Gregory, C. D. (2008). *CX3CL1/fractalkine is released from apoptotic lymphocytes to stimulate macrophage chemotaxis*. https://doi.org/10.1182/blood-2008-06

Trzebanski, S., Kim, J. S., Larossi, N., Raanan, A., Kancheva, D., Bastos, J., Haddad, M., Solomon, A., Sivan, E., Aizik, D., Kralova, J. S., Gross-Vered, M., Boura-Halfon, S., Lapidot, T., Alon, R., Movahedi, K., & Jung, S. (2024). Classical monocyte ontogeny dictates their functions and fates as tissue macrophages. *Immunity*, *57*(6), 1225-1242.e6. https://doi.org/10.1016/j.immuni.2024.04.019

Ullal, A. J., & Pisetsky, D. S. (2010). The release of microparticles by Jurkat leukemia T cells treated with staurosporine and related kinase inhibitors to induce apoptosis. *Apoptosis*, *15*(5), 586–596. https://doi.org/10.1007/s10495-010-0470-3

Urbano, P. C. M., Soccol, V. T., Teixeira, V. N., Oliveira, P. G., Filippin, L. I., Bonat, W. H., de Oliveira, C., Rossi, G. R., Xavier, R. M., & Azevedo, V. F. (2015). Effect of pegylated phosphatidylserine-containing liposomes in experimental chronic arthritis. *BMC Pharmacology and Toxicology*, *16*(1). https://doi.org/10.1186/s40360-015-0022-0

Uribe-Querol, E., & Rosales, C. (2020). Phagocytosis: Our Current Understanding of a Universal Biological Process. In *Frontiers in Immunology* (Vol. 11). Frontiers Media S.A. https://doi.org/10.3389/fimmu.2020.01066

Wang, X., Du, W., Li, Y., Yang, H.-H., Zhang, Y., Akbar, R., Morgan, H., Peng, T., Chen, J., Sadayappan, S., Hu, Y.-C., Fan, Y., Huang, W., & Fan, G.-C. (2024). *Macrophage-enriched Sectm1a promotes efficient efferocytosis to attenuate ischemia/reperfusion-induced cardiac injury*. https://doi.org/10.1172/jci

Wanke, F., Gutbier, S., Rümmelin, A., Steinberg, M., Hughes, L. D., Koenen, M., Komuczki, J., Regan-Komito, D., Wagage, S., Hesselmann, J., Thoma, R., Brugger, D., Christopeit, T., Wang, H., Point, F., Hallet, R., Ghosh, S., Rothlin, C. V., Patsch, C., & Geering, B. (2021). Ligand-dependent kinase activity of MERTK drives efferocytosis in human iPSC-derived macrophages. *Cell Death and Disease*, *12*(6). https://doi.org/10.1038/s41419-021-03770-0

Westman, J., & Grinstein, S. (2021). Determinants of Phagosomal pH During Host-Pathogen Interactions. In *Frontiers in Cell and Developmental Biology* (Vol. 8). Frontiers Media S.A. https://doi.org/10.3389/fcell.2020.624958

Weyand, C. M., & Goronzy, J. J. (2021). The immunology of rheumatoid arthritis. In *Nature Immunology* (Vol. 22, Issue 1, pp. 10–18). Nature Research. https://doi.org/10.1038/s41590-020-00816-x

Winn, N. C., Volk, K. M., & Hasty, A. H. (2020). Regulation of tissue iron homeostasis: The macrophage “ferrostat.” In *JCI Insight* (Vol. 5, Issue 2). American Society for Clinical Investigation. https://doi.org/10.1172/jci.insight.132964

Wu, J., Feng, Z., Chen, L., Li, Y., Bian, H., Geng, J., Zheng, Z. H., Fu, X., Pei, Z., Qin, Y., Yang, L., Zhao, Y., Wang, K., Chen, R., He, Q., Nan, G., Jiang, X., Chen, Z. N., & Zhu, P. (2022). TNF antagonist sensitizes synovial fibroblasts to ferroptotic cell death in collagen-induced arthritis mouse models. *Nature Communications*, *13*(1). https://doi.org/10.1038/s41467-021-27948-4

Wynn, T. A., & Barron, L. (2010). Macrophages: Master regulators of inflammation and fibrosis. In *Seminars in Liver Disease* (Vol. 30, Issue 3, pp. 245–257). https://doi.org/10.1055/s-0030-1255354

Wynn, T. A., & Ramalingam, T. R. (2012). Mechanisms of fibrosis: Therapeutic translation for fibrotic disease. In *Nature Medicine* (Vol. 18, Issue 7, pp. 1028–1040). https://doi.org/10.1038/nm.2807

Yang, S., Zhao, M., & Jia, S. (2023). Macrophage: Key player in the pathogenesis of autoimmune diseases. In *Frontiers in Immunology* (Vol. 14). Frontiers Media S.A. https://doi.org/10.3389/fimmu.2023.1080310

Ying, J.-F., Lu, Z.-B., Fu, L.-Q., Tong, Y., Wang, Z., Li, W.-F., & Mou, X.-Z. (2021). The role of iron homeostasis and iron-mediated ROS in cancer. In *Am J Cancer Res* (Vol. 11, Issue 5). www.ajcr.us/

Zhang, F., Ayaub, E. A., Wang, B., Puchulu-Campanella, E., Li, Y., Hettiarachchi, S. U., Lindeman, S. D., Luo, Q., Rout, S., Srinivasarao, M., Cox, A., Tsoyi, K., Nickerson-Nutter, C., Rosas, I. O., & Low, P. S. (2020). Reprogramming of profibrotic macrophages for treatment of bleomycin-induced pulmonary fibrosis. *EMBO Molecular Medicine*, *12*(8). https://doi.org/10.15252/emmm.202012034

Zhang, Y. Y., Han, Y., Li, W. N., Xu, R. H., & Ju, H. Q. (2024). Tumor iron homeostasis and immune regulation. In *Trends in Pharmacological Sciences* (Vol. 45, Issue 2, pp. 145–156). Elsevier Ltd. https://doi.org/10.1016/j.tips.2023.12.003

Zhao, H., Tang, C., Wang, M., Zhao, H., & Zhu, Y. (2023a). Ferroptosis as an emerging target in rheumatoid arthritis. In *Frontiers in Immunology* (Vol. 14). Frontiers Media SA. https://doi.org/10.3389/fimmu.2023.1260839

Zhao, H., Tang, C., Wang, M., Zhao, H., & Zhu, Y. (2023b). Ferroptosis as an emerging target in rheumatoid arthritis. In *Frontiers in Immunology* (Vol. 14). Frontiers Media SA. https://doi.org/10.3389/fimmu.2023.1260839

Zhao, H., Wu, L., Yan, G., Chen, Y., Zhou, M., Wu, Y., & Li, Y. (2021). Inflammation and tumor progression: signaling pathways and targeted intervention. In *Signal Transduction and Targeted Therapy* (Vol. 6, Issue 1). Springer Nature. https://doi.org/10.1038/s41392-021-00658-5

Zheng, Y., Wei, K., Jiang, P., Zhao, J., Shan, Y., Shi, Y., Zhao, F., Chang, C., Li, Y., Zhou, M., Lv, X., Guo, S., & He, D. (2024). Macrophage polarization in rheumatoid arthritis: signaling pathways, metabolic reprogramming, and crosstalk with synovial fibroblasts. In *Frontiers in Immunology* (Vol. 15). Frontiers Media SA. https://doi.org/10.3389/fimmu.2024.1394108

Zhou, Q., Meng, Y., Li, D., Yao, L., Le, J., Liu, Y., Sun, Y., Zeng, F., Chen, X., & Deng, G. (2024). Ferroptosis in cancer: From molecular mechanisms to therapeutic strategies. In *Signal Transduction and Targeted Therapy* (Vol. 9, Issue 1). Springer Nature. https://doi.org/10.1038/s41392-024-01769-5

Zhou, Y., Wang, Y., Chen, H., Xu, Y., Luo, Y., Deng, Y., Zhang, J., & Shao, A. (2021). Immuno-oncology: are TAM receptors in glioblastoma friends or foes? In *Cell Communication and Signaling* (Vol. 19, Issue 1). BioMed Central Ltd. https://doi.org/10.1186/s12964-020-00694-8

6. Appendix:

6.1 Appendix A: Initial Assay Development Using Incucyte Live-Cell Imaging System

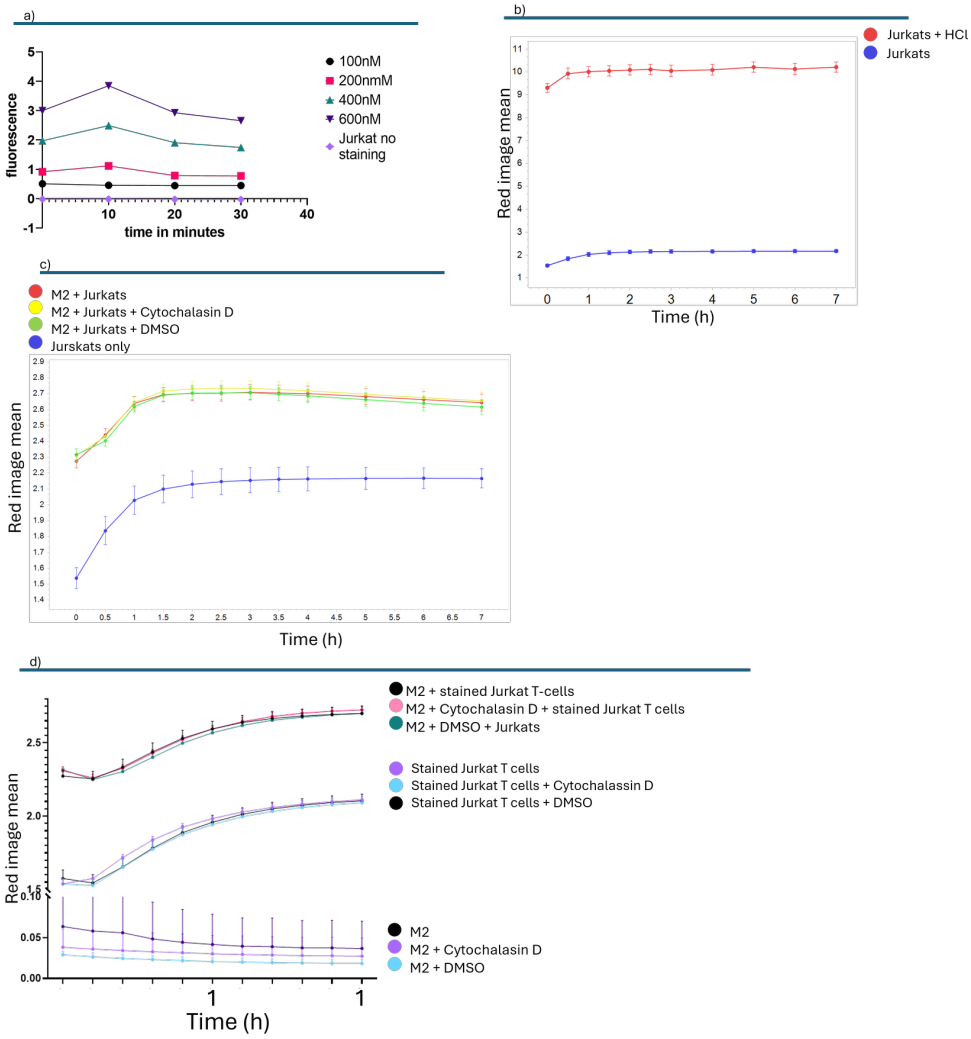

Figure 6-1 Initial Assay Development Using Incucyte Live-Cell Imaging System a) *Titration of pHrodo™ Red SE on apoptotic Jurkat T cells.* Apoptosis was induced with 1 µM staurosporine for 3 hours. Jurkat cells were subsequently stained with increasing concentrations of pHrodo™ Red SE (100 nM, 200 nM, 400 nM, and 600 nM). A concentration of 400 nM was selected for further experiments as it provided a robust and clearly detectable fluorescent signal without evidence of saturation. b) *Acidification assay to simulate phagolysosomal environment.* Jurkat T cells stained with 400 nM pHrodo™ Red SE were treated with HCl to mimic the acidic environment of the phagolysosome. A clear distinction in fluorescence was observed between untreated and HCl-treated cells, validating the pH-sensitivity of the dye. c) *Efferocytosis assay using M2-like macrophages.* Efferocytosis of pHrodo™ Red-labeled apoptotic Jurkat T cells was assessed using M2-like macrophages derived from monocyte-derived macrophages (MDMs) differentiated with M-CSF, IL-10, and dexamethasone. Over a 7-hour period, there was no significant difference in fluorescence kinetics between untreated macrophage conditions and those treated with the actin polymerization inhibitor Cytochalasin D (yellow), indicating a lack of detectable efferocytic activity. Jurkat-only controls displayed comparable signal kinetics to efferocytosis conditions, suggesting dye signal may not be specific to phagocytosis. d) *Validation in independent M2 differentiation and enhanced time-resolution imaging.* Findings were confirmed in an independent M2 differentiation experiment with higher temporal resolution. Fluorescence kinetics remained indistinguishable between Jurkat-only and macrophage co-culture conditions, and Cytochalasin D had no observable inhibitory effect. Based on these results, this approach was not pursued further for efferocytosis quantification.

6.2 Appendix B Titration of Mφ Antibodies

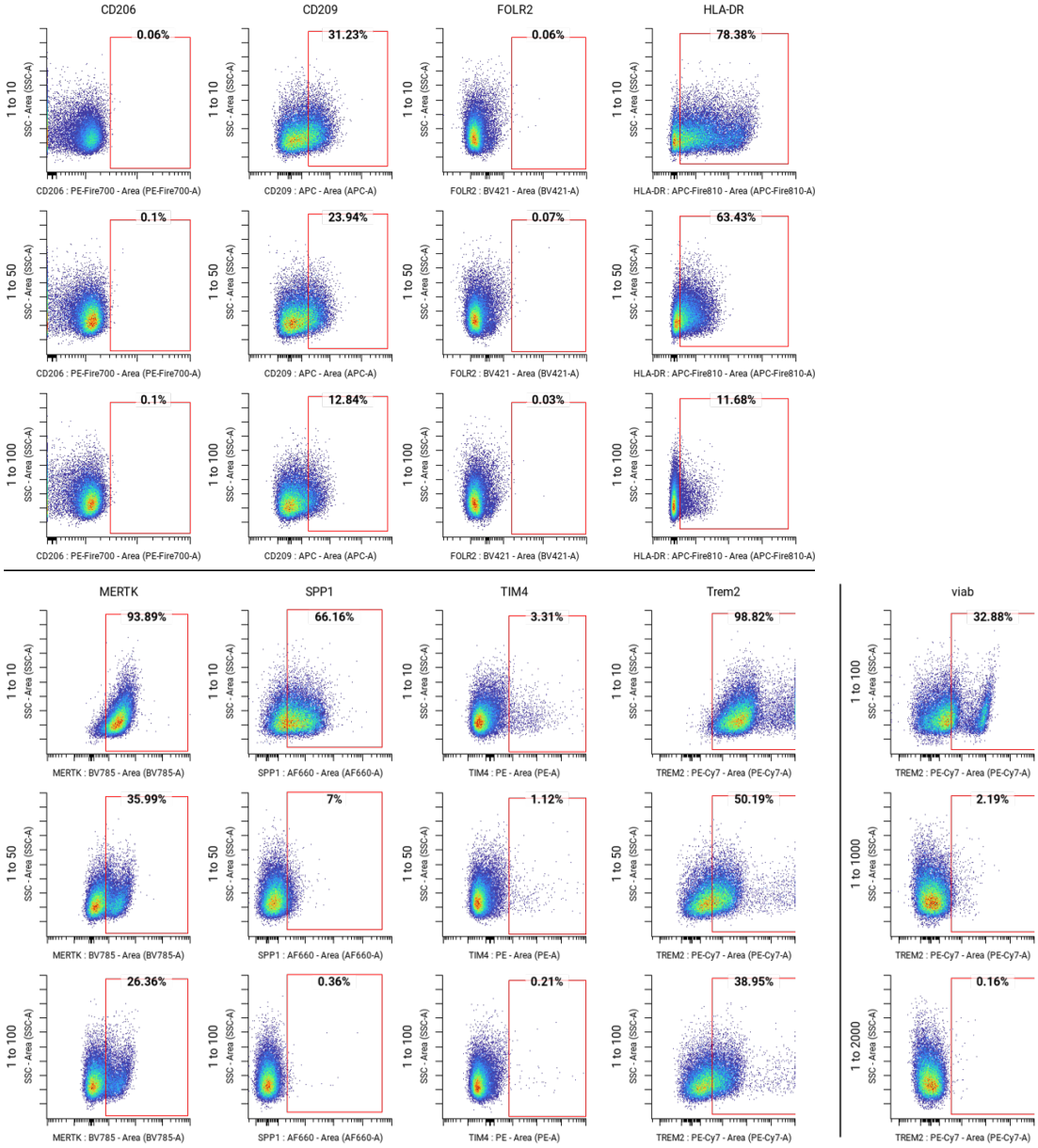

Figure 6-2 Mφ antibody titration. Antibody titration based on previous titrations done in our team for conventional flow cytometry. 1 to 10 1 to 50 and 1 to 100 dilutions were tested.

6.3 Appendix C - iMφ Sorting Strategy

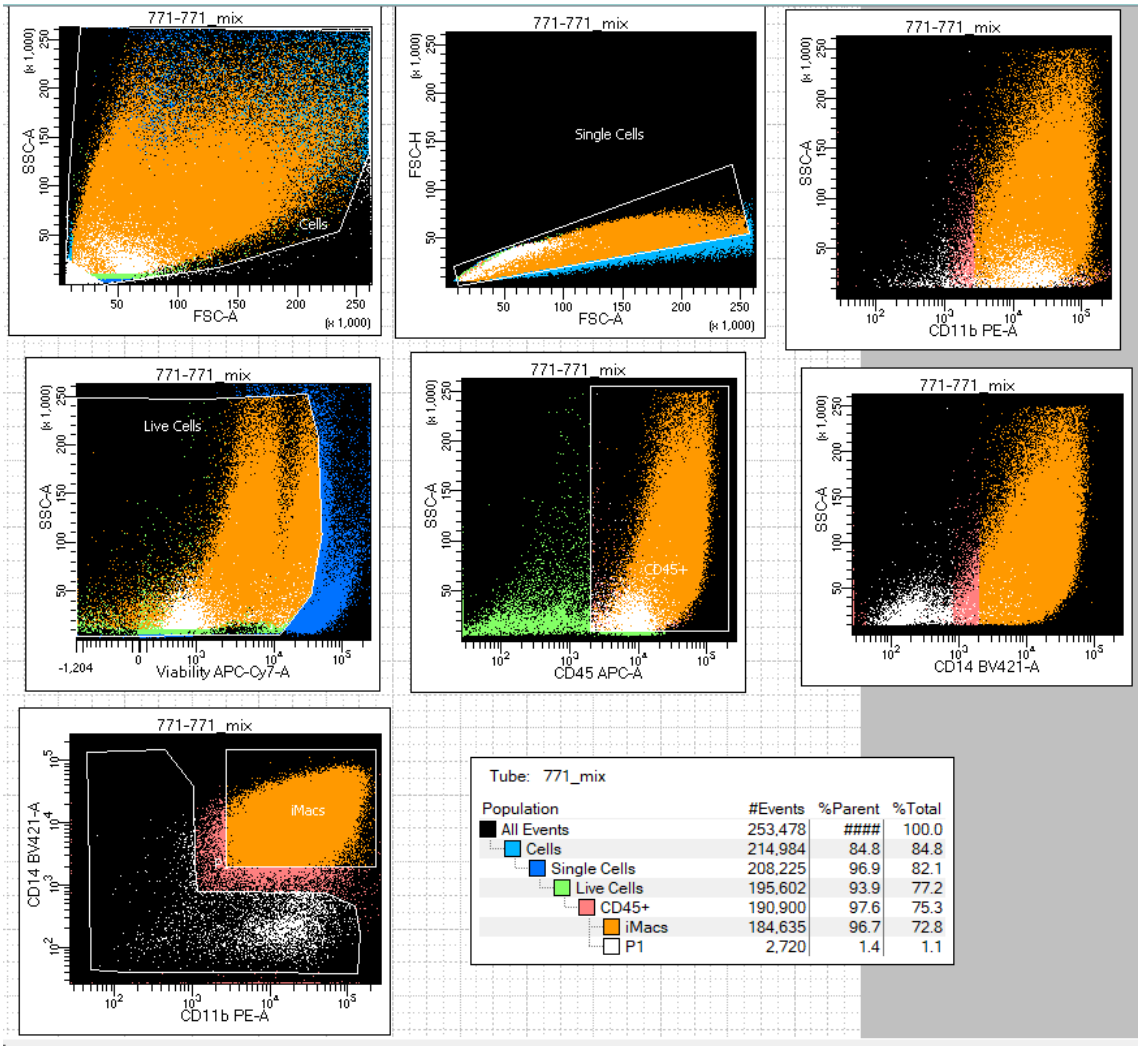

Figure 6-3 Sorting strategy of iMφ post differentiation. iMφ were sorted on day 28 and day 42 of differentiation protocol. Supernatants including the floating cells were collected and pooled together. Staining was performed regarding general staining protocol. iMφ population was gated based on debtry and doublet exclusion. Then we gated for viability (Zombie NIR). From this viable population, we identified CD45 positive cells (75.3% of total cells) and from these we further identified macrophages based on CD14 and CD11b positive signal, resulting in a 72,8% positive fraction if iMφ. Positive gates were created using unstained and single stained controls. Sorting was performed on FACS Aria Fusion II.

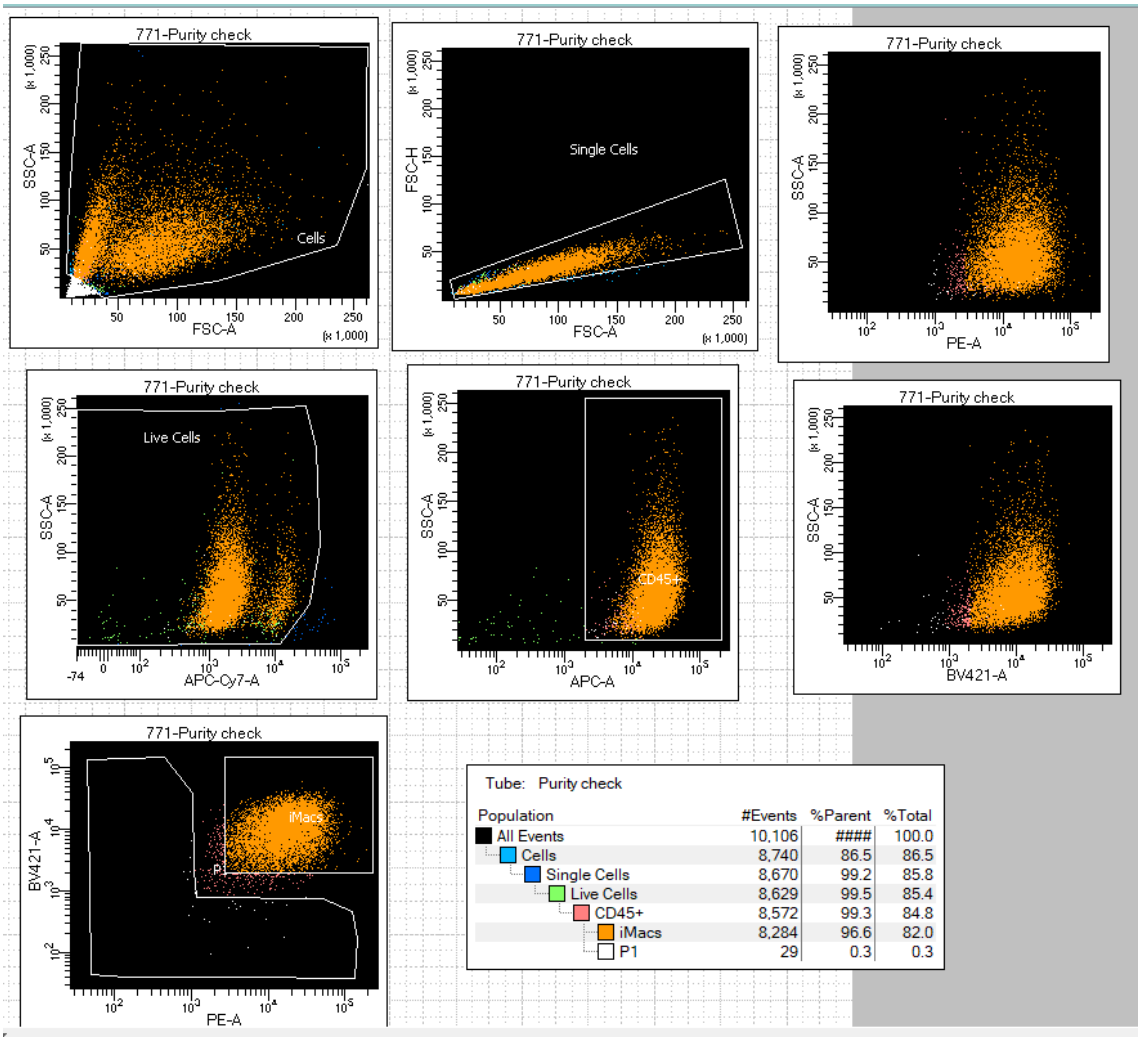

Figure 6-4 Puritiy check of sorted iMφ post differentiation. iMφ were sorted on day 28 and day 42 of differentiation protocol. Supernatants including the floating cells were collected and pooled together. Staining was performed regarding general staining protocol. iMφ population was gated based on Debry and doublet exclusion. Then we gated for viability (Zombie NIR). From this viable population, we identified CD45 positive cells (75.3% of total cells) and from these we further identified macrophages based on CD14 and CD11b positive signal. Purity checked revealed a 82.0% are iMφ and survived the sorting process. Positive gates were created using unstained and single stained controls. Sorting was performed on FACS Aria Fusion II.

6.4 Appendix D – iMφ Platform Characterization Across Harvests

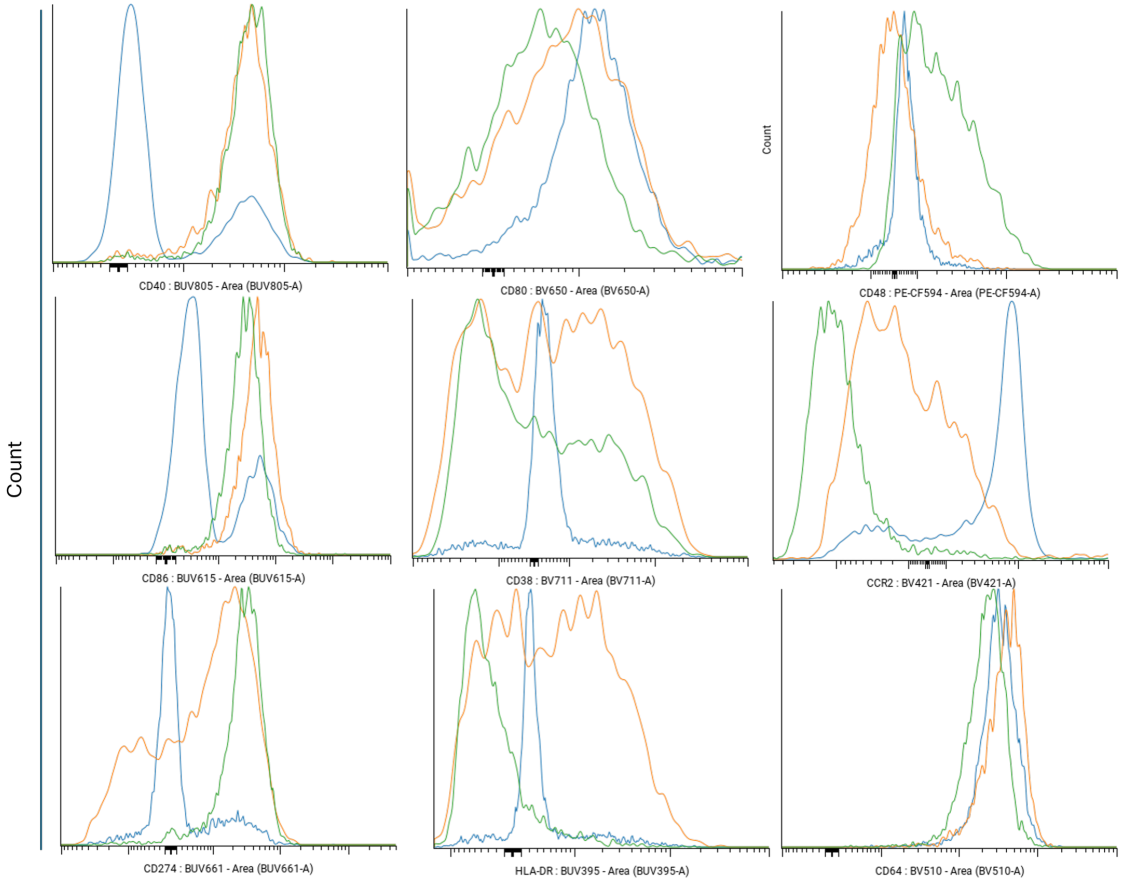

Figure 6-5 Multi-spectral flow cytometry analysis of efferocytosis-associated marker expression in sorted iMφ across independent differentiation harvests. iMφ were pre-gated to exclude debris, doublets, non-viable cells. and CD45 negative cells. iMφ were independently differentiated and harvested at two timepoints: Harvest 1 (orange), collected on day 28 and maintained in post-differentiation culture until analysis, and Harvest 2 (green), collected on day 42. All samples were stained and analyzed on day 46 using a multi-spectral flow cytometer. Unstained control from Harvest 1 is shown in blue. Marker expression profiles are overlaid to compare efferocytosis-associated phenotypes between harvests. Slight decrease in TREM2 and FOLR2 expression from Harvest one to Harvest two. Expression of CD40, CD86, CD274. CD48 only expressed in Harvest 2 . N=4. Data acquisition was performed on a SONY ID7000 cytometer with spectral unmixing and autofluorescence correction. Downstream analysis was conducted using CellEngine.

6.5 Appendix E – Panels used

a) Panel used for assay optimization experiments (Chapter 3.1.11, 3.1.12)

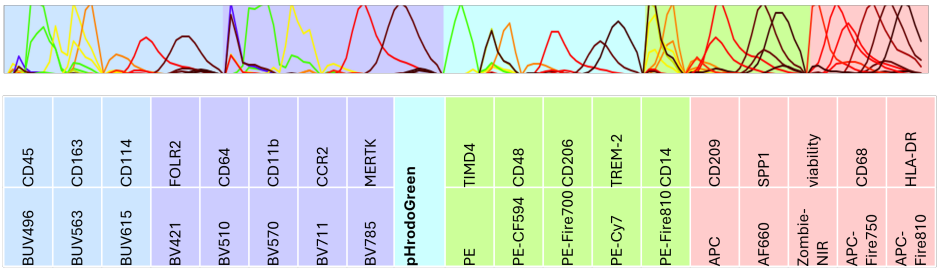

b) Panel used for iMicroglia testing (Chapter 3.2.1)

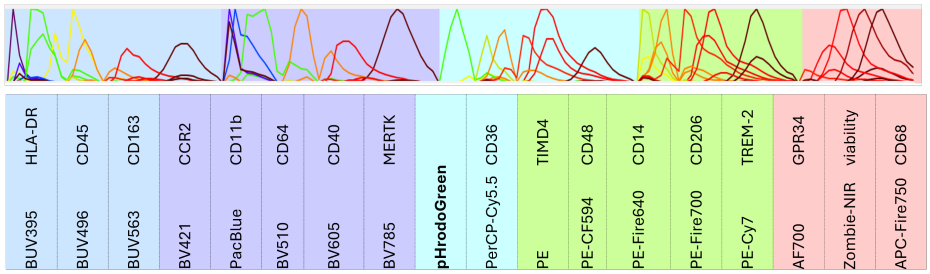

c) Panel used for Perturbations and platform comparison (Chapters 3.2.1, 3.2.2)

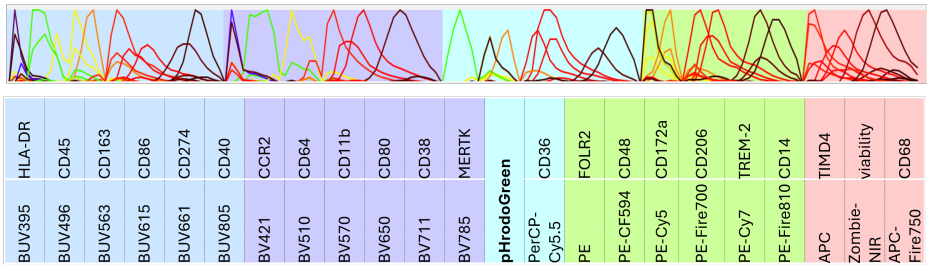

d) Panel used for iron metabolism experiment on MDMs (Chapter 3.1.16)

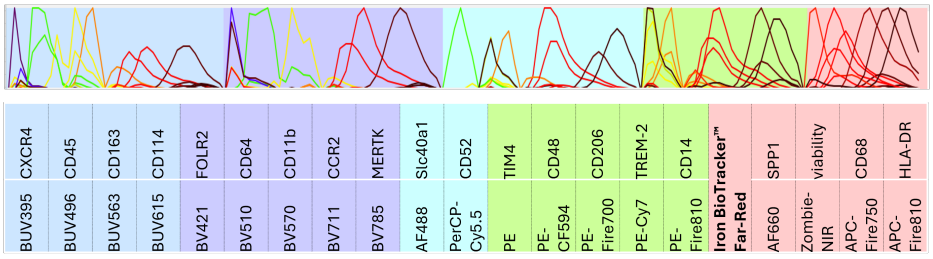

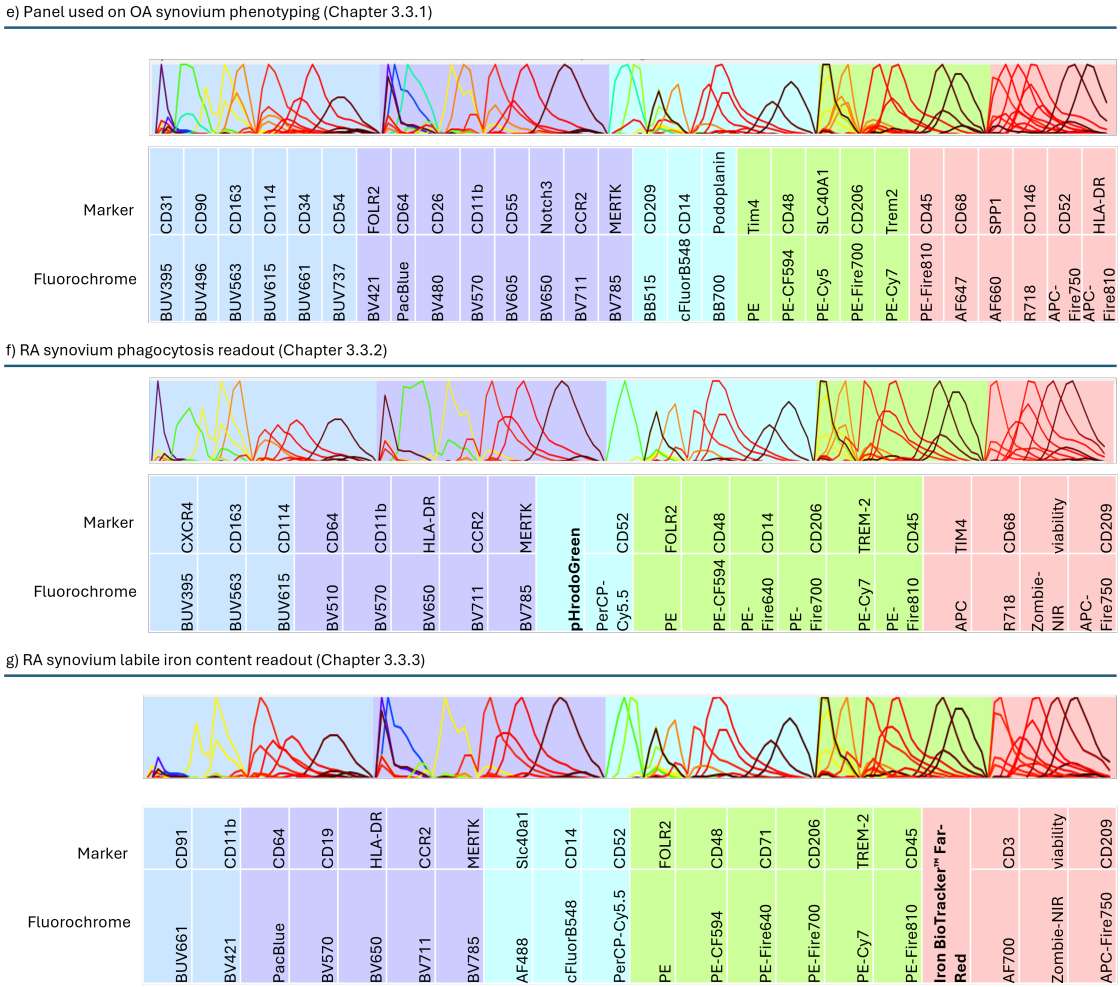

Figure 6-6 Flow cytometry panels used for various experimental setups. Colors indicate the excitation laser lines: blue = 355 nm, purple = 405 nm, turquoise = 488 nm, green = 561 nm, and red = 637 nm. a) Panel used for efferocytosis assay optimization. pHrodo Green was measured exclusively using the 488 nm laser to minimize spectral spillover and prevent false-positive signals. Markers included CD45, CD64, and CD11b as general leukocyte markers; CD163, CD206, FOLR2, TREM2, MERTK, and TIMD4 as markers associated with tissue-resident macrophages and efferocytosis; CD48 as an immune-regulatory marker; CCR2 as a marker of infiltrating macrophages; CD114 as a myeloid lineage marker; and HLA-DR as a marker of antigen presentation. b) Panel used for iMicroglia characterization, with an expanded marker set including GPR34, a microglia-specific marker. c) Panel used for perturbation studies employing pharmacological inhibitors and for platform comparisons between monocyte-derived macrophages (MDMs) and iPSC-derived macrophages. d) Panel used for iron metabolism studies, incorporating antibodies against iron transporters such as CD91, CD71, and SLC40A1. Iron Tracker signal was acquired using the 637 nm (red) laser. e) Panel used for osteoarthritis (OA) phenotyping. In addition to macrophage markers, the panel includes structural cell markers such as podoplanin, CD90, CD55, and Notch3. f) Panel used for pilot phagocytosis assays, containing macrophage and leukocyte markers. pHrodo Green-labeled *E. coli* bioparticles were detected on the 488 nm laser. g) Panel used for labile iron assays in rheumatoid arthritis (RA) synovial tissue. This panel included additional iron-specific markers as well as CD19 and CD3 to identify B and T cells, respectively, alongside monocyte/macrophage markers.

6.6 Appendix F: CD45 negative fraction over time

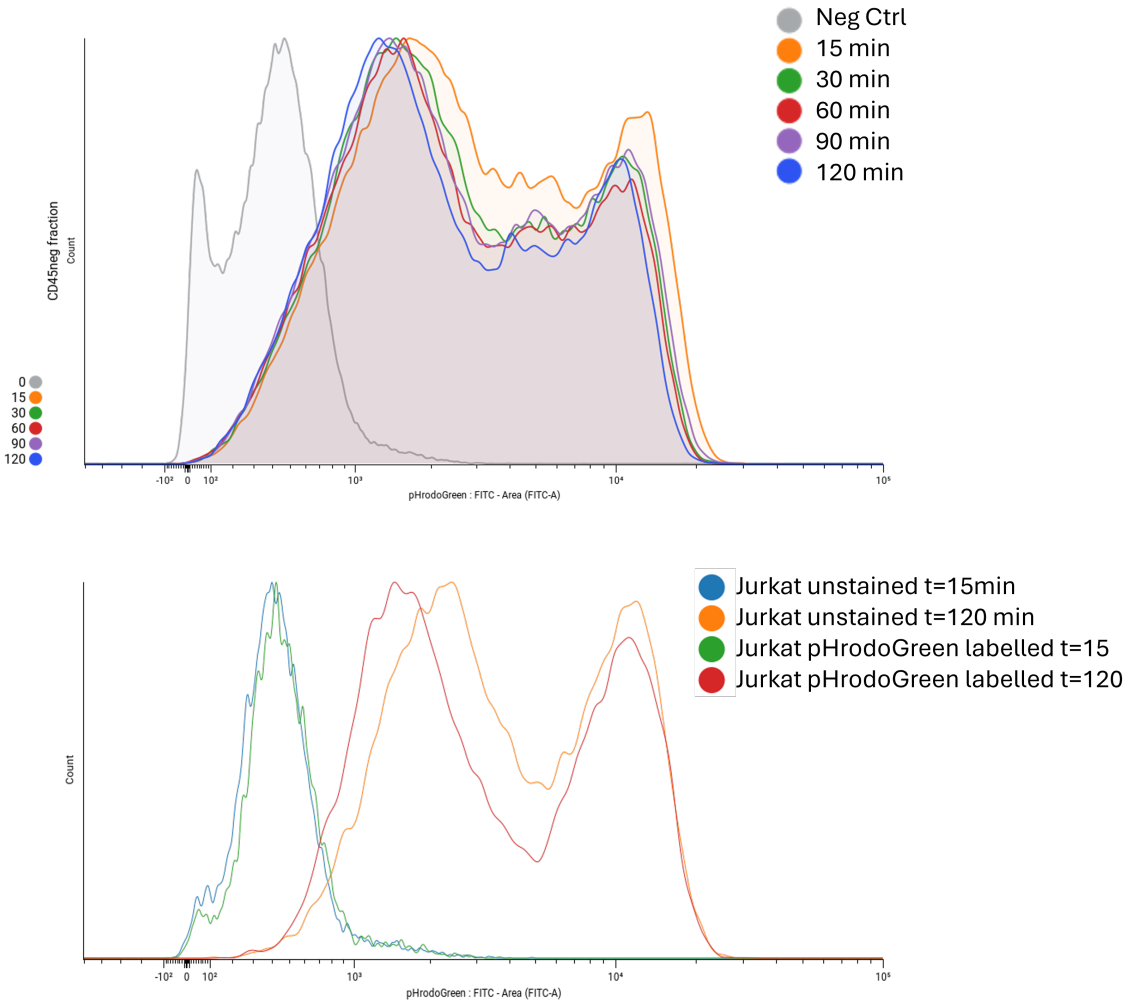

Figure 6-7 Additional efferocytosis control. A= CD45 negative fraction pHrodoGreen dynamics over time. a) Histograms represent the increase in pHrodo™ Green fluorescence signal at 15, 30, 60, 90, and 120 minutes, as measured on the SONY ID7000 analyzer. Jurkat T cells were not removed from the co-culture during the time course. *N = 2* b) Jurkats only wells. Detected at T = 15 nad t =120 minutes. Data acquisition was performed using the SONY ID7000 software with unmixing and autofluorescence correction. Downstream analysis was conducted using Cell Engine. Data shown are representative of *N = 2* independent experiments.

6.7 Appendix G: Capacity for efferocytosis of apoptotic Jurkat T cells across in vitro macrophage platforms

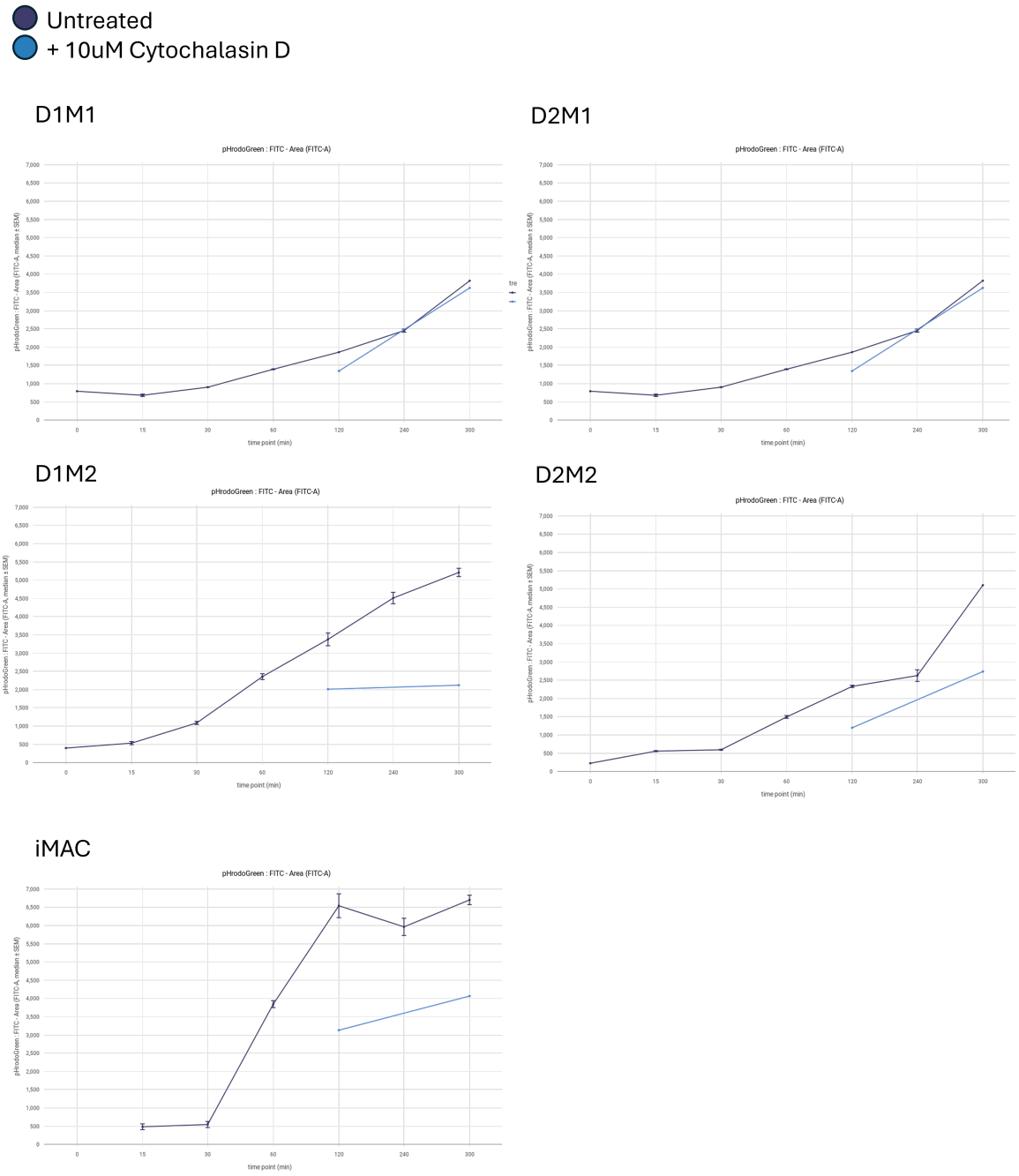

Figure 6-8 Supplementary material for figure 3-20 .Capacity for efferocytosis of apoptotic Jurkat T cells across in vitro macrophages. Quantification of efferocytosis kinetics measured as median pHrodo™ Green fluorescence intensity over time. Comparison of pHrodo™ Green fluorescence in untreated M1-like, M2-like and iPSC-derved macrophages (dark blue) versus M1-like, M2-like and iPSC-derved macrophages pre-treated with 10 µM Cytochalasin D, an actin polymerization inhibitor (light blue), and exposed to apoptotic Jurkat T cells. Cytochalasin D treatment significantly impaired efferocytosis capacity. *(n = 4 per condition)*. Data were acquired using the SONY ID7000 spectral flow cytometer, unmixed and autofluorescence-corrected using SONY ID7000 software. Data analysis including histogram and plot generation was performed with CellEngine.

6.8 Appendix H: Gating strategy used for platform comparison.

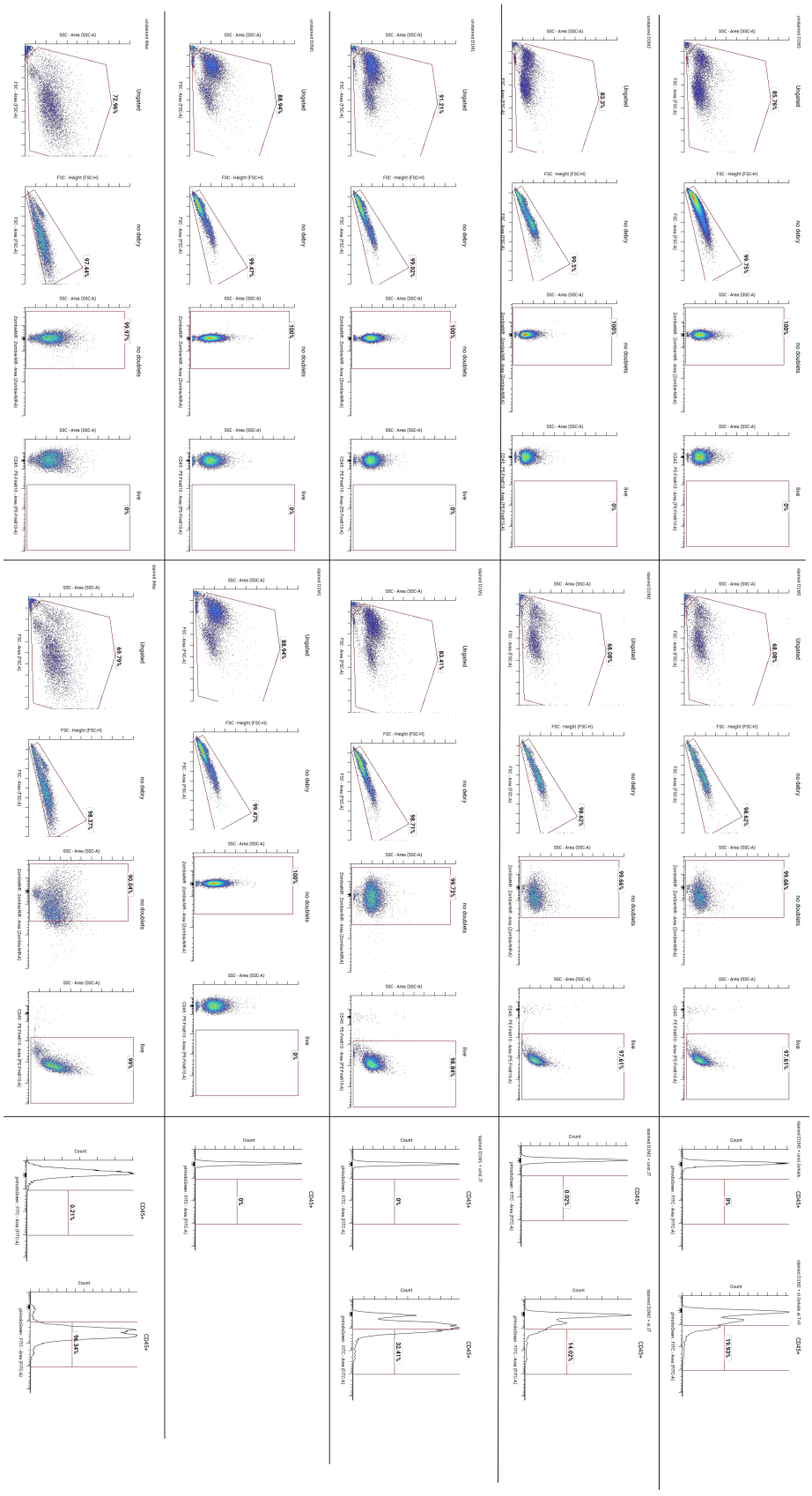

Figure 6-9 Gating strategy used for platform comparison. For all conditions, debris was excluded based on FSC-A vs. SSC-A, and doublets were excluded using FSC-A vs. FSC-H on unstained control samples. Viable cells were gated as

Zombie NIR-negative, and macrophages were identified by CD45 positivity. To define the gate for pHrodo Green-positive signal, pre-labelled macrophages incubated with non-labelled apoptotic Jurkat T cells were used. The positive pHrodo-Green gate was set on the CD45+ fraction to exclude non-bound Jurkat T cells, which were not stained with theantibody cocktails. Stained macrophages were chosen for this purpose, as they exhibited higher baseline fluorescence in the pHrodo Green channel compared to unstained controls and the allow discrimination from Jurkat T cells.

6.9 Appendix I: Platform comparison based on marker expression

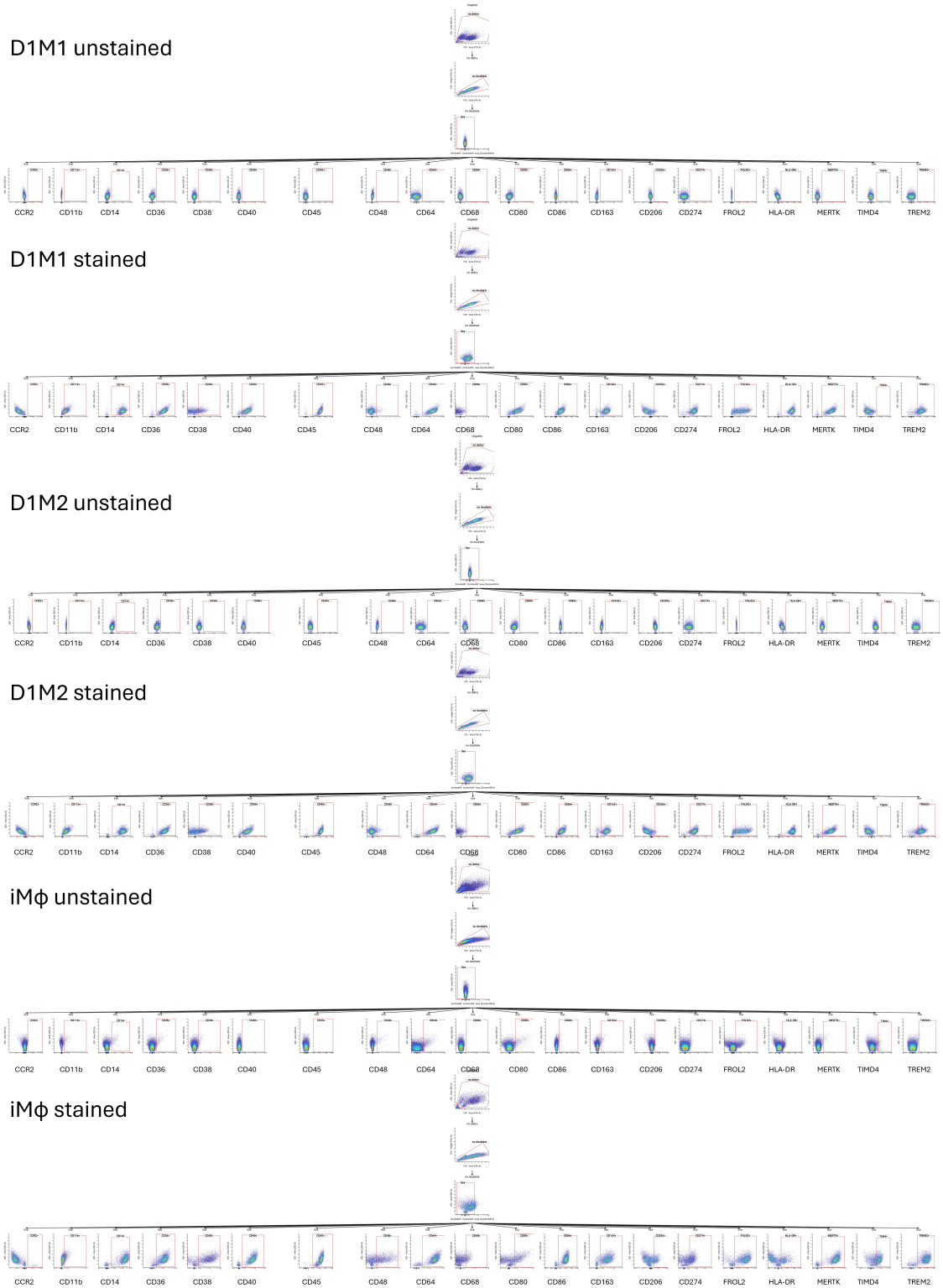

Figure 6-10 Supplementary Material: Supporting data for the heatmap presented in Figure 3-18. Marker expression profiles for different macrophage platforms, comparing stained versus unstained samples. All markers were analyzed within the live cell gate (Zombie NIR-negative), following exclusion of debris and doublets. Positive and negative gates were defined based on the corresponding unstained controls.

6.10 Appendix J: Detect iron metabolism in macrophages and allows phenotyping of iron metabolism associated markers

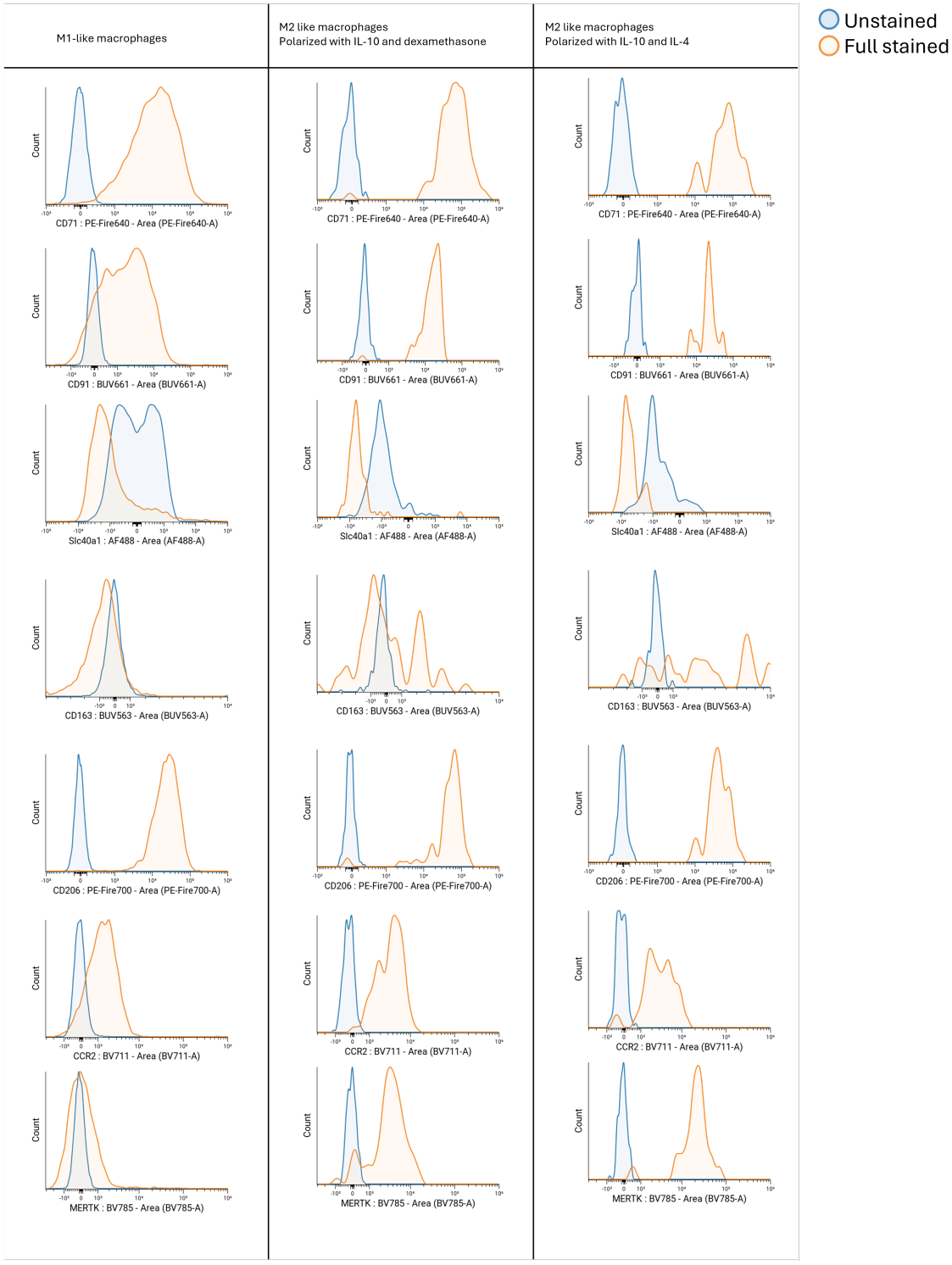

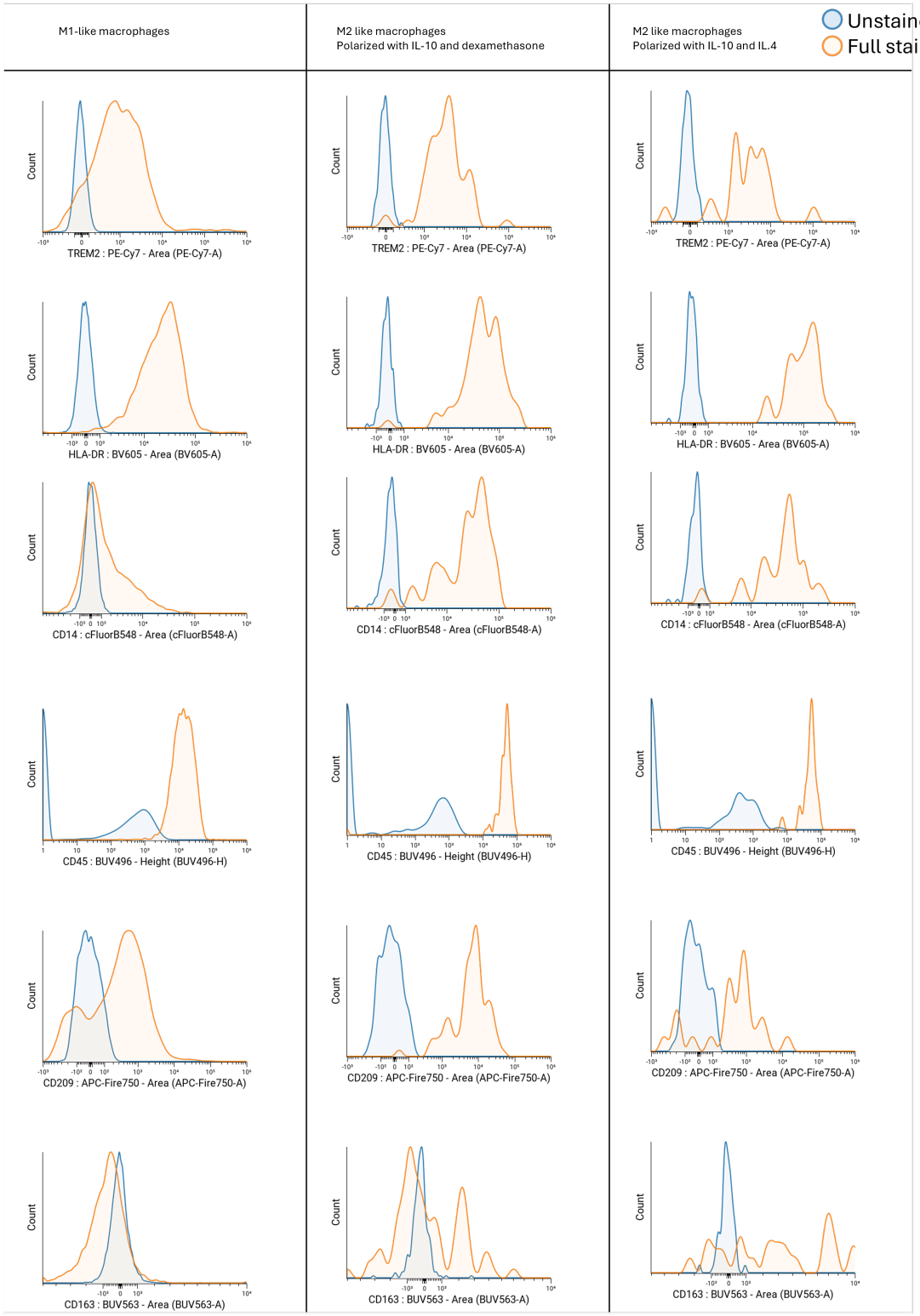

Figure 6-11 Supplementary Material: Proof-of-principle for an iron metabolism assay in macrophage subtypes. Histograms display the expression of surface markers, comparing unstained controls (blue) with fully stained samples (orange). Macrophage subtypes include M1-like macrophages polarized with GM-CSF, IFN-γ, and LPS; M2a-like macrophages polarized with M-CSF, IL-10, and dexamethasone; and M2b-like macrophages polarized with M-CSF, IL-10, and IL-4. Histograms were generated from live, single cells, excluding debris and doublets. Markers showing positive signal: TREM2, MERTK, HLA-DR, FOLR2, CD206, CD45, CD14, CCR2, CD91, and CD71 were included in the heatmap presented in Figure 3-16. Samples were acquired on a SONY ID7000 spectral flow cytometer, with spectral unmixing and autofluorescence correction performed using SONY ID7000 software. Histogram were generated using CellEngine. Sample size: n = 2.

6.11 Appendix K: Expression of efferocytosis-associated surface markers in differentially polarized iMφ

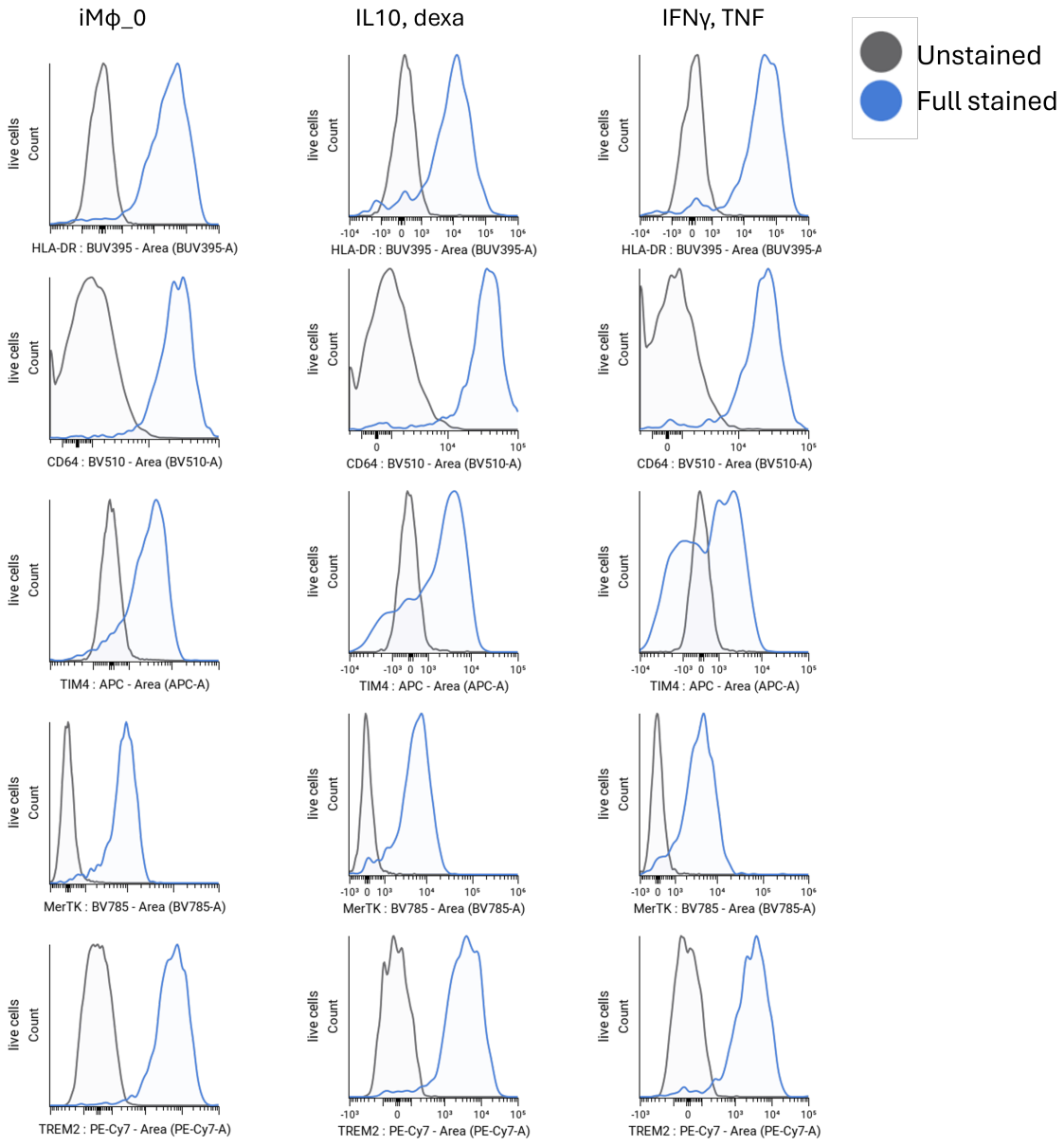

Figure 6-12 Supplementary Material: Polarization experiment of iPSC derived macrophages (iMφ) corresponding to data presented in Figure 3–19. Histograms compare unstained controls (grey) with fully stained iMφ samples (blue). These histograms were used to confirm specific marker expression and to exclude false-positive signals prior to inclusion in the heatmap. Data were gated to exclude debris and doublets. Samples were acquired using the SONY ID7000 spectral flow cytometer, with spectral unmixing and autofluorescence correction performed using SONY ID7000 software. Histograms were generated using CellEngine. The experiment was performed with n = 4 biological replicates; one representative replicate is shown.

6.12 Appendix L: Pharmacological modulation of efferocytosis markers in iMφ under different polarization conditions.

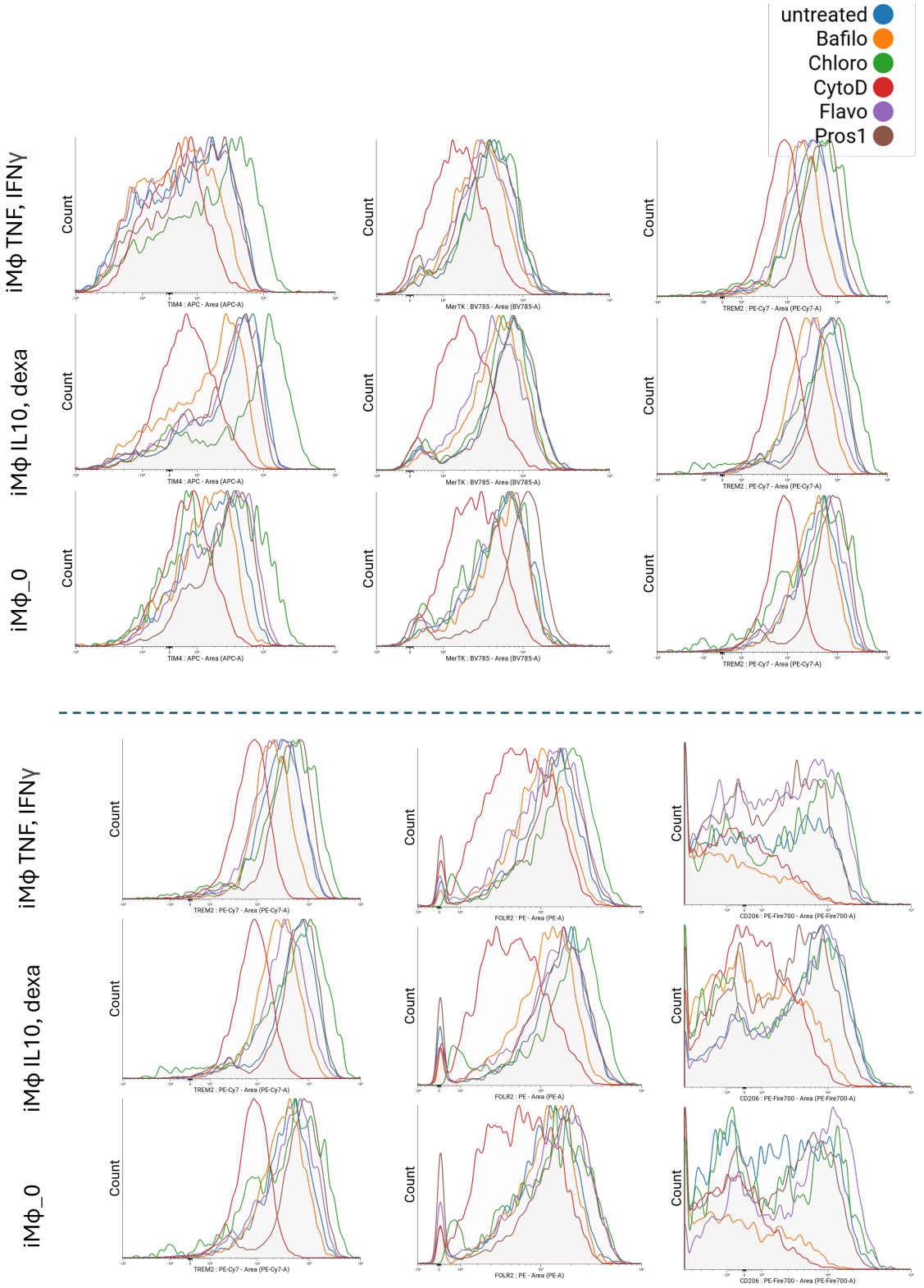

Figure 6-13 Impact of cytokine polarization and efferocytosis modulators on efferocytosis-linked surface marker expression in iMΦ. CytoD: 10 µM Cytochalasin D; Chloro: 100 nM Chloroquine; Bafilo: 10 µM Bafilomycin A1; Flavo: 10 µM Flavopiridol; Pros1: 5 µM Protein S1. bHistograms showing eefferocytosis linked markers expression across different treatment conditions and efferocytosis modulators. Data were obtained from gated viable CD45^{+} single cells, with debris

and doublets excluded. Samples were acquired using a Sony ID7000 spectral analyzer with the DISCOVERER M assay. Spectral unmixing and autofluorescence correction were performed using Sony ID7000 software. Data analysis was conducted with CellEngine.

6.13 Appendix M: Synovial fluid patient group anaylsis

a)

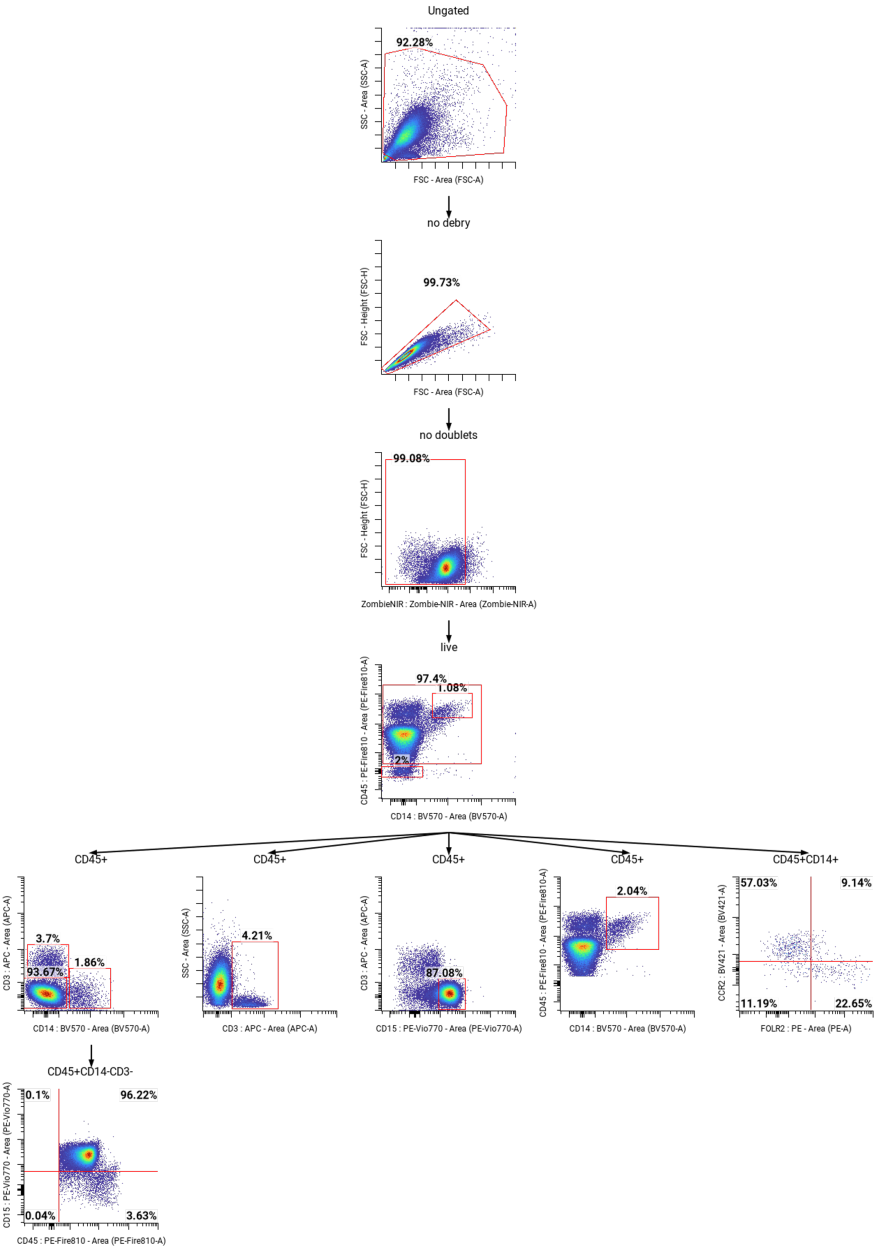

b)

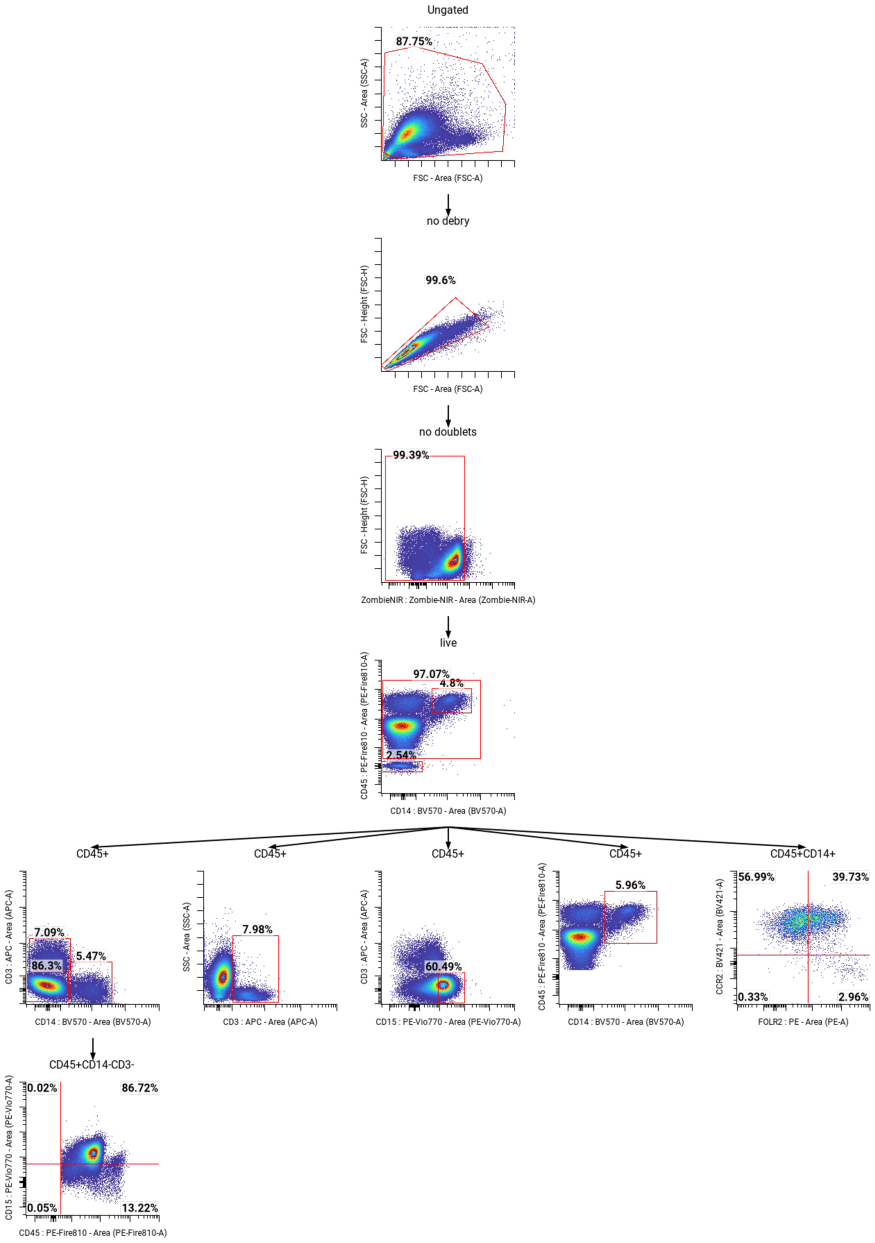
Ungated
87.75%
SSC - Area (SSC-A)
FSC - Area (FSC-A)
no debry
99.6%
FSC - Height (FSC-H)
FSC - Area (FSC-A)
no doublets
99.39%
FSC - Height (FSC-H)
ZombieNIR : Zombie-NIR - Area (Zombie-NIR-A)
live
97.07%
4.8%
2.54%
CD45 : PE-Fire810 - Area (PE-Fire810-A)
CD14 : BV570 - Area (BV570-A)
CD45+
CD45+
CD45+
CD45+
CD45+CD14+
7.09%
86.3%
5.47%
CD3 : APC - Area (APC-A)
CD14 : BV570 - Area (BV570-A)
7.98%
SSC - Area (SSC-A)
CD3 : APC - Area (APC-A)
60.49%
CD3 : APC - Area (APC-A)
CD15 : PE-Vio770 - Area (PE-Vio770-A)
5.96%
CD45 : PE-Fire810 - Area (PE-Fire810-A)
CD14 : BV570 - Area (BV570-A)
56.99%
39.73%
0.33%
2.96%
CCR2 : BV421 - Area (BV421-A)
FOLR2 : PE - Area (PE-A)
CD45+CD14-CD3-
0.02%
86.72%
0.05%
13.22%
CD15 : PE-Vio770 - Area (PE-Vio770-A)
CD45 : PE-Fire810 - Area (PE-Fire810-A)

c)

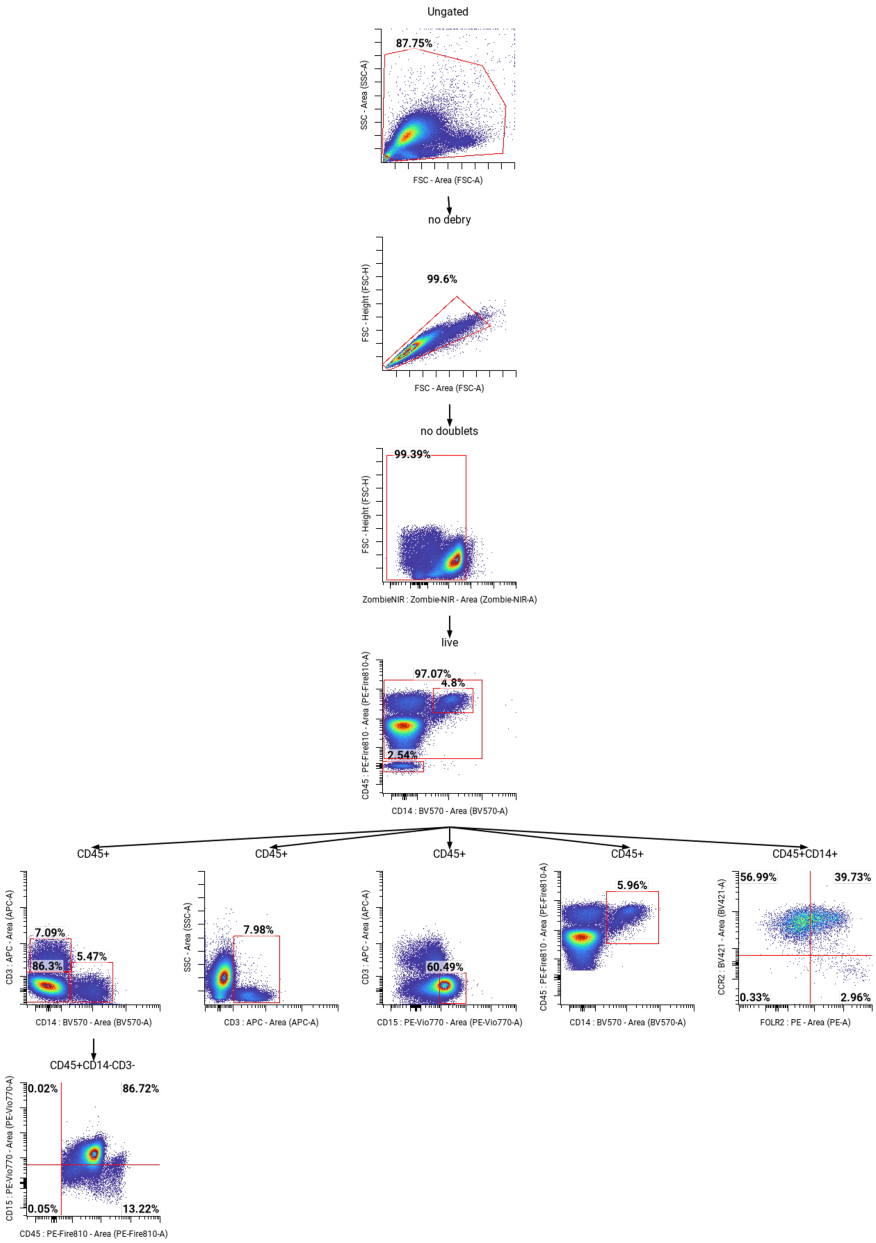

Figure 6-14 Additional plots to support analysis of human synovial fluid cells from arthritis patients using the *Discover Mφ* assay and spectral flow cytometry. Viable synovial fluid cells were thawed and enzymatically treated with hyaluronidase and DNase I to generate single-cell suspensions. Cells were subsequently labeled with a multidimensional antibody panel for spectral flow cytometry-based immunophenotyping. a) Gating strategy used to identify major synovial fluid cell populations. CD45 and CD14 expression were used to distinguish leukocytes ($CD45^+$), monocytes/macrophages ($CD45^+CD14^+$), and $CD45^-$ structural cells. Further discrimination of macrophage subsets was achieved using CCR2 and FOLR2, allowing the identification of infiltrating monocytes/macrophages ($CCR2^+FOLR2^-$) and tissue-resident macrophages ($CCR2^-FOLR2^+$).

Danksagung

Firstly, I would like to thank PD Dr. Mojca Frank-Bertoncelj for her guidance, inspiring scientific discussions and input throughout my doctoral research. Like many PhD journeys, ours included both challenges and productive moments, but ultimately led to valuable results for which I am grateful.

I would also like to sincerely thank my TAC members, Prof. Schulz and Prof. Reichel, for their consistently valuable insights and thoughtful perspectives from outside the research group. Their exceptional availability, kindness, and willingness to provide timely support and constructive feedback were a constant source of motivation and are deeply appreciated.

I am grateful to the members of the PTA team for contributing to the environment in which this work was developed. I would like to thank Dr. Jeinmy Carolina Gámez Villamizar, Dr. Swathi Lingam, and Dr. Janine Lückgen for their support during this time. Special thanks go to the interns and master's students Horia Boursas, María del Pilar Palacios Cisneros, and Nika Bostic, with whom I had the pleasure of working. Their dedication and contributions during key experiments were invaluable to the success of this project. I would like to extend my sincere thanks to Tomasz Stadler, who has been far more than a colleague. His friendship, humor, relentless encouragement, and well-timed memes helped me through long nights, weekend shifts, and moments of exhaustion. Without his presence and his occasional pressure to go for a rage-run, this journey would have been significantly more difficult. Certain carefully imported supplies from Poland may also have contributed to maintaining morale at crucial moments.

I would like to thank JJIM for funding the project and BioMedX Institute for providing the facilities and an environment that enabled interdisciplinary collaboration. Special thanks go to Dr. Thomas Rückle for his support in navigating team dynamics and to my internal mentor Dr. Ozdemirhan Sercin for inspiring scientific discussions throughout my time at BioMedX.

Mein besonderer Dank gilt meinen Eltern Claudia und Martin, die mich auf meinem gesamten Weg bis zum Doktortitel begleitet und unterstützt haben, sei es im Sport oder im Akademischen. Ihr habt mich stets ermutigt, meine eigenen Entscheidungen zu treffen, mir mit Rat zur Seite gestanden und mich immer gestärkt, wenn es schwierig wurde. Ohne eure bedingungslose Unterstützung, euer Vertrauen und euren unerschütterlichen Glauben an mich wäre dieser Weg nicht möglich gewesen. Ebenso danke ich meinen Brüdern, die, obwohl sie ganz andere Wege gehen und sich für ganz andere Dinge begeistern, immer hinter mir standen.

Außerdem möchte ich meinem Freund David danken, den ich während meiner Promotionszeit kennengelernt habe. In schwierigen Phasen hat er mir geholfen, Dinge einzuordnen, mich emotional gestützt und mich nicht zuletzt mit gutem Essen versorgt. Seine Ruhe, seine Perspektiven und seine Fürsorge haben mir sehr geholfen, die herausfordernden Zeiten dieser Arbeit zu meistern. Er hat unvergessliche Urlaube organisiert, um mir den Kopf freizumachen, und unser Zuhause zu einem Ort gemacht, an dem ich mich ausruhen, sicher fühlen und neue Kraft schöpfen konnte. Ebenso danke ich seiner Familie, bei der ich von Anfang an herzlich aufgenommen wurde und mich immer willkommen fühlen durfte.

Zuletzt möchte ich meiner besten Freundin Caro danken, die immer für mich da ist, auch über räumliche Distanz hinweg. Ihre aufbauenden Gespräche, ihre Unterstützung und ihre Fähigkeit, mir in schwierigen Momenten zuzuhören, bedeuten mir sehr viel. Die gemeinsamen Auszeiten und Urlaube mit ihr waren wertvolle Erholungsmomente, die mir neue Energie gegeben haben.

Publikationsliste

Published

Edalat, S. G., Gerber, R., Houtman, M., Lückgen, J., Teixeira, RL., Cisneros, M., Pfanner, T., et al. (2024). *Molecular maps of synovial cells in inflammatory arthritis using an optimized synovial tissue dissociation protocol.* IScience, 27(6). DOI: 10.1016/j.isci.2024.109707

Planned submissions with working manuscript titles

Pfanner, T.*, Stadler, S.*, et al. (2025). *Discoverer Mϕ* – a spectral flow cytometry assay for macrophage phenotypes and functions across tissues and perturbations. (In preparation; submission planned 07/2025).

Pfanner T,* Lueckgen J.* et al. (2025). *Functional mapping of synovial macrophages in remission and active arthritis.* (In preparation; submission planned 08/2025).

*Authors contributed equally

Co-authored submissions with working manuscript titles

Lückgen J., et al. Sublining fibroblast-like synoviocytes at the intersection of tissue repair and fibrosis (submission planned winter /2025).

.. CRISPR Screen identifies regulators of microglia differentiation and efferocytosis. (submission planned for winter /2025).

Award-Winning Conference Presentations

Pfanner, T., et al. (2025, April 8–10). Discoverer Mϕ – a spectral flow cytometry assay for analysis of macrophage phenotypes and functions across tissues, pathologies and perturbations [Poster presentation]. Resolution Days 2025, Frankfurt, Germany. EFIS-EJI Young Investigator Travel Award.

Pfanner, T., et al. (2024). Fantastic macrophage functions and where to find them [Talk]. BioMedX Science Retreat 2024, Landau, Germany. Best Flash Talk Award.

Pfanner, T., et al. (2024). Developing multiparameter spectral flow cytometry assay with efferocytosis readout for macrophage phenotyping [Poster presentation]. BioMedX Science Retreat 2024, Landau, Germany. Awarded Best Flash Talk.

Conference Presentations

Pfanner, T., et al. (2024, September). Functional mapping of human tissue macrophages across organs, inflammatory pathologies, and drug perturbations [Poster presentation]. Human Cell Atlas Meeting, Milan, Italy.

Lückgen, J., Crowell, H. J., Pfanner, T., et al. (2025, April 8–10). Spatially resolved functional maps of synovial macrophages and structural cells in remission and inflammatory arthritis [Conference talk and poster presentation]. Resolution Days 2025, Frankfurt, Germany.

Lückgen, J., Pfanner, T., et al. (2024, October 9). Pro-resolving macrophages hold potential for cell-based therapy in immune-mediated inflammatory diseases [Conference talk]. BioRN Annual Conference 2024, Heidelberg, Germany.

Lückgen, J., Martinez-Martin, N., Pfanner, T., et al. (2024, September 29–30). Architecture of inflamed human synovial joint at a single cell resolution [Poster presentation]. Human Cell Atlas General Meeting, Milan, Italy.

Stadler, T., Pfanner, T., et al. 2025. iPSC-Derived Tissue-Resident-Like Immune Cells: A Platform for Identifying Pro-Resolution Molecular Targets with CRISPR- and Drug-Based Perturbations. [Poster presentation]. Resolution Days 2025, Frankfurt, Germany.

Übereinstimmungserklärung

LMU LUDWIG-MAXIMILIANS-UNIVERSITÄT MÜNCHEN | Promotionsbüro Medizinische Fakultät | MMRS

Erklärung zur Übereinstimmung der gebundenen Ausgabe der Dissertation mit der elektronischen Fassung

Pfanner, Tamara

Name, Vorname

Hiermit erkläre ich, dass die elektronische Version der eingereichten Dissertation mit dem Titel:

**Foundations for Pro-Resolution Target Discovery:
Integrating Human Macrophage Phenotypic and Functional Diversity in Homeostasis and Immune-Mediated Inflammatory Diseases**

in Inhalt und Formatierung mit den gedruckten und gebundenen Exemplaren übereinstimmt.

Heidelberg, 28.11.2025 — Ort, Datum

Tamara Pfanner — Ihre Unterschrift

Affidavit

Eidesstattliche Versicherung

Pfanner, Tamara

Name, Vorname

Ich erkläre hiermit an Eides statt, dass ich die vorliegende Dissertation mit dem Titel:

**Foundations for Pro-Resolution Target Discovery:
Integrating Human Macrophage Phenotypic and Functional Diversity in Homeostasis and Immune-Mediated Inflammatory Diseases**

selbständig verfasst, mich außer der angegebenen keiner weiteren Hilfsmittel bedient und alle Erkenntnisse, die aus dem Schrifttum ganz oder annähernd übernommen sind, als solche kenntlich gemacht und nach ihrer Herkunft unter Bezeichnung der Fundstelle einzeln nachgewiesen habe.

Ich erkläre des Weiteren, dass die hier vorgelegte Dissertation nicht in gleicher oder in ähnlicher Form bei einer anderen Stelle zur Erlangung eines akademischen Grades eingereicht wurde.

Heidelberg, 28.11.2025 — Ort, Datum

Tamara Pfanner — Ihre Unterschrift